Contactless Method for Studying the Parameters of the Electrode Region of an RF Discharge

A. F. Aleksandrov, V. A. Ryaby, V. P. Savinov, and V. G. Yakunin

Moscow State University, Vorob'evy gory, Moscow, 119899 Russia

Received May 5, 2002

Abstract—A nonintrusive contactless method for studying the parameters of the electrode region of a capacitive low-pressure RF discharge is proposed. The method involves the measurements of dc and ac electric voltages at the elements of the discharge circuit with subsequent calculations of both the electrostatic potential drop across the electrode sheath and the sheath thickness by using relations derived in the paper. For a collisionless electrode sheath, the density of the positive-ion current onto the electrode and the charge density at the plasma boundary are determined. It is shown experimentally that the method can be successfully applied to studying capacitive RF discharges with inner or outer electrodes. © 2002 MAIK "Nauka/Interperiodica".

1. INTRODUCTION

Experimental studies of the physical characteristics of boundary space-charge sheaths are important for both the investigation of the mechanisms governing capacitive RF discharges (CRFDs), which are widely used in practice, and the control of the plasmochemical processes in microelectronic industry. In manufacturing systems in which processed substrates are located on the discharge electrodes, space-charge electrode sheaths (SCESs) are immediately adjacent to the surfaces of the processed plates. Therefore, the studies of the characteristics of the electrode region enable the monitoring of the internal system parameters characterizing the state of the working medium immediately in the processing region. It is evident that only this type of monitoring can ensure the high reproducibility of a technological process.

In this paper, we propose a contactless method for monitoring the quasi-steady characteristics of a CRFD used in plasmochemical reactors, namely, the potential drop U_s across the SCES and the SCES thickness d_s. In the case of a collisionless electrode sheath, widely met in practice, this method also allows one to determine the density of the positive-ion current j_i from the plasma onto the electrode and the charge density $n_e = n_i$ at the SCES–plasma boundary.

The method proposed implies the space and time averaging of the quantities under study; hence, the highest accuracy can be achieved when diagnosing a reactor with a uniform processing of the plate surface.

This method was experimentally tested in CRFDs in helium at gas pressures of 0.3–0.5 torr and RF-field frequencies of $f = 0.64$–2 MHz. The experiments were carried out in a discharge tube with inner electrodes; simultaneously, Langmuir probe measurements were performed. Fairly good agreement between the results obtained with these two methods (within 10–15% for

the U_s measurements) allowed us to apply the contactless method to studying CRFDs with outer electrodes; previously, experimental techniques for such measurements were unavailable.

2. THEORY

We consider a CRFD with plane electrodes E_1 and E_2 of areas S_1 and S_2, respectively. The electrodes are coated with dielectric films; the capacitances between the electrodes and the imaginary second plates on the side of the interelectrode space are C_1^* and C_2^* (Fig. 1). A coupling capacitor C_{01} is introduced into the circuit between the RF oscillator and the electrode E_1. The electrode E_2 is grounded through a coupling capacitor C_{02}, which is introduced to accomplish the measurement method proposed. The physical scheme of the CRFD under study is shown in Fig. 1a. Here, the hatched domain inside the discharge gap shows the plasma, which is separated from the electrodes by SCESs with quasi-steady thicknesses d_{s1} and d_{s2}.

Our approach is based on three basic assumptions:

(i) The conduction ion current through the sheath is quasi-steady; i.e.,

$$1/\tau < \omega \ll \omega_{Le}, \qquad (1)$$

where τ is the time during which an ion traverses the sheath, $\omega = 2\pi f$ is the angular frequency of the RF field, and ω_{Le} is the electron plasma frequency at the sheath boundary.

(ii) The displacement current plays a dominant role in the sheath; i.e., the following relation between the

(a)

(b)

Fig. 1. (a) Physical model of the CRFD under study and (b) the equivalent circuit of the discharge: U_{01}, U_{02}, and U_d are voltmeters for measuring the quasi-steady voltages; V_{01} and V_d are voltmeters for measuring ac voltages; and R_p, L_p, and C_p are the resistance, inductance, and capacitance of the CRFD plasma, respectively.

resistance and the capacitive reactance of the SCES is satisfied:

$$R_{s1,2} \gg \frac{1}{\omega C_{s1,2}}. \tag{2}$$

In this case, the SCESs can be represented as capacitances $C_{s1,2}$ in the discharge equivalent circuit (see Fig. 1) [1].

(iii) The contribution of charged particles to the permittivity ε_s of the sheath is negligible; i.e., $\varepsilon_s \approx 1$.

Then, we can write the following set of equations:

$$q_1 = U_{s1}C_{s1} = U_1^*C_1^* = U_{01}C_{01}, \tag{3}$$

$$q_2 = U_{s2}C_{s2} = U_2^*C_2^* = U_{02}C_{02}, \tag{4}$$

$$U_d + U_{s1} - U_{s2} - U_1^* + U_2^* = 0, \tag{5}$$

$$V_{01}/V_d = C_d/C_{01}, \tag{6}$$

where q_1 (q_2) is the quasi-steady value of the charge at the capacitor C_{s1} (C_{s2}) [according to the electrostatic induction law, the same charge is induced at the neighbor capacitors C_1^* (C_2^*) and C_{01} (C_{02})]; U_{s1} (U_{s2}) is the quasi-steady potential drop across the corresponding SCES; U_d is the total quasi-steady voltage drop across

the discharge; and V_{01} and V_d are the ac voltage drops at the capacitor C_{01} and the discharge capacitor C_d, respectively.

Equation (5) describes the balance of the electrostatic voltages in the discharge, whose interelectrode distance is d. Equation (6) describes the distribution of the ac voltage across the circuit segment between points B and D and on the capacitor C_{01} (Fig. 1b); i.e., there is a sort of a capacitive divider of the RF voltage drop in the discharge circuit.

The unknown variables in Eqs. (3)–(6) are the SCES parameters U_{s1}, U_{s2}, C_{s1}, and C_{s2}.

Combining Eqs. (3)–(6), we find

$$U_{s2} = U_{s1} + U_d - U_{01}C_{01}/C_1^* + U_{02}C_{02}/C_2^*. \tag{7}$$

The total discharge capacitance C_d can be written as

$$C_d = (C_{s1}^{-1} + C_{s2}^{-1} + C_1^{*-1} + C_2^{*-1})^{-1} + C_E,$$

where C_E is the interelectrode capacitance of the discharge gap. Taking this formula into account and using

Eqs. (3), (4), (6), and (7), we find

$$U_{s1} = [V_d/(V_{01}C_{01} - V_dC_E)$$

$$+ C_1^{*-1}(U_{01}C_{01}/U_{02}C_{02} - 1) \qquad (8)$$

$$- U_d/U_{02}C_{02} - 2/C_2^*](1/U_{01}C_{01} + 1/U_{02}C_{02})^{-1}.$$

The SCES thicknesses d_{s1} and d_{s2} can be determined by using Eqs. (3) and (4) and the formula for the capacitance of a plane capacitor $C_s = \varepsilon_s S/4\pi d_s$.

As a result, in view of assumption (iii), we obtain

$$d_{s1} = S_1 U_{s1}/4\pi U_{01}C_{01}, \qquad (9)$$

$$d_{s2} = S_2 U_{s2}/4\pi U_{02}C_{02}. \qquad (10)$$

In Eqs. (5)–(8), the measured quantities are the dc and ac voltages at the capacitor C_{01} and the discharge electrodes, as well as the dc voltage at the capacitor C_{02}.

Turning from the physical model of the CRFD circuit to an actual experimental circuit and the measurement procedure, we will justify the applicability of the method proposed.

An idea to represent a SCESs as capacitors under condition (2) was first proposed in [2] and was, then, verified experimentally by one of us [3] with the method of the so-called "ionization capacitor."

In our case too, the resistance of the plasma column is assumed to be much less than both the plasma reactance and the SCES impedances:

$$R_p \ll 1/\omega C_p, \quad R_p \ll \omega L_p,$$

$$R_p \ll R_{s1,2}, \quad R_p \ll 1/\omega C_{s1,2}, \qquad (11)$$

where C_p and L_p are the plasma capacitance and inductance, respectively.

In order to justify the adopted model, let us make some estimates for our experimental conditions: the working gas is He; $p = 0.5$ torr; $f = 2$ MHz; $\omega = 1.3 \times 10^7$ s^{-1}, $d_{s1,2} \approx 1$ cm; the field strength in the sheath is $E_s \approx 100$ V/cm; the electron–neutral and ion–neutral collision frequencies are $\nu_{en} \approx 10^9$ s^{-1} and $\nu_{in} \approx 10^7$ s^{-1}, respectively; the plasma electron density in the center of the discharge is $n_e \approx 10^8$–10^9 cm^{-3} [4] (for RF voltages used); and the ion mass is $M = 6.64 \times 10^{-24}$ g.

First, we verify whether inequality (1) holds. We have $\tau = d_s/v_i$, where the average ion velocity in the sheath is $v_i = b_i E_s$, the ion mobility being $b_i = e/M\nu_{in}$. It follows from here that $\tau \approx 5 \times 10^{-7}$ s and $1/\tau = 2 \times 10^6$ s$^{-1} < \omega$. In the above range of the plasma charge densities, we have 0.6×10^9 s$^{-1} \leq \omega_{Le} \leq 1.9 \times 10^9$ s^{-1} and, consequently, $\omega_{Le} \gg \omega$. Hence, inequality (1) holds.

Next, we verify whether inequality (2) holds. Taking into account the experimental value of the ion density in the SCES ($n_{is} \approx 10^7$–10^8 cm^{-3}) and the values of the
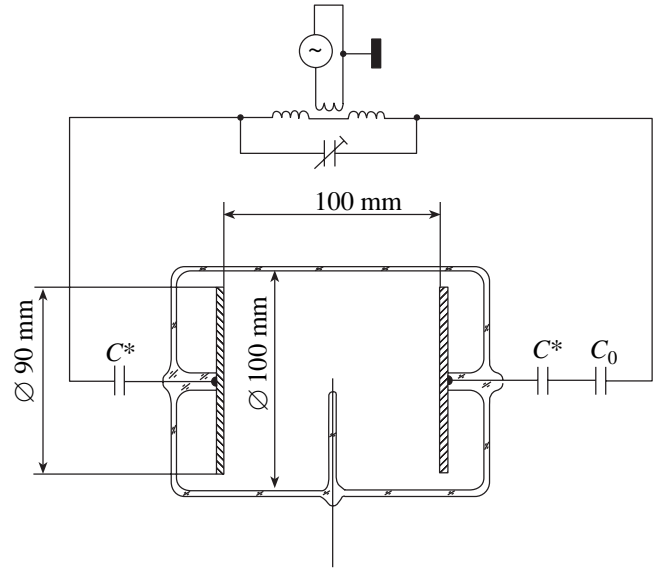
Fig. 2. Schematic of a discharge tube with inner electrodes for conducting contactless and probe measurements.

electrode area ($S = 78$ cm^2) and the SCES capacitance ($C_s = S/4\pi d_s = 7$ pF), we find the SCES capacitive reactance,

$$1/\omega C_s \approx 10 \text{ k}\Omega.$$

The SCES resistance can be estimated as $R_s = d_s/\sigma_{is}S$, where $\sigma_{is} = e^2 n_{is}/M\nu_{in}$ is the sheath conductance. It follows from here that $R_s \gg 30$ kΩ; i.e., inequality (2) holds.

According to [1], the ions make the main contribution to the sheath permittivity:

$$\varepsilon_s = 1 - \frac{\omega_{Li}^2}{\omega^2 + \nu_{in}^2},$$

where ω_{Li} is the plasma ion frequency. In this case, it follows from the experimental data of [4] that, under our testing conditions (see Figs. 4, 5), we have

$$\omega_{Li}^2 \ll \omega^2 + \nu_{in}^2, \quad \varepsilon_s \approx 1.$$

Then, we verify whether inequalities (11) hold under our experimental conditions. Let us compare the plasma resistance R_p and the plasma reactances $1/\omega C_p$ and ωL_p. First, we consider the expression for the plasma capacitance

$$C_p = \varepsilon_p S/4\pi d_p,$$

where $\varepsilon_p \approx 1 - \omega_{Le}^2/(\omega^2 + \nu_{en}^2)$ is the plasma permittivity [1] and d_p and S are the length and cross-sectional area of the plasma column, respectively. Note that, when $\omega_{Le} \leq \nu_{en}$, we have $\varepsilon_p > 0$ and the plasma reactance is capacitive in nature. In contrast, when the inequality
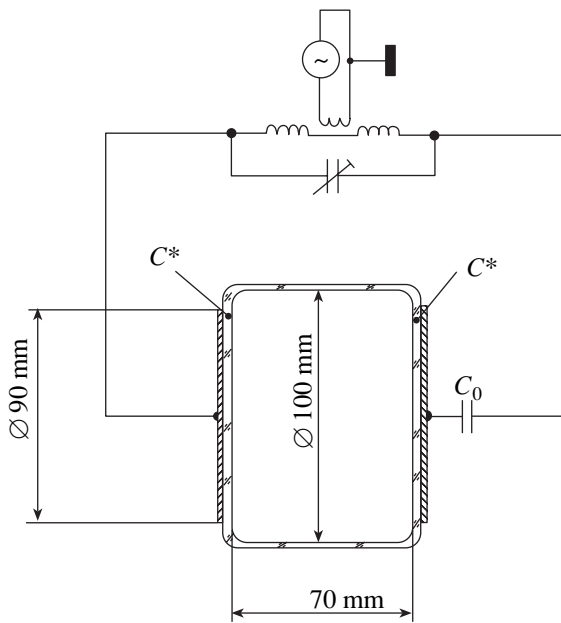
Fig. 3. Schematic of a discharge tube with outer electrodes for conducting contactless measurements of the SCES parameters.
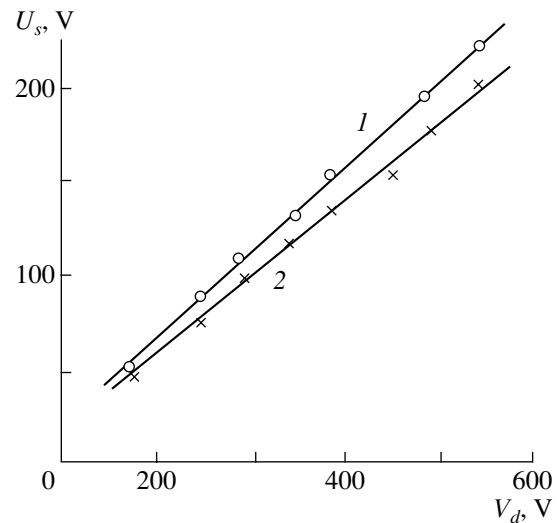

Fig. 4. Quasi-steady voltage drop U_s across the SCES of a discharge with inner electrodes as a function of the amplitude V_d of the applied RF voltage (CRFD in helium, $p = 0.5$ torr, $f = 1$ MHz, and $C_0 = 10$ pF): (*1*) probe measurements and (*2*) contactless measurements.

$\omega_{Le}^2 > \omega^2 + \nu_{en}^2$ holds, we have $\varepsilon_p < 0$ and the plasma reactance is inductive in nature.

Taking into account the above discharge parameters, it is easy to find the relations between the resistance and capacitive reactance of the plasma,

$$\frac{R_p}{1/\omega C_p} \leq 2 \times 10^{-2},$$

and between the resistance and inductive reactance of the plasma,

$$2 \times 10^{-3} \leq \frac{R_p}{1/\omega L_p} \leq 9 \times 10^{-3}.$$

In a similar way, by analyzing the relations between the plasma resistance and the capacitive reactance and resistance of the SCES, we obtain

$$2 \times 10^{-1} \leq \frac{R_p}{1/\omega C_s} \leq 2 \times 10^{-2},$$

$$\frac{R_p}{R_s} \approx 10^{-2}.$$

Hence, inequalities (11) also hold under our experimental conditions.

The breakdown of the discharge gap and the development of the discharge are accompanied by the formation of SCESs, which enable the CRFD to arrive at a steady state. As was observed experimentally [5], in a steady-state CRFD, the net electric charge arriving at the electrode over one RF-field period ($T \leq 10^{-6}$ s) is

zero. Accordingly, the quasi-steady parameters of the SCES capacitor (namely, the capacitance C_s, the charge q_s, and the sheath thickness d_s) remain constant. In this case, the charge q_s maintains the quasi-steady voltage U_s across the SCES, so the charge of the electrons arriving from the plasma at the electrode over one RF-field period balances the charges of both the incoming positive ions and the electrons emitted from the electrode surface.

In the CRFD circuit segment (Fig. 1b) consisting of the series-connected capacitors C_{01}, C_1^*, and C_{s1}, the active element is the capacitor C_{s1}. It is the charge on its plates, q_{s1}, that governs the physical processes in the SCES. Note that all of the series-connected capacitors of the circuit, including in the measurement capacitor C_{01}, acquire this quasi-steady charge q_{s1}.

The quasi-steady voltages U_{01}, U_{02}, and U_d in the experimental circuit were measured by C-95 electrostatic voltmeters with a small input capacitance of $C' = 5$ pF. The measuring circuit of these devices is an open circuit for direct currents, which excludes the charge leakage from the capacitor under study through the measuring circuit. To exclude the influence of the RF voltage on the voltmeter readings, we used an integrator consisting of two resistors R and a capacitor C with a properly chosen parameters (Fig. 1b).

To avoid a possible influence of the dc electric circuit of the output stage of the RF oscillator on the operation of the experimental circuit, the RF power was fed to the discharge gap through a transformer (Figs. 2, 3).

The RF voltages V_{01} and V_d were measured by V7-15 electronic voltmeters with a high internal resistance. These devices were equipped with DN-2 voltage dividers and remote high-resistance heads with a low input capacitance; this allowed us to operate over wide ranges of frequencies (5 kHz–300 MHz) and voltages ($V \leq 1$ kV). Similar measurements were also performed with C-95 voltmeters.

Thus, the method proposed includes the measurements of the voltage at several external elements of the CRFD circuit and the calculations of the sought parameters by using the above formulas and the known parameters of the experimental setup.

It can be easily seen that, in a particular case of a very long discharge gap ($C_E \approx 0$) or when the dielectric film on the electrode surfaces is either absent or extremely thin (i.e., when the values of C_1^* and C_2^* are large), Eqs. (5)–(8) are considerably simplified.

If positively charged ions in the SCES do not collide with atoms (which occurs when the ion mean free path satisfies the inequality $\lambda_i = 1/n_a Q_{ia} \geq d_s$, where n_a is the atom density and Q_{ia} is the resonant charge-exchange cross section for ions; this condition is usually satisfied at gas pressures of $p \leq 10^{-1}$ torr), then the ion current density at the electrodes can be estimated by the Child–Langmuir formula [6]

$$j_i = \frac{1}{9\pi}\sqrt{\frac{2e}{M_i}}\frac{U_s^{\frac{3}{2}}}{d_s^2},$$

where e is the electron charge and M_i is the ion mass. With a known electron temperature T_e, according to the Bohm formula [6]

$$j_i \approx 0.8 e n_i \sqrt{\frac{2kT_e}{M_i}},$$

we can estimate the ion density at the boundary of the quasineutral plasma:

$$n_i = 1.25 j_i / e \sqrt{\frac{2kT_e}{M_i}}.$$

2. EXPERIMENTAL TESTING OF THE CONTACTLESS DIAGNOSTIC METHOD

The method was tested in a symmetric CRFD with plane inner or outer electrodes (Figs. 2, 3).

In the experiments, we used sealed tubes filled with helium. The plane inner electrodes 90 mm in diameter were spaced by 100 mm. The outer electrodes 90 mm in diameter were spaced by 78 mm and separated from the discharge by optically transparent quartz plates 4 mm thick. Both types of discharges satisfied the condition

$$C_E \ll C_0 V_0 / V_d.$$
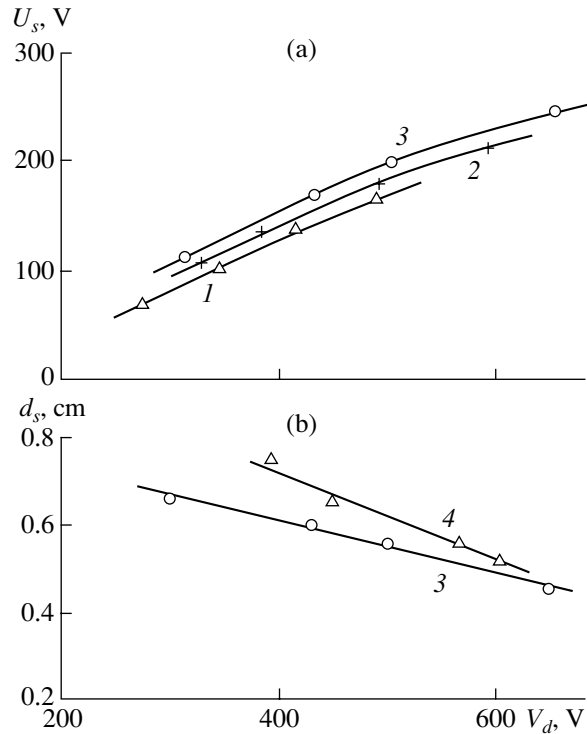
Fig. 5. (a) Quasi-steady potential drop U_s across the SCES and (b) the SCES thickness d_s a discharge with outer electrodes as functions of the amplitude V_d of the applied RF voltage (CRFD in helium, $p = 0.5$ torr, and $C_0 = 10$ pF) for the RF-field frequency $f =$ (1) 0.64, (2) 1, (3) 2, and (4) 1.6 MHz.

In this case, expressions (7) and (8) for a discharge with outer electrodes can be reduced to one formula

$$U_s = U_0 C_0 (V_d / 2V_0 C_0 - 1/C^*).$$

This formula becomes even simpler for a discharge with inner electrodes:

$$U_s = U_0 V_d / 2V_0.$$

The SCES thickness for both types of discharges is defined by the formula

$$d_s = S U_s / 4\pi U_0 C_0.$$

In the first stage of experiments, we used a CRFD with inner electrodes at gas pressures of 0.3–0.5 torr and RF-field frequencies of 0.64–2 MHz. The contactless measurements of the quasi-steady voltage U_s were checked with a special probe circuit consisting of high-value resistors and an M-193 microammeter shunted with a capacitor. The parameters of this circuit were chosen so as to ensure the high measurement accuracy. The probe was located in the center of the discharge gap.

To verify whether instrumental effects influence the contactless measurements, we checked the dependence

of the measured quasi-steady voltage U_s on the capacitance of the measuring capacitor C_{01}. In the course of experiment, the capacitance C_{01} was varied within 10–30000 pF. In this case, the values of U_s measured by two methods differed by 10–15% irrespective of the capacitance C_{01}.

Let us compare the RF-field period ($T \approx 10^{-6}$ s) with the discharge times τ_{01} and τ_{02} of the measuring capacitors ($C_{01} = C_{02} = 50$ pF), taking into account the equivalent electric circuit (Fig. 1b), in which the electrostatic voltmeters U_{01}, U_{02}, and U_d break the circuit for direct currents and the electronic voltmeters V_{01} and V_d have internal resistances of $R_{01} = R_d = R_V \approx 10^6 \; \Omega$.

(i) For the capacitor C_{01} (CRFDs with outer or inner electrodes), we have

$$\tau_{01} = R_{01}C_{01} = R_V C_{01} \approx 5 \times 10^{-5} \text{ s,}$$

i.e.,

$$\tau_{01} \gg T.$$

(ii) For the capacitor C_{02} in the case of a CRFD with outer electrodes, we have

$$\tau_{02} \approx (R_d + R_{01})C_{02}$$
$$= 2R_V C_{02} \approx 10^{-4} \text{ s} \gg T;$$

and, in the case of a CRFD with inner electrodes, we have

$$\tau_{02} \approx (2R_s + R_p + R_{01})C_{02}$$
$$\approx R_V C_{02} \approx 5 \times 10^{-5} \text{ s} \gg T.$$

Hence, the charges of the capacitors C_{01} and C_{02} change only slightly over one RF-field period and the measured quasi-steady voltages U_{01} and U_{02} are nearly constant.

These data testify to the correctness of the contactless measurements of the quasi-steady potential drop U_s across the SCES.

The results of measurements by both methods are presented in Fig. 4. The agreement between these measurements can be considered satisfactory, taking into account both the systematic measurement errors discussed below and the fact that the probe measurements were conducted locally in the center of discharge at the tube axis.

Before performing measurements in a CRFD with outer electrodes, we carried out a model experiment. We used a CRFD with inner electrodes, whereas the dielectric coating of outer electrodes was modeled by capacitors whose capacitance ($C^* = 50$ pF) was equal to the preliminarily measured capacitance of the quartz wall at the end of the discharge tube (Fig. 2). The U_s values measured in this experiment by the probe and contactless methods differed by nearly 10%.

Naturally, the parameters of the SCES in a discharge with outer electrodes were determined by the contactless method only. The results of these measurements are presented in Fig. 5. It can be seen that the measured values of the SCES parameters U_s and d_s are close to the corresponding values for a CRFD with inner electrodes. The U_s value increases with increasing RF-field frequency, as was previously observed in [4].

3. DISCUSSION OF RESULTS

Strictly speaking, a correct comparison of the values of the quasi-steady potential drops U_s across the electrode sheaths measured with the probe and contactless methods is possible only if we know the distribution of the electrostatic potential in a discharge. Since we did not examine these distributions in our study, a comparative analysis was performed by using the relevant data available in the literature. In this context, we note the experiment of [7], where it was shown that there may exist some quasi-steady potential difference between the center of the discharge and the SCES boundary. This effect was not taken into account in the contactless method.

As can be seen in Fig. 4, the difference between the data obtained by the two methods is systematic in character: the curve obtained by the contactless method lies below that obtained from probe measurements. In addition to the above-said, there is at least one more reason for the discrepancy observed. The matter is that, in the equivalent electric circuit of the CRFD, the electrode sheath is represented as a plane capacitor. However, in a real situation, only one plate of this capacitor (namely, the electrode surface) is plane. The second plate is substantially curved because of the nonuniform radial distribution of the charged-particle density in the discharge tube. Clearly, the actual SCES capacitance is lower and the RF voltage drop across the sheath is greater, which results in a larger potential drop U_s across the sheath due to the so-called "RF-detection" effect [8]. Hence, a correction of the parameters of the near-electrode capacitor C_s should reduce the observed 10–15% discrepancy with the results of the approved probe technique.

In summary, we can conclude that the experimental testing of the nonintrusive contactless method has demonstrated its high efficiency. The method made it possible to measure for the first time the parameters of the electrode region of a CRFD with outer electrodes; the results of these measurements are of considerable interest, in particular, for plasmochemical technology.

REFERENCES

1. A. F. Aleksandrov, Zh. Tekh. Fiz. **35**, 35 (1965) [Sov. Phys. Tech. Phys. **10**, 24 (1965)].
2. E. Appleton and F. Childs, Philos. Mag. **10**, 969 (1930).
3. A. F. Aleksandrov and A. A. Kuzovnikov, Izv. Vyssh. Uchebn. Zaved., Radiofiz. **11**, 1548 (1968).
4. V. L. Kovalevskiĭ and V. P. Savinov, Fiz. Plazmy **20**, 322 (1994) [Plasma Phys. Rep. **20**, 292 (1994)].
5. V. P. Savinov and V. G. Yakunin, in *Proceedings of the 19th International Conference on Phenomena in Ionized Gases, Belgrad, 1989*, p. 220.
6. Yu. P. Raizer, *Gas Discharge Physics* (Springer-Verlag, Berlin, 1991; Nauka, Moscow, 1992).
7. A. A. Kuzovnikov and V. P. Savinov, Vestn. Mosk. Gos. Univ., Ser. 3: Fiz., Astron., No. 2, 215 (1973).
8. H. Butler and G. Kino, Phys. Fluids **6**, 1346 (1963).

Translated by N.F. Larionova

Measurement of the Electric Conductivity of Tungsten in a Continuous Liquid-to-Gas Transition

V. N. Korobenko, A. D. Rakhel, A. I. Savvatimskiy, and V. E. Fortov

Institute for High Energy Densities, Associated Institute for High Temperatures, Russian Academy of Sciences,
Izhorskaya ul. 13/19, Moscow, 125412 Russia

Abstract—A method is developed that makes it possible to investigate the transition of a metal from a condensed to a gaseous phase while maintaining almost uniform temperature and pressure distributions in the sample. The method consists in the pulsed Joule heating of a sample in the form of a thin foil strip placed between two relatively thick glass plates. This method is used to measure the conductivity of tungsten in a process during which the pressure in the sample is maintained at a level of 40–60 kbar and the density of the sample decreases from the normal solid density to a density 20 to 30 times lower. It is found that, along the 40-kbar isobar, the density dependence of the conductivity of tungsten changes radically at a certain density value, at which it has a pronounced kink. At the kink, the density of tungsten is approximately ten times lower than its characteristic solid density, and the internal energy is about two times the sublimation energy. The method makes it possible to carry out experiments with the almost isobaric heating of tungsten in the parameter range in which the effect in question takes place. No such effect is detected in nonisobaric processes. © *2002 MAIK "Nauka/Interperiodica".*

1. INTRODUCTION

The problem of transitions of metals from a liquid to a gaseous phase was considered in the well-known paper by Zel'dovich and Landau [1]. They noticed that there is no qualitative difference between metallic and dielectric states at finite temperatures; therefore, transitions from one state to another may be continuous. Since metal vapors are dielectrics, transitions from a condensed metal phase to a gaseous dielectric phase may also be continuous. The question then arises as to the character of the phase diagrams of metals in the region where these transitions take place. Zel'dovich and Landau [1] predicted that low-melting-point metals should undergo two separate first-order phase transitions, specifically, liquid-to-vapor and metal-to-dielectric transitions. Moreover, the critical point for the latter transition was predicted to lie in the range of temperatures and pressures that are much higher than those for the liquid-to-vapor transition. In [1], it was also predicted that, for refractory metals, the liquid-to-vapor and metal-to-dielectric transition curves should coincide.

Subsequent measurements carried out in [2, 3] for low-melting-point metals showed that, as the density decreases, the metal-to-dielectric transition actually occurs separately from the liquid-to-vapor transition. However, it was found that, during the metal-to-dielectric transition, the speed of sound, electric conductivity, and other physical parameters change continuously, in contrast to the case of liquid-to-vapor transition. For mercury, the density at which the metal-to-dielectric transition occurs is higher than the critical-point density for the liquid-to-vapor transition, while, for alkali metals, this transition occurs at densities close to the critical-point density. However, the question about the critical point for the metal-to-dielectric transition remained unanswered because of the difficulties in performing precise measurements at high pressures and temperatures. Efforts to obtain reliable experimental data for refractory metals were also unsuccessful.

In a number of papers, attempts were made to measure the electric conductivity of refractory metals in a wide density range. In [4–7], this was done by means of the exploding wire technique. A segment of a straight wire was placed into a condensed medium (water, a glass capillary, or a plastic shell) and was heated by a current pulse of density $(3–5) \times 10^7 \, \text{A cm}^{-2}$. The following parameters were measured: the current through the sample, the voltage drop across it, and (in some cases) the diameter of the expanding plasma column formed by an exploding wire. The plasma electric conductivity was determined assuming that the temperature, pressure, and other quantities are uniformly distributed over the plasma column. Shadow images of the plasma column made certain that the column is actually axially symmetric and uniform along its length. However, efforts to control the radial distributions of the quantities were unsuccessful. Moreover, in some cases, it was impossible to avoid evaporation. The reason is that the evaporation (which is of a volume nature when the Joule heating rate is high [8]) also leads to an increase in the electric resistance of the column and thus can be regarded as the beginning of the metal-to-dielectric transition.

Earlier, two of us [9] proposed an original technique realizing the transition of condensed metal into a gaseous state while maintaining uniform distributions of the temperature and pressure in the sample. The technique consists in the pulsed Joule heating of a sample in the form of a thin foil strip placed between two relatively thick glass plates. In the present paper, we report the results from experiments utilizing this method to measure the electric conductivity of tungsten in a process during which the pressure in the sample was maintained at a level of 40–60 kbar and the density decreased from the normal solid density to a density 20 to 30 times lower. Since such pressures are several times higher than the critical pressure for the liquid-to-vapor phase transition ($P_c \approx 11$–13 kbar [8]), evaporation did not manifest itself in our experiments. Our experimental results show that, along the isobar $P = 40$ kbar, the density dependence of the conductivity of tungsten changes radically at a certain density value, at which it has a pronounced kink. At the kink, the density of tungsten is approximately ten times lower than its normal solid density, and the internal energy is about two times the sublimation energy.

Our paper is organized as follows. First, we analyze the experimental method proposed here. We estimate the effect of different factors that violate the uniformity of the sample and show that, under certain conditions, the nonuniformities are small. Then, we present a hydrodynamic model that makes it possible to describe the dynamics of pulsed Joule heating under conditions close to the actual experimental conditions. This model was used to determine the parameters of experiments in which the sample remained uniform and the characteristic pressures were held at a high level (in order to avoid the liquid-to-vapor phase transition). When discussing the results obtained, we start with the main methodological problem—an analysis of the nonuniformity of the sample during the measurements. We present clear evidence that, in our experiments, the sample indeed remains uniform. We also compare our experimental results with the data from other experiments and from some theoretical calculations.

To conclude the introduction, note that, from a practical standpoint, the measurements of the electric conductivity of refractory metals over a wide range of densities are also of interest in connection with investigations of the processes during which an intense pulsed action induces a transition of metal from a condensed into gaseous state. In particular, such measurement data are required for modeling current switches [10], the influence of high-power laser radiation on metals [11, 12], and the dynamics of the collapse of multiwire arrays in devices for producing hot plasmas [13, 14].

2. UNIFORM HEATING METHOD

We consider the process of pulsed Joule heating of a foil strip whose length l, width h, and thickness d satisfy the inequalities $l \gg h \gg d$. The characteristic heating time t is assumed to be such that $h/c_1 \gg t \gg d/c_1$, where c_1 is the speed of sound in a metal. These conditions allow the problem to be treated in a one-dimensional formulation, in which the matter is assumed to move only in one direction, i.e., perpendicular to the plane of the foil.

Joule heating gives rise to the thermal expansion of a metal, which thus performs mechanical work on the glass plates. Since the sonic time scale d/c_1 in the sample is short, it can be expected that the pressure will be distributed uniformly over the metal and the characteristic pressure magnitude will be determined by the inertia of glass. If the time scale D/c_2 (where D is the plate thickness and c_2 is the speed of sound in glass) is longer than the characteristic time of the problem, then there is not enough time for the compression wave in glass to reach the free plate boundary. Consequently, the pressure in the sample will remain high (provided that the heating power will not change).

In order for the foil to be heated uniformly, the electric field should be uniform across the foil, which indicates that the skin depth $\delta = c/\sqrt{2\pi\sigma\omega}$ (where σ is the electric conductivity, ω is the characteristic frequency of the current variations, and c is the speed of light in a vacuum) should be larger than the half-thickness of the foil. For the conductivity $\sigma = 10^{16}$ s^{-1} (which is on the order of the electric conductivity of liquid tungsten) and for the frequency $\omega = 3 \times 10^6$ rad/s of the current variations, we obtain $\delta \approx 0.1$ cm.

Another factor that violates the uniformity of the sample is the effect of the ponderomotive forces. Under the action of these forces, the pressure profile becomes parabolic, the characteristic pressure being about Ij/c^2, where I is the amplitude of the current and j is its density. The contribution of a current with the amplitude $I = 10$ kA and density $j = 10^7$ A cm^{-2} to the pressure is about 1 kbar. The temperature distribution may become nonuniform because of the heat dissipation in glass. The thickness of the layer across which the temperature is nonuniform is about $\sqrt{\chi t}$, where χ is the thermal diffusivity of tungsten and t is the characteristic time scale of the process. For $t \sim 10^{-7}$ s and $\chi \sim 0.1$ cm^2 s^{-1}, we obtain a thickness of about 1 μm. We can easily see that, for foils with the dimensions $l \sim 1$ cm, $h \sim 10^{-1}$ cm, and $d \sim 10^{-3}$ cm and for glass plates with a thickness of about $D \sim 1$ cm, the conditions for uniform heating are satisfied and the problem may well be treated in a one-dimensional formulation. More precise estimates can be obtained by taking into account such factors as the actual time evolution of the heating power, the thermodynamic properties of tungsten, and the dynamics of the motion of glass plates. A self-consistent model that describes the heating dynamics with allowance for these factors will be presented below. Now, we turn to a description of our experiment.
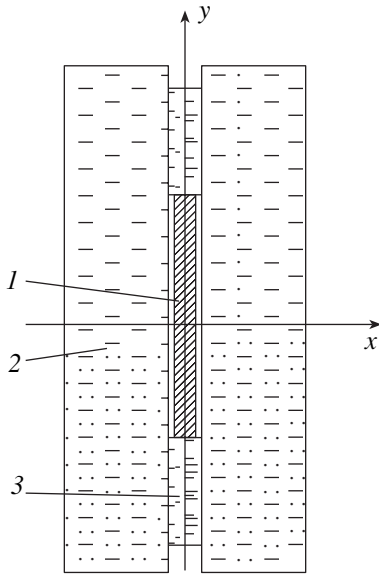
Fig. 1. Transverse cross section of the sample: (*1*) foil, (*2*) sapphire plate, and (*3*) mica plate. The current flows in a direction perpendicular to the plane of the figure.

3. DESCRIPTION OF THE EXPERIMENT

The experiments were carried out with tungsten foil strips with a thickness of 20–22 μm, width of 1.5–3.0 mm, and length of 10.0–11.5 mm, placed between two thick polished sapphire (or glass) plates, each with a thickness of 5–7 mm, width of 10 mm, and length of 10.0–11.5 mm. The side slits were covered by two thin mica strips (Fig. 1). The foil was placed so that the gap between its surface and the plate was minimal. The gap width, which was governed by the surface roughness of the sample and its nonuniformity, was smaller than 5–7 μm. The pulsed heating of the sample was accomplished by discharging a 72-μF capacitor bank with a charging voltage of about 18 kV. The discharge circuit with a total inductance of about 240 nH included a 0.3-Ω ballast resistor and a 1.35-Ω shunt resistor, connected in parallel to the sample.

We carried out 11 experiments with tungsten foils. We measured the time dependences of the current $I(t)$ through the sample and the voltage drop $U(t)$ across it. The signals from the Rogowski coil and voltage divider were recorded by a TDS-754C four-channel digital oscillograph with a time resolution of 1 ns. The active component of the voltage drop across the sample was calculated from the formula $U_R = U - L_f dI/dt$, where L_f is the inductance of the foil. The resistance of the sample and the heat released in it per unit mass were determined from the equations

$$R = \frac{U_R}{I}, \quad q = \frac{1}{m}\int_0^t I(t')U_R(t')dt',$$

where *m* is the mass of the sample. The electric conductivity was calculated from the relationship $\sigma = l/(SR)$, where $S = hd(t)$ is the cross-sectional area of the sample. The foil thickness $d(t)$ as a function of time was calculated using a hydrodynamic model and assuming that *l* and *h* are constant.

4. SELF-CONSISTENT MODEL OF THE HEATING DYNAMICS

The set of equations describing the dynamics of the pulsed foil heating consists of the equations of motion (the mass, momentum, and energy conservation laws), Maxwell's equations, and the equations for the total current flowing through the foil (the energy and charge conservation laws for the discharge circuit forming the current pulse). We introduce a Cartesian coordinate system such that the *x*-axis is perpendicular to the plane of the foil and the *y*-axis is aligned with the foil (Fig. 1). In the problem treated in a one-dimensional formulation, the matter moves only in the *x* direction and the only nonzero components of the electric and magnetic fields are the *z*- and *y*-components, respectively. Hence, the equations of motion have the form

$$\frac{\partial \rho}{\partial t} + \frac{\partial (\rho v)}{\partial x} = 0, \tag{1}$$

$$\frac{\partial (\rho v)}{\partial t} + \frac{\partial}{\partial x}(\rho v^2 + P) = -\frac{1}{c}jH, \tag{2}$$

$$\frac{\partial}{\partial t}\left(\rho\varepsilon + \frac{\rho v^2}{2}\right) + \frac{\partial}{\partial x}\left[\rho v\left(w + \frac{v^2}{2}\right)\right] = jE'. \tag{3}$$

Here, ρ, v, P, and ε are the density, velocity, pressure, and specific internal energy, respectively; $w = \varepsilon + P/\rho$ is the specific enthalpy; and E' is the electric field strength in the frame of reference moving with an element of the medium. Equations (1)–(3) are written in a Gauss system of units. According to the Lorentz transformation formula, we have $E' = E + vH/c$, where E is the electric field strength in the laboratory frame and the current density j obeys Ohm's law $j = \sigma E'$. Since, under the above conditions, the effects of heat conduction, viscosity, and heat transport by radiation are insignificant, the corresponding terms do not enter the equations of motion.

Maxwell's equations reduce to the two equations

$$\frac{\partial E}{\partial x} = \frac{1}{c}\frac{\partial H}{\partial t}, \tag{4}$$

$$\frac{\partial H}{\partial x} = \frac{4\pi}{c}j, \tag{5}$$

where the displacement currents are neglected.

The boundary conditions relate the magnetic field strength at the foil surface to the current flowing

through the foil and the electric field strength to the active component of the voltage drop across the foil:

$$H(a, t) = \frac{2\pi}{c} \frac{I(t)}{h}, \qquad (6)$$

$$E'(a, t) = U_R(t)/l, \qquad (7)$$

where $a = d(t)/2$ is the half-thickness of the foil. The boundary conditions for the hydrodynamic quantities are as follows: the pressure at the outer surface of the glass plate is constant (and is equal to 1 atm) and the boundary between the metal and the glass is a contact discontinuity. The initial conditions are assumed to be natural: the matter is at rest, the pressure and temperature are equal to their normal values, the current in the circuit is absent, and the charging voltage of the capacitor bank is equal to the initial voltage.

In order to close the set of equations of the hydrodynamic model, we need to know the thermodynamic functions of tungsten and its conductivity in a region of the phase diagram from the condensed state (a solid body under normal conditions) to the gaseous state (plasma). The thermodynamic functions for the metal-to-dielectric transition were obtained semiempirically. For the liquid-to-vapor phase transition, the thermodynamic functions were taken from [15]. The procedure for choosing the parameters was described in [8], in which it was also shown that these functions give a reasonable description (with an accuracy of 10%) of the thermal expansion of liquid tungsten and the liquid-to-vapor phase transition (up to the critical point). The ionization effects are described in the average-atom approximation [16], and the electric conductivity was calculated in accordance with [8, 17].

5. RESULTS OF NUMERICAL SIMULATIONS

When solving the set of equations of the hydrodynamic model, we used two different numerical methods. Specifically, Eqs. (1)–(3) were solved by the Godunov method [18], and Maxwell's equations (4) and (5) were solved by the sweep method [19]. Figure 2 illustrates how the thermodynamic state of the sample in the (P, T) plane changes during the pulsed Joule heating of a 20-μm-thick foil between two 0.5-cm-thick glass plates. The parameters of the circuit and the sample dimensions correspond to experiment no. 3 (in the series of experiments reported here). The triangles refer to points that are separated in time by the same interval equal to 150 ns, starting from the time at which the current is switched on. Figure 2 shows the phase trajectories representing two layers of the sample: layer 1 is a surface layer and layer 2 is a layer near the symmetry plane. These two layers correspond to two cells of the spatial grid in Lagrangian coordinates. Within the volume of the sample, the number of mesh points in the grid is 40–60, and, within the volume of the glass plate, the number of mesh points is 500–1000. The difference in the trajectories of the surface and the central layers
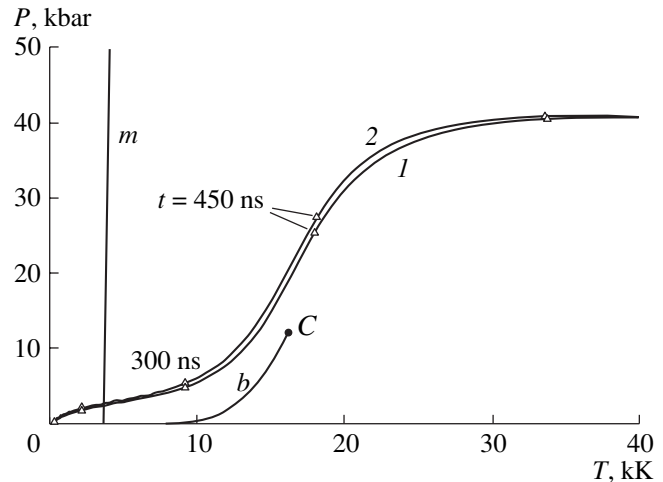

Fig. 2. Changes in the state of a metal foil between two glass plates during pulsed Joule heating: (*1*) surface layer, (*2*) layer near the symmetry plane, (*m*) melting curve, (*b*) boiling curve, and (*C*) critical point. The triangles refer to times separated by a time interval of 150 ns, starting from the time at which the current is switched on.
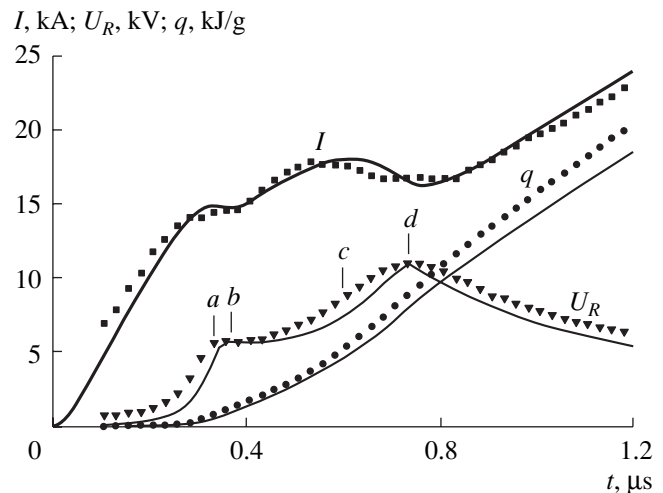

Fig. 3. Time dependences of the current I through the sample, the active component U_R of the voltage drop, and the Joule heat q released in the sample. The symbols show the data obtained from experiment no. 3, and the solid curves show the calculated results. The characteristic times are as follows: (*a*) the beginning of melting; (*b*) the end of melting; (*c*) the time at which the amount of heat released in the sample reaches the sublimation energy, and (*d*) the transition to a dielectric (plasma) state.

reflects the nonuniformity of the thermodynamic state of the sample. The trajectories are seen to lie substantially above the boiling curve b. The nonuniformity of the pressure is no higher than 1 kbar, and the nonuniformity of the temperature is no higher than 500 K.

Figure 3 shows the calculated and measured time dependences of the current I flowing through the sam-
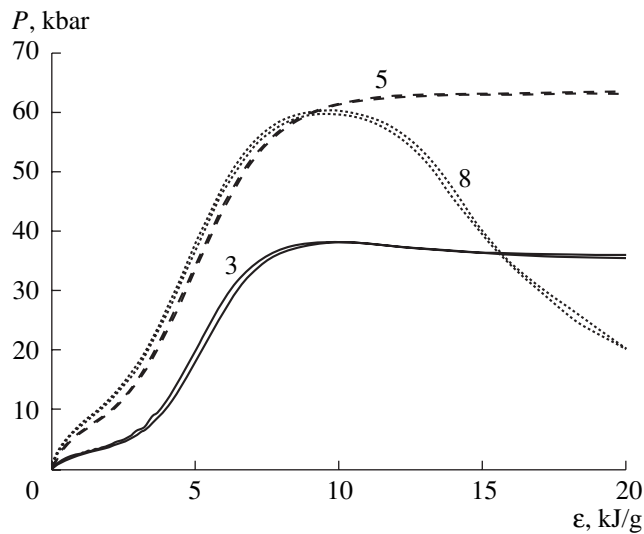
Fig. 4. Changes in the state of a metal foil in the (P, ε) plane during pulsed Joule heating in experiment nos. 3, 5, and 8. The calculations were carried out for prescribed time evolutions of the current and the Joule heating power. Each of the experiments is illustrated by the two curves representing two layers of the sample: the surface layer and the layer near the symmetry plane.

ple, the active component U_R of the voltage drop across the sample, and the Joule heat release q per unit mass. The measured time evolutions are seen to agree with the calculated ones to within 5–10%. It should be noted that such a good agreement between the measured and calculated evolutions was achieved only after having constructed a detailed equivalent scheme of the discharge circuit and having determined its parameters. Because of the presence of distributed (parasitic) inductances and capacitances, the scheme turned out to consist of five contours. We can clearly see that the voltage curve has three kinks, which correspond to the beginning (point *a*) and end (point *b*) of the melting process and to the transition to a dielectric (plasma) state (point *d*). Point *c* corresponds to the time at which the amount of heat released in the sample reaches the sublimation energy (4.6 kJ/g [20]).

The behavior of the electric conductivity during the metal-to-dielectric transition is described by an interpolation formula constructed according to [21]. The densities at the beginning and end of the transition serve as adjustable parameters. Without going into the details of the corresponding calculations, we only note that the adjustable parameters were chosen so as to reproduce the time evolution of the heating power with reasonable accuracy. This adjustment was needed only to analyze the temperature and pressure distributions in the sample that correspond to the specific time evolution of the Joule heating power.

The results of our simulations allowed us to solve several important methodological problems. First, we succeeded in choosing the parameters of the circuit and

the geometric dimensions of the sample so that the sample was heated fairly uniformly and the liquid-to-gas transition was continuous (in which case a transition to a two-phase liquid–gas state did not occur). Note that, in experiments [4–7], a transition to a two-phase state occurred in the initial stage of the process. In [8], it was shown that such transitions inevitably lead to the formation of highly nonuniform temperature and density distributions (because the speed of sound decreases considerably during the transition from a liquid state to a two-phase state). The second conclusion that can be derived from analyzing the numerical result concerns the estimates of errors in measuring the current and voltage. It was found that these errors were no larger than 3–5%. This follows from a comparison of the measured time dependences of the current and voltage with those calculated for the initial stage of the process during which the sample was in a condensed state (because the condensed state can be described using the reliable data on the thermal expansion and electric resistance [8, 22]). The high degree of uniformity of the sample and good accuracy of the measurements of the current and voltage enabled us to determine the electric conductivity by taking the following approach. The resistance of the sample and the heat released in it were measured in experiments, while the thickness of the sample was calculated by solving hydrodynamic equations (1)–(3) only. In this approach, the current and the Joule heating power were assumed to be known functions of time (which were taken from experiment) and the right-hand sides of Eqs. (1)–(3) were represented as follows:

$$\frac{1}{c}jH = \frac{4\pi}{c^2}\frac{I^2(t)}{S^2(t)}x, \tag{8}$$

$$jE' = \frac{1}{\rho}\frac{dq}{dt}. \tag{9}$$

All of the results reported below were obtained precisely by this approach.

6. ANALYSIS OF THE UNIFORMITY OF THE SAMPLE

The results of the calculations carried out for prescribed time dependences of the current and the Joule heating power are presented in Fig. 4, which illustrates how the state of the sample changes in experiment no. 3 (which was carried out with glass plates), experiment no. 5 (carried out with 5-mm-thick sapphire plates), and experiment no. 8 (carried out with 1.5-mm-thick sapphire plates). The results are given in the (P, ε) plane, rather than in the (P, T) plane, because the internal energy can be measured directly (in the initial stage, the internal energy is almost same as the Joule heat q). The parameters of experiment nos. 3 and 5 were the same, except for the material of the plates. It can be seen that the method proposed here makes it possible to substantially change the pressure level solely by changing from
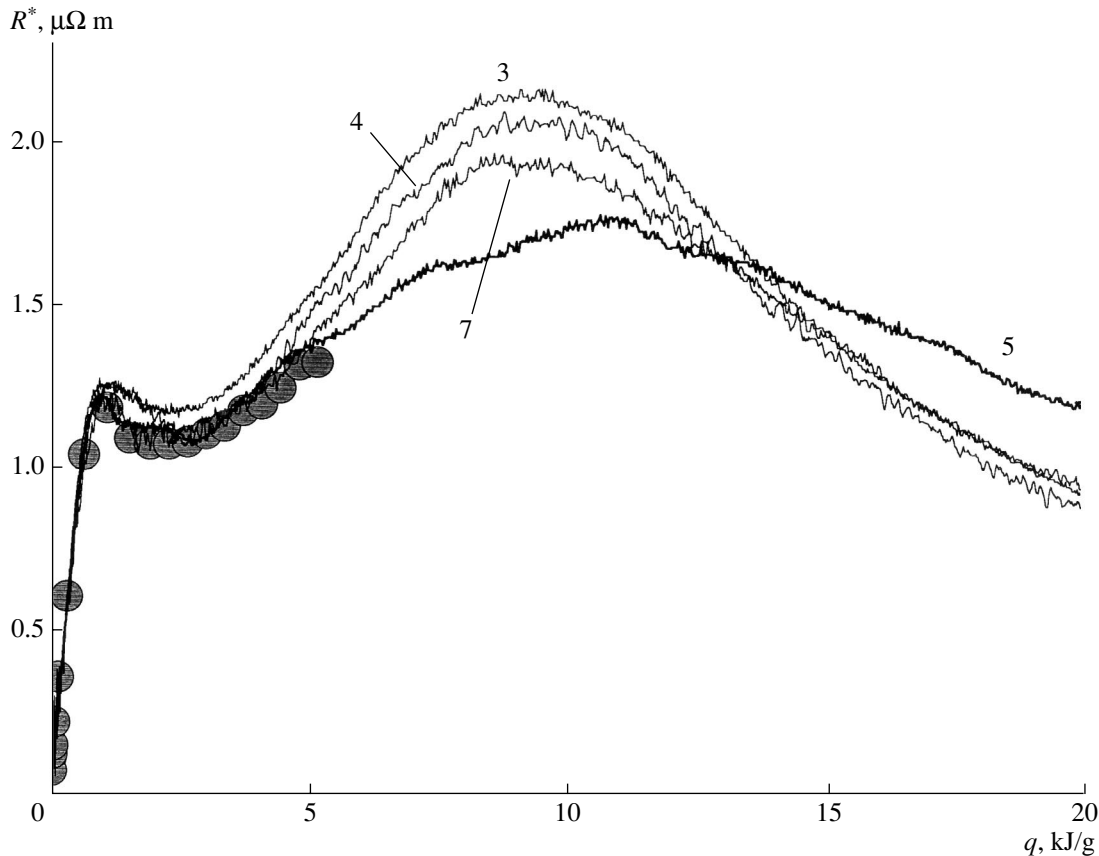
Fig. 5. Normalized resistance R^* (the resistance normalized by multiplying by the ratio of the initial cross-sectional area of the foil strip to its initial length) vs. specific heat q released in the sample for experiment nos. 3, 4, 5, and 7. The circles show the data obtained in [8].

one material of the plates to another. It follows from the figure that, for q in the range from 7–8 to 20 kJ/g, the heating processes in experiment nos. 3 and 5 are nearly isobaric. Each of the three experiments is illustrated by the phase trajectories representing two layers of the sample: the surface layer and a layer near the symmetry plane. In order to relate these trajectories to the time dependences shown in Fig. 3, we note that, when the heat released in the sample in experiment no. 3 is equal to $q = 10$ kJ/g, the internal energy differs from it by 10% and this difference increases to 15% when $q = 15$ kJ/g.

Experiment no. 8 was performed with thin sapphire plates. It can be seen in Fig. 4 that the pressure reduces appreciably even when the internal energy increases to about 12 kJ/g. In experiment no. 8, the rarefaction wave from the free surface of the plate reached the sample in a shorter time than in experiment nos. 3 and 5. It is noteworthy that, at low internal energies, the curves for experiment no. 8 almost coincide with those for experiment no. 5 and, at higher internal energies, they cross the curves for experiment no. 3.

Figure 5 shows the resistance of the sample as a function of the specific heat release for experiment nos. 3, 4, 5, and 7. We present these dependences because

both of these quantities can be measured directly. For convenience in comparing our results with the data obtained in other works, we normalize the resistance by multiplying by the ratio of the initial cross-sectional area of the foil strip to its initial length: $R^* = RS_0/l$; for a uniform sample, the resistance so normalized is proportional to the ratio ρ/σ. It can be seen from Fig. 5 that our results agree well with the data obtained in [8], in which the electric conductivity was measured directly at pressures between 10 and 20 kbar and at densities ranging from the normal solid density to a density about four times lower. In Fig. 5, the curves that refer to experiment nos. 3, 4, and 7 are seen to have pronounced maxima in the range of q values from 8 to 12 kJ/g. The reproducibility of the data for the region of the maxima is fairly high. To make this evident, we show in Fig. 5 the data obtained in experiment nos. 3 and 4, which were performed under the same conditions. The two corresponding curves are seen to differ by no more than 5%. This difference characterizes the accuracy with which the parameters of our experiments are reproduced. It follows from the figure that our results differ from the data obtained in [8] by the same amount.
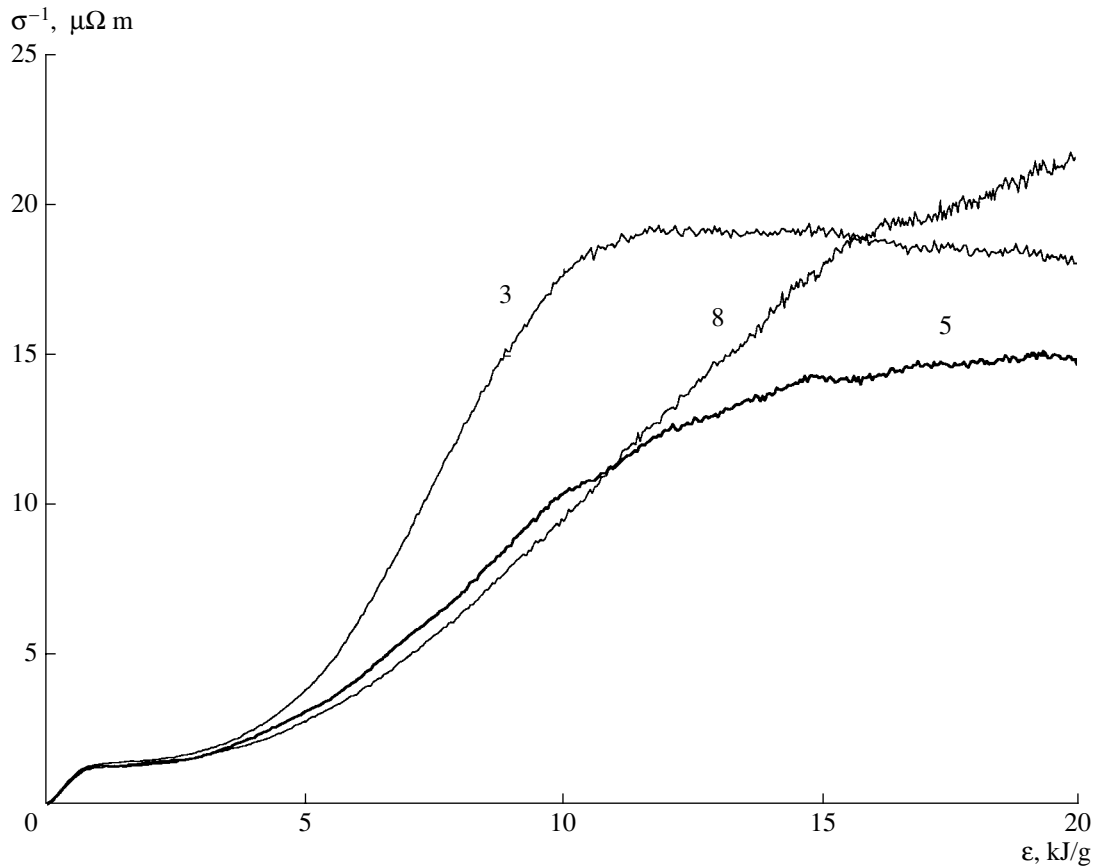
Fig. 6. Resistivity σ^{-1} vs. specific internal energy ε for experiment nos. 3, 5, and 8.

Experiment no. 7 was carried out with a wide foil ($h = 3$ mm). The parameters of the discharge circuit were chosen in such a way that the time dependence of the specific heating power was close to that for experiment no. 3. The width of the foil strips in experiment nos. 3, 4, and 5 was 1.5 mm. It is clear that the change of the expansion of the foil from being one-dimensional to being two-dimensional depends on the initial width-to-thickness ratio of the foil. The larger this ratio, the longer the time during which the expansion is one-dimensional. According to Fig. 5, the results of experiment nos. 3, 4, and 7 agree to within 5–10%, which is just the measurement accuracy. We can thus conclude that, in these experiments, the expansion of the foil was one-dimensional.

The questions about the one-dimensional character of the expansion of the foil and about the influence of the boundary effects when the expansion is substantial was examined in more detail. Numerical simulations showed that the time during which the pressure in the metal decreased was the shortest in the experiment with thin sapphire plates (experiment no. 8), because the rarefaction wave from the free surface of the plate reached the sample in a shorter time than in other experiments. In Fig. 4, the curves for experiment no. 8 cross those for experiment no. 3. This indicates that the metal reaches

the same thermodynamic state (the state at the intersection point of the curves) in different ways. It is clear that, when the quantities are distributed uniformly over the sample, the resistivities in these states should be the same. From Fig. 6, which shows the resistivity as a function of the specific internal energy, we see that, for experiment nos. 3 and 8, the resistivities at this value of the internal energy (about 16 kJ/g) actually coincide (to within measurement error). Hence, we can conclude that the expansion of the samples in these experiments was one-dimensional and that the nonuniformity of the expanding samples was insignificant, at least for internal energies up to 16 kJ/g.

7. DISCUSSION OF THE RESULTS

Figure 7 illustrates how the resistivity depends on the relative volume (the volume normalized to the specific volume v_0 of a solid body under normal conditions). We can see that this dependence is different for solid, liquid, and gaseous states. In the liquid phase, the resistivity is approximately proportional to the specific volume; i.e., the ratio σ/ρ remains almost constant. Over the range of relative volumes from 9 to 11, the dependence changes its character (experiment no. 3). For larger relative volumes, the resistivity approaches a
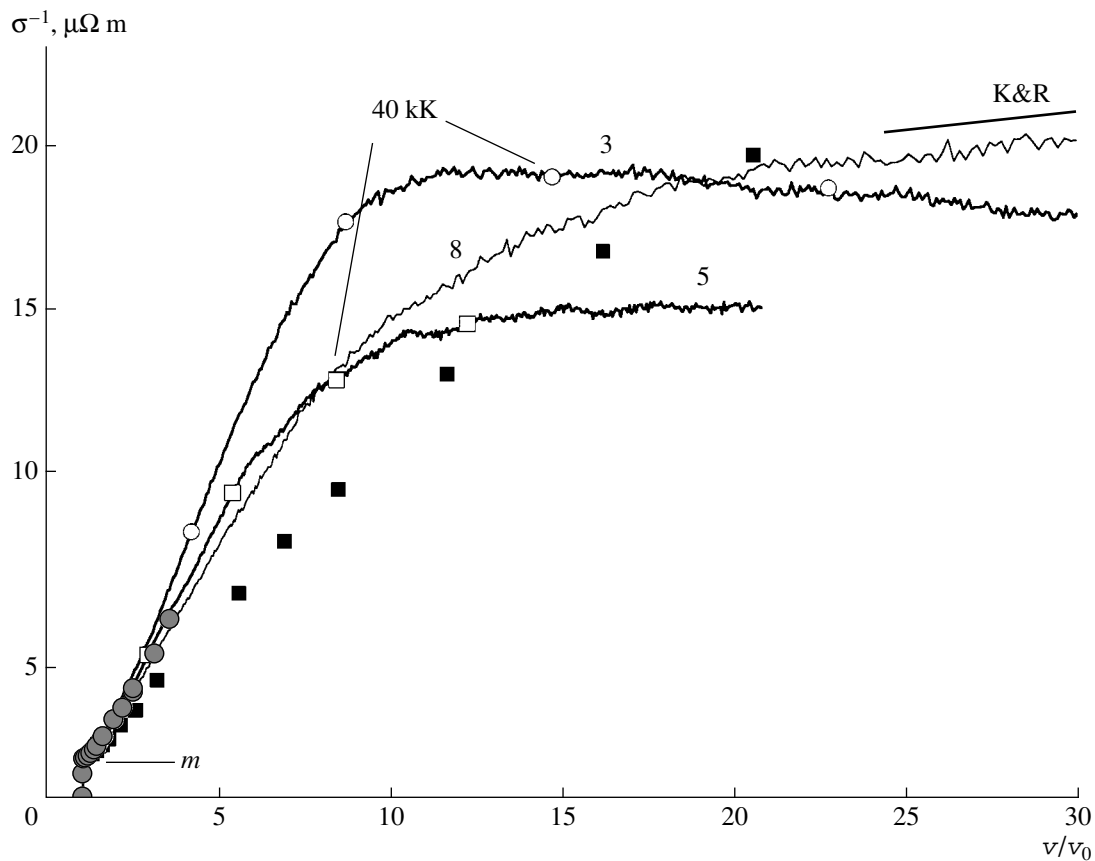
Fig. 7. Resistivity σ^{-1} of tungsten vs. relative volume for experiment nos. 3, 5, and 8. The kink indicated by the arrow (point *m*) corresponds to the end of melting. Open circles and open squares refer to temperatures in the range from 10 to 50 kK, with a step of 10 kK. The bold line K&R shows the results of theoretical calculations for the $T = 30$ kK isotherm [24]. Closed circles are for the data of [8, 22], and closed squares are for the data of [6].

constant value. Note that, for relative volumes larger than 5, the heating processes in experiment nos. 3 and 5 were nearly isobaric. Thus, the dependence of the resistivity on the specific volume changes its character along an isobar. As the pressure increases from 40 to 60 kbar, the dependence becomes substantially flatter, in which case the range of relative volumes where the character of the dependence changes becomes larger by a factor of approximately 3. It should be noted that the dependence referring to experiment no. 8, in which the pressure decreased, does not have any singularities (kinks).

Note that the change of the character of the dependence of the resistivity on the specific volume is directly related to the maximum in the dependence of the resistivity on the heat dissipated in the sample (Fig. 5) and, therefore, cannot depend on the accuracy with which the thermodynamic functions for tungsten are described. It could, however, be suspected that the maximum itself is associated with radiative losses. Since the power of these losses is highly sensitive to temperature, the effect of radiation can manifest itself as a kink (maximum) in the dependence $R^*(\varepsilon)$. In fact,

the plasma conductivity is proportional to $T^{2/3}$ and depends weakly (logarithmically) on the plasma density. The ratio ρ/σ should decrease with density, because radiative losses stabilize the temperature (and conductivity) at a certain level. Our estimates show that, for an atom density of 6×10^{21} cm^{-3} (which corresponds to a relative volume of about $v/v_0 \approx 10$) and a temperature of 3 eV, the photon mean free path is about 10^{-6} cm. As a result, the plasma is opaque to radiation, which is emitted exclusively from a thin surface layer. Consequently, radiative losses cannot significantly change the energy balance and the dynamics of motion of the bulk of the sample.

In Fig. 7, we also plot the data from other experiments. Our results are seen to agree satisfactorily with the experimental findings of [8, 22]. The dependence obtained in [6] differs from those obtained in [8, 22] because of a large systematic error in determining the volume of the sample and the active component of the voltage drop. In the experiments of [6], the wires were heated in glass capillaries such that the ratio of the inner diameter of the capillary to the initial wire diameter was large. The primary source of error was that the volume

of the sample was determined by recording the luminosity of the expanding plasma column through the thick capillary wall.

The experiments of [23] were aimed at investigating polyurethane plasma. It was found that, as the temperature increased to about 7–10 eV, the resistivity approached a constant level of about 25 μΩ m. This resistivity value remained unchanged as the density decreased by several orders of magnitude. In [7], a similar effect was observed for aluminum.

Let us now turn to theoretical papers. It can be seen from Fig. 7 that the theory developed in [24] yields resistivity values that are close to those obtained in experiment nos. 3 and 8 (and predicts an analogous character of the dependence of the resistivity on the specific volume). However, the calculations carried out in [24] refer to the $T = 30$ kK isotherm. The temperature obtained in our calculations for the range of relative volumes from 25 to 30 in experiment no. 3 is about two times higher.

It is of interest to estimate the characteristic densities corresponding to the transition of tungsten from a metallic to dielectric state. According to the predictions made in [21], this transition is continuous and is not a first-order phase transition. The density corresponding to this transition is determined from the condition that the fraction of the classically accessible volume for valence electrons amounts to about 30%. At a low temperature, the corresponding specific volume v/v_0 is approximately equal to 5. At a temperature of $T \sim I_1/3$ (where I_1 is the first ionization energy), the metal-to-dielectric phase transition should completely disappear. For tungsten, this temperature is about 30 kK. Hence, the effect revealed in our experiments seems to be unrelated to the theoretical predictions of [21].

8. CONCLUSION

The method proposed here allowed us to maintain the sample in a uniform state during a continuous transition of tungsten from a liquid to a gaseous state. As a result, the tungsten density decreased from the normal solid density to a density 20 to 30 times lower. Using this method, we have carried out experiments on the isobaric heating of tungsten in a gaseous state. We have found that the conductivity-to-density ratio for tungsten in a condensed phase remains almost constant at densities ranging from the density corresponding to the melting point to those that are approximately ten times lower than the normal solid density. At lower densities, the dependence of the conductivity on the density along the 40-kbar isobar changes its character: the conductivity becomes independent of density and approaches a nearly constant value. This change in the character of the dependence manifests itself as a kink in the corresponding experimental curve. As the pressure increases from 40 to 60 kbar, the density dependence of the conductivity near the kink becomes substantially flatter.

Finally, no such effect has been detected in nonisobaric processes.

REFERENCES

1. Ya. B. Zel'dovich and L. D. Landau, Zh. Éksp. Teor. Fiz. **14**, 32 (1944).
2. I. K. Kikoin and A. P. Senchenkov, Fiz. Met. Metalloved. **24**, 843 (1967).
3. F. Hensel, J. Phys.: Condens. Matter **2**, 33 (1990).
4. H. Hess, H. Schneidenbach, and A. Kloss, Phys. Chem. Liq. **37**, 719 (1999).
5. A. W. DeSilva and J. D. Katsouros, Int. J. Thermophys. **20**, 1267 (1999).
6. S. Saleem, J. Haun, and H.-J. Kunze, Phys. Rev. E **64**, 056403 (2001).
7. F. J. Benage, W. R. Shanahan, and M. S. Murillo, Phys. Rev. Lett. **83** (15), 2953 (1999).
8. A. D. Rakhel, A. Kloss, and H. Hess, Int. J. Thermophys. **23**, 1369 (2002).
9. V. N. Korobenko and A. D. Rakhel, Int. J. Thermophys. **20**, 1259 (1999).
10. V. A. Burtsev, N. V. Kalinin, and A. V. Luchinskiĭ, *Electric Explosions of Conductors and Their Use in Electrophysical Facilities* (Énergoatomizdat, Moscow, 1990).
11. S. I. Anisimov, Ya. A. Imas, G. I. Romanov, and Yu. V. Khodyko, *Effect of High-Power Radiation on Metals* (Nauka, Moscow, 1970).
12. H. M. Milchberg, R. R. Freeman, S. C. Davey, and R. M. More, Phys. Rev. Lett. **61**, 2364 (1988).
13. R. B. Spielman, C. Deeney, G. A. Chandler, *et al.*, Phys. Plasmas **5**, 2105 (1998).
14. J. P. Chittenden, S. V. Lebedev, J. Ruiz-Camach, *et al.*, Phys. Rev. E **61**, 4370 (2000).
15. D. A. Young, Report No. UCRL-52352 (Lawrence Livermore National Laboratory, Livermore, CA, 1977).
16. M. M. Basko, Teplofiz. Vys. Temp. **23**, 483 (1985).
17. A. D. Rakhel, *Report on the Session of the Scientific Council on Physics of Low-Temperature Plasma of the Russian Academy of Sciences, Moscow, November 28–29, 1999*.
18. S. K. Godunov, A. V. Zabrodin, M. Ya. Ivanov, *et al.*, *Numerical Solution of Multidimensional Problems of Gas Dynamics* (Nauka, Moscow, 1976).
19. A. A. Samarskiĭ and Yu. P. Popov, *Difference Methods for Solving Gas Dynamics Problems* (Nauka, Moscow, 1980).
20. D. A. Young, *Phase Diagrams of the Elements* (Univ. of California Press, Berkley, 1991).
21. A. A. Likal'ter, Usp. Fiz. Nauk **162** (7), 119 (1992) [Sov. Phys. Usp. **35**, 591 (1992)].
22. A. Kloss, A. D. Rakhel, and H. Hess, Int. J. Thermophys. **19**, 983 (1998).
23. R. L. Shepherd, D. R. Kania, and L. A. Jones, Phys. Rev. Lett. **61**, 1278 (1988).
24. S. Kuhlbrodt and R. Redmer, Phys. Rev. E **62**, 7191 (2000).

Translated by O.E. Khadin

One-Dimensional Model of the Debye Layer
near a Dielectric Surface

A. I. Morozov* and V. V. Savel'ev**

*Nuclear Fusion Institute, Russian Research Centre Kurchatov Institute, pl. Kurchatova 1, Moscow, 123182 Russia
**Keldysh Institute of Applied Mathematics, Russian Academy of Sciences, Miusskaya pl. 4, Moscow, 125047 Russia

Abstract—A study is made of the processes occurring in a low-density plasma near a dielectric wall. A one-dimensional non-steady-state model of the electron dynamics is constructed that takes into account secondary electron emission. The Vlasov–Poisson equations are solved numerically. According to the results obtained, the steady-state potential distribution that forms at a low temperature of the incident electrons gives rise to a wall layer whose characteristic thickness is about several Debye lengths and in which the electrons are decelerated. In this case, the electron density is lowest near the wall. The situation in which the temperature of the incident electrons is high is far more complicated: the solution is quasi-periodic in character and the electron density near the wall is the highest. © 2002 MAIK "Nauka/Interperiodica".

1. INTRODUCTION

The structure of the Debye layer (DL), which always arises near a dielectric wall that is in contact with a plasma, as yet has been insufficiently studied. The DL structure in a collisionless plasma is most frequently analyzed by using the formula

$$(1 - \sigma)j_{en}\exp\left(-\frac{eU_{\mathrm{D}}}{kT_e}\right) = j_{in} \tag{1}$$

and the expression for the energy flux onto the surface. In formula (1), j_{en} and j_{in} are the electron and ion flux densities at the boundary of the DL, σ is the secondary electron emission coefficient, and $U_{\mathrm{D}} > 0$ is the potential jump across the DL. In some cases, however, it is precisely the structure of the DL and its properties that significantly govern the plasma behavior. In particular, they determine the distinctive features of the processes that occur in a stationary plasma thruster (SPT) [1–3]. These processes are fairly complicated for a number of reasons. First of all, the distribution function of the electrons incident on the surface is substantially non-Maxwellian. Second, in the SPT channel, there are many plasma electrons with energies ε at which the secondary electron emission coefficient $\sigma(\varepsilon)$ is larger than unity. Third, the surface of the dielectric wall of the channel is not perfectly smooth because, on the one hand, the dielectric material is coarse-grained, and, on the other hand, it is subject to erosion by high-energy electrons. These electrons produce complicated structures at the dielectric surface with a quasi-period in the millimeter range [4], which is only one order of magnitude larger than the DL thicknesses estimated from the electron thermal velocity and the electron plasma frequency.

For SPTs, the construction of adequate DL models incorporating the above features is aimed primarily at determining the scales of the near-wall conductivity [5, 6] and of the heat fluxes onto the walls. However, to determine these scales requires the knowledge of the distribution function of the secondary electrons. For the known distributions of the incident electrons, the DL theory for SPTs should be developed on the basis of the Vlasov equation for the electron distribution function (EDF) $f_e(t, \mathbf{r}, \mathbf{v})$ in a self-consistent electric field $\mathbf{E}$ and a prescribed magnetic field $\mathbf{H}$:

$$\frac{\partial f_e}{\partial t} + \mathbf{v} \cdot \frac{\partial f_e}{\partial \mathbf{r}} - \frac{e}{m}\left(\mathbf{E} + \frac{1}{c}\mathbf{v} \times \mathbf{H}\right) \cdot \frac{\partial f_e}{\partial \mathbf{v}} = 0,$$
$$\Delta\Phi = -4\pi e(n_i - \int f_e d\mathbf{v}). \tag{2}$$

Equations (2) should be supplemented with the corresponding boundary conditions. In the case of a classical steady-state DL, the Debye radius in an SPT is one order of magnitude smaller than the electron Larmor radius; hence, the effect of the magnetic field on the electrons can be neglected. Note, however, that, in many cases, the classical DL[1] under the SPT conditions is likely to evolve into an unsteady structure whose thickness substantially exceeds the Debye radius r_{D}. Hence, such a dynamic DL should be calculated over a region whose length is much larger than $\gg r_{\mathrm{D}}$, which can make it necessary to take into account the magnetic field. Our objective here is to find out the general features of DLs for which $\sigma(\varepsilon) > 1$ without assuming their steady-state behavior, but making a number of additional simplifying assumptions. The most important of

---

[1] Debye layers in the case of a steady-state non-Maxwellian EDF and $\sigma(\varepsilon) > 1$ were analyzed in [7].

these, together with the above assumption that the effect of the magnetic field on the electrons can be neglected, are the assumptions that the velocity of the incident ions is constant ($\varepsilon_i \gg eU_D$) and that the electrons moving from infinity toward the wall obey a Maxwellian distribution, as well as the assumption that the wall surface is smooth. With these assumptions, it is natural to start by constructing a one-dimensional model.

2. EQUATIONS OF A ONE-DIMENSIONAL MODEL

We consider one of the simplest possible formulations of a one-dimensional problem of the local DL structure near a dielectric wall. Let x be the coordinate across the layer (the point $x = 0$ lies deep in the plasma, and the point $x = L$ corresponds to the wall position) and let V be the electron velocity component in the x direction. The EDF $f_e(t, x, V)$ is described by the kinetic equation

$$\frac{\partial f_e}{\partial t} + V \frac{\partial f_e}{\partial x} - \frac{e}{m} E \frac{\partial f_e}{\partial V} = 0, \tag{3}$$

in which the potential $\Phi(x)$ of the electric field E satisfies Poisson's equation

$$\frac{\partial^2 \Phi}{\partial x^2} = -4\pi e(n_{i0} - n_e). \tag{4}$$

Since the ions are relatively heavy and have a relatively high energy and the Debye radius is small, we can assume that the ion density n_i and the ion velocity V_i within the DL are both constant, $n_i = n_0 \equiv \text{const}$ and $V_i = V_{i0} \equiv \text{const}$.

For simplicity, we also assume that the electric field changes its sign at the dielectric surface and its magnitude remains the same. Then, the boundary condition at the wall can be written as

$$E(L) = -2\pi\rho, \tag{5}$$

where ρ is the surface charge density; the possible surface conductivity of the dielectric is neglected. The potential at the wall surface is assumed to be zero:

$$\Phi(0) = 0. \tag{6}$$

At the left boundary, we impose the simplest physically realistic and mathematically noncontradictory condition for the EDF. Specifically, we assume that, at $x = 0$, the electrons with $V > 0$ obey a Maxwellian distribution:

$$f_e(t, 0, V) = n_{e0} \left(\frac{m}{2\pi T_{e0}}\right)^{1/2} \exp\left(-\frac{mV^2}{2T_{e0}}\right), \tag{7}$$

where the parameters n_{e0} and T_{e0} are the density and temperature of the incident electrons.

In order to write the equation for ρ and impose the boundary condition on f_e at $x = L$, we need to adopt a certain model for the secondary electron emission at the wall. We will assume that, when an electron with energy ε_p collides with the wall, one of the three events can occur: (i) the incident electron is absorbed by the wall (in which case the wall acquires the electron's negative charge), (ii) the incident electron knocks one secondary electron with energy ε out of the wall, and (iii) the incident electron knocks out two secondary electrons with energies ε_1 and ε_2. Let $P_0(\varepsilon_p)$ be the probability of the first event, $P_1(\varepsilon, \varepsilon_p)$ the probability density of the second event, and $P_2(\varepsilon_1, \varepsilon_2, \varepsilon_p)$ the probability density of the third event. We also introduce the notation $W_0(\varepsilon_p) = P_0(\varepsilon_p)$ and denote by $W_1(\varepsilon_p) = \int P_1(\varepsilon, \varepsilon_p)d\varepsilon$ the probability for one secondary electron to be produced and by $W_2(\varepsilon_p) = \int P_2(\varepsilon_1, \varepsilon_2, \varepsilon_p)d\varepsilon_1 d\varepsilon_2$ the probability for two secondary electrons to be produced. Then, by definition, the secondary electron emission coefficient $\sigma(\varepsilon_p)$ (the mean number of secondary electrons knocked out of the wall by an incident electron with energy ε_p) is equal to

$$\sigma(\varepsilon_p) = W_1(\varepsilon_p) + 2W_2(\varepsilon_p).$$

The corresponding normalization condition has the form

$$W_0(\varepsilon_p) + W_1(\varepsilon_p) + W_2(\varepsilon_p) = 1.$$

For further analysis, we introduce the probability density of an event in which exactly two secondary electrons are produced, the energy of one of which being ε:

$$P_{2,1}(\varepsilon, \varepsilon_p) = P_{2,2}(\varepsilon, \varepsilon_p) = \int P_2(\varepsilon_1, \varepsilon, \varepsilon_p)d\varepsilon_1.$$

The equation for the surface charge density ρ can be written as

$$\frac{d\rho}{dt} = en_{i0}V_{i0} - e\int_0^\infty V f_e(t, L, V)(W_0(\varepsilon) - W_2(\varepsilon))dV. \tag{8}$$

Here, we assume that each ion striking the wall is neutralized there by an electron.

Finally, we need to write the boundary condition for the EDF at the wall ($x = L$). To do this, we determine the number of secondary electrons,

$$|V|F^-(\varepsilon)d\varepsilon$$
$$= \int_0^\infty V_p F^+(\varepsilon_p)d\varepsilon_p(P_1(\varepsilon, \varepsilon_p) + 2P_{2,1}(\varepsilon, \varepsilon_p))d\varepsilon, \tag{9}$$

where we denote by $F^\pm(\varepsilon)$ the energy distribution functions of the primary (incident) and secondary (emitted)

electrons (plus and minus sign, respectively). For the velocity distribution function, we finally obtain

$$f^-(t, L, V)$$

$$= m\int_0^\infty (P_1(\varepsilon, \varepsilon_p) + 2P_{2,1}(\varepsilon, \varepsilon_p))V_p f^+(t, L, V_p)dV_p, \qquad (10)$$

$$V < 0.$$

The functions characterizing secondary electron emission were chosen in the following way:[2]

$$W_0(\varepsilon) = P_{00}\exp\left(-\frac{\varepsilon^2}{\varepsilon_{00}^2}\right), \quad W_2(\varepsilon) = 1 - \exp\left(-\frac{\varepsilon^2}{\varepsilon_{20}^2}\right), \qquad (11)$$

$$W_1(\varepsilon) = 1 - W_0(\varepsilon) - W_2(\varepsilon),$$

where the parameters P_{00}, ε_{00}, and ε_{20} should, of course, be such that $W_1(\varepsilon) \geq 0$. Then, we choose the model functions that are associated with the spectrum of the secondary electrons and are consistent with functions (11). Under the assumption that the total energy of the secondary electrons cannot be higher than the energy of the incident electron, we can write

$$P_1(\varepsilon, \varepsilon_p) = \begin{cases} 4P_{10}\dfrac{\varepsilon}{\varepsilon_p}\left(1 - \dfrac{\varepsilon}{\varepsilon_p}\right), & \varepsilon \leq \varepsilon_p \\[3mm] 0, & \varepsilon > \varepsilon_p, \end{cases} \qquad (12)$$

$$P_2(\varepsilon_1, \varepsilon_2, \varepsilon_p)$$

$$= \begin{cases} 4P_{20}\dfrac{\varepsilon_1 + \varepsilon_2}{\varepsilon_p}\left(1 - \dfrac{\varepsilon_1 + \varepsilon_2}{\varepsilon_p}\right), & \varepsilon_1 + \varepsilon_2 \leq \varepsilon_p \\[3mm] 0, & \varepsilon_1 + \varepsilon_2 > \varepsilon_p, \end{cases} \qquad (13)$$

where P_{10} and P_{20} are functions of ε_p. Then, we can readily establish that $P_{10}(\varepsilon_p) = \dfrac{3}{2\varepsilon_p} W_1(\varepsilon_p)$ and $P_{20}(\varepsilon_p) = \dfrac{3}{\varepsilon_p^2} W_2(\varepsilon_p)$ and obtain

$$P_{2,1}(\varepsilon, \varepsilon_p)$$

$$= \begin{cases} 2\dfrac{W_2(\varepsilon_p)}{\varepsilon_p}\left(2\left(\dfrac{\varepsilon}{\varepsilon_p}\right)^3 - 3\left(\dfrac{\varepsilon}{\varepsilon_p}\right)^2 + 1\right), & \varepsilon \leq \varepsilon_p \\[3mm] 0, & \varepsilon > \varepsilon_p. \end{cases} \qquad (14)$$

Hence, we have derived a closed set of equations and boundary conditions for determining f_e, Φ, and ρ.

[2] To the best of our knowledge, these functions have not yet been determined experimentally.
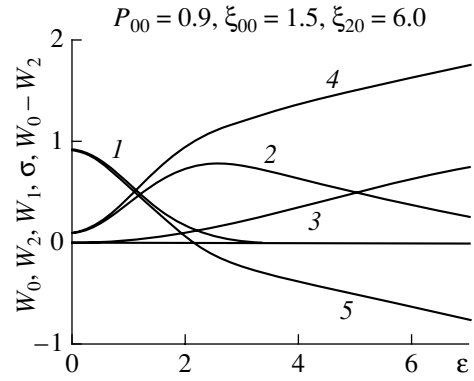
Fig. 1. Secondary-electron emission functions (1) W_0, (2) W_1, (3) W_2, (4) σ, and (5) $W_0 - W_2$ calculated for $\xi_{00} = 1.5$ and $\xi_{20} = 6.0$.

3. CALCULATED RESULTS

The calculations were carried out for the main parameters typical of an SPT. The velocity of the incident ions was $V_{i0} \approx 10^6$ cm/s,[3] and the ion density was $n_{i0} \approx 10^{11}$ cm^{-3} ($n_{i0} = n_{e0}$). In the calculations, we varied the temperature T_{e0} of the electrons incident to the wall.

In what follows, it is natural to use the units of measurement that are suitable for our problem. Specifically, we express the density in units of n_{e0}, the velocity in units of the characteristic thermal velocity $V_{T0} = (T_{e0}/m)^{1/2}$, the length in units of the Debye radius $r_{D0} = (T_{e0}/4\pi e^2 n_{e0})^{1/2}$, the time in units of $t_0 = r_{D0}/V_{T0}$, the energy in units of T_{e0}, and the electric field in units of $4\pi e n_{e0} r_{D0}$. In these units, the basic equations of the model have the form

$$\frac{\partial f_e}{\partial t} + V\frac{\partial f_e}{\partial x} - E\frac{\partial f_e}{\partial V} = 0,$$

$$\frac{d^2\Phi}{dx^2} = n_e - 1, \qquad (15)$$

$$\frac{d\rho}{dt} = V_{i0} - \int_0^\infty V f_e(t, x_0, V)(W_0(\varepsilon) - W_2(\varepsilon))dV.$$

The four significant dimensionless parameters of the problem are the length of the system $l = \dfrac{L}{r_{D0}}$ (in units of the Debye radius) and the three parameters P_{00}, $\xi_{00} = \dfrac{\varepsilon_{00}}{T_{e0}}$, and $\xi_{20} = \dfrac{\varepsilon_{20}}{T_{e0}}$ of the secondary electron emission. The results to be described were obtained for $l = 10$ and $P_{00} = 0.9$. As an example, Fig. 1 shows the second-

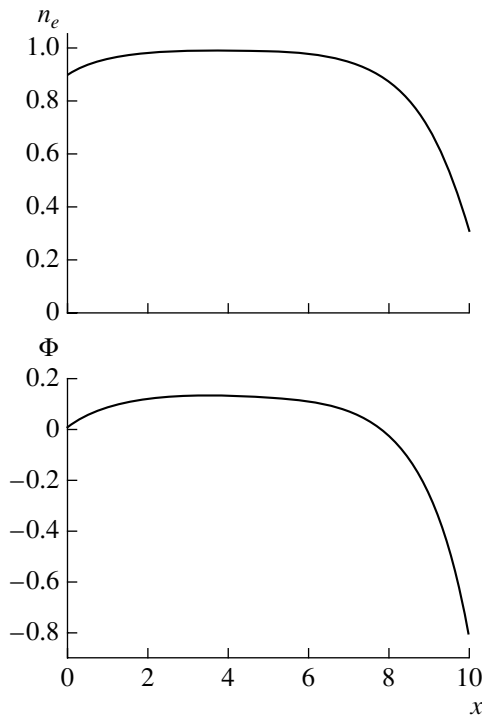[3] By this is meant the velocity component normal to the wall surface.

Fig. 2. Steady-state spatial profiles of the electron density and electric potential for $\xi_{00} = 1.5$ and $\xi_{20} = 6.0$.
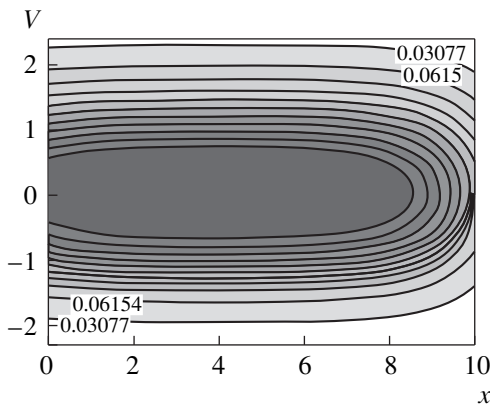

Fig. 3. Contours of the EDF in steady state for $\xi_{00} = 1.5$ and $\xi_{20} = 6.0$.

ary-electron emission functions calculated for $\xi_{00} = 1.5$ and $\xi_{20} = 6.0$.

When solving Eqs. (15) numerically, we integrated the transport equation by using two difference methods [8, 9], which were found to yield nearly the same results.

We begin with the case of "low" temperatures, $\xi_{00} = 1.5$ and $\xi_{20} = 6.0$ (Fig. 1). Our computations show that, in this case, the solution relaxes to a steady state. Figure 2

illustrates the distributions of the electron density $n_e(x)$ and potential $\Phi(x)$ over the interval $(0, l)$. The electron density at the wall is maximum ($n_e(l) = 0.3$), and the potential of the wall and its charge are both negative ($\Phi(l) = -0.8$ and $\rho(l) = -1.4$). Hence, in the case of low temperatures, we deal with a classical DL, which prevents slow electrons from reaching the wall. The DL is as thick as several Debye radii. Figure 3 shows the contours of $f_e(x, V)$. In steady state, these contours are simply electron trajectories in phase space (x, V). We can see that slow electrons are reflected from the Debye potential barrier, while electrons with thermal energies and higher reach the wall. All of the secondary electrons emitted from the wall surface gain energy when passing through the DL. It is of interest to address the question of the energy flux carried by the electrons to the wall. To answer this question, we calculated the two quantities

$$G^+ = \int_0^\infty V \frac{V^2}{2} f_e(l, V) dV, \quad G^- = \int_{-\infty}^0 |V| \frac{V^2}{2} f_e(l, V) dV, \quad (16)$$

which are the energy fluxes of the incident and secondary electrons, respectively. The result is $G^+ = 0.15$ and $G^- = 0.05$, which indicates that about one-third of the energy of the incident electrons is carried by the secondary electrons away from the wall.

At high temperatures, the main parameters behave in a qualitatively different fashion. Let us consider the numerical results obtained for $\xi_{00} = 0.25$ and $\xi_{20} = 1.0$. In this case, the solution does not relax to a steady state. After a certain time, which depends on the particular choice of the initial conditions, the solution becomes nearly periodic. Figure 4 shows the time evolutions of the electron density, electric potential, and surface charge density at $x = l$. As may be seen, the charge on the wall is always positive ($\rho \approx 1.9$) and the electron density at the wall, $n_e(l) \approx 4$, is higher than that in the plasma. In view of such behavior of the electron density, the DL described by this solution can naturally be called the anti-Debye layer. The potential oscillates with the largest amplitude and changes sign with a period of about six (recall that time is normalized to the reciprocal of the characteristic plasma frequency). Figure 5 shows the spatial profiles of the electron density and electric potential at different instants in a time interval approximately equal to the oscillation period. Figure 6 displays the trajectories of ten electrons starting with different initial velocities at the time $t \approx 610$ from the left (five electrons) and right (the other five) boundaries. A comparison with Fig. 3 allows us to conclude that the electron trajectories possess some new property, namely, that slow secondary electrons can return to the wall. Figure 7 illustrates how the electron distribution function depends on V at different points x. The plots in this figure were calculated for the time at which $\Phi(l) > 0$. That the distribution function at $x = l$ is double-humped is explained by the fact that the elec-
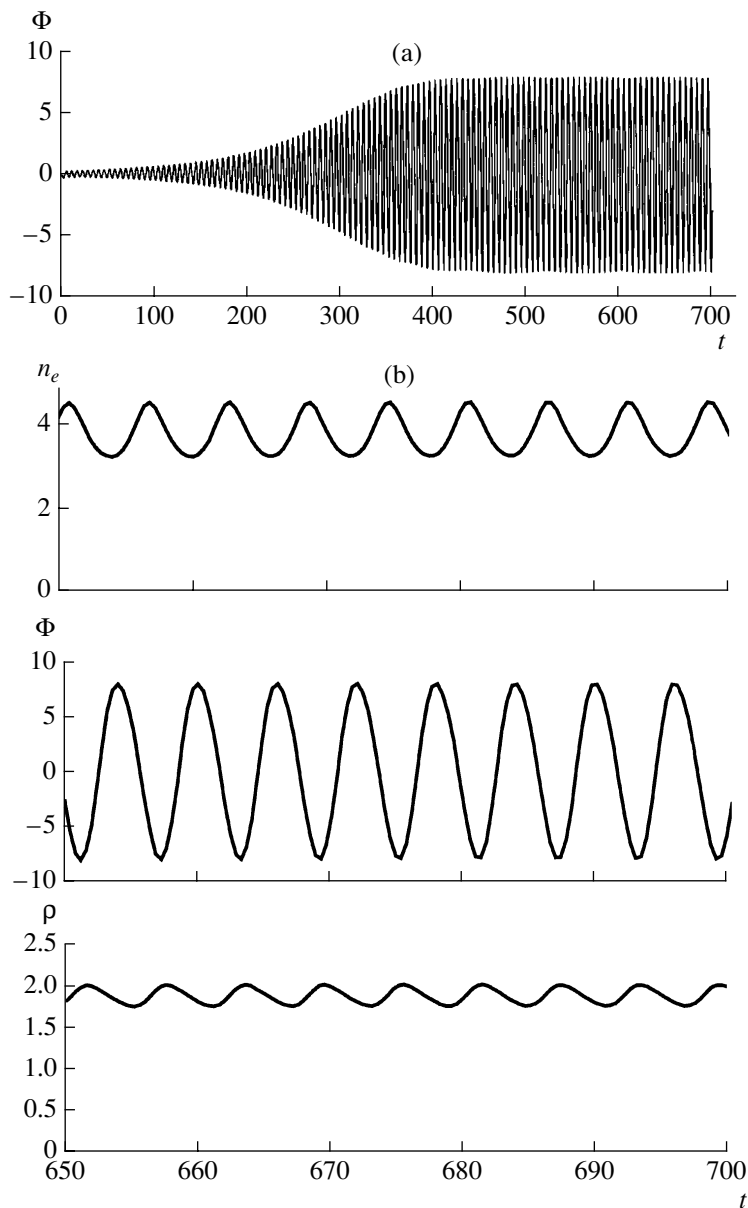
Fig. 4. Calculated time evolutions of (a) the electric potential ($0 < t < 700$) and (b) the electron density, electric potential, and surface charge density ($650 < t < 700$) at the wall ($x = l$) in the case of high electron temperatures ($\xi_{00} = 0.25$ and $\xi_{20} = 1.0$).

trons moving toward the wall are accelerated, while those moving away from the wall are decelerated. The corresponding time-averaged energy fluxes are equal to $\langle G^+ \rangle = 0.81$ and $\langle G^- \rangle = 0.40$.

The question naturally arises of how the final results depend on the length l of the computation region and, accordingly, on boundary condition (7). The calculations carried out for $l = 15$ show that the main characteristic property (an increase in the electron density near the wall) is preserved. Figure 8 shows a representative spatial profile of the electron density, calculated for $l = 15$. The characteristic oscillation frequency also

remains unchanged, although the potential at the wall oscillates with a somewhat larger amplitude. On the whole, however, the question of how to formulate the "correct" condition at the left boundary has gone unanswered.

Our numerical calculations show that, as the electron temperature grows, the layer evolves into an unsteady structure and the effective layer thickness slightly increases, which somewhat limits the applicability of our model (in which the ion velocity and density are assumed to be constant) and, especially, of the above boundary conditions in studying DLs. Note also
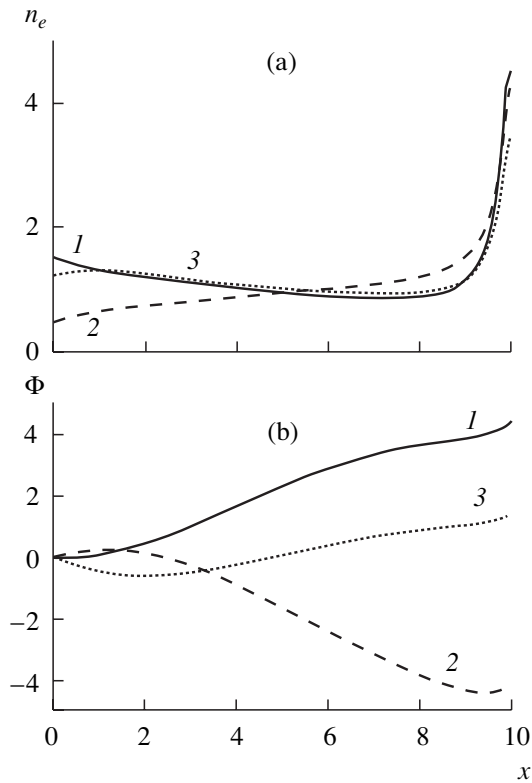
Fig. 5. Spatial profiles of the electron density and electric potential in an unsteady regime ($\xi_{00} = 0.25$ and $\xi_{20} = 1.0$) at different instants. Curves *1* and *2* were calculated for the times at which the potential at the wall is the highest and the lowest, respectively, and curve *3* corresponds to an instant between these times.

Fig. 6. Trajectories of ten electrons that start from (a) the left (five electrons) and (b) the right (the other five) boundary at the time $t \approx 610$ in an unsteady regime ($\xi_{00} = 0.25$ and $\xi_{20} = 1.0$).

Fig. 7. Electron distribution function vs. velocity for $\xi_{00} = 0.25$ and $\xi_{20} = 1.0$ at different points $x = $ (*1*) 0.0, (*2*) 2.5, (*3*) 5.0, (*4*) 7.5, and (*5*) 10.
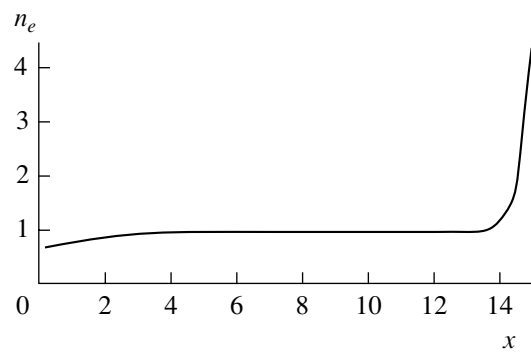
Fig. 8. Spatial profile of the electron density for $l = 15$, $\xi_{00} = 1.5$, and $\xi_{20} = 6.0$.

that, in our earlier paper [2], we reported the results of numerically solving the problem in a formulation that differs by some details from the above formulation. Although the results obtained in [2] and in the present paper are quantitatively different, the qualitative conclusions are the same.

4. CONCLUSION

We have proposed a fairly simple one-dimensional non-steady-state model that describes the formation of a DL at a dielectric surface with allowance for secondary electron emission. The model is based on the set of Vlasov–Poisson equations and the equation for the surface charge density.

Our simulations carried out for low temperatures of the incident electrons revealed the formation of a classical DL, which screens the surface from slow electrons. The surface itself is found to acquire a negative charge.

In simulations carried out for high temperatures of the incident electrons, we failed to achieve a steady-state regime. The solution obtained is quasi-periodic in character, the electron density at the wall is higher than that in the plasma, and the wall surface acquires a positive charge. The last circumstance necessitates the development of models that explicitly take into account the ion dynamics and thus are capable of describing the possible reflection of ions from the wall.

REFERENCES

1. A. I. Morozov, *Physical Concepts of Electrical-Propulsion Engines* (Atomizdat, Moscow, 1978).

2. A. I. Morozov and V. V. Savelyev, *Reviews of Plasma Physics*, Ed. by B. B. Kadomtsev and V. D. Shafranov (Consultant Bureau, New York, 2000), Vol. 21, p. 203.

3. *Encyclopedia of Low-Temperature Plasma*, Ed. by V. E. Fortov (Nauka, Moscow, 2000), Vol. 3, p. 444.

4. B. A. Arkhipov, R. Yu. Gnizder, N. A. Maslennikov, and A. I. Morozov, Fiz. Plazmy **18**, 1241 (1992) [Sov. J. Plasma Phys. **18**, 641 (1992)].

5. A. I. Bugrova, A. I. Morozov, and V. K. Kharchevnikov, Fiz. Plazmy **18**, 963 (1992) [Sov. J. Plasma Phys. **18**, 501 (1992)].

6. A. I. Morozov and V. V. Savel'ev, Fiz. Plazmy **27**, 607 (2001) [Plasma Phys. Rep. **27**, 570 (2001)].

7. A. I. Morozov, Fiz. Plazmy **17**, 672 (1991) [Sov. J. Plasma Phys. **17**, 393 (1991)].

8. C. Z. Cheng and G. Knorr, J. Comput. Phys. **22**, 330 (1976).

9. P. K. Smolarkiewitcz, J. Comput. Phys. **54**, 325 (1984).

Translated by I.A. Kalabalyk

Stability of a Stationary Double Layer

V. A. Turikov

Russian University of Peoples' Friendship, ul. Miklukho-Maklaya 6, Moscow, 117198 Russia

Received May 17, 2002

Abstract—Electrostatic oscillations in a stationary beam double layer are studied in the hydrodynamic approximation. An analysis of the solutions to the linearized equations for perturbations shows that the double layer in an unbounded plasma may be subject only to convective instability, in which case the perturbations localized inside the region of the potential jump escape from the plasma without distorting the steady field structure. The double layer in a bounded plasma is investigated numerically by a particle-in-cell method. It is established that, as is the case in the Pierce system, the governing role in the stability of the double layer is played by the field of the charges induced on the surfaces of the conducting electrodes. © 2002 MAIK "Nauka/Interperiodica".

1. INTRODUCTION

The double layer (DL) in a plasma is the region of a self-consistent potential drop maintained by the appropriate distributions of accelerated and reflected particles. The DLs, which can be either stationary or moving, have been investigated in many laboratory and numerical experiments (see reviews [1–4]). Interest in DLs was greatly stimulated by a paper by Block [5], who pointed out for the first time that they may play an important role in the acceleration of particles to high energies in the Earth's magnetosphere. Later, the regions of the potential jump that can be interpreted as DLs were repeatedly observed in space experiments [6, 7]. At present, DLs are invoked to explain a large number of astrophysical phenomena [8]: they are considered as possible mechanisms for energy release in solar flares, the acceleration of electron beams driving X-ray emission from pulsars, etc.

The DL structure assumes the presence of charged particle beams, which makes DLs *a priori* unstable. The instabilities may result in an insignificant deformation of the potential profile in the layer or may even destroy the layer completely. The instabilities associated with the growing perturbations that propagate toward the DL from a low-potential region and the instabilities in the region of the potential drop are thought to be the most dangerous [2]. In studying a DL in an infinite plasma, Wahlberg [9, 10] arrived at the conclusion about the trapping of plasma electron oscillations in the layer and the development of the absolute instability. However, since such perturbations should be carried by charged particle beams to homogeneous regions of the system, the oscillations are unlikely to be trapped within the layer. This is confirmed, in particular, by the results of numerical simulations described in Section 4 of the present work.

In Section 2, the stability of a stationary DL in an unbounded plasma is studied theoretically. The main objective is to clarify whether the instability can occur in the region of the potential jump. Note that most of the papers on the stability of DLs dealt with unbounded plasmas [9–12]. The use of an unbounded plasma approximation is justified in situations in which the time required for perturbations to propagate through the entire system is much longer than the characteristic time scales on which the field associated with the conducting boundaries grows [13]. If this condition is not satisfied, then the boundaries can radically change the nature of oscillations in the layer [14, 15]. The problem of the stability of a DL in a bounded plasma is discussed in Section 4 on the basis of the results obtained in numerical experiments.

2. MODEL OF A BEAM DOUBLE LAYER

According to Shamel's classification [11], for a beam DL the particle distributions in phase plane have the form of isolated beams (see the phase distributions discussed in Section 4). In homogeneous regions outside the beam layer, the electron and ion densities are the same. Note that stationary DLs of this type are most often encountered in laboratory and numerical experiments. They belong to the class of so-called strong DLs [3], in which the potential energy of the particles can be hundreds of times higher than their thermal energy.

Further analysis will be based on a simplified model of a beam DL in which the accelerated particles are described by monoenergetic beams and the reflected particles obey a Boltzmann distribution. In this model, Poisson's equation for the steady-state potential in the layer has the form [15]

$$
\frac{d^2\Phi}{dX^2} = 2\left\{ \frac{1}{\sqrt{1+\Phi}} - \frac{1}{\sqrt{1+\Psi-\Phi}} \right.
$$

$$
\left. + \left(1 - \frac{1}{\sqrt{1+\Psi}}\right)\left[\exp\left(\frac{\Phi-\Psi}{\beta}\right) - \exp\left(-\frac{\Phi}{\beta}\right)\right]\right\}. \tag{1}
$$

Here, the following notation is introduced: $X = x\omega_0/v_{0e}$, $\omega_0 = (4\pi e^2 n_0/m_e)^{1/2}$, n_0 is the plasma density in the homogeneous regions, v_{0e} is the electron beam velocity at the entrance to the DL, $\Phi = 2e\varphi/m_e v_{0e}^2$ is the dimensionless potential, $\Psi = 2e\varphi_0/m_e v_{0e}^2$ is the dimensionless potential amplitude, $\beta = 2T_e/m_e v_{0e}^2$, and T_e is the temperature of the reflected electrons. Poisson's equation (1) was derived under the simplifying assumption $T_e = T_i$ (where T_i is the temperature of the reflected ions) and with the use of the Langmuir condition [1] $m_e v_{0e}^2 = m_i v_{0i}^2$ (where v_{0i} is the ion beam velocity at the entrance to the DL), which ensures that the electric field vanishes at infinity ($X \longrightarrow \pm\infty$). The origin of the coordinate system is chosen to be located at the center of the layer. In order for the trajectories of the accelerated and reflected particles to be separated in phase plane, it is also assumed that the condition $\Psi/\beta \gg 1$ is satisfied.

We define the width of the DL by the relationship

$$\delta = \frac{\Psi}{|d\Psi/dX|_{\max}}.$$

From Eq. (1), the width of a DL with a high potential amplitude ($\Psi \gg 1$) can be expressed as [15]

$$\delta \approx 0.55\Psi^{3/4}. \tag{2}$$

Expression (2) implies that the higher the potential in a beam DL, the larger the layer width. As will be shown below, this circumstance has a decisive influence on the layer stability conditions inside the region of the potential drop. Note that, in studies on the properties of DLs, it is often assumed that the parameters δ and Ψ may change independently of one another. However, this assumption may yield erroneous results. Thus, Gedalin *et al.* [14] investigated the stability of DLs with an infinitely narrow and infinitely high potential jump. However, as can be seen from expression (2), such layers have nothing in common with actual DLs.

3. STABILITY OF A DOUBLE LAYER IN AN UNBOUNDED PLASMA

3.1. Electron Oscillations in the Region of the Potential Drop

In the cold beam approximation, we assign the dependence $\exp(-i\Omega T)$ (where $T = \omega_0 t$) to perturbed quantities in order to write the equations for the electron perturbation amplitudes in the following dimensionless form:

$$\frac{d}{dX}(G^{-1}V_{\text{ef}} + GN_{\text{ef}}) - i\Omega N_{\text{ef}} = 0, \tag{3}$$

$$\frac{d}{dX}(GV_{\text{ef}}) - i\Omega V_{\text{ef}} - \frac{d\Phi_1}{dX} = 0, \tag{4}$$

$$\frac{d}{dX}(N_{\text{er}}^{(0)}V_{\text{er}}) - i\Omega N_{\text{er}} = 0, \tag{5}$$

$$\frac{d\Phi_1}{dX} + i\Omega V_{\text{er}} = 0, \tag{6}$$

$$\frac{d^2\Phi_1}{dX^2} - N_{\text{ef}} - N_{\text{er}} = 0. \tag{7}$$

Here, $G(X) = \sqrt{1 + \Phi(X)}$; $V_{\text{ef},r} = v_{\text{ef},r}^{(1)}/v_{0e}$ and $N_{\text{ef},r} = n_{\text{ef},r}^{(1)}/n_0$ are the perturbed velocities and perturbed densities of the accelerated (fast) and reflected electrons, respectively; $\Phi_1 = 2e\varphi^{(1)}/m_e v_{0e}^2$ is the perturbed potential; and $N_{\text{er}}^{(0)} = N_{r0}\exp[(\Phi - \Psi)/\beta]$ with $N_{r0} = 1 - 1/\sqrt{1 + \Psi}$.

The set of Eqs. (3)–(7) differs from the standard set for a uniform beam–plasma system in that the coefficients of the linearized equations are coordinate-dependent. In this case, reflected particles are treated as a cold plasma whose density falls off to zero inside the layer. However, even with this highly simplified approach, in which the thermal motion of accelerated particles is neglected, it is impossible to find a general analytic solution to Eqs. (3)–(7). For further analysis, it is expedient to switch to the field E_{ef} of the density perturbation of an accelerated electron beam [9]:

$$\frac{dE_{\text{ef}}}{dX} = -N_{\text{ef}}.$$

Then, Eqs. (3)–(7) reduce to the following equation for the field E_{ef}:

$$A_e = E_{\text{ef}}\exp\left[\frac{1}{2}\int(3G' - 2i\Omega)/G\,dX\right]. \tag{8}$$

Making the replacements we arrive at the Schrödinger-type equation

$$\frac{d^2A_e}{dX^2} + Q(X)A_e = 0, \tag{9}$$

where

$$Q(X) = \frac{1}{G^3}\left[\frac{\Omega^2}{\Omega^2 - N_{\text{er}}^{(0)}} - \frac{3}{4}G(2G''G - G'^2)\right]. \tag{10}$$

In the limit $X \longrightarrow -\infty$ ($\Phi \longrightarrow 0$), we have $Q(X) = 1$. In the case $\text{Im}\,\Omega > 0$, the field E_{ef} increases exponentially to the left of the layer, in accordance with relationship (8). In an unbounded system, this situation is physically impossible, because, to the left of the layer, there is only a homogeneous electron beam. Consequently, the layer may be subject only to a convective instability with $\text{Im}\,\Omega = 0$. Wahlberg [9, 10] revealed the absolute instability of electron oscillations in the region

of the potential drop; however, this absolute instability is likely attributed to the specific structure of the layer considered in those studies.

In the high-potential region, the accelerated and reflected particles form a beam–plasma system, which is subject to a convective instability with the spatial growth rate

$$\mathrm{Im}\, K = \frac{1}{\sqrt{G^3(N_{r0}/\Omega^2 - 1)}} \quad \text{for} \quad \Omega^2 < N_{r0}.$$

The singularity, specifically, an infinitely large value of $\mathrm{Im}\, K$ at $\Omega^2 = N_{r0}$, is eliminated by taking into account the electron thermal motion [16]. In this case, a DL in an unbounded plasma may remain stable because the perturbations in the region where the steady-state field is localized are carried away by a flow of accelerated particles. The layer can be destroyed by an instability occurring in the region of the potential drop under the condition $\Omega^2 < N_{\mathrm{er}}^{(0)}(X)$. In this case, we can distinguish between two possible situations. If Ω^2 is close to N_{r0}, then the spatial growth rate can be large but the region where the above condition holds is narrow if all particles that move from the infinitely remote region $X = +\infty$ toward the layer are reflected. This situation occurs when $\Psi \gg \beta$; accordingly, the perturbations do not have enough time to grow to any significant amplitude. If Ω^2 is not too close to N_{r0}, this region is longer and may even be comparable in length to the DL. However, from quantum mechanics (the phenomenon of tunneling through the potential barrier), it is known that the solutions to Schrödinger equation (9) that describe the spatial distribution of perturbations change insignificantly in the region of a sharp potential drop. In the particular case at hand, this can be shown by expanding the function $N_{\mathrm{er}}^{(0)}(X)$ in a series around the point X_0, where $N_{\mathrm{er}}^{(0)}(X_0) = \Omega^2$. With this expansion, Eq. (9) becomes

$$\frac{d^2 A_e}{dy^2} + \frac{c}{y} A_e = 0, \quad y = X - X_0, \quad c^{-1} = G^3 \Phi'/\beta|_{X = X_0}.$$

The general solution to this equation can be expressed in terms of the modified Bessel functions [17]:

$$A_e = \sqrt{y}[C_1 I_1(\sqrt{4cy}) + C_2 K_1(\sqrt{4cy})].$$

We see that the general solution is nearly constant around the point $y = 0$ and is proportional to $\propto \sqrt{y}\exp(\sqrt{4cy})$ for $y \longrightarrow +\infty$. Consequently, the characteristic size of the region where the perturbation grows is $\delta_i = 1/4c$. For a large-amplitude DL, we take into account expression (2) to obtain $\delta_i \simeq 2\Psi^{7/4}/\beta \gg \delta$, which indicates that the perturbation does not have enough time to grow significantly in the region of the potential drop. This conclusion also applies to a DL

with a low potential, for which we also have $\delta_i \simeq \Psi/(4\sqrt{2}\,\beta) \gg \delta$.

For $X > X_0$, the second term in expression (10) is small and positive, thereby reducing the spatial growth rate of perturbation associated with the first term. We can convince ourselves of this by setting $G' \simeq \Psi\Phi^{-1/2}/2\delta$ and $G'' \simeq -\Psi^2\Phi^{-3/2}/4\delta^2$ for $\Psi \gg 1$ and $G' \simeq \Psi/2\delta$ and $G'' \simeq -\Psi^2/4\delta^2$ for $\Psi \ll 1$.

Hence, in the region of the potential drop, the beam cannot be convectively unstable. The electron oscillations can grow only in the high-potential region to the right of the layer.

3.2. Stability of a Double Layer with Allowance for Ion Motion

We start by considering plasma oscillations in homogeneous regions on both sides of the layer. In these regions, the solutions to the linearized equations for perturbations are proportional to $\exp[i(KX - \Omega T)]$, and the corresponding dispersion relations for three beams to the left and right of the layer have the form

$$1 - \frac{\mu(1 - \sigma)}{\Omega^2} - \frac{1}{(\Omega - K)^2} - \frac{\mu\sigma}{(\Omega + \sqrt{\mu}K/\sigma)^2} = 0, \quad (11)$$

$$1 - \frac{\mu}{(\Omega + \sqrt{\mu}K)^2} - \frac{1 - \sigma}{\Omega^2} - \frac{\sigma}{(\Omega - K/\sigma)^2} = 0, \quad (12)$$

where $\mu = m_e/m_i$ and $\sigma = 1/\sqrt{1 + \Psi}$.

The system under consideration may be subject to absolute instability if Eqs. (11) and (12) with $\mathrm{Im}\,\Omega > 0$ have the same solutions for real values of K. Since the left-hand sides of these equations reduce to polynomials of degree 6 in the variable Ω, the equations can be solved only numerically. Solutions describing the absolute instability were sought by calculating the deviation of the frequency Ω_- to the left of the DL at fixed K values from the frequency Ω_+ to the right of the DL for all possible values of K:

$$\delta\Omega = [(\mathrm{Re}\,\Omega_- - \mathrm{Re}\,\Omega_+)^2 + (\mathrm{Im}\,\Omega_- - \mathrm{Im}\,\Omega_+)^2]^{1/2}.$$

Figure 1 shows the plots of the minimum value of $\delta\Omega$ versus K in a homogeneous low-potential region. The plots were calculated for two branches of solutions to Eqs. (11) and (12) with $\mathrm{Im}\,\Omega > 0$ at $\Psi = 10$ and $\mu = 5 \times 10^{-4}$. We can see that $\delta\Omega_{\min}$ vanishes only in the trivial case $K = 0$. An analogous situation occurs at other values of Ψ and μ. We thus can conclude that, in an unbounded plasma with mobile ions, the instability of a beam DL is always convective in nature. Note that familiar criteria for determining the type of instability [13, 16] are inapplicable to DLs because of their essential nonuniformity. The Buneman convective instability in a homogeneous low-potential region in an unbounded plasma should in principle lead to the

destruction of the layer. In a bounded plasma, the stability of the DL is governed by the boundary conditions on the field perturbations and by the sources injecting particles into the system (see Section 4).

In studying the Buneman instability in the region of the potential drop in the case of a DL with a high potential, we can neglect the effect of reflected particles and exclusively consider the interaction of the electron and ion accelerated beams. The linearized equations for ion perturbations can be written in the form

$$\frac{d}{dX}(F^{-1}V_{if} - \sqrt{\mu}FN_{if}) - i\Omega N_{if} = 0, \qquad (13)$$

$$\frac{d}{dX}(\sqrt{\mu}FV_{if}) + i\Omega V_{if} - \mu\frac{d\Phi_1}{dX} = 0, \qquad (14)$$

where $F(X) = \sqrt{1 + \Psi - \Phi(X)}$, $V_{if} = v_{if}^{(1)}/v_{0e}$, and $N_{if} = n_{if}^{(1)}/n_0$. Keeping in mind that the instability is convective in nature, we assume that the frequency Ω in Eqs. (13) and (14) is real.

For electron perturbations, we make replacement (8). For ions perturbations, we make the replacement

$$A_i = E_{if}\exp\left[\frac{1}{2}\int\left(3F' - \frac{2i\Omega}{\sqrt{\mu}}\right)F^{-1}dX\right],$$

where $dF_{if}/dX = N_{if}$. Then, using Eqs. (3), (4), (13), and (14), we arrive at the following set of equations:

$$\frac{d^2A_e}{dX^2} + Q_eA_e = -\frac{A_i}{G^3}\exp[-i(\Theta + \theta)], \qquad (15)$$

$$\frac{d^2A_i}{dX^2} + Q_iA_i = -\frac{A_e}{F^3}\exp[i(\Theta + \theta)], \qquad (16)$$

where $Q_e = \left[1 - \frac{3}{4}G(2G''G + G'^2)\right]G^{-3}$, $Q_i = \left[1 - \frac{3}{4}F(2F''F + F'^2)\right]F^{-3}$, $\theta = \Omega\int G^{-1}dX$, and $\Theta = \frac{\Omega}{\sqrt{\mu}}\int F^{-1}dX$.

In the central region of the layer, the functions $Q_{e,i}(X)$ change insignificantly because G' and F' are nearly constant in this region and G'' and F'' are nearly zero, in which case we have $Q_e(X = 0) = Q_i(X = 0) = Q_0$. Figure 2 shows the dependence $Q_e(X)$ obtained by numerically solving Poisson's equation (1) with $\Psi = 5.0$ and $\beta = 0.2$.

Inside the DL, Eqs. (15) and (16) can be regarded as the equations of two oscillators having the same frequency $\sqrt{Q_0}$ and interacting parametrically at a slowly varying frequency proportional to Ω. For $\Psi \gg 1$, we
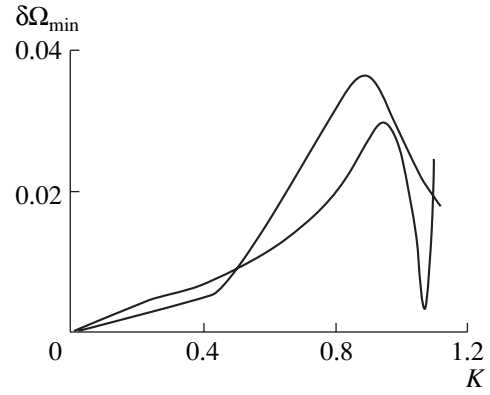
Fig. 1. Dependence of $\delta\Omega_{min}$ on the wavenumber in the low-potential region of a DL for $\Psi = 10$ and $\mu = 0.0005$.
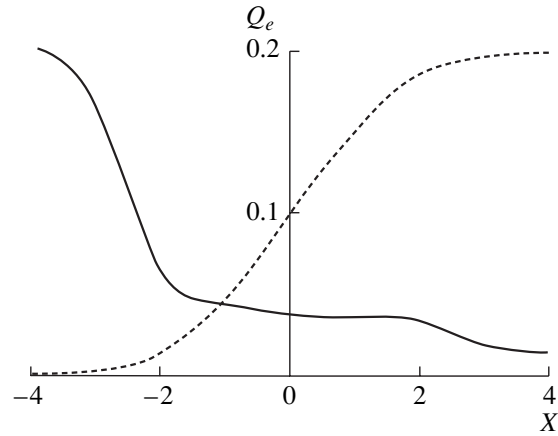
Fig. 2. Dependence of Q_e on the coordinate for $\Psi = 5$, $\beta = 0.2$, and $\Omega = 0.5$. Here and in subsequent analogous figures, the dotted curve represents the initial profile of the steady-state potential.

perform an analysis similar to that carried out in the case of electron oscillations (see Section 2) and take expression (2) into account to obtain the approximate expression $Q_0 \approx 5.3\Psi^{-3/2}$. In this case, the spatial period of "natural" oscillations in the X direction in Eqs. (15) and (16) is equal to

$$L_0 \approx 2.7\Psi^{3/4}.$$

In order for a resonant interaction between the oscillators to occur in the system under consideration, the amount by which the variable X changes should be several times larger than L_0. However, inside the layer, X varies by no more than δ, which satisfies the condition $\delta \ll L_0$ by virtue of expression (2). Consequently, spatial oscillations cannot grow in the region of the potential drop. It may be said that the Buneman convective instability does not have time to develop.
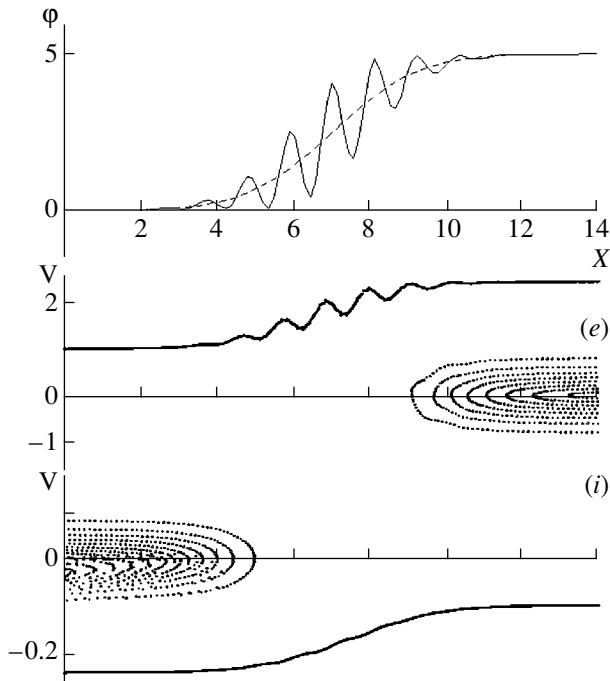
Fig. 3. Initial perturbation in the region of the potential drop for $\Psi = 5$, $\beta = 0.5$, $\mu = 0.01$, and $L = 14$: (*e*) phase plane of the electrons and (*i*) phase plane of the ions.

4. NUMERICAL SIMULATIONS OF A DOUBLE LAYER IN A BOUNDED PLASMA

The linear theory of the stability of a DL in a bounded plasma was constructed in [14, 15]. However, the conditions that were used in those papers to join the solutions in the region of the potential jump may be justified only in the case of a small-amplitude DL ($\Psi < 1$). Because of serious mathematical difficulties, the problem of the stability of a DL in a bounded plasma cannot be solved in the general case even in a linear approximation. That is why it is necessary to carry out numerical experiments, which is a common practice in such situations.

In most papers devoted to numerical simulations of DLs, the problem is formulated in the following two main ways. In the first way, it is assumed that the electron and ion beams are injected into the system from two opposite electrodes with a given potential difference [18, 19]. The second way supposes that the plasma between the electrodes is initially homogeneous and nonmoving and that the electrodes are held at a constant potential applied to them at the initial instant [20, 21]. Both formulations make it possible to analyze the complicated transient processes accompanying the formation of a DL.

In the present paper, numerical simulations are aimed at investigating the stability of a DL; accordingly, the formulation of the problem differs from the above two traditional formulations. Specifically, the

problem was solved by a one-dimensional version of the particle-in-cell method with the following boundary conditions for the potential at the surfaces of the conducting electrodes:

$$\phi(X = 0) = 0, \quad \phi(X = L) = \Psi.$$

The initial potential profile was formed self-consistently by numerically generating the initial particle distribution in phase plane in accordance with the DL model described in Section 2. This formulation of the problem ensures that there are no perturbations in the initial stage of simulation and also makes it possible to follow the evolution of a DL during the development of instability. In simulations, the initial particle distribution was maintained by particle sources at the ends of the system. The accelerated particles were injected at fixed velocity and density. The source of the reflected particles formed a directed particle flow described by a half-Maxwellian distribution function. The half-Maxwellian distribution was generated by using the "quiet start" model [22] in order to reduce the fluctuations of the space charge associated with random particle positions in the cell. The time step ΔT was varied from 0.01 to 0.25, and the spatial step ΔX was varied from 0.05 to 0.5 (the dimensionless variables T and X were defined above). The electron-to-ion mass ratio $\mu = m_e/m_i$ was varied from 0.0005 to 0.01. The number N_c of particles in the cell was from 20 to 150, and the number of cells was from 50 to 200.

Numerical experiments show that the beam of accelerated particles carries away initial perturbations localized in the region of the potential jump without distorting the steady-state field distribution (Figs. 3, 4). This result confirms the theoretical conclusions reached in Section 3 when analyzing the stability of a DL in an unbounded system. In this case, the conducting boundaries of the electrodes do not have time to come into play because of the short time it takes the perturbation to traverse the layer. The system turns out to be extremely stable against such perturbations, even when their amplitude is comparable with the amplitude of the steady-state potential in the layer. On longer time scales, the system behaves as if there were no initial perturbations within the layer. In this case, the charges induced on the conducting electrode surfaces play a decisive role in the evolution of the system, as is the case with the Pierce instability of an electron beam between the electrodes [23].

In the case of sufficiently narrow homogeneous regions, a virtual cathode (a minimum in the electric potential) accompanied by the appearance of reflected electrons forms near the electrode with the lower potential in the nonlinear stage of the instability. This case is illustrated in Fig. 5. The initial profile of the steady-state potential is seen to be distorted insignificantly. On longer time scales, the distributions to which the field and the particles have relaxed remain unchanged. Such a structure in the nonlinear stage of the Pierce instabil-
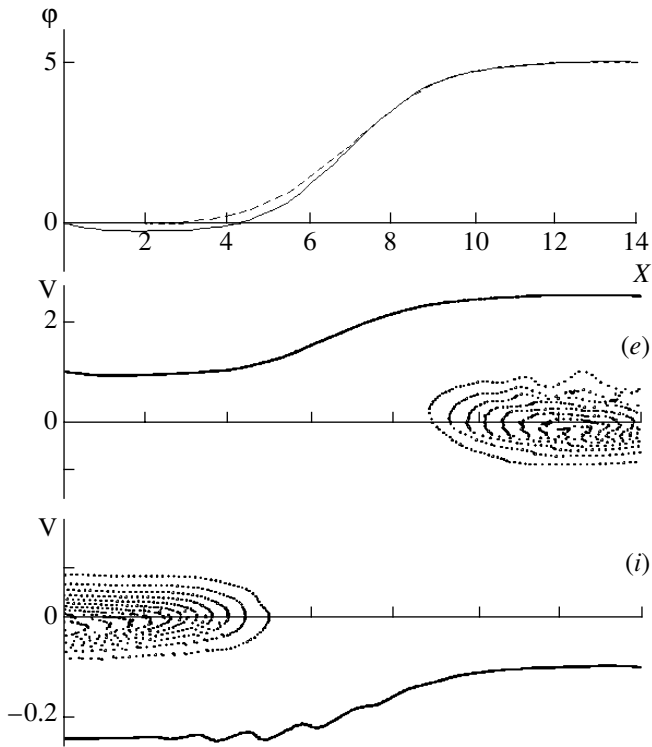
Fig. 4. State of a DL at time $T = 3$ for the initial perturbation shown in Fig. 3.
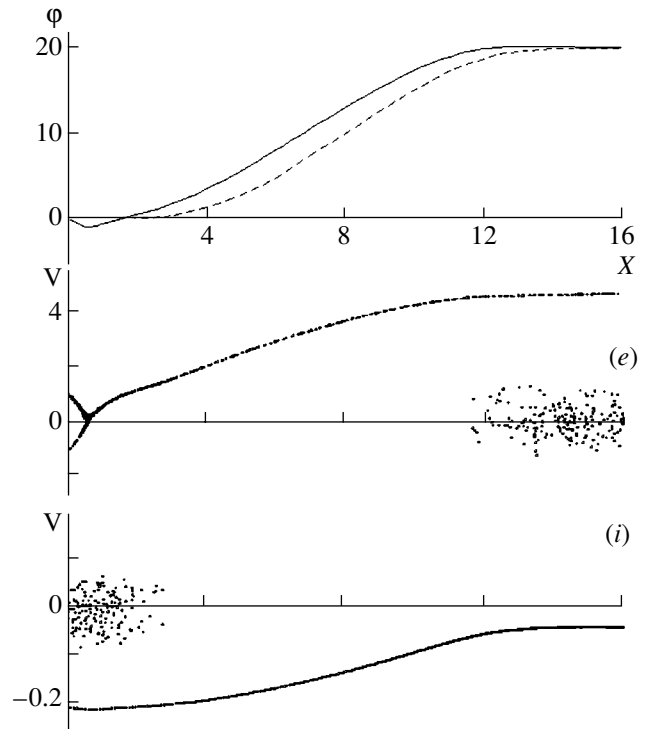
Fig. 5. Formation of a virtual cathode in the low-potential region of a DL at time $T = 75$ for $\Psi = 20$, $\beta = 0.5$, $\mu = 0.0005$, and $L = 16$.
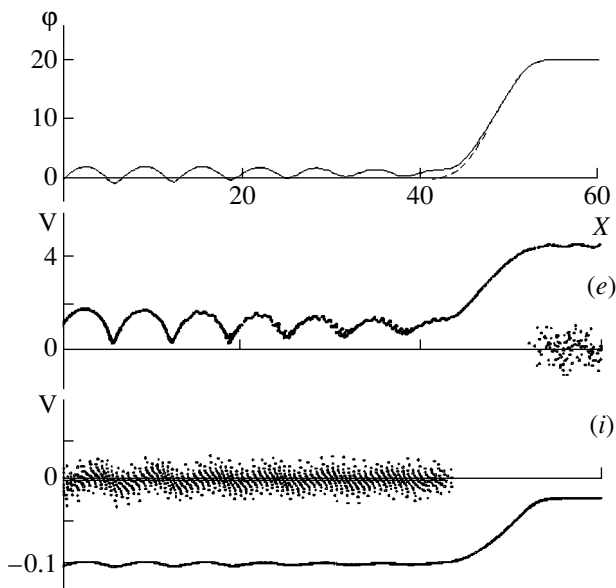
Fig. 6. Formation of the modulated distributions of the potential and of the velocities of free electrons in the low-potential region of a DL at time $T = 40$ for $L = 60$, the distance from the cathode to the layer center being $d = 48$. Here and in the subsequent figures, the values of the parameters Ψ, β, and μ are the same as those in Fig. 5.
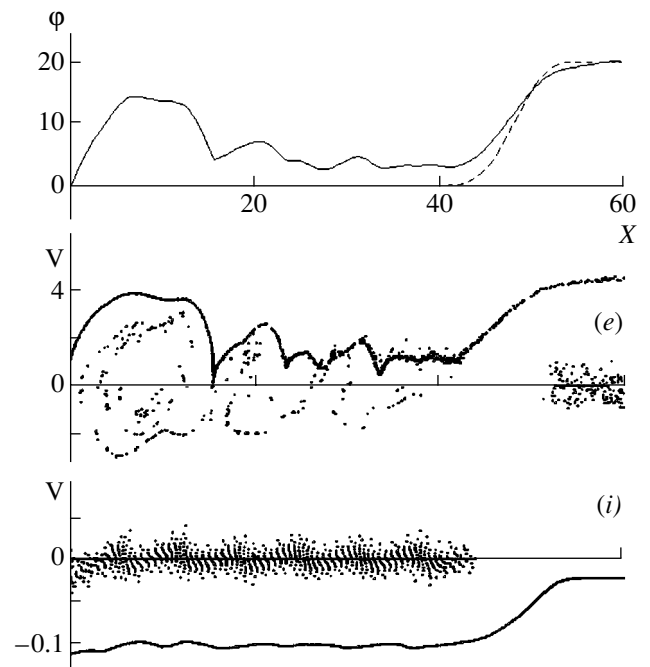
Fig. 7. Explosive increase in the potential in the low-potential region of a DL at time $T = 55$.
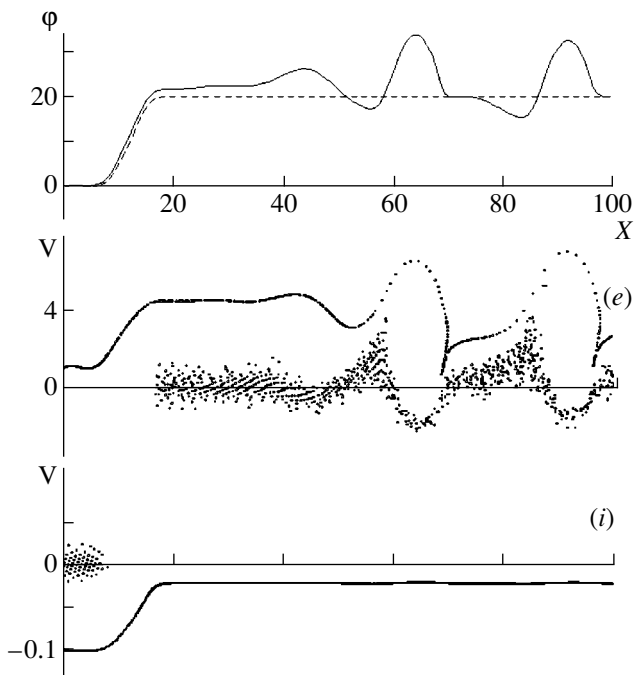
Fig. 8. Nonlinear stage of the beam instability in the high-potential region of a DL at time $T = 11$ for $L = 100$ and $d = 12$.

ity was also captured numerically by Burinskaya and Volokitin [24]. The formation of the structure is related to the additional field generated by the induced charges.

As the region with a low potential becomes wider, the instability begins to proceed in precisely the same way as in a long uniform system consisting of an electron beam and mobile ions [25]. After a time interval of about the transit time of free electrons through the region with low potential, the modulated distributions of the field and the electron velocities form to the left of the layer (Fig. 6). In this stage, a fairly intense ion motion indicates the development of a Buneman instability in a bounded plasma system. However, this instability differs significantly in properties from the conventional Buneman instability in an unbounded layer because the spatial scales of structures like those shown in Fig. 6 coincide with the scales characteristic of the case of immobile ions. Consequently, the initial stage of the instability is dominated by the electron motion in the field of induced charges, as is the case in the Pierce system. On longer time scales, the ions are entrained in plasma oscillations; as a result, the instability growth rate increases. As the amplitude of the perturbation grows, the electrons become trapped in the potential wells. Then, the potential in the zones around the maxima of the modulated distribution increases in an explosive manner (Fig. 7), as is the case in a uniform system investigated in [25]. The perturbations grow most intensely near the cathode. Further, the zone where the potential has originally increased in an explosive man-

ner expands and overlaps with the similar zones arising later. As a result, the potential increases to an amplitude of about Ψ over the entire region between the cathode and the layer and the initial stationary structure is destroyed completely. Numerical experiments show that, in the case of a long region with a low potential, the lifetime of a DL may be as long as about the ion plasma period, which is in agreement with the data from laboratory and satellite measurements [3, 4, 6, 7].

The beam instability to the right of the DL was analyzed by modeling a system with a short low-potential region. A high-potential region whose length exceeds a certain limiting length is subject to the beam instability. The limiting length increases with increasing temperature of the reflected electrons (the parameter β) and with increasing potential amplitude Ψ. The vortices arising in phase plane in the strongly nonlinear stage of the instability destroy the layer (Fig. 8). Although the right boundary of the system is transparent to the accelerated electrons, it reflects the field perturbations, thereby preventing their convective transport away from the layer. The characteristic time scales on which the instability develops in this region are about the plasma period of the reflected electrons, which is much shorter than the corresponding time scales in the low-potential region. Hence, we can conclude that, from the standpoint of increasing the lifetime of a DL, situations in which the region of the potential drop is close to the electrode with the higher potential are more favorable.

5. CONCLUSION

The stability of a beam DL has been investigated both theoretically and numerically. It has been shown that the instability of a beam DL in an unbounded plasma is of a convective nature. The electron perturbations localized in the region of the potential jump escape from it without distorting the initial stationary DL structure. The Buneman convective instability does not have time to develop inside the DL because the electrons and ions are efficiently accelerated by the steady-state field of the layer.

The problem of the stability of a DL in a plasma between two electrodes held at fixed potentials has been studied by numerical simulations. It has been shown that this plasma system is stable against perturbations in the region of the potential jump even when the perturbation amplitude is comparable with the amplitude of the steady-state potential in the layer. In the case of short homogeneous regions, the formation of a virtual cathode near the electrode with the lower potential is accompanied by an insignificant distortion of the steady-state potential, in which case the overall DL structure remains unchanged. It has been established that, in a system with a long low-potential region and a short high-potential region, the instability is associated exclusively with the field of the charges induced on the surfaces of the conducting electrodes. The scenario for instability growth is analogous to that in the

case of a bounded homogeneous plasma with an electron beam. It has been concluded that the lifetime of a DL in this system may be as long as the ion plasma period.

REFERENCES

1. V. A. Liperovskiĭ and M. I. Pudovkin, *Anomal Resistance and Double Layers in the Magnetosphere Plasma* (Nauka, Moscow, 1983).

2. A. S. Volokitin and V. V. Krasnosel'skikh, Itogi Nauki Tekh., Ser.: Issled. Kosm. Prostranstva **28**, 129 (1988).

3. M. A. Raadu, Phys. Rep. **178** (2), 25 (1989).

4. N. Hershkowitz, Space Sci. Rev. **41**, 351 (1985).

5. L. P. Block, Cosmic Electrodyn. **3**, 349 (1972).

6. M. H. Boehm and F. S. Mozer, Geophys. Res. Lett. **8**, 607 (1981).

7. R. Bostrom, G. Gustaffson, B. Holback, *et al.*, Phys. Rev. Lett. **61**, 82 (1988).

8. H. Alfven, IEEE Trans. Plasma Sci. **14**, 779 (1986).

9. C. Wahlberg, J. Plasma Phys. **22**, 303 (1979).

10. C. Wahlberg, J. Plasma Phys. **26**, 317 (1981).

11. H. Shamel, Z. Naturforsch. A **38**, 1170 (1985).

12. G. Knorr and C. R. Goertz, Astrophys. Space Sci. **31**, 209 (1974).

13. A. M. Fedorchenko and N. Ya. Kotsarenko, *Absolute and Convective Instabilities in Gaseous and Solid-State Plasmas* (Nauka, Moscow, 1981).

14. M. E. Gedalin, V. V. Krasnosel'skikh, and D. S. Lominadze, Fiz. Plazmy **11**, 870 (1985) [Sov. J. Plasma Phys. **11**, 508 (1985)].

15. V. A. Turikov and I. V. Ul'yanitskiĭ, Fiz. Plazmy **25**, 929 (1999) [Plasma Phys. Rep. **25**, 855 (1999)].

16. A. B. Mikhailovskii, *Theory of Plasma Instabilities* (Atomizdat, Moscow, 1975; Consultants Bureau, New York, 1974), Vol. 1.

17. E. Kamke, *Differentialgleichungen*, Bd. 1: *Gewöhnliche Differentialgleichungen* (Geest and Portig, Leipzig, 1964; Nauka, Moscow, 1971).

18. N. G. Belova, A. A. Galeev, R. Z. Sagdeev, and Yu. S. Sigov, Pis'ma Zh. Éksp. Teor. Fiz. **31**, 551 (1980) [JETP Lett. **31**, 518 (1980)].

19. N. Singh, Plasma Phys. **24**, 639 (1982).

20. R. F. Hubbard and G. Joyce, J. Geophys. Res. A **84** (8), 4297 (1979).

21. T. Yamamoto, J. Plasma Phys. **34**, 271 (1985).

22. Yu. A. Berezin and Yu. A. Vshivkov, *Particle Method in the Dynamics of Tenuous Plasmas* (Nauka, Novosibirsk, 1980).

23. N. V. Kuzelev and A. A. Rukhadze, *Electrodynamics of Dense Electron Beams in Plasma* (Nauka, Moscow, 1990).

24. T. M. Burinskaya and A. S. Volokitin, Fiz. Plazmy **9**, 453 (1983) [Sov. J. Plasma Phys. **9**, 261 (1983)].

25. T. M. Burinskaya and A. S. Volokitin, Fiz. Plazmy **10**, 989 (1984) [Sov. J. Plasma Phys. **10**, 567 (1984)].

Translated by I.A. Kalabalyk

PLASMA ACCELERATORS

Global Characteristics of an ATON Stationary Plasma Thruster Operating with Krypton and Xenon

A. I. Bugrova*, A. S. Lipatov*, A. I. Morozov**, and L. V. Solomatina*

*Moscow State Institute of Radioengineering, Electronics, and Automation, pr. Vernadskogo 78, Moscow, 117454 Russia
**Russian Research Centre Kurchatov Institute, pl. Kurchatova 1, Moscow, 123182 Russia
Received April 19, 2002

Abstract—The global characteristics of an ATON stationary plasma thruster operating on xenon and krypton are investigated. It is shown that, with krypton, the thrust at the same mass flow rate of the working gas is greater and the efficiency is somewhat lower than those with xenon. An efficiency of ~60% was achieved with krypton for the specific impulse attaining 3000 s. The jet divergence is $\sim \pm 22°$ for krypton and $\sim \pm 11°$ for xenon. © *2002 MAIK "Nauka/Interperiodica".*

1. INTRODUCTION

In [1–3], the principles of operation of a stationary Hall-current plasma accelerator of the second generation (an ATON stationary plasma thruster) with unsurpassed characteristics were described. When operating with xenon at an input power of ≥750 W, the thruster efficiency can attain 70%, which is 15% higher than the maximum efficiency achieved in conventional stationary plasma thrusters (SPTs). The jet divergence in the ATON SPT is significantly smaller than that in conventional plasma accelerators, such as M-70 and SPT-100. Thus, the divergence half-angle in the ATON SPT is as small as ±11°, whereas in conventional accelerators (SPT-100), it is ±45° [4].

Such high parameters of an ATON SPT operating with Xe were achieved by creating a proper electric potential profile in the annular channel in order to ensure the required focusing of ions in the channel and to separate the plasma flow from the channel wall in the acceleration region.

In recent years, much attention has been attracted to the operation of SPTs with other working gases. Interest in this problem stems from the high cost of Xe and its limited production in the world.

The studies were carried out in an ATON SPT of the A-3 type, which is shown schematically in Fig. 1. The inner diameter of the outer insulator was 60 mm, the channel length was 24 mm, and the gap width was $b = 12$ mm. The experiments were performed in the input power range $W \leq 2.0$ kW. With each working gas, the accelerator operated under optimum conditions, which were characterized by the minimum discharge current. The pressure in the chamber was 10^{-4} torr.

This paper is aimed at studying the local and global characteristics of an ATON SPT operating with Xe (or with Kr as an alternative working gas).

2. SCALING LAW

According to the scaling law [5, 6], an accelerator operating with the same working gas Xe but with different mass flow rates operates in the same (with respect to the global characteristics) mode if the value of the parameter α,

$$\alpha \equiv \frac{\dot{m}}{S} b, \qquad (1)$$

is the same. Here, $\dot{m}$ is the mass flow rate of the working gas, S is the channel cross-sectional area, and b is the channel width.

As was shown in [5, 6], the parameter α can be rewritten in the form

$$\alpha = \frac{1}{\sqrt{\Lambda_*}} \left(\frac{\varepsilon T_0}{\beta^2} \right)^{1/2}, \qquad (2)$$
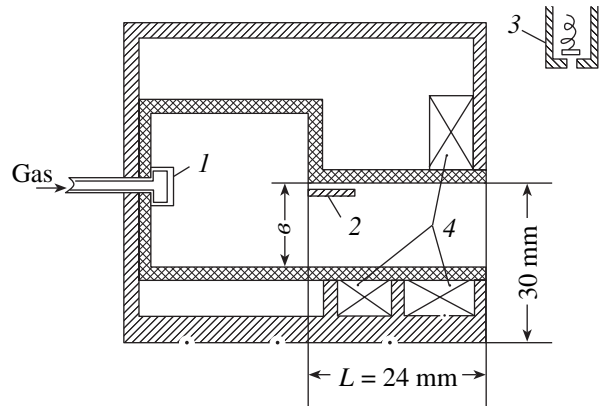

Fig. 1. Schematic of an A-3 SPT: (*1*) gas distributor, (*2*) anode, (*3*) cathode, and (*4*) magnetic coils.

where $\Lambda_* = \Lambda\delta$; $\Lambda = \lambda_{ion}/L$ is the ionization length; L is the effective channel length over which the electric field is sufficiently high; $\delta = \varepsilon/(eU_d)$, ε being the ion energy cost, which is close to the quantity ΔU that determines the energy spent on ionization and other losses; U_d is the discharge voltage; T_0 is the temperature of the working-gas atoms at the inlet into the SPT channel; and $\beta(T_e, A) = \langle\sigma v\rangle$ is the ionization coefficient, which depends on the electron temperature T_e and the sort of the working gas. However, expression (2) is inconvenient to use. For this reason, we clarify its physical meaning and put it into a practically usable form. Indeed, it follows from expressions (1) and (2) that

$$\left(\frac{\dot{m}}{S}b\right)^2 \sim \frac{eU_d}{\beta^2}T_0 = \text{const.} \qquad (3)$$

Hence, the mass flow rate of the working gas is a universal function of the main accelerator parameters U_d, b, S, and T_0. Apparently, this conclusion is accurate to within β. Since β depends only slightly on the properties of the working gas and, moreover, the electron energy distribution function and its time evolution in the accelerator channel are not known with certainty, the conclusion about the equality of the mass flow rates for thrusters that have the same sizes, but operate with different working gases is accurate to a factor of 2.

3. GLOBAL PARAMETERS OF THE A-3 MODEL

3.1. Current–Voltage Characteristics and Discharge-Current Fluctuations

Figure 2a shows the static current–voltage characteristics of a model plasma accelerator operating with Xe and Kr. The characteristics were obtained under the optimum (with respect to the magnetic field) operating conditions at the same mass flow rate $\dot{m} = 2.3$ mg/s. It is seen from the figure that, in the voltage range $250\,\text{V} \leq U_d \leq 400$ V for Xe and $300\,\text{V} \leq U_d \leq 500$ V for Kr, the discharge current depends only slightly on the voltage, which indicates the high degree of ionization of the working gas.

For Xe in the above voltage range, the discharge current either is equal to the mass current $J_{\dot{m}} = m_a n_a v_a S$ expressed in amperes (the subscript "a" denotes atoms of the working gas) or somewhat exceeds the value of $J_{\dot{m}}$ because of the presence of a "transit" electron current and a certain fraction of doubly charged ions (10–12%).

When Kr is used as a working gas, the discharge current is substantially higher than the mass current. This may be attributed to the worse focusing of the plasma flow in the channel as compared to the case of Xe and, consequently, to the different near-wall conductivity, which affects the discharge current [7].
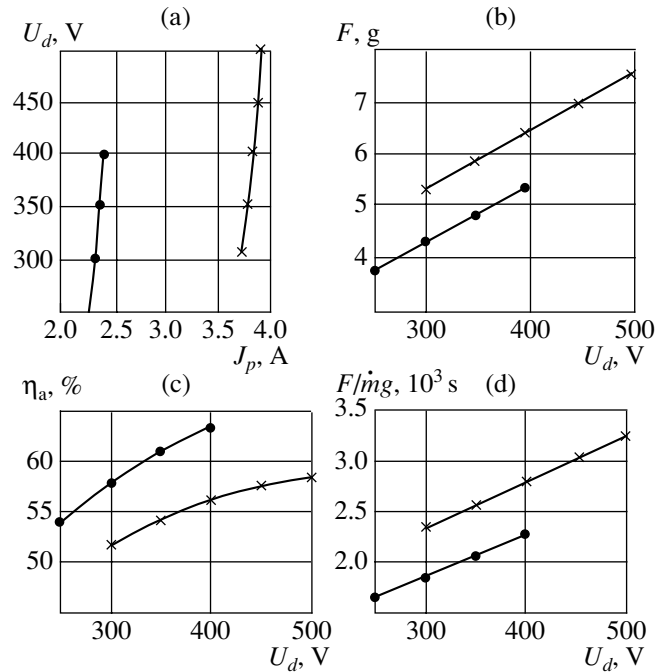
Fig. 2. (a) Current–voltage characteristics of the discharge and the dependences of (b) the thrust, (c) efficiency, and (d) specific impulse on the discharge voltage at $\dot{m} = 2.3$ mg/s for Kr (crosses) and Xe (circles).

When operating with both of these gases, the discharge-current fluctuations in the frequency range 1–300 kHz are $\tilde{J}/\bar{J} \leq 0.1$–0.2.

3.2. Thrust Characteristics

The test device was equipped with a torsion three-filament balance with a relative measurement error of $\leq \pm 3\%$. Figure 2b shows the results of thrust measurements at the mass flow rate $\dot{m} = 2.3$ mg/s for Xe and Kr. It can be seen from the figure that, at the same mass flow rate, the thrust for Kr is greater than for Xe. This is explained by the fact that, at the same mass flow rate and a sufficiently high degree of ionization of the working gas (see Fig. 2a, illustrating the current–voltage characteristic of the discharge), the number of the created ions is inversely proportional to the atomic mass, and, consequently, the number of Kr ions producing the thrust is greater than the number of Xe ions. The curves describing the thrust as a function of the mass flow rate and the discharge voltage can be approximated by the formula

$$F = \theta\sqrt{2e(U_d - \Delta U)/M}. \qquad (4)$$

A comparison of the variations in F for Xe and Kr shows that the value of θ is the same for both gases; i.e., in spite of a smaller fraction of doubly charged ions in

Table 1

$\dot{m}_a$, mg/s	1.5	2	2.3	2.5
U_d, V	400	400	400	400
J_p, A	2.5	3.3	3.9	4.2
F, g	3.6	5.3	6.4	7.25
η, %	42	51	55	60
$F/\dot{m}g$, s	2400	2650	2780	2900

the case of Kr, their contribution to the thrust is the same as that for Xe.

Estimates of ΔU [1] (which can be regarded as the average potential of the ionization region) for Xe at $\theta \sim 1$ give the value $\Delta U = 40$ V. For Kr, we have $\Delta U = 60$ V. As is known, this quantity is related to the ionization loss power. As was expected, the ionization losses in Kr are higher, because the ionization energy for Kr is higher than for Xe.

Although the thrust for Kr is higher than for Xe, the thruster efficiency for Kr is lower (Fig. 2c). This is a consequence of the fact that the mass current for Kr is substantially higher than for Xe, whereas the ionization losses for Xe are lower. Figure 2d shows the specific impulse as a function of the discharge voltage for Xe and Kr at the same mass flow rates. It can be seen from the figure that the specific impulse of a thruster operat-

ing with Kr is substantially higher, which can be attributed to the higher velocity of the plasma flow.

As the voltage increases from 300 to 500 V, the thruster efficiency increases from 52 to 58%; the specific impulse at 500 V attains 3240 s. Table 1 presents the global characteristics of a thrust operating with Kr for the same voltage and different mass flow rates. Thus, for $U_d = 400$ V and the mass flow rate $\dot{m} = 2.5$ mg/s, the thruster efficiency attains 60% for a specific impulse of 2900 s.

From the known values of the thrust F and the mass flow rate $\dot{m}$, we can determine the average mass flow velocity:

$$V_F = \frac{F}{\dot{m}} = \theta\sqrt{2e(U - \Delta U)/M}. \qquad (5)$$

The values of V_F for Xe and Kr are compared in Fig. 3. The figure also shows the velocities of singly charged ions,

$$V_U = \sqrt{\frac{2eU}{M}}, \quad V_\Delta = \sqrt{2e(U - \Delta U)/M}, \qquad (6)$$

calculated from the total voltage applied between the anode and cathode of the thruster and from the potential difference between the ionization region and the cathode. It is seen from the figure that the difference between V_F and V_Δ for Kr is larger than for Xe. This indicates that the fraction of doubly ionized ions for Xe is greater than for Kr.

4. LOCAL PLASMA PARAMETERS IN THE CHANNEL AND JET OF THE ACCELERATOR

The local plasma parameters in the channel and the jet of the accelerator were measured with a plane face probe. The probe size was chosen such that the probe only slightly perturbed the plasma. For this reason, the measurements in the channel were performed with a face probe with a working surface area of $S = 0.2$ mm^2.

The local plasma parameters in the accelerator channel were measured with the help of five wall probes located at distances of 5, 15, 20, and 25 mm from the anode. In the plasma jet, the measurements were performed with a similar probe that could be displaced in the longitudinal and radial directions ($0 \leq z \leq 30$ cm, $0 \leq r \leq 20$ cm).

Figure 4(I) shows the axial profiles of the plasma potential, electron temperature, and electron density in the channels of accelerators operating with Xe and Kr at $\dot{m} = 2$ mg/s and $U_d = 300$ V. It is seen that, for Kr, the electron temperature in the ionization region is lower and the electron density n_e is higher than for Xe. The latter may be explained by the fact that, at the same mass flow rates, the number of Kr atoms entering the accelerator channel is greater than that of Xe atoms by
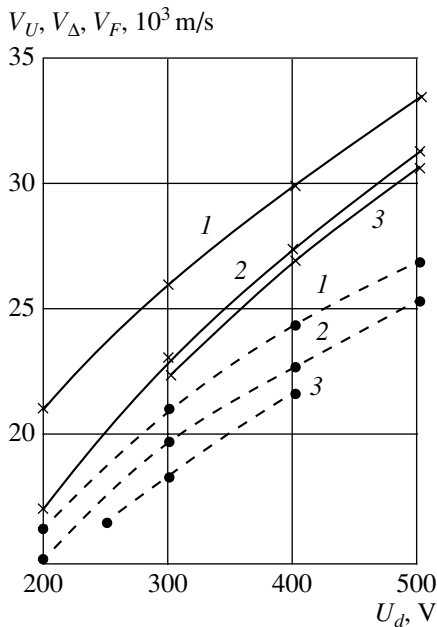
$V_U, V_\Delta, V_F, 10^3$ m/s

Fig. 3. Dependences of (*1*) V_U, (*2*) V_Δ, and (*3*) V_F on the discharge voltage at $\dot{m} = 2.3$ mg/s for Kr (crosses) and Xe (circles).
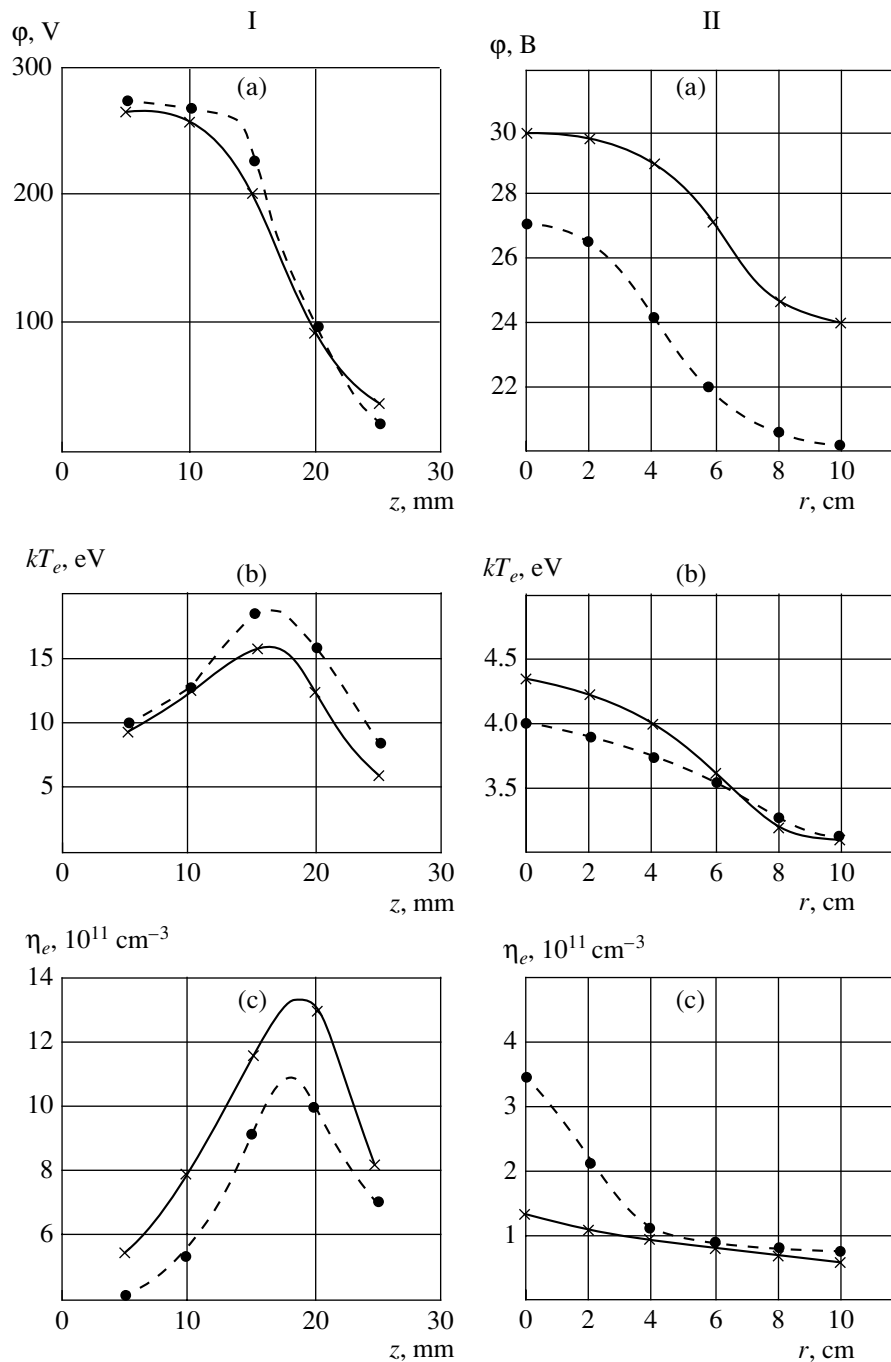
Fig. 4. Distributions of the (a) plasma potential, (b) electron temperature, and (c) electron density (I) in the channel and (II) in the jet behind the outlet of the accelerator at $\dot{m} = 2$ mg/s and $U_d = 300$ V for Kr (crosses) and Xe (circles); the anode and the accelerator outlet are located at $z = 0$ and 25 mm, respectively.

a factor of nearly 1.6, whereas the cross section for electron-impact ionization for Xe in the given electron energy range is greater than that for Kr by a factor of 1.5.

It can also be seen that, for Kr, the accelerating potential is somewhat lower than for Xe. In the case of Xe, the plasma potential remains constant at a distance of 12–13 mm from the anode and then drops. This

means that, in this case, the electric field occupies a region of length ~13 mm. For Kr, the potential is constant at a distance of 10–11 mm from the anode and then drops. In this case, the electric field occupies a region of length ~15 mm.

The electron temperature distribution in both cases is bell-shaped. The full width at half-maximum corre-
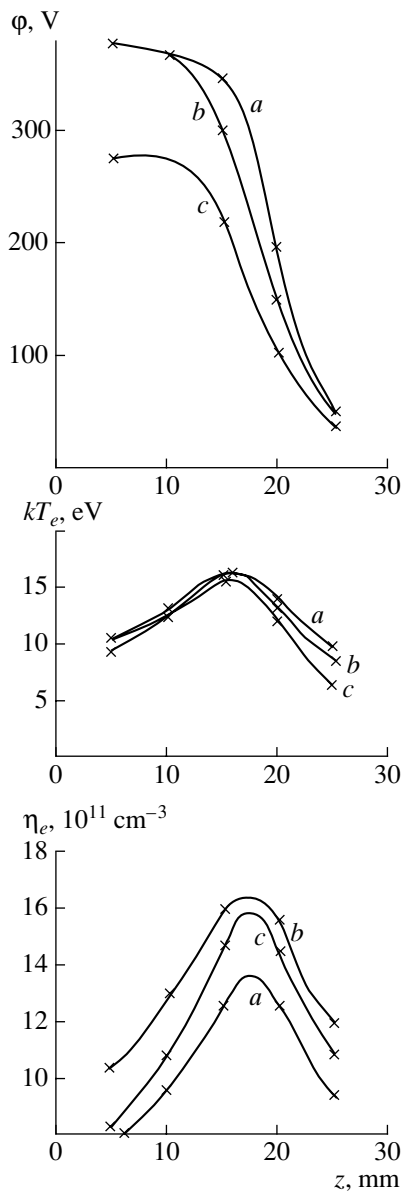
Fig. 5. Distributions of the potential, electron temperature, and electron density along the channel (the anode is located at $z = 0$) for Kr at (*a*) $\dot{m} = 2$ mg/s and $U_d = 400$ V, (*b*) $\dot{m} = 2.3$ mg/s and $U_d = 400$ V, and (*c*) $\dot{m} = 2.3$ mg/s and $U_d = 300$ V.

sponds to the size of the region occupied by the electric field.

Figure 4(II) shows the radial profiles of the plasma potential, electron temperature, and electron density in

Table 2

$\dot{m}_a$, mg/s	2	2	2.3	2.3
U_d, V	300	400	300	400
$\pm\alpha/2$	27°	25°	24°	22°

the accelerator jet at a distance of $z = 30$ cm from the outlet in accelerators operating with Xe and Kr at $\dot{m} = 2$ mg/s and $U_d = 300$ V. A comparison of the local parameters of accelerators operating with Kr and Xe shows that the electric potential and the electron temperature at the jet axis ($r = 0$) are higher for Kr. This means that, for Kr, these parameters decrease more slowly with distance from the outlet.

Figure 5 shows the axial profiles of the local plasma parameters in the channel of an accelerator operating with Kr in different regimes. It can be seen that, as the voltage is increased at a constant mass flow rate, the size of the anode region where the potential is constant does not change and only the electric field in the ionization region increases. As the mass flow rate is increased at a constant discharge voltage, the size of the anode region and the field strength in the ionization region remain unchanged, whereas the gradient of the potential decreases substantially near the anode region and the outlet. The variations in the mass flow rate and the discharge voltage do not affect (within the measurement error) the electron temperature in the ionization region. At the same time, the charged-particle density increases proportionally to the mass flow rate, the voltage being kept constant.

The divergence of the plasma jet was measured with a double electric probe [1]. The probe was located at a distance of $z = 20$ cm from the outlet of the accelerator and could be displaced in the radial direction. For every operating regime, we measured the profile of the ion current onto the probe. These curves were then used to calculate the half-angle of the jet divergence for Kr. The value of $\alpha/2$ was determined from the condition that 95% of the ion flow fell within the cone with the vertex angle α. The data on $\alpha/2$ are presented in Table 2.

It is seen from the table that the half-angle of the jet divergence varies from $\pm22°$ to $\pm27°$, depending on the operating conditions. This value is substantially greater than that for an accelerator operating with Xe, where the half-angle of the jet divergence is $\pm11°$.

5. CONCLUSIONS

The experiments have shown that, in accordance with the scaling law, a stable high-performance SPT operation can be achieved with Kr. In this case, the following effects have been observed:

(i) At the same (as for Xe) mass flow rate of the working gas, the specific impulse (thrust) is greater than with Xe.

(ii) The efficiency of a thruster operating with Kr is lower than that operating with Xe. This is explained by the higher ionization energy of Kr and, hence, the higher energy cost of an ion.

(iii) The jet divergence obtained with Kr is greater than that with Xe. However, this disadvantage appar-

ently stems from the nonoptimized operation of the output section of the source (the outlet–cathode region).

REFERENCES

1. A. I. Morozov, A. I. Bugrova, A. V. Desyatskov, *et al.*, Fiz. Plazmy **23**, 587 (1997) [Plasma Phys. Rep. **23**, 587 (1997)].
2. A. I. Morozov, V. M. Balebanov, A. I. Bugrova, *et al.*, Prikl. Fiz., No. 2, 106 (2000).
3. A. I. Bugrova, A. S. Lipatov, A. I. Morozov, and V. K. Kharchevnikov, Pis'ma Zh. Tekh. Fiz. **25** (11), 64 (1999) [Tech. Phys. Lett. **25**, 448 (1999)].
4. B. A. Arkhipov, A. S. Boder, R. Gnizdor, *et al.*, in *Proceedings of the International Electrical Propulsion Conference, Moscow, 1995*, paper 39.
5. A. I. Morozov and I. V. Mel'nikov, Zh. Tekh. Fiz. **44**, 544 (1974) [Sov. Phys. Tech. Phys. **19**, 340 (1974)].
6. A. I. Bugrova, N. A. Maslennikov, and A. I. Morozov, Zh. Tekh. Fiz. **61** (6), 45 (1991) [Sov. Phys. Tech. Phys. **36**, 612 (1991)].
7. A. I. Morozov, *Physical Concepts of Electrical-Propulsion Engines* (Atomizdat, Moscow, 1978).

Translated by N.F. Larionova

Charge and Energy Spectra of Fast Multicharged Ions in a Laser Plasma

M. R. Bedilov, I. Yu. Davletov, and Sh. D. Sultanov
Ulugbek National University of Uzbekistan, Tashkent, 700095 Uzbekistan
Received May 20, 2001; in final form, March 15, 2002

Abstract—In measuring the charge and energy spectra of the ions of a single-element laser plasma, in addition to thermal ions, fast multicharged ions are recorded that are accelerated by the electric field of laser radiation in the region of the critical plasma density. The charge and energy spectra of Co ions with the charge numbers $z = 1$–3 are measured at laser intensities of $q = 5 \times 10^{11}$–10^{12} W/cm^2. The energy spectra of these ions are broad and are located on the high-energy side ($z_{max} = 3$, $E > 5.0$ keV) with respect to the thermal ions ($z_{max} = 9$, $E < 4.0$ keV). The increase in q to 10^{14} W/cm^2 results in an increase in the charge number of both thermal and fast ions. © 2002 MAIK "Nauka/Interperiodica".

The studies of the distribution of the absorbed laser energy in a single-element plasma, as well as the charge and energy spectra of the accelerated (fast) ions, are important for the problem of laser plasma heating. The results of these studies are of interest for creating efficient multicharged ion sources, local element analyzers, nonlinear optical media, and plasma lasers. A large number of theoretical and experimental studies have been devoted to investigating the charge and energy characteristics of thermal ions in a single-element laser plasma [1–6]. As for fast ions, the integral (over charges and energies) characteristics of the jet expansion and the velocity distributions of the fast light CD_2, CH_2, and SiO_2 two-element plasma ions at $q = 5 \times 10^{13}$–10^{15} W/cm^2 were studied in [1, 7–12]. It was found that the proton (H^+) velocity (3×10^8–7×10^8 cm/s) is higher than the velocities of C^{6+}, C^{5+}, C^{4+}, and C^{3+} ions (10^8–3×10^8 cm/s), the velocity distributions of different carbon ions are similar to each other, and the distribution functions of carbon ions cut off abruptly near $v \approx 4 \times 10^8$ cm/s. Note that the generation of fast ions in a two-element laser plasma depends on the plasma element composition. Studying the mechanisms for the production of fast and thermal ions in a single-element plasma is important for understanding the features of the spectra of the fast ions. These data allow a deeper insight into the mechanisms for the interaction of laser radiation with a single-element plasma. However, the question of the charge and energy spectra of fast ions in a single-element laser plasma still remains open. Thus, in this study, in addition to the charge and energy spectra of thermal ions, the corresponding spectra of fast ions in a single-element laser plasma are studied at moderate intensities of laser radiation ($q = 10^8$–10^{14} W/cm^2).

The measurements were carried out with a laser mass-spectrometer [6] that consisted of a laser, an ion source chamber, a time-of-flight analyzer with an electrostatic mass-spectrometer, a vacuum chamber, and a recording system. In the experiments, we used a neodymium laser with a pulse energy of ~5 J and pulse duration of 50 ns, which enabled a laser intensity of $q_{max} = 10^{14}$ W/cm^2 on the target surface. After the amplifying stage, a polarization stack was placed; the degree of laser polarization behind the stack was no lower than 95%. A lens with a focal length of 9 cm focused the laser radiation into a spot ~10 μm in diameter. The angle of incidence of laser radiation with respect to the normal to the target surface could be varied in the range $\alpha = 18°$–$85°$. The scatter in the laser pulse energy was 10–15%. The residual vacuum in the system was ~10^{-6} torr. Cobalt plates that were previously employed in the studies of thermal ions were used as single-element targets. At some distance from the target, a system for analyzing the mass, charge, and energy spectra of multicharged laser-plasma ions was placed. The analyzing system consisted of a dynamic 150-cm-long time-of-flight analyzer and an electrostatic mass-spectrometer with a resolution of $\Delta m/m \sim 0.01$. In contrast to [13, 14], the system allowed the study of both thermal and fast ions in a wide energy range. The dynamic time-of-flight analyzer was used to separate ions with different velocities. During the plasma expansion into a vacuum, the plasma density decreased to a value of $<10^9$ cm^{-3}, at which plasma ions could be separated from electrons by the electric field of the analyzer; the current density in the analyzer decreased to a value of $<10^{-7}$ A/cm^2, at which the effect of the ion-beam space charge after plasma separation could be neglected. The laser-plasma ions were recorded in the direction along the target normal. Every reading was averaged over five laser pulses and was processed with a PC. Note that, in [13], a method was proposed for controlling the relation between the parameters of the initial (nonlaser) plasma

and the formed ion beam; the method was based on the separation of the ions and electrons in a rarefied plasma by applying an electric field of 70 kV/cm. Based on this method, in [14], an experimental facility was created that allowed a complex study of the laser-plasma parameters, including mass-spectrometer measurements of the ion component, as well as the measurements of the reflection coefficient and the spectra of soft X radiation. A technique used in the our study differs from that used in [13, 14] not only in the methods for the ion-beam formation, but also in the means for recording and investigating multicharged ions (here, we use a dynamic mass-spectrometer instead of a static Thomson mass-spectrometer used in [13]); all this can affect the experimental data on both the thermal and the fast multicharged laser-plasma ions.

Studies of the charge and energy spectra of Co ions in the laser-intensity range $q = 10^8$–10^{12} W/cm^2 show that the laser plasma contains thermal and fast multicharged ions that differ in energies and maximum charge numbers. Note that, at laser intensities of $q = 5 \times 10^{11}$ W/cm^2 and the angle of incidence $\alpha = 18°$, together with the thermal Co ions, fast Co ions were clearly observed in the charge and energy spectra. In addition to Co ions, all the mass spectra also showed single-charged C^+ and O^+ ions of impurities adsorbed on the target surface. It was shown experimentally that the fast-ion spectra depend on the polarization of laser radiation. Figure 1 presents typical energy spectra of the thermal and fast multicharged Co ions for $q = 10^{12}$ W/cm^2, $\alpha = 18°$, and p-polarized laser radiation. It can be seen from the figure that the ion energy spectrum can be conventionally divided in three ranges. In the first energy range ($0.05 < E < 4.0$ keV), there are thermal plasma ions with a maximum charge number of $z_{max} = 9$. For $q = 10^{12}$ W/cm^2 and s-polarization, the maximum charge number is $z_{max} = 7$. The lower the laser intensity, the lower the maximum charge number z_{max} of the thermal ions. At laser intensities as low as $q = 3 \times 10^{11}$ W/cm^2, the maximum charge number is $z_{max} = 5$ independently of laser polarization. In the second energy range ($4.0 < E < 5.0$ keV), regardless of laser polarization, no Co ions were recorded. Moreover, no Co ions were recorded in the entire ion mass spectrum when the laser intensity was decreased to $q = 10^8$ W/cm^2. Finally, in the third energy range ($E \geq 5.0$ keV), starting from $q = 5 \times 10^{11}$ W/cm^2, fast ions were recorded whose charge numbers depended on laser polarization (recall that no fast ions were recorded in the energy range $4.0 < E < 5.0$ keV at the same laser intensity, although in the first energy range, thermal ions with the maximum charge number $z_{max} = 5$ were observed at such q values). The increase in the laser intensity to $q = 10^{12}$ W/cm^2 not only increases the maximum charge number of the fast ions to $z_{max} = 3$, but also spreads out their energy spectrum to $E = 14$ keV (recall that at $q = 10^{12}$ W/cm^2, the maximum charge number of
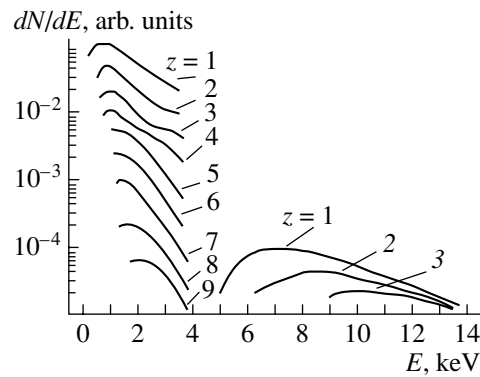

Fig. 1. Energy spectra of the thermal ($z = 1$–9, $E < 4.0$ keV) and fast ($z = 1$–3, $E > 5.0$ keV) multicharged Co ions for p-polarized laser radiation at $q = 10^{12}$ W/cm^2 and $\alpha = 18°$.

the thermal ions is $z_{max} = 9$). Note that the energy spectra of both the fast and the thermal ions are wide and single-peaked; the higher the charge number, the higher the energy corresponding to the spectral maximum. We also note that, for $q = 5 \times 10^{11}$ W/cm^2 and s-polarized laser radiation, no fast ions were observed in the ion mass spectra. The increase in q by two orders of magnitude (to $q = 10^{14}$ W/cm^2) led to an increase in the charge numbers of both the thermal ($z_{max} = 16$) and fast ($z_{max} = 9$) ions. Therefore, the experimental data on the thermal and fast ions in the laser intensity range $q = 10^{12}$–10^{14} W/cm^2 can be summarized as follows:

(i) No new features in the charge and energy distributions of the thermal ions have been found, except that the ion charge number increases with the laser intensity q and that, together with the thermal ions, fast ions are produced.

(ii) For both types of ions (thermal and fast), the changes in the energy distributions at different charge numbers (both for $z = 1$–3 at $q \leq 10^{12}$ W/cm^2 and for $z > 3$ at $q = 10^{12}$–10^{14} W/cm^2) are rather similar, although the mechanisms for producing these ions are different.

(iii) For both types of ions, the maximum charge number increases with q; however, the threshold q values are very different for different ion species (see Fig. 2). It can be seen that, for p-polarized laser radiation and $\alpha = 18°$, fast ions appear at $q \geq 5 \times 10^{11}$ W/cm^2.

A temporal analysis of the laser-plasma ions shows that there are two groups of ions that differ in the time of flight. Obviously, the shorter the time of flight of ions from the target to the detector, the higher their energy; hence, the ion group with the shorter time of flight corresponds to the fast (high-energy) ions. The above ion groups differ in both the duration of the ion-packet expansion and the maximum ion charge number z_{max}. The higher the charge number, the shorter the expansion time. Calculations show that, under the above experimental conditions, the velocity of the fast ions is $\geq 10^8$ cm/s. A temporal analysis of the laser-plasma ions
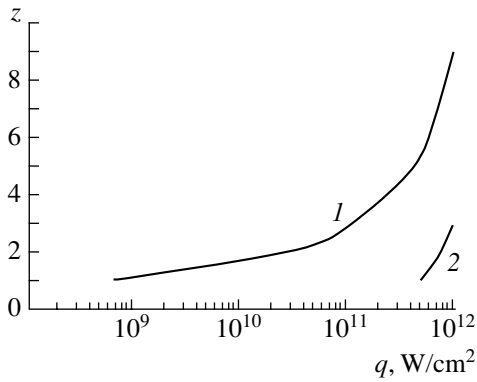
Fig. 2. Maximum charge numbers z of the (*1*) thermal and (*2*) fast multicharged Co ions vs. laser intensity q for *p*-polarized laser radiation and $\alpha = 18°$.

allows us to estimate the fractions of both the fast and the thermal ions. Under the given conditions, the calculated number of fast ions is 10^9 (about 10^{-6}% of the thermal ion number). An analysis of the results obtained shows that the yields of the thermal and fast multicharged ions, as well as their maximum charge numbers z_{max} and maximum energies E_{max}, depend on the processes of laser absorption, the ionization of the target atoms, and the recombination and acceleration of the plasma ions. The rates of these processes depend on both the laser parameters (laser intensity, laser wavelength, and polarization) [3, 4]; the density and element composition of the target; and, to some extent, the angle of incidence α of laser radiation onto the plasma [5]. Note that, for the normal incidence of laser radiation, the total reflection of laser radiation occurs near the critical point where the plasma permittivity ε is zero [15]. For the above parameters of laser radiation, the electric field in the vicinity of this point can be as high as ~10^9 V/cm [16]. For the normal incidence or sufficiently large α values, the above field singularity at the point $\varepsilon = 0$ disappears.

Under our experimental conditions, the incidence angle $\alpha = 18°$ is optimum for providing the maximum yield of the thermal and fast ions from the plasma. Seemingly, it is this α value that is optimum for the efficient conversion of the electromagnetic wave into a plasma wave. In the course of conversion, the plasma electrons acquire high energy and tend to escape from the plasma; however, the positive ion space charge prevents this escape. As a result, an electric double layer is formed, whose self-consistent electric field accelerates multicharged ions. Hence, the higher the number of the produced high-energy electrons, the higher the energy and number of the fast ions. The ion expansion velocity is the highest at $\alpha = 18°$; consequently, it is this α value at which the recombination loss of the multicharged ions is the lowest and the degree of quenching of the ionization states is maximum. The efficient conversion

of laser radiation into the particle energy leads to the formation of a plasma state with a higher degree of ionization. However, the recombination of both the thermal and fast ions decreases the degree of ionization and contributes to the energy spectrum of the ions with low charge numbers. We note that the maximum fast-ion energy $E \approx 14.5$ keV, measured with a mass-spectrometer, agrees with the results of [16], where the ion energy was measured by the collector method.

To conclude, the charge and energy spectra of thermal and fast multicharged ions in a single-element laser plasma have been studied as functions of the intensity, polarization, and incidence angle of laser radiation. For $q = 5 \times 10^{11}$ W/cm², $\alpha = 18°$, and *p*-polarized laser radiation, along with the thermal ions, fast multicharged Co ions have been recorded with energies and maximum charge number quite different from those of the thermal ions.

REFERENCES

1. N. G. Basov, Yu. A. Zakharenkov, A. A. Rupasov, *et al.*, *Diagnostics of Dense Plasmas* (Nauka, Moscow, 1989).

2. Yu. A. Bykovskiĭ and V. N. Nevolin, *Laser Mass Spectrometry* (Énergoatomisdat, Moscow, 1985).

3. M. R. Bedilov, Yu. A. Bykovskiĭ, and D. Kuramatov, Kvantovaya Élektron. (Moscow) **14**, 1675 (1987).

4. M. R. Bedilov, Yu. A. Bykovskiĭ, and D. Kuramatov, Kvantovaya Élektron. (Moscow) **18**, 79 (1991).

5. M. R. Bedilov and A. Kholbaev, Kvantovaya Élektron. (Moscow) **15**, 223 (1988).

6. M. R. Bedilov and K. Khaitboev, Prib. Tekh. Éksp., No. 6, 171 (1996).

7. H. Arechi and Y. Sakagani, Appl. Phys. Lett. **30**, 187 (1977).

8. G. N. McCall, F. Young, and A. W. Ehler, Phys. Rev. Lett. **30**, 1116 (1973).

9. P. M. Compbell, R. R. Johnson, and P. Hammerling, Phys. Rev. Lett. **39**, 274 (1977).

10. R. Decoste and B. N. Ripin, Appl. Phys. Lett. **31**, 68 (1977).

11. N. E. Andreev, Yu. A. Zakharenkov, N. N. Zorev, *et al.*, Zh. Éksp. Teor. Fiz. **76**, 978 (1979) [Sov. Phys. JETP **49**, 492 (1979)].

12. V. P. Silin, Zh. Éksp. Teor. Fiz. **76**, 976 (1979) [Sov. Phys. JETP **49**, 492 (1979)].

13. L. I. Krupnik, P. A. Demchenko, and N. G. Shulika, *Plasma Diagnostics* (Atomizdat, Moscow, 1973), p. 240.

14. N. B. Buyanov, V. A. Gribkov, N. V. Kalachev, *et al.*, Kratk. Soobshch. Fiz., No. 6, 7 (1983).

15. V. L. Ginzburg, *The Propagation of Electromagnetic Waves in Plasmas* (Nauka, Moscow, 1967; Pergamon, Oxford, 1970).

16. P. Wagli and T. P. Donaldson, Phys. Rev. Lett. **40**, 875 (1978).

Translated by N.N. Ustinovskiĭ

Possibility of Revealing the Role of Nonresonant Energy Exchange between Electrons and CO Molecules at High Vibrational Levels

I. V. Kochetov, A. K. Kurnosov, A. P. Napartovich, and S. L. Shnyrev

Troitsk Institute for Innovation and Fusion Research, State Scientific Center of the Russian Federation,
Troitsk, Moscow oblast, 142190 Russia

Received May 23, 2002

Abstract—An experimental method providing information about the interaction of electrons with excited CO molecules at high vibrational levels is proposed and justified theoretically. The suggested experimental scheme is based on the use of two successive discharge pulses under the conditions prevailing in an electroionization CO laser. The first pulse should ensure a sufficiently high energy input in order for a nonequilibrium vibrational distribution function to form. The second pulse serves to study the effect of the electric current on the vibrational distribution function of excited molecules at high vibrational levels. The theoretical analysis is based on the simultaneous solution of the Boltzmann equation for the electron energy distribution function and the vibrational kinetic equations realistically describing the multiquantum vibrational–vibrational exchange processes. The calculated results show that the sensitivity of the proposed measurement technique promises to be high. © 2002 MAIK "Nauka/Interperiodica".

1. INTRODUCTION

The problem of the interaction between electrons and excited carbon monoxide molecules at high vibrational levels in a low-temperature plasma has recently attracted increased interest in connection with the various manifestations of these processes in experiments. Thus, the investigations of the parameters of an electroionization CO laser based on transitions between high-lying levels of the first vibrational overtone [1] revealed the strong effect of a non-self-sustained discharge on the laser parameters. Specifically, the laser efficiency was found to increase rapidly after the discharge was switched off. Basov *et al.* [1] supposed that this phenomenon reflects the significant role of the superelastic collisions between electrons and vibrationally excited carbon monoxide molecules. At a qualitative level, the energy exchange between electrons and vibrationally excited molecules were discussed as far back as 1980 by Basov *et al.* [2], who pointed out that the "plateau" region in the distribution function can be dominated by superelastic collisions between electrons and CO molecules. In calculating the electron energy balance in a $CO : N_2 : He$ mixture, Islamov *et al.* [3] analytically specified the steady-state vibrational distribution function (VDF) with the fixed effective vibrational temperature of excited CO molecules at the first vibrational level and with the fixed translational temperature. They showed that, at high vibrational levels, the reverse energy flux from molecules to electrons can predominate over the direct flux. Further progress in theoretical investigations requires the simultaneous solution of the Boltzmann equation for the electron energy distribution function (EEDF) and the vibrational kinetic equations.

The role of the energy exchange between electrons and vibrationally excited molecules was also discussed in papers on the optical pumping of CO-containing mixtures by CO lasers [4–6]. Adamovich *et al.* [4] found experimental evidence for the effect of the electrons produced during the optical pumping of CO-containing mixtures by resonant radiation on the VDF. At the electron density $n_e \approx 10^{11}$ cm^{-3}, the switching-on of a constant external field whose strength is insufficient to maintain a self-sustained discharge leads to the withdrawal of electrons from the optical pumping region. As a result, the electron density decreases by approximately three orders of magnitude and the populations of the high vibrational levels of CO molecules increase appreciably. Adamovich and Rich [5] solved the kinetic equations for the populations of vibrational levels together with the Boltzmann equation for the EEDF. This approach enabled them to qualitatively explain the above experimental findings in terms of the effect of superelastic collisions between electrons and vibrationally excited molecules. However, they failed to reach a quantitative agreement with the experiment. One of the possible causes for this discrepancy between theory and experiment is the lack of reliable experimental data on the cross sections for the interactions between electrons and vibrationally excited molecules. Another possible cause is that the electron density n_e and the populations of the vibrational levels are determined with insufficient accuracy (see [6]). Note that Adamovich and Rich [5] used the single-quantum

vibrational–vibrational (VV) exchange approximation. However, in, e.g., [1], it was pointed out that this approximation leads to significant errors in calculating the populations of the vibrational levels above the twentieth level. Although there is a wealth of experimental information about the cross sections for electron interaction with unexcited molecules, the data on the corresponding cross sections for the interactions with vibrationally excited molecules are still lacking. In this context, it is worthwhile to look for the experimental conditions under which the reliable information on the processes in question can be extracted.

A direct approach to the experimental investigation of the mutual influence of electron kinetics and vibrational kinetics requires the simultaneous measurement of the EEDF and the population distribution of the vibrational levels. However, it is clear that such measurements are difficult to perform directly. By means of numerical models for calculating the EEDF and the dynamics of the VDF, it is possible to carry out numerical simulations of experiments; in this way, the required information can be derived from a comparison of the calculated results with the experimental data. However, it is not a trivial task to perform such experiments. The experimental data on the dynamic parameters are generally much more informative than the data on the steady-state parameters. Another important factor that governs the extent to which the mathematical processing of experimental data is adequate is the spatial uniformity of the plasma. The reason is that, in a nonuniform plasma, the particle balance is, in particular, affected by the transport processes, about which information is, as a rule, lacking.

In this paper, we theoretically justify a method that makes it possible to investigate the interaction between vibrationally excited molecules and electrons under the conditions prevailing in an electroionization CO laser. Under these conditions, it is comparatively easy to ensure the plasma homogeneity over the entire volume to be investigated and to employ laser methods for obtaining additional information about the dynamic parameters. The experimental scheme proposed here is based on the use of two successive discharge pulses. The first pulse should ensure a sufficiently high energy input in order for the nonequilibrium VDF to form. The second pulse serves to study the effect of the electric current on the VDF at high vibrational levels by measuring the dynamics of the populations of these levels or the parameters of the amplification and generation of a selective CO laser. An important point here is that, in order to provide the conditions under which the interaction between electrons and vibrationally excited molecules is most efficient, the time delay between the two pulses should be controlled so as to ensure the formation of the VDF at high vibrational levels. For the conditions investigated in [7], which reports the results of experimental and theoretical studies on the dynamics of the small-signal gain (SSG) for high transitions in the first vibrational overtone band of a CO molecule, the time delay should be about 100 μs.

2. THEORETICAL MODEL

The numerical model of the system consists of two coupled parts, one of which describes the vibrational kinetics and the other describes the electron kinetics. The simultaneous solution of the corresponding two sets of equations makes it possible to describe the dynamics of the energy exchange between electrons and molecular vibrations. The electrons interact with vibrationally excited molecules in very different ways, depending on the number v of the vibrational level. For $v \leq 9$, the electron scattering proceeds through a transient negative ion state, the resonant scattering cross section being large. Also, the electrons are subject to potential scattering, the cross section for which increases monotonically with the number of the level to about 10^{-16} cm^2 for $v \geq 30$. A plateau that appears in the VDF at a sufficiently high energy input is characterized by very high local vibrational temperatures. Under the conditions typical of an electroionization CO laser, these temperatures appreciably exceed the electron temperature. Consequently, in the electron–molecule energy exchange at the plateau in the VDF, the energy is transferred predominantly from molecules to electrons.

In our model, we use the theory of multiquantum VV exchange, which realistically describes the processes occurring at high vibrational levels [8]. The rate constants of the kinetic processes, including those of the processes of vibrational–translational (VT) relaxation and also the probabilities of spontaneous emission for transitions at the fundamental frequency and at the first and second vibrational overtones of a CO molecule, were taken from [7]. The set of kinetic equations describing the dynamics of the populations of individual vibrational levels can be represented in the following schematic form:

$$\frac{dn_v}{dt} = R_{e-V}^v + R_{VV}^v + R_{VT}^v + R_{SP}^v + R_{IND}^v, \quad (1)$$

where R_{e-V}^v, R_{VV}^v, R_{VT}^v, R_{SP}^v, and R_{IND}^v are the rates of the populating (depopulating) of the level v by electron impact and due to VV exchange, VT relaxation, and the spontaneous and induced emission, respectively. In the kinetic equations, the terms describing multiquantum VV exchange have the form

$$R_{VV}^v = \sum_{m \geq 1} (W_{v+m, v} n_{v+m} + W_{v-m, v} n_{v-m} \\ - (W_{v, v+m} + W_{v, v-m}) n_v. \quad (2)$$

Here, the frequency $W_{v+m, n}$ of transitions from the level $v + m$ to the level v in the VV exchange processes is

defined as $W_{v+m, n} = \sum_{i \geq m} Q_{i-m, i}^{v+m, v} n_i$, where $Q_{i-m, i}^{v+m, v}$ are the rate constants of the m-quantum exchange.

The equations of the first part of our model, namely, kinetic equations (1) for the populations of the vibrational levels of carbon monoxide molecules and the equations for the induced emission intensity [9], were solved together with the equation of the second part, namely, the Boltzmann equation for the EEDF in the two-term approximation.

In the Boltzmann equation, we took into account the electron energy loss in elastic collisions with atoms and molecules, the excitation of the rotational and vibrational levels of molecules, the excitation of the electronic levels of atoms and molecules, and their ionization. The cross sections for electron scattering by unexcited CO and He molecules were taken from [10, 11] and [12], respectively. The set of cross sections for He [12] consists of the transport cross section, two cross sections for the excitation of effective electronic levels, and the ionization cross section. The cross sections for the resonant vibrational excitation of a CO molecule from the ground state were taken from [11]; in accordance with the recommendations of [13, 14], we increased them by a factor of 1.3. The cross sections for superelastic collisions were determined using the principle of detailed balance. The cross sections for the resonant excitation of molecules at levels $v \neq 0$ and for the elastic scattering of electrons by them were calculated following [15]. We assumed that for transitions with $\Delta v = 1$ and 2, CO molecules at the vibrational levels $v = 9$ and higher are excited as a result of potential scattering and described this excitation in the Born approximation. It should be noted that the results obtained by calculating the cross section for the excitation of the first vibrational level of CO molecules near the excitation threshold in the Born approximation agree well with the measured data [13].

The Boltzmann equation was solved numerically by an integration–interpolation method, which was used to construct a three-point, conservative, first-order finite-difference scheme. The resulting set of equations was solved by the sweep method and then by iterating on the EEDF in the nonlinearity parameter until the convergence condition was satisfied for the given relative accuracy ε. The number of cells in the interval of integration over energy was 2000, and the relative accuracy was $\varepsilon = 10^{-5}$. In solving the Boltzmann equation for the EEDF numerically, the code controlled the total electron energy balance. In our computations, the total electron energy was conserved with an accuracy of no worse than 1%.

We simulated a CO : He = 1 : 4 mixture under conditions close to those in the experiments of [7]: the initial gas temperature was $T_0 = 100$ K, the initial gas density was $N_0 = 0.12$–0.18 amagat, and the specific energy input in the first pulse was $Q_0 = 180$–300 J l^{-1} amagat^{-1} (1 amagat = 2.686754×10^{19} cm^{-3}, which corresponds to Loschmidt's number). The numerical results to be presented in the next section were obtained for a fixed energy input ($Q_0 = 200$ J l^{-1} amagat^{-1}) and a fixed gas density ($N_0 = 0.18$ amagat) and, thus, are representative for the above parameter ranges. The following three parameters were also fixed: the electric field strength E_0 in the first pulse was $E_0 = 290$ V/cm, the parameter E/N was 0.6×10^{-16} V cm^2, and the durations of the first and second pulses were taken to be the same (30 μs). In simulations, it was assumed that the second discharge pulse was switched on 150 μs after switching on the first pulse. The electric field in the second pulse was the same as or weaker than that in the first pulse. The current value of E/N was determined with allowance for the gas density dynamics. The gas density was assumed to change during the thermal gas expansion caused by direct heating and the heating related to vibrational relaxation. Estimates show that, under the conditions characteristic of the experiments performed in [1, 7], the gas density can be assumed to be constant ($N \approx$ const) for several tens of microseconds after the first pulse is switched on. In later stages, the heated active medium expands into a large buffer volume at a nearly constant pressure ($P \approx$ const); in this case, the change in the density of the active medium was approximately calculated by means of a homogeneous model. The time evolution $N(t)$ of the density of the active medium was calculated from the following functional dependence, which models the transition to isobaric expansion:

$$N(t) = N_0 \exp\left(-\frac{t}{\tau}\right) + N_0 \frac{T_0}{T}\left(1 - \exp\left(-\frac{t}{\tau}\right)\right).$$

Here, $\tau = \Delta r / v_S$, where Δr is the characteristic transverse dimension of the active medium, v_S is the speed of sound, and T is the gas temperature. An analogous approach was used earlier in [16]. The translational temperature of the active medium was calculated from the equation

$$\frac{dT}{dt} = \frac{W}{NC_V} + \frac{kT}{NC_V}\frac{dN}{dT},$$

where W is the heat release power density associated with direct heating and vibrational relaxation, N is the density of atoms and molecules in the active medium, and k is Boltzmann's constant. The dynamics of the density of the active medium was also taken into account in solving the kinetic equations for the populations of the vibrational levels.

3. RESULTS

After switching on a pump pulse under conditions typical of an electroionization CO laser, the energy is exchanged between electrons and molecules primarily due to the resonant excitation of CO molecules from the ground state. During resonant excitation, superelastic
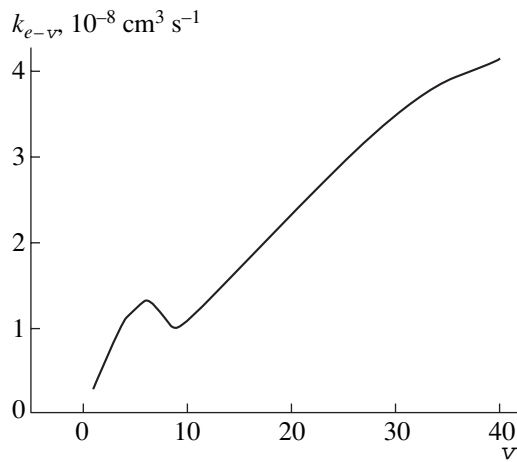
k_{e-v}, 10^{-8} cm^3 s^{-1}

Fig. 1. Rate constant of the process $CO(v) + e \longrightarrow CO(v+1) + e$ vs. number v of the vibrational level at the time at which the pump pulse terminates. The parameter E/N is 0.6×10^{-16} V cm^2 and the specific energy input is 200 J l^{-1} amagat^{-1}.
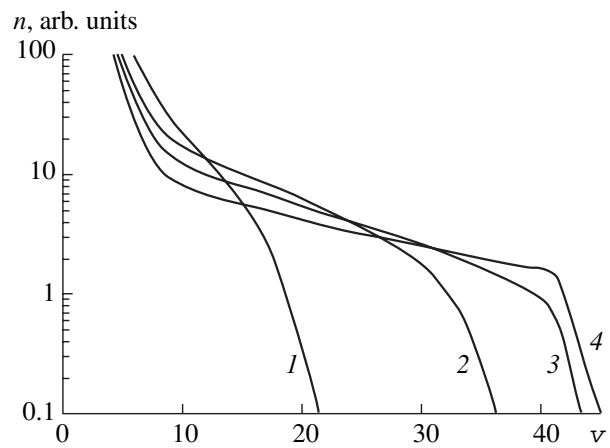
n, arb. units

Fig. 2. Time evolution of the VDF. Shown are the plots of the VDF at different instants: (*1*) 30 (the time at which the main discharge pulse is switched off), (*2*) 60, (*3*) 120, and (*4*) 150 μs. The current density is 4.1 A cm^{-2}, the parameter E/N is 0.6×10^{-16} V cm^2, and the specific energy input is 200 J l^{-1} amagat^{-1}.

collisions play an increasingly important role and, on the whole, lead to additional heating of the electrons. The distribution of the excited molecules over the vibrational levels during VV exchange is described by a nonequilibrium VDF [17] with a pronounced plateau, at which the effective vibrational temperature can be as high as several tens of thousands of degrees. The interaction of electrons with excited molecules at the vibrational levels $v > 9$ is dominated by potential scattering. The electron–molecule energy exchange is, as a rule, governed by the interaction of electrons with excited molecules at low vibrational levels, because the relative fraction of molecules in the plateau region is usually smaller than 1%.

The interaction of electrons with excited molecules at high vibrational levels is illustrated in Fig. 1, which shows the rate constants of the electron-initiated single-quantum transitions versus the number of the vibrational level. These rate constants were calculated by using the model of a self-consistent evolution of the EEDF and VDF for the time at which the first pump pulse terminates. It should be noted that the rate constants are insensitive to the degree of vibrational excitation because of the low threshold of the process under consideration. The plot in Fig. 1 makes it possible to estimate the conditions under which a direct interaction of electrons with CO molecules becomes important. Thus, our estimates show that, for the vibrational levels $v = 30$–35, the characteristic frequency of VV exchange just before the second pulse is switched on is about 0.5×10^6 s^{-1}. Accordingly, the competition between the direct interaction of electrons with excited molecules at these vibrational levels and the VV exchange processes should be the most pronounced when the frequency of the electron–molecule interac-

tion is equal to or higher than the VV exchange frequency. According to Fig. 1, this occurs in the electron density range $n_e \geq 1.5 \times 10^{13}$ cm^{-3}.

The evolution of the VDF after the pump pulse is switched off is displayed in Fig. 2. We can see that the time delay between the two pulses was chosen to be long enough for the nonequilibrium VDF to form. The evolution of the VDF after switching on the second discharge pulse with the same electric field as in the first pulse (the discharge current density being 4.1 A/cm^2) is shown in Fig. 3. At the beginning of the second pulse,
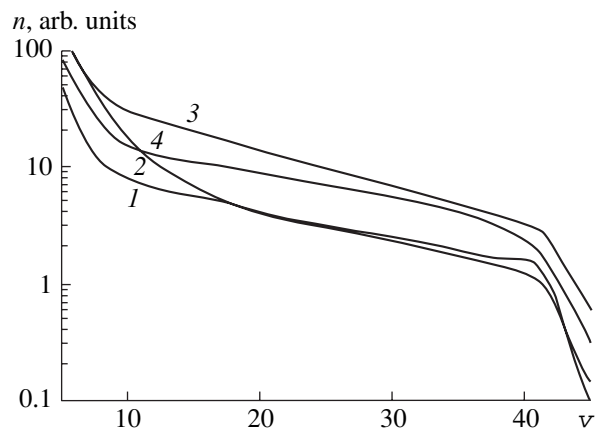
n, arb. units

Fig. 3. Time evolution of the VDF after switching on the second pulse. Shown are the plots of the VDF at different instants: (*1*) 150 (the time at which the second pulse is switched on), (*2*) 160, (*3*) 200, and (*4*) 250 μs. The specific energy input in the second pulse is 365 J l^{-1} amagat^{-1} and the current density is 4.1 A cm^{-2}.
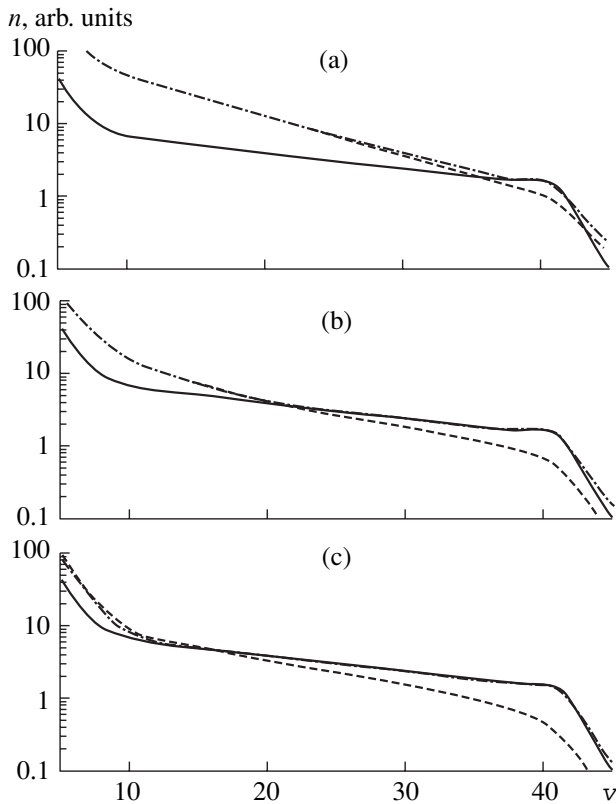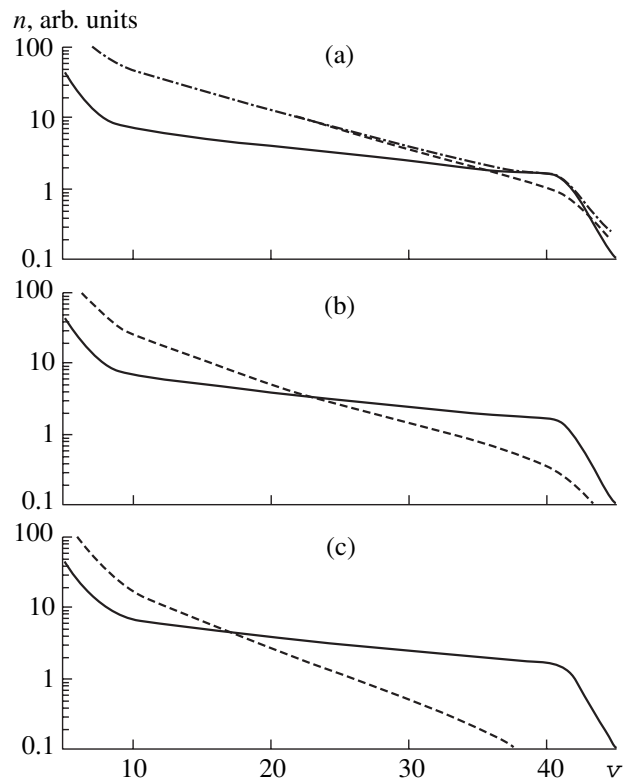
Fig. 4. Effect of the electric field strength E in the second discharge pulse on the VDF at the end of the second pulse ($t = 180$ μs). The calculations were carried out for $E =$ (a) 290, (b) 145, and (c) 96.7 V/cm. The solid and dashed curves were calculated with the second pulse being switched off and on, respectively, and the dashed-and-dotted curves were calculated without allowance for the interaction of electrons with excited CO molecules at the vibrational levels $v \geq 10$. The electron density in the second pulse is $n_e \approx 1.5 \times 10^{13}$ cm^{-3}, and the current density is proportional to E.

Fig. 5. Effect of the electric field strength E in the second discharge pulse on the VDF at the end of the second pulse ($t = 180$ μs). The calculations were carried out for $E =$ (a) 290, (b) 145, and (c) 96.7 V/cm. The solid and dashed curves were calculated with the second pulse being switched off and on, respectively, and the dashed-and-dotted curves were calculated without allowance for the interaction of electrons with excited CO molecules at the vibrational levels $v \geq 10$. The current density in the second pulse is fixed and equal to 4.1 A cm^{-2}.

the vibrational levels at the lower part of the plateau in the VDF (for $v < 10$) are rapidly populated; then, as a result of VV exchange, the higher vibrational levels also begin to be populated. In this case, about 100 μs after the second pulse is switched on, a VDF is established with a somewhat higher plateau than before the second pulse. Hence, the change in the populations of high vibrational levels after the second pulse is switched on is governed by the rapid VV exchange between the low and high vibrational levels, in which case a direct interaction of electrons with excited molecules at high vibrational levels plays a minor role. This conclusion is confirmed by Fig. 4a, which presents the results of simulations carried out under the assumption that the rate constants of the interaction between electrons and excited CO molecules at the vibrational levels $v \geq 10$ are zero.

The evolution of the VDF after switching on the second pulse with a weaker electric field ($E_0/2$ and $E_0/3$) than in the first pulse but at approximately the same

electron density ($n_e \approx 1.5 \times 10^{13}$ cm^{-3}) is illustrated in Figs. 4b and 4c. The effects that can be observed in these figures are governed mainly by the fact that the VDF at low vibrational levels is perturbed to a lesser extent because of a significantly lower pump power. A comparison between the curves calculated without and with allowance for potential scattering shows that the changes in the VDF at the vibrational levels $v = 30$–35 due to superelastic collisions amount to 25–50%. Figure 5 illustrates the time evolution of the VDF after the second discharge pulse is switched on. The computations were carried out for a fixed current density ($J = 4.1$ A cm^{-2}) and for three different electric field strengths (E_0, $E_0/2$, and $E_0/3$). Since, in a CO : He mixture, the electron drift velocity depends approximately linearly on E/N and since the current density is fixed, the electron densities n_e in Figs. 5b and 5c are higher than those in Figs. 4b and 4c by a factor of two and three, respectively. In Fig. 5, the values of the VDF at high vibrational levels are seen to be appreciably
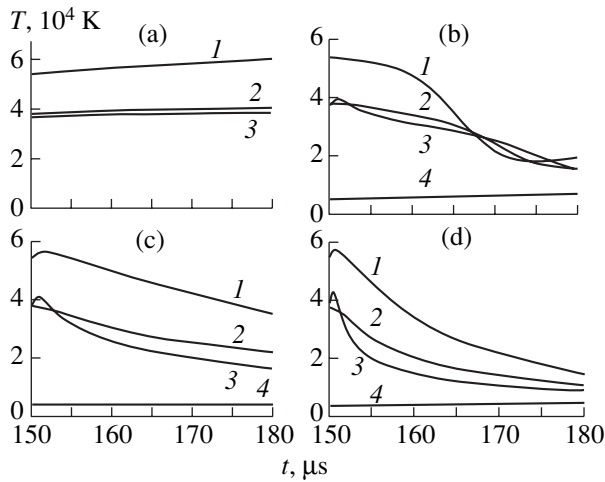
Fig. 6. Effect of the second discharge pulse on the time evolution of the effective vibrational temperatures at the vibrational levels $v = (1)$ 25, (2) 30, and (3) 35 and on the time evolution of the effective electron temperature (curves *4*). The calculations were carried out (a) without the second pulse and with the electric field strength E in the second pulse being equal to (b) 290, (c) 96.7, and (d) 96.7 V/cm. In plot (c), the current density in the second pulse is three times lower than that in plot (b). In plot (d), the current density in the second pulse is equal to 4.1 A cm^{-2}, which is the same current density as in plot (b).

Fig. 7. Effect of the second discharge pulse on the time evolution of the SSG at (a) transition 29–27 P(12) and (b) transition 35–33 P(12). The calculations were carried out (*1*) without second pulse and with the electric field strength E in the second pulse being equal to (2) 290, (3) 145, and (4) 96.7 V/cm. The current density in the second pulse is proportional to E, and the electron density is $n_e \approx 1.5 \times 10^{13}$ cm^{-3}.

smaller than those in Fig. 4; this effect is attributed to a direct energy exchange between electrons and molecules.

In order to illustrate the dynamics of the electron–molecule interaction at different electric field strengths and different electron densities, we present in Fig. 6 the time evolutions of the effective vibrational temperatures at high vibrational levels ($v = 25$, 30, and 35) and of the effective electron temperature. The calculations were carried out with the second pulse being switched on and off. The time evolutions in Fig. 6 show that, first, at the instant at which the second pulse is switched on, the effective vibrational temperatures are many times higher than the effective electron temperature, and, second, the rate at which these temperatures are equalized during the second pulse depends strongly on the electron density and is relatively insensitive to the electric field strength.

According to the results presented in Figs. 4–6, experimental measurements of the dynamics of the VDF at high vibrational levels in a discharge plasma with a sufficiently high electron density can provide the most detailed information about the kinetics of the interaction of electrons with highly excited CO molecules. The required conditions can readily be achieved through ionization by an electron beam. The traditional methods for measuring the VDF [4] are too complicated to yield its evolution. Laser diagnostic techniques may turn out to be more suitable for these purposes, because the amplification parameters should change
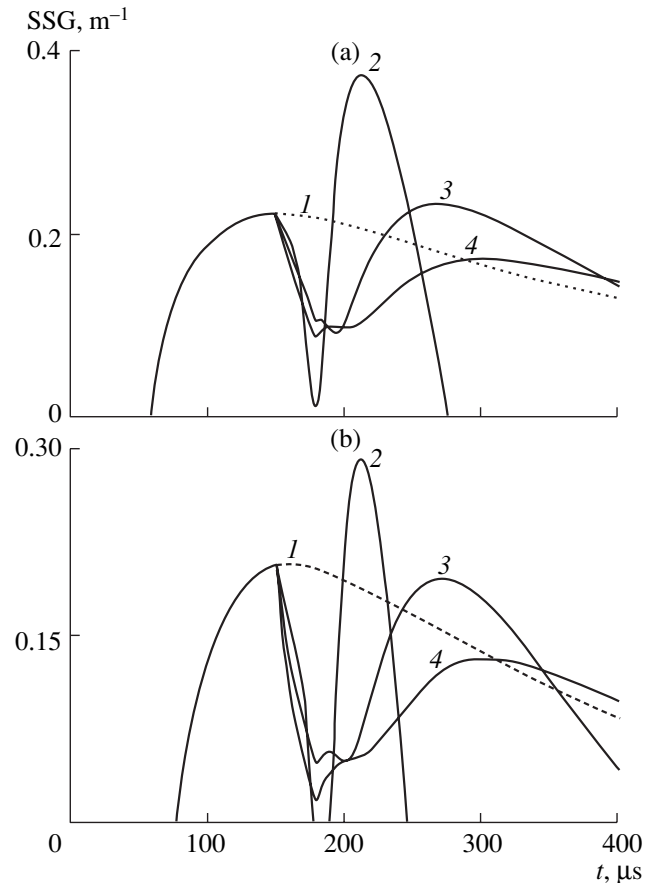
during the evolution of the VDF after the second discharge pulse is switched on [18]. In order to analyze this effect, we numerically investigated the sensitivity of the dynamics of the SSG of a CO laser at the overtone after the second pulse was switched on to the processes of energy exchange between electrons and molecules at high vibrational levels. The results of calculations of the SSG dynamics at the first-overtone transitions 29–27 P(12) and 35–33 P(12) after the second pulse is switched on are illustrated in Fig. 7. These vibrational–rotational transitions were chosen because the experimental data on the SSG dynamics at them are available [7]. The curves in Fig. 7 were computed for three different electric field strengths in the second pulse and for $n_e \approx$ const, in which case the current density is approximately proportional to the field strength. In Fig. 7, we also show the calculated time evolution of the SSG without the second pulse. The results illustrated in Fig. 7 provide clear evidence for the strong influence of the second current pulse on the SSG

dynamics. After switching on the second pulse that is identical to the first pulse (Fig. 7b, curve *2*), the signal is seen to be absorbed (rather than amplified) for a short time. This effect can be understood from Fig. 3, which demonstrates how progressively higher vibrational levels are excited. After the excitation wave approaches a given vibrational level, the gain intensifies to a larger extent than if there were no second pulse. As the electric field decreases (and, accordingly, the energy input decreases in proportion to the square of the field strength), the gain is suppressed predominantly by the direct interaction of electrons with excited molecules at high vibrational levels. In this interaction, the gain is weakened for a longer time but to a smaller extent. The second maximum in the SSG is attributed to the additional energy input to the low vibrational levels and has nearly the same height as the first maximum, which is associated only with the first pulse.

A clearer insight into the role of the direct interaction between electrons and excited molecules at high vibrational levels may be gained from a comparison between the gain dynamics in the case of two pulses and that in the case in which all of the processes under discussion are artificially "switched off." The results of this comparison are demonstrated in Figs. 8a–8c, which show time evolutions of the SSG at the transition 29–27 P(12). The difference between the curves calculated for $E = E_0/2$ and $E_0/3$ is seen to be the largest; the reason for this is that the weaker the field, the less important the effect of the energy input into the low vibrational levels. Figure 8d illustrates the influence of the energy exchange between electrons and excited CO molecules at high vibrational levels for $E = E_0/3$ and for the electron density higher than that in Figs. 8a–8c by a factor of approximately three, in which case the current density $J = 4.1$ A cm^{-2} in the second pulse coincides with that in the first pulse. One can see that the direct electron–molecule interaction at the plateau in the VDF is even more important.

Taking into account the fact that the laser intensity may be more sensitive to the interaction details in comparison with the gain, we also investigated the effect of the second pulse on the laser intensity dynamics at the same transitions 29–27 P(12) and 35–33 P(12) (Fig. 9). Note that, just after the second discharge pulse is switched on, the calculated laser intensity is seen to increase and then to decrease. The laser oscillation at the transition 35–33 P(12) is seen to terminate in the three cases with different electric field strengths. From a practical standpoint, the measurements of the dynamics of the radiation intensity after the second pulse is switched on can be beneficial for diagnosing the role of superelastic collisions only at a qualitative level, because quantitative measurements require that the reproducibility of the shape of the pulse of the emitted radiation be high and that there be no pulsations.
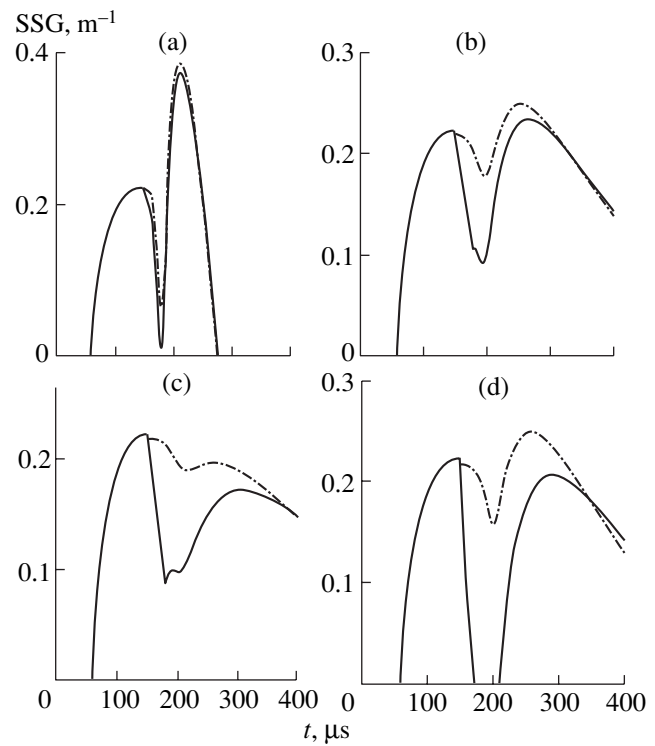
Fig. 8. Effect of the second discharge pulse on the time evolution of the SSG at the transition 29–27 P(12) for $E =$ (a) 290, (b) 145, (c) 96.7, and (d) 96.7 V/cm. In plots (a)–(c), the current density in the second pulse is proportional to E and the electron density is $n_e \approx 1.5 \times 10^{13}$ cm^{-3}. In plot (d), the current density in the second pulse is equal to 4.1 A cm^{-2}, which is the same current density as in plot (a). The solid and dashed-and-dotted curves were calculated with and without allowance for the interaction of electrons with excited CO molecules at the vibrational levels $v \geq 10$.
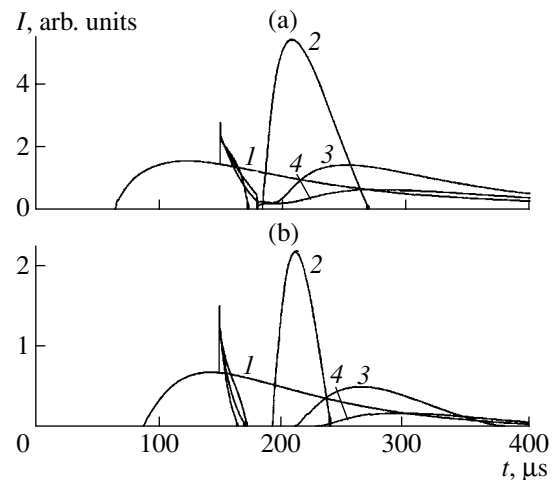

Fig. 9. Effect of the second discharge pulse on the time evolution of the laser intensity at (a) transition 29–27 P(12) and (b) transition 35–33 P(12). The calculations were carried out (*1*) without second pulse and with the electric field strength E in the second pulse being equal to (*2*) 290, (*3*) 145, and (*4*) 96.7 V/cm. The current density in the second pulse is proportional to E, and the electron density is $n_e \approx 1.5 \times 10^{13}$ cm^{-3}.

4. CONCLUSIONS

We have given a theoretical justification of the method that makes it possible to investigate the interaction of electrons with highly excited molecules by using two successive discharge pulses under the conditions prevailing in an electroionization CO laser. In comparison with the method that was proposed by Adamovich and Rich [5] and in which the nonequilibrium VDF is formed by means of CO laser radiation, the method proposed here has the following advantages: (i) the active medium is much more uniform in space than that in the case of optical pumping [19] (this circumstance greatly facilitates the processing of measured data), (ii) a non-self-sustained discharge provides the possibility of varying the electron density over a much wider range in comparison with the case of optical pumping [6] and also of varying the effective electron temperature by changing the reduced electric field, and (iii) the use of the active medium of an electroionization CO laser makes it possible to apply laser methods to diagnosing the VDF.

We have formulated the conditions under which the dynamics of the VDF at high vibrational levels is governed by the direct interaction of electrons with vibrationally excited molecules, thereby making the experimental measurements as informative as possible. We have shown that the second pulse can significantly deform the VDF at high vibrational levels, in which case the interaction mechanism and the magnitude of the effect depend strongly on the electron density and the energy input into the discharge. At a comparatively high energy input, the VDF is perturbed predominantly by the rapid VV exchange between the low and high vibrational levels. As the energy input in the second pulse decreases, superelastic collisions begin to play a dominant role in the evolution of the VDF at high vibrational levels; the amplitude of the observed variations increases sharply with n_e. Under these conditions, the experimental measurements of the dynamics of the VDF can provide the most detailed information about the processes of the interaction between electrons and excited CO molecules at high vibrational levels.

In view of the relative simplicity of laser methods for measuring the dynamics of the SSG and the laser efficiency in comparison with the methods for determining the dynamics of the VDF from the measured spectra, we have investigated the potentialities for using laser methods to derive quantitative information on the dynamics of the VDF. The results of our calculations show that the sensitivity of such laser measurement techniques promises to be high.

REFERENCES

1. N. G. Basov, A. A. Ionin, A. A. Kotkov, *et al.*, Kvantovaya Élektron. (Moscow) **30**, 771 (2000).

2. N. G. Basov, V. A. Danilychev, A. A. Ionin, and I. B. Kovsh, Tr. Fiz. Inst. Akad. Nauk SSSR **116**, 54 (1980).

3. R. Sh. Islamov, Yu. B. Konev, and B. A. Mirzakarimov, Preprint No. 3-333 (Inst. of High Temperatures, USSR Acad. Sci., Moscow, 1991).

4. I. V. Adamovich, S. Saupe, M. J. Grassi, *et al.*, Chem. Phys. **173**, 491 (1993).

5. I. V. Adamovich and J. W. Rich, J. Phys. D **30**, 1741 (1997).

6. E. Plonjes, P. Palm, I. V. Adamovich, and J. W. Rich, J. Phys. D **33**, 2049 (2000).

7. A. A. Ionin, Yu. M. Klimachev, A. A. Kotkov, *et al.*, in *Proceedings of the International Conference LASERS 2000, Albuquerque, NM, 2000* (STS, McLean, VA, 2001).

8. A. A. Ionin, Yu. M. Klimachev, Yu. B. Konev, *et al.*, Kvantovaya Élektron. (Moscow) **30**, 573 (2000).

9. A. A. Ionin, A. A. Kotkov, A. K. Kurnosov, *et al.*, Opt. Commun. **155**, 197 (1998).

10. J. E. Land, J. Appl. Phys. **49**, 5716 (1978).

11. H. Ehrhardt, L. Langhans, F. Linder, and H. S. Taylor, Phys. Rev. **173**, 222 (1968).

12. N. A. Dyatko, I. V. Kochetov, A. P. Napartovich, and M. D. Taran, Teplofiz. Vys. Temp. **22**, 1048 (1984).

13. G. N. Haddad and H. B. Milloy, Aust. J. Phys. **36**, 473 (1983).

14. N. L. Aleksandrov, I. V. Kochetov, and A. P. Napartovich, Khim. Vys. Energ. **20**, 291 (1986).

15. N. L. Aleksandrov, A. M. Konchakov, and E. E. Son, Zh. Tekh. Fiz. **49**, 1200 (1979) [Sov. Phys. Tech. Phys. **24**, 661 (1979)].

16. Yu. S. Akishev, A. V. Dem'yanov, I. V. Kochetov, *et al.*, Teplofiz. Vys. Temp. **20**, 818 (1982).

17. C. E. Treanor, J. W. Rich, and R. G. Rem, J. Chem. Phys. **48**, 1798 (1968).

18. N. G. Basov, A. A. Ionin, A. A. Kotkov, *et al.*, Kvantovaya Élektron. (Moscow) **30**, 859 (2000).

19. I. V. Kochetov, A. K. Kurnosov, J. P. Martin, and A. P. Napartovich, Kvantovaya Élektron. (Moscow) **25**, 315 (1995).

Translated by G.V. Shepekina

Numerical Simulations of Trichel Pulses in a Negative Corona in Air

Yu. S. Akishev, I. V. Kochetov, A. I. Loboĭko, and A. P. Napartovich

*Troitsk Institute for Innovation and Fusion Research, State Scientific Center of the Russian Federation,
Troitsk, Moscow oblast, 142190 Russia*

Received May 30, 2002

Abstract—Numerical simulations of a negative corona in air demonstrate that the experimentally observed regime of self-oscillations, known as Trichel pulses, is well described by a three-dimensional axisymmetric model that is based on the standard transport equations and in which only the ion-induced secondary electron emission at the cathode is taken into account. The quantitative difference between the measured and calculated values of the mean current and the pulse repetition rate most likely stems from the insufficiently large dimensions of the computation region and from the fact that the point shape adopted in simulations somewhat inexactly conforms to that used in experiments. It was found that the transverse discharge structure near the cathode radically changes during the pulse. Specifically, as the current grows, a cathode sheath forms at the discharge axis and expands over the cathode surface. When the current falls off, the cathode sheath is rapidly destroyed; as a result, the characteristic field structure is well defined only near the discharge axis and becomes virtually indistinguishable as the current decreases by an order of magnitude. © *2002 MAIK "Nauka/Interperiodica"*.

1. INTRODUCTION

As far back as 1938, Trichel [1] discovered regular pulsations of a current flowing in a negative corona discharge in air. The pulsations occurred in a certain voltage range, the pulse repetition rate depended on the experimental conditions, and the pulse duration was about a hundred nanoseconds. He attributed the pulsations to the screening of the electric field by a cloud of positive ions generated near the point during electron-impact ionization. By now, steady-state Trichel pulses in negative corona discharges in various gases have been investigated in a large number of experimental works (see, e.g., [2–4]). In particular, Loeb [2] asserted that Trichel pulses form only in discharges in electronegative gases. Zentner [3] measured the current rise time of a pulse and found that it can be as short as 1.3 ns. The establishment of Trichel pulses after a rapid switching-on of the high voltage was studied only in a few papers (see [5–7]). It was found that the first pulse differs appreciably in shape, amplitude, and duration from subsequent pulses. The time required for a regular (steady-state) sequence of pulses to be established is determined by the drift transit time of the negative ions from the cathode to the anode.

Among theoretical studies dealing with numerical simulations of the shape of the Trichel pulses, there are papers [8, 9], in which only the shape of the first Trichel pulse was computed under the assumption that the cross-sectional area of the current channel is constant, and paper [10], in which the steady-state sequence of Trichel pulses was simulated on the basis of a 1.5-dimensional model with a given shape of the current channel. The results of these simulations agree well with the experimental data on the current–voltage and frequency characteristics and also on the establishment dynamics of the pulses [7]. However, the equations of the 1.5-dimensional model were derived under the assumptions that cannot be justified without reference to a more precise model and, moreover, are *a priori* approximate. A strict approach requires the use of a three-dimensional numerical model that can formally be reduced to a two-dimensional axisymmetric model (the two variables being the radius and the distance along the discharge axis).

A further argument in favor of the advantages of using a three-dimensional model to calculate Trichel pulses comes from the visual observations of the luminosity of a negative corona near the point. In the regime of Trichel pulses, the luminous region is seen to be a wide cone (a wide "corona") with the vertex at the needle point [2]. When the mean current increases to about 130 μA, the pulsed regime terminates in a jumplike manner. Our observations showed that, after the termination, the luminous cone becomes far narrower. We attribute this effect to the fact that Trichel pulses are accompanied by pulsations of the current channel in the corona.

A distinctive feature of the corona is the existence of a region of highly nonuniform electric field before the breakdown. One of the electrodes is a needle or a thin wire. The electric field is very strong near this electrode and falls off abruptly with distance from it. Trichel pulses are generated due to a highly nonuniform electric field near the cathode. The characteristic dimen-
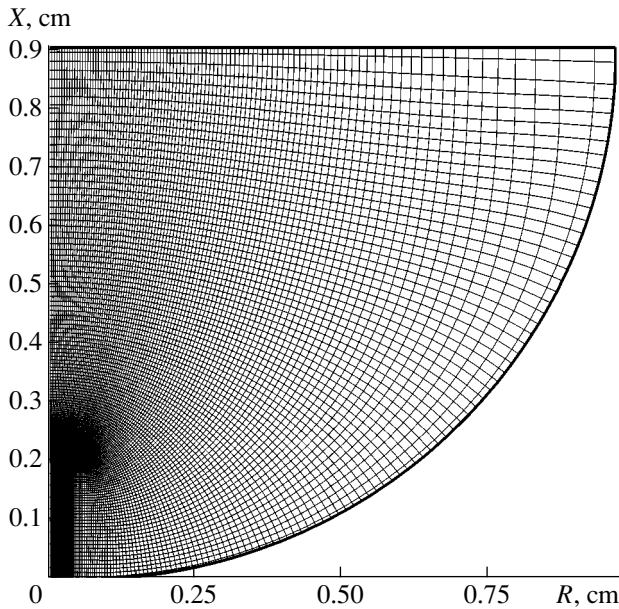
X, cm

Fig. 1. Spatial mesh; the cells are the smallest near the cathode, the minimum cell size being 6×10^{-5} cm.

sions of the region where the most important physical processes under consideration occur are smaller than the characteristic spatial scales of the problem (the interelectrode distance) by four orders of magnitude. This necessitates using nonuniform spatial computation meshes: the cells are small near the needle's point and increase in size when away from it. The approach based on such meshes is also exploited to model dielectrics barrier discharges [11]. In simulating microdischarges in a barrier discharge, it is sufficient to use a computation region with characteristic dimensions of about one millimeter, whereas the corona should be simulated on a computation region of at least one centimeter in size. However, the largest difference between the simulations of microdischarges and Trichel pulses is in the time scales of the important physical processes. The characteristic time scale of the microdischarge evolution and the streamer propagation is about several tens of nanoseconds, which is the characteristic time scale of an individual Trichel pulse. In order to understand the mechanism for the regular repetition of Trichel pulses, it is necessary to simulate at least several pulses until negative ions fill the entire interelectrode gap. For coronas in a short interelectrode gap, this occurs in about several tens of microseconds. All this necessitates the development of new algorithms for multidimensional simulations of Trichel pulses. Such an algorithm was developed in [12]. Preliminary results from simulations of the first two Trichel pulses were reported in [13]. In the present paper, we give a detailed description of the model of steady-state Trichel pulses in a negative corona in the atmospheric air between a

needle and a plane and present the relevant numerical results.

2. THEORETICAL MODEL AND NUMERICAL ALGORITHM

In order to describe the pulsed regime of a negative corona in a needle–plane electrode configuration, it is sufficient to solve the continuity equations for electrons and positive and negative ions and also Poisson's equation. The electron drift velocity can usually be determined from the solution to the Boltzmann equation for electrons; however, in our model, it is set to be proportional to the electric field strength. The ion drift velocities are determined from the known ion mobilities. The positive and negative ion components are each assumed to be dominated by one ion species. The above equations are supplemented with an equation for the electric circuit.

The spatial needle–plane electrode configuration is assumed to be axisymmetric. This indicates that the model equations can be solved in the variables X and R, where X is the distance from the cathode along the discharge axis and R is the radius. The boundary conditions for positive and negative ions are evident: their densities vanish at the anode and cathode surfaces, respectively. The electrons are assumed to be produced only through the ion-induced secondary emission at the cathode.

The cathode shape is different in different experiments. To be specific, we adopt a model cathode configuration that is often used in experiments: a cylinder with a rounded hemispherical cap of the same radius. The computation region is additionally bounded by a dielectric sphere, which is assumed to have an insignificant impact on the discharge dynamics.

As was mentioned in the Introduction, simulations of Trichel pulses require the development of new numerical algorithms. In order to satisfy the requirements of discrete approximations, the simulations were carried out on a nonuniform curvilinear mesh whose boundary was made consistent with the configurations of the electrodes. Since the cathode shape may be to a large extent arbitrary, the algorithm was devised with the use of a mesh generator that adjusted the mesh automatically to conform to the boundary conditions. The numerical scheme developed for simulations is conservative in the sense of conserving the total current for any curvilinear mesh. However, the smaller the deviation of the curvilinear mesh from being orthogonal, the better the convergence of the iteration scheme underlying the algorithm and, accordingly, the higher the computational speed. The numerical mesh on which the simulations were carried out is shown in Fig. 1.

The problem of controlling the computational accuracy is associated with the discretization method. Thus, certain conservation laws should be satisfied in both the discrete and continuous approximations. In this respect,

the approach based on the method of finite elements provides a simpler way to obtain conservative approximations than the approach based on a finite-difference method. That is why we used a finite-element method with the self-consistent approximation of the geometric quantities in curvilinear coordinates.

The discrete model equations were constructed from the integral forms of both the continuity equations for the particle densities and Poisson's equation. The resulting finite-difference equations were solved by successive iterations with the help of an explicit-implicit scheme. The complete computer algorithm involves the following steps:

(i) The source terms in the continuity equations for the charged particles and the particle densities are calculated in the mesh cells, while the particle drift fluxes are calculated at the cell boundaries.

(ii) At each iteration step, the "new" densities of the charged particles and the plasma conductivity are calculated by solving the continuity equations.

(iii) The new values of the electric potential in the cells and the electric field at the cell boundaries are determined by solving Poisson's equation.

(iv) The total current is calculated by integrating the total current density.

(v) The new value of the cathode voltage is calculated from the equation for the electric circuit.

(vi) The convergence condition for iterations is

$$\left| I^{s+1} - I^s \right| \le \varepsilon_1 I^s + \varepsilon_2,$$

where I^s is the total current at the sth iteration step, ε_1 is the relative error, and ε_2 is the absolute error. If this condition is not satisfied, then the iterative procedure is repeated starting with the first step.

3. RELAXATION PROCESS AND INTEGRAL CURRENT CHARACTERISTICS

The results that will be described in detail below were obtained in simulating a negative corona between a 0.06-mm-radius cylindrical cathode with a hemispherical cap of the same radius and a planar anode placed at a distance of 7 mm from the tip of the hemisphere. The length of the cylindrical part of the cathode is 2 mm. An additional insulating boundary of the computation region is assumed to be a sphere of radius 9.06 mm. The corona is coupled to the voltage source through a 100-kΩ ballast resistor. The plasma kinetic parameters are taken to correspond to air at room temperature and at a relative humidity of 65%. The main results to be presented were computed for a source voltage of 4.2 kV.

Numerical simulations show that the parameters of a sequence of pulses relax to steady-state values after about 25 pulses. As can be seen in Fig. 2, the current peaks do not differ in height after the fourth pulse, the minimum current value decreases monotonically from
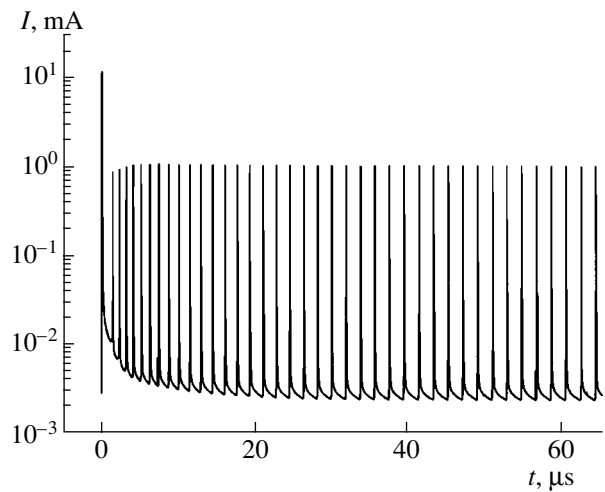
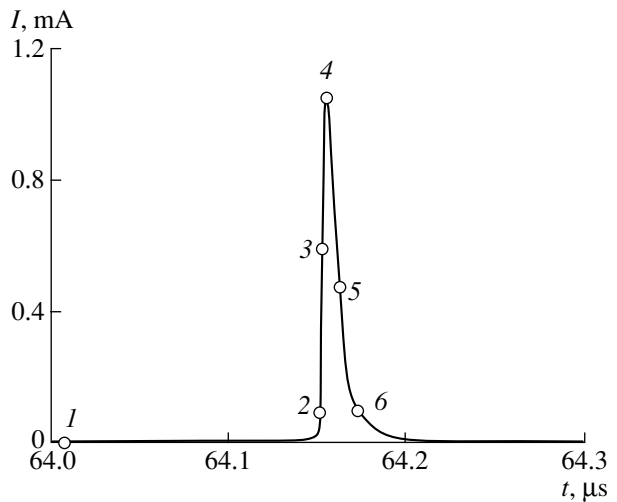**Fig. 2.** Establishment of the Trichel pulses.

Fig. 3. A detailed shape of a steady-state Trichel pulse. At point *1*, the current is minimum. Points *2* and *6* correspond to a level of 0.1 of the peak height, and points *3* and *5* correspond approximately to the half-height of the peak current. At point *4*, the current is maximum.

pulse to pulse and ceases to change after about twelfth pulse, and the pulse repetition rate relaxes in the longest time and becomes constant only after 25th pulse. In the steady state, the ratio of the peak current to the minimum current is equal to 442.

It is convenient to represent the dependence of the mean current I on the source voltage U_0 (it is this dependence that is usually measured in experiments) as a so-called reduced current–voltage (*I–V*) characteristic, which is the dependence of the ratio I/U_0 on U_0. As a rule, the reduced *I–V* characteristic has the form of a straight line. Because of the large number of input parameters (including the cathode shape), we failed to find the experimental data that conform exactly to the
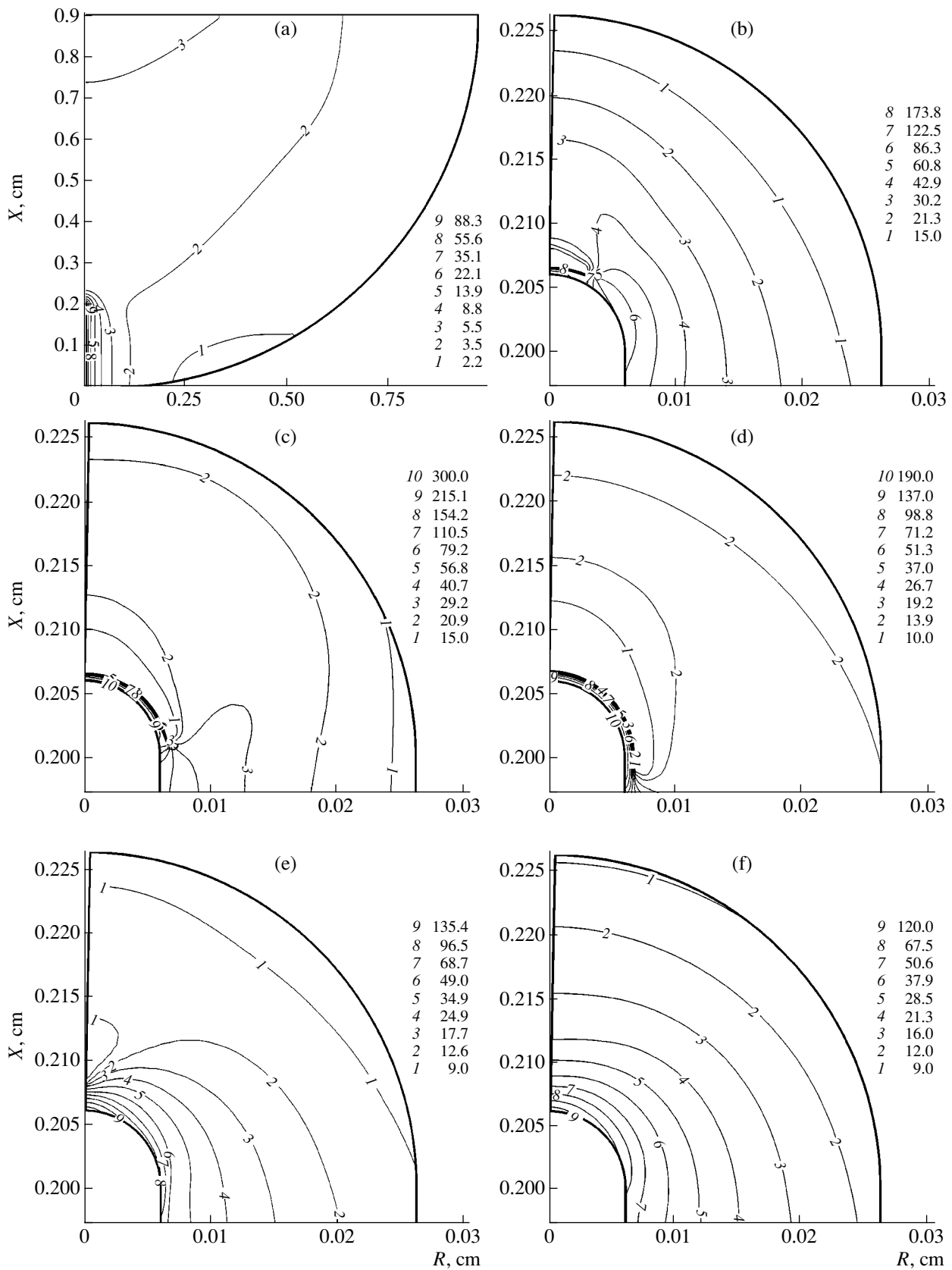
Fig. 4. Distributions of the electric field strength at times (a) *1*, (b) *2*, (c) *3*, (d) *4*, (e) *5*, and (f) *6*. The contours are marked by successive numbers with the corresponding electric field strengths (in kV/cm).
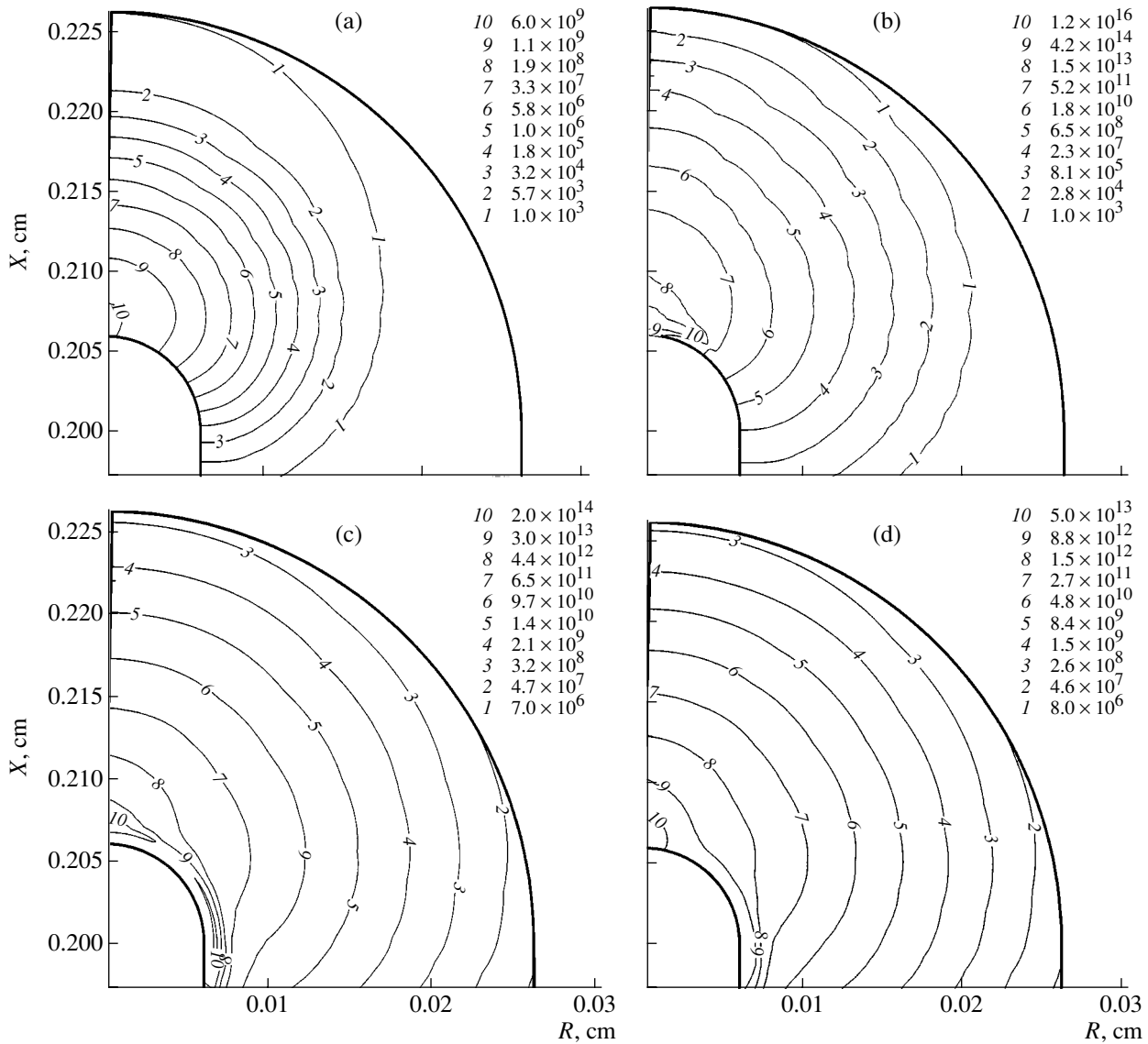
Fig. 5. Distributions of the density of positive ions in a small region near the cathode at times (a) *1*, (b) *2*, (c) *4*, and (d) *5*. The contours are marked by successive numbers with the corresponding density values (in cm⁻³).

conditions of our simulations. In addition, estimates show that the restriction on the anode size associated with a compromise between the accuracy of computations and the computational time can affect the mean current value and the pulse repetition rate. This is also confirmed by experiments carried out with finite-size anodes [14]. As a result, the theoretical and experimental reduced *I–V* characteristics are both straight lines; however, the slope of the theoretical characteristic and the voltage at which the current vanishes differ from those obtained experimentally. Specifically, the calculated voltage is equal to 0.8 kV, whereas the measured voltage is 2.4 kV. The slope of the calculated reduced *I–V* characteristic is smaller than the experimental one by a factor of 2.3. At a source voltage of 6 kV and higher, the calculated pulse repetition rate essentially

coincides with the rate measured under experimental conditions close to the conditions of our simulations. However, at a voltage of 4 kV, the calculated rate differs from the measured one by a factor of more than 2. It should be noted that, according to the experiments of [14], an additional boundary in the form of a cylindrical dielectric screen around the current channel leads to the same effects, namely, a decrease in the current and an increase in the pulse repetition rate.

4. STEADY-STATE REGIME

The shape of a steady-state current pulse is shown in Fig. 3. One can see that at the leading edge of the pulse there are no singularities, which contradicts the predictions of the 1.5-dimensional model [10]. The current
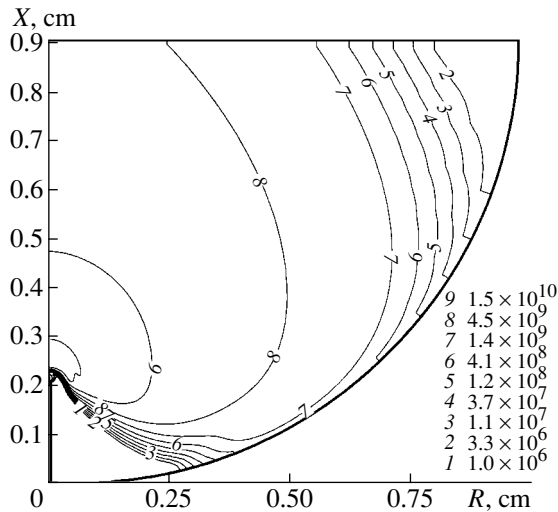
Fig. 6. Distribution of the density of negative ions over the entire computation region at time *1*, at which the current is minimum. The contours are marked by successive numbers with the corresponding density values (in cm^{-3}).

rise time is approximately equal to 100 ns. The full width at half-maximum of the pulse is about 12 ns. The trailing edge of the pulse is more gentle: the current decreases by one order of magnitude in about 20 ns. In order to thoroughly analyze the spatial dynamics of the plasma components, we chose the six points that are indicated in Fig. 3. At point *1*, the current is minimum ($I_{min} = 2.4$ μA), and it is maximum ($I_{max} = 1.06$ mA) at point *4*. Points *3* and *5* approximately correspond to the half-height of the current peak, and points *2* and *6* correspond to a level of 0.1 of the peak height.

5. DYNAMICS OF THE SPATIAL DISTRIBUTIONS OF THE PLASMA PARAMETERS

The general features of the dynamics of the distributions of the plasma components and the electric field can be understood from Fig. 4, which shows the contours of the electric field strength in the *R–X* (radius vs. distance along the discharge axis) plane. However, the evolution process under consideration is somewhat difficult to illustrate graphically because the structures in the discharge volume develop in a highly nonuniform manner: at short distances from the cathode (shorter than a millimeter), the charged particle densities and the electric field change by many orders of magnitude on nanosecond time scales. Consequently, the computed electric field distribution is viewable over the entire computation region only in simulations carried out for minimum corona currents, in which case the space charge distorts the field insignificantly (Fig. 4a).

The electric field distributions calculated for five subsequent times, *2–6*, are shown in Figs. 4b–4f, respectively. For illustrative purposes, these figures display the distributions only over a small part of the discharge volume near the cathode tip. As can be seen in Fig. 4b, the electric field is first redistributed near the discharge axis; at the cathode surface, it becomes three times stronger than that at time *1*. At two subsequent times, *3* and *4*, we distinctly see the formation of a sheath, which expands over the cathode surface until the current rises to its peak value (time *4*). It is worth noting that, at the peak current, the maximum field at the cathode surface is weaker than at the earlier times. After the current passes through its peak value, the cathode sheath is rapidly destroyed, so it is not seen in Figs. 4e and 4f. Looking carefully at Figs. 4b–4d, one can see that the region of the weaker electric field arises near the region of the stronger field at the cathode surface and expands together with the cathode sheath. The above characteristic features of the evolution of the electric field distribution near the cathode are obviously associated with an electron-impact avalanche ionization, followed by the screening of the electric field by the produced positive ions.

This character of the evolutionary process is confirmed by Fig. 5, which illustrates the distribution of the density of positive ions in a small region near the cathode. When the current is minimum (Fig. 5a), the ion density is low and varies rather smoothly in space. As the current increases (Figs. 5b, 5c), a region of high ion density arises near the axis and then expands over the cathode surface, in which case the ion density is the highest at a distance of about 10 μm from the cathode. According to Fig. 5d, the characteristic structure of the cathode sheath becomes indistinguishable at the half-height of the current peak.

In contrast to positive ions, negative ions gradually evolve over almost the entire discharge volume. The characteristic distribution of negative ions at the time at which the current is minimum is depicted in Fig. 6.

Like positive ions, electrons are concentrated near the cathode surface because, as they drift away from the cathode, they are rapidly attached to oxygen molecules. The evolution of the spatial electron distribution is illustrated in Fig. 7. Because of the high electron drift velocity in the electric field, the contours of the electron density are characteristically stretched out along the field. The divergence of the contours originating from a region near the tip of the needle (Figs. 7a, 7b, 7d) is explained by the fact that the ion density is elevated in this region (cf. Figs. 5a, 5b). Recall that, in the discharge volume, the electrons are produced only through the ion-induced secondary emission. At the peak current (Fig. 7c), the electron emission current is distributed uniformly over the part of the discharge region shown in Fig. 7. The rapid destruction of the cathode sheath gives rise to the characteristic pattern of the contours of the electron density diverging from the axial region (Fig. 7d).

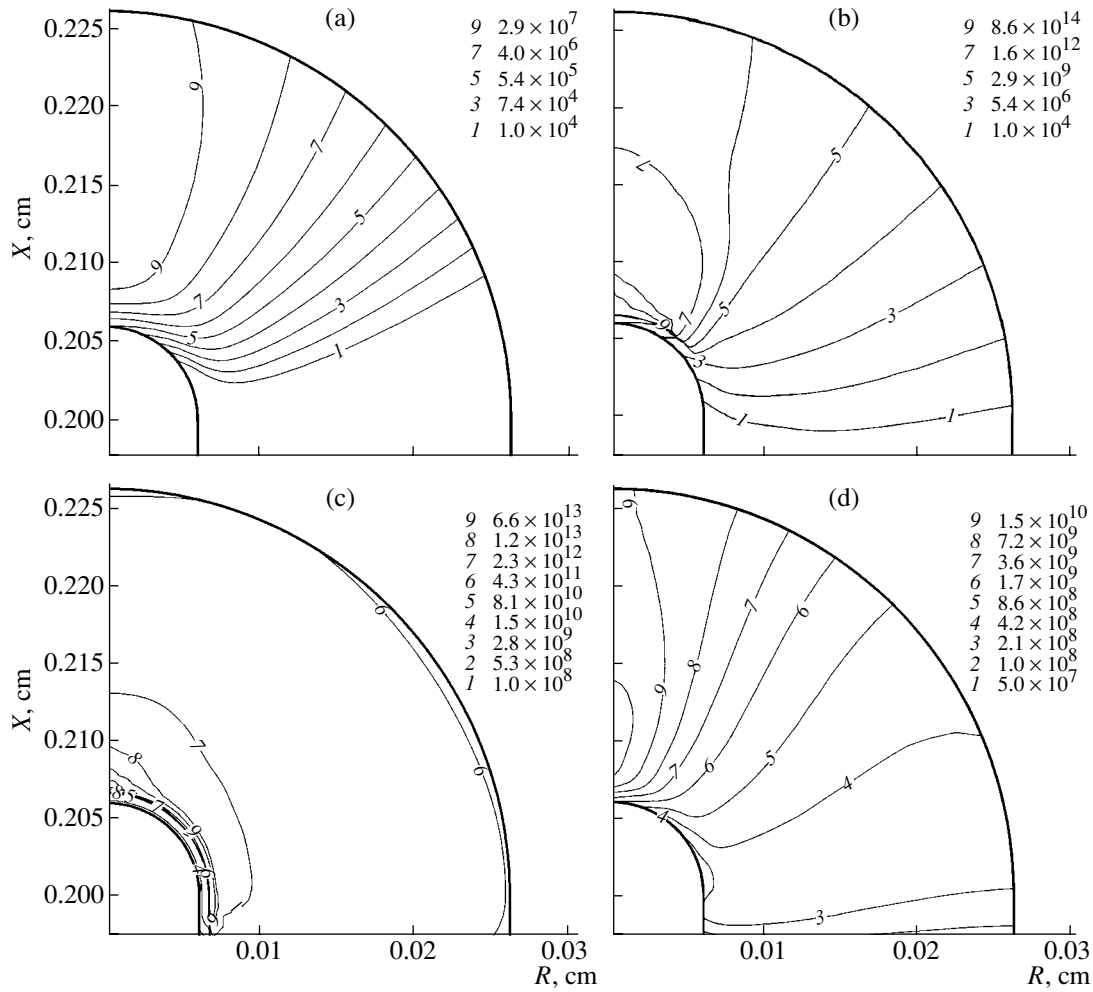A more detailed comparison between the spatial distributions of the physical quantities at different times is

Fig. 7. Electron density distributions in a small region near the cathode at times (a) *1*, (b) *2*, (c) *4*, and (d) *6*. The contours are marked by successive numbers with the corresponding density values (in cm^{-3}).

provided by Figs. 8–11, which show the profiles of the electric field and charged particle densities along the discharge axis. Figure 8 shows that, at the leading edge of the pulse, there remains a deep minimum (up to a level of about 400 V/cm) in the axial electric field profile at a distance of about 10 μm from the cathode. An increase in the electric field at distances farther from the cathode surface and the maximum that forms in the electric field profile and moves away from the cathode are attributed to the electron attachment and the production of slowly moving negative ions (see Figs. 9, 10). We note that, as the current begins to rise (Fig. 9, time *2*), the maximum electron density at the axis becomes higher than that at all subsequent times, in particular, at the peak current. Figure 11 shows the same effect for positive ions, whose maximum density is higher than 3×10^{15} cm^{-3}. The formation and destruction of the cathode sheath are clearly illustrated in Fig. 12, which presents the potential profile along the discharge axis. At a level of 0.1 of the peak current (time *2*), the potential drop across the sheath is maxi-
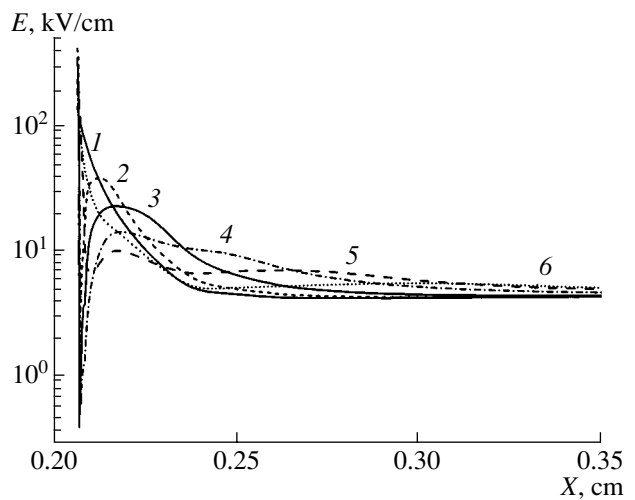
Fig. 8. Electric field profiles along the discharge axis. Different times are indicated by numerals in accordance with Fig. 3.
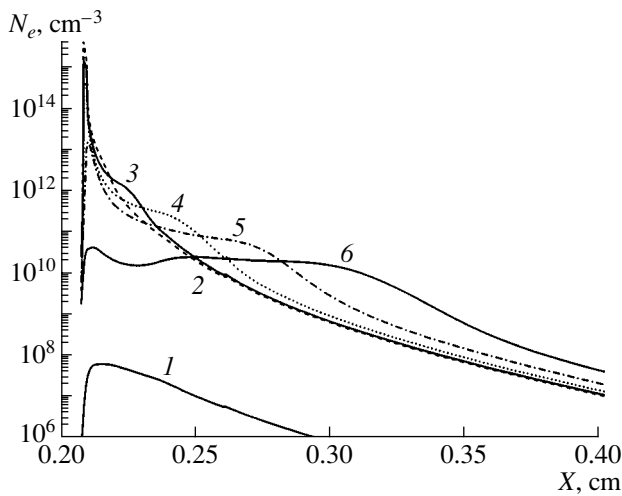
Fig. 9. Electron density profiles along the discharge axis. Different times are indicated by numerals in accordance with Fig. 3.
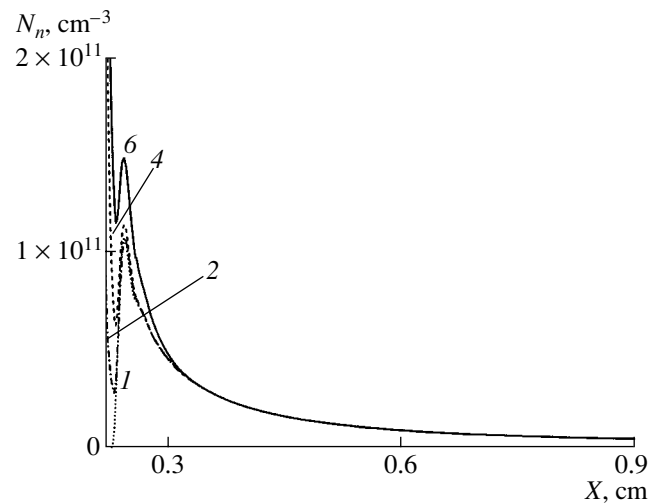

Fig. 10. Negative-ion density profiles along the discharge axis. Different times are indicated by numerals in accordance with Fig. 3.
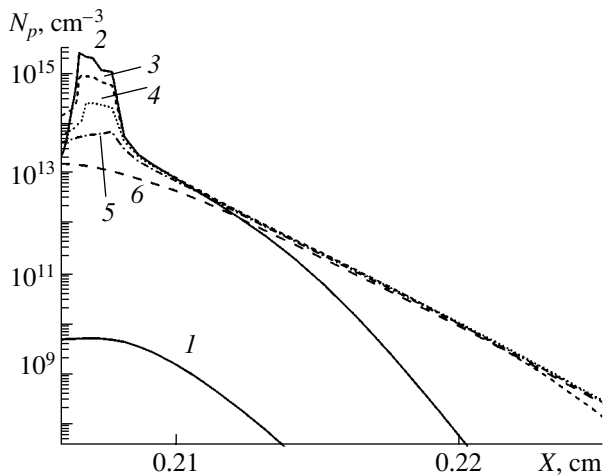

Fig. 11. Positive-ion density profiles along the discharge axis. Different times are indicated by numerals in accordance with Fig. 3.
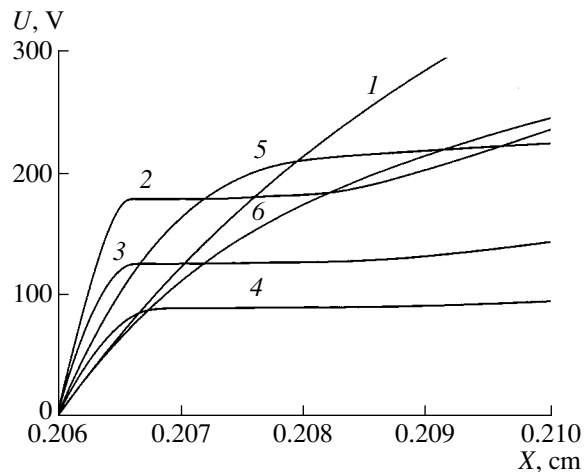

Fig. 12. Potential profiles along the discharge axis. Different times are indicated by numerals in accordance with Fig. 3.

mum and is approximately equal to 180 V. At the peak current, the potential drop is about 90 V. As the current falls off (time *5*), the electric field in the cathode sheath becomes stronger than that at the peak current, and the region of the stronger field becomes larger. In this case, the characteristic potential drop across the sheath is about 210 V.

6. DYNAMICS OF THE DISTRIBUTIONS OF THE PLASMA PARAMETERS OVER THE CATHODE SURFACE

The above-described dynamics of the spatial distributions of the discharge plasma parameters provides clear evidence for the substantial restructuring of the cathode sheath. This restructuring should manifest itself in the dynamics of the current density distribution over the cathode surface. Figure 13 illustrates how the distribution of the total current density over the cathode surface evolves in time. Since the actual current density varies by many orders of magnitude, Fig. 13 compares the profiles of the current density normalized to its values at the discharge axis at the different times for which the profiles were calculated. The vertical line is the coordinate at which the cylindrical cathode surface becomes a spherical surface. At time *2*, the total current density changes its sign four times, which is obviously
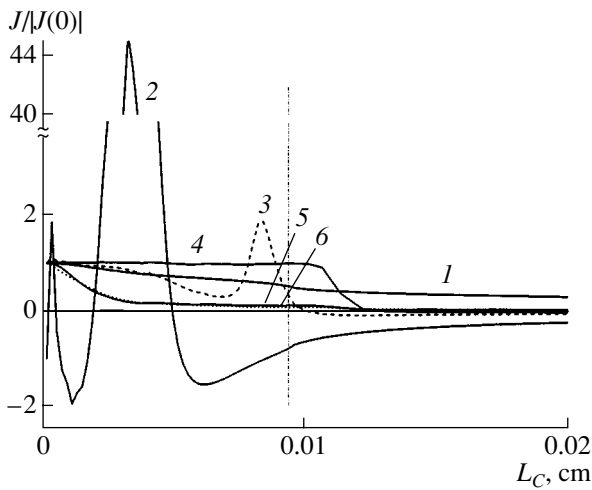
Fig. 13. Distributions over the cathode surface of the total current density normalized to its corresponding instantaneous value at the discharge axis. The abscissa is the coordinate L_C along the cathode surface. Different times are indicated by numerals in accordance with Fig. 3; nearly coincident curves 5 and 6 are shown by the solid and dotted lines, respectively.
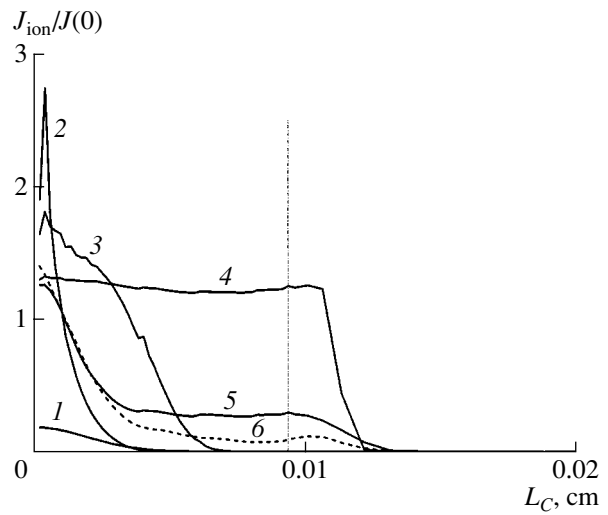

Fig. 14. Distribution over the cathode surface of the ion current density normalized to the corresponding instantaneous total current density at the discharge axis. Different times are indicated by numerals in accordance with Fig. 3.
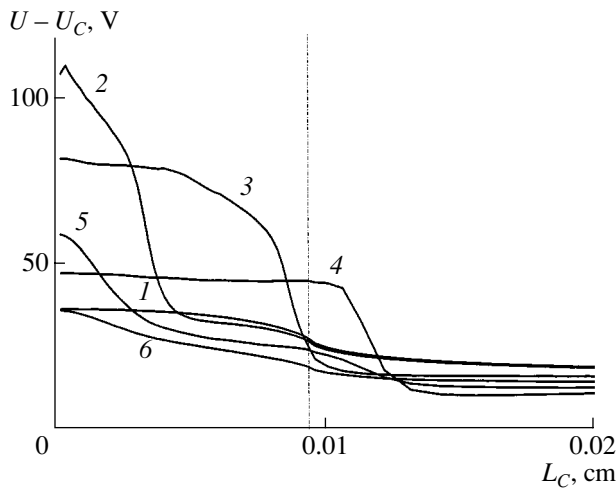

Fig. 15. Potential profiles along the mesh line at a distance of 3 μm from the cathode surface. Different times are indicated by numerals in accordance with Fig. 3.
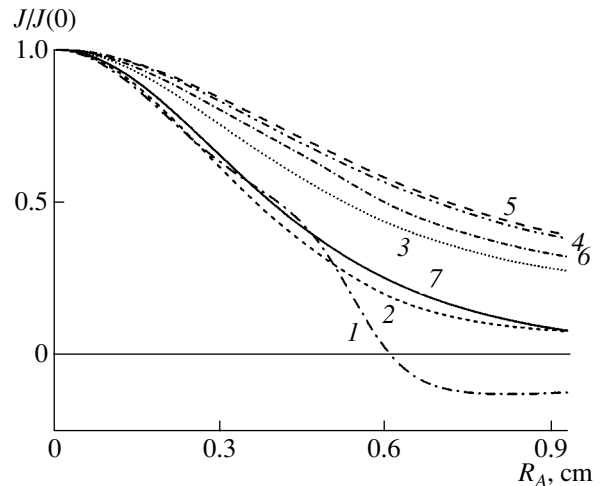

Fig. 16. Radial profiles of the normalized total current density at the anode surface. Different times are indicated by numerals in accordance with Fig. 3. The abscissa is the radial coordinate R_A at the anode surface. Curve 7 is the Warburg profile.

explained as being due to the displacement current variation produced by a change in the electric field at the cathode surface. In the axial region, the current density changes sharply, in which case the positive maximum current density at a distance of about 33 μm from the axis is higher than that at the axis by a factor of 44. The current density is negative everywhere, except in a 30-μm-wide ring region on the spherical surface and a narrow ring region near the axis; this indicates that the field in these regions decreases. Then, at time 3, the current density is seen to peak at an appreciably larger dis-

tance from the axis and to be lower in magnitude. Obviously, the position of the peak is determined by the boundary of the cathode sheath, which begins to form at the discharge axis and to expand over the cathode surface. At the peak current (time 4), the total current density is distributed uniformly and the flat part of the profile extends beyond the boundary between the cylinder and the hemisphere. As the pulse current falls off, the current density is redistributed in such a way that it concentrates near the discharge axis. The total current density at the cathode is the sum of the current density
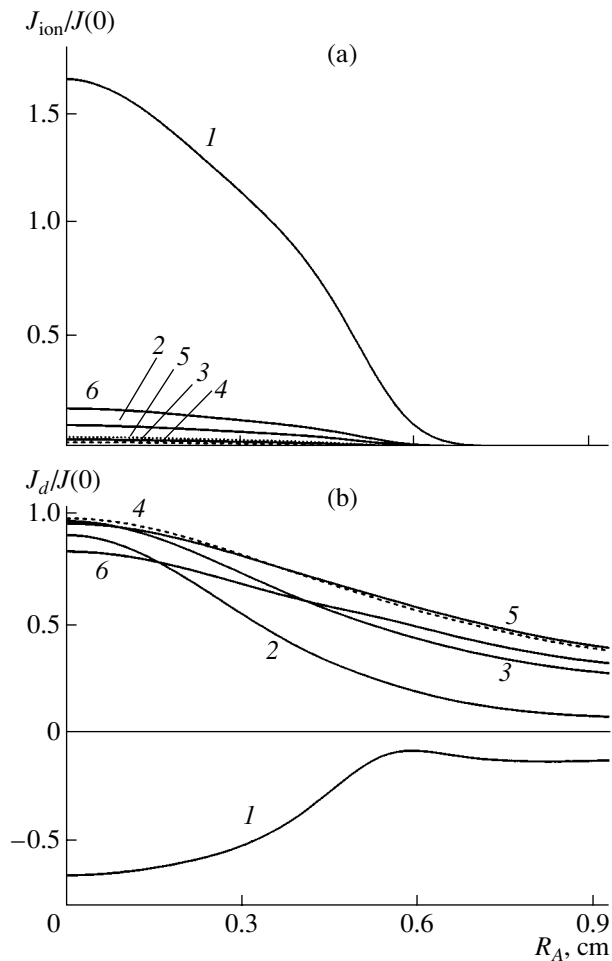
$J_{ion}/J(0)$

(a)

$J_d/J(0)$

(b)

R_A, cm

Fig. 17. Radial profiles of (a) the ion current density and (b) the displacement current density, both normalized to the total current density at the discharge axis. Different times are indicated by numerals in accordance with Fig. 3.

of positive ions and the displacement current density (the electron current amounts to 0.01 of the ion current). The dynamics of the ion current density normalized to the total current density at the discharge axis is illustrated in Fig. 14. A narrow peak near the axis at time *2* in Fig. 13 is attributed to the ion contribution to the total current density. Obviously, the peak near the boundary of the cathode sheath arises because the electric field in this region increases, thereby intensifying the ionization. This pattern of the discharge evolution is confirmed by Fig. 15, which shows how the potential varies along the line of the numerical mesh that is at a distance of 3 μm from the cathode surface. We see that, at the leading edge of the pulse, the region of the stronger electric field forms near the discharge axis; then, this region expands and the electric field in it decreases. As the current falls off, the region of the stronger field becomes progressively smaller; however, the electric field at different points decreases nonsimultaneously, remaining fairly strong near the discharge axis.

7. DYNAMICS OF THE DISTRIBUTIONS OF THE DISCHARGE PARAMETERS OVER THE ANODE SURFACE

It is expected that the complicated plasma dynamics near the cathode will affect the current dynamics at the anode surface, at which the total current density is a sum of the current density of negative ions and the displacement current density. Since the ratio of the areas of the regions over which the currents are collected by the anode and cathode is as large as about 335, the current density at the anode surface is much lower than that at the cathode surface. Figure 16 shows the distributions of the normalized total current density over the anode surface at the same times as in Fig. 3. During the pulse (curves *2–6*), the current flows through the entire accessible region of the anode surface. Interestingly, when the current is minimum, the total current density is negative at the anode periphery. This can be explained by comparing the distributions of the ion current density (Fig. 17a) and the displacement current density (Fig. 17b). In simulating Trichel pulses with the help of a 1.5-dimensional model [10], it was mentioned that, between the pulses, the potential drop across the drift region decreases, and that across the cathode region increases. For this reason, the displacement current is positive at the cathode surface (cf. Figs. 13, 14) and is negative at the anode surface. In this case, the ion current at the anode turns out to be localized in a smaller region (with a radius of about 7 mm, see Fig. 17a); as a result, the displacement current is dominant at the anode periphery.

In Fig. 16, we also show the well-known Warburg distribution, which describes the time-averaged current distribution over the anode surface. The way the data output was organized in the code did not enable us to directly calculate the mean current density at the anode surface. However, taking into account the fact that the displacement current does not contribute to the period-averaged total current, one can see that the radial profile of the ion current is essentially unchanged and, thus, it can be regarded as a mean current density profile. Comparing Fig. 16 with Fig. 17a, we can see that the calculated profile of the mean current density is markedly narrower than the Warburg profile. With allowance for the fact that, in accordance with the Warburg distribution, the current density at the boundaries of the computation region is nonzero, we can conclude that the size of this region at the anode surface was chosen to be too small; as a result, its boundaries affect the discharge parameters. The same conclusion has been drawn above when comparing the integral parameters of the corona discharge with the experimental data.

8. CONCLUSION

The results from the numerical simulations of a negative corona in air demonstrate that the experimentally observed regime of self-oscillations, known as Trichel

pulses, is well described by a three-dimensional axisymmetric model that is based on the standard transport equations and in which the electrons are assumed to be produced only through the ion-induced secondary emission at the cathode. The quantitative difference between the measured and calculated mean currents and pulse repetition rates most likely stems from the insufficiently large dimensions of the computation region. It is found that the transverse discharge structure near the cathode radically changes during the pulse. Specifically, as the pulse current grows, a cathode sheath forms at the discharge axis and expands over the cathode surface. At the trailing edge of the pulse, the cathode sheath is rapidly smeared out; as a result, the characteristic field structure is well defined only near the discharge axis and becomes virtually indistinguishable when the current decreases by an order of magnitude. The characteristic spatial scale on which the plasma parameters near a needle-shaped cathode of radius 60 μm change sharply is about several tens of microns. The characteristic potential drop across the cathode sheath is no higher than 200 eV, which is appreciably lower than the conventional cathode fall in a glow discharge. This result is not surprising, because the sheath exists for only about ten nanoseconds.

It is expedient to compare the above results with the results from the 1.5-dimensional simulations carried out in [10], in which the shape of the current channel was specified on the basis of general considerations and the channel parameters were adjusted so that the calculated results coincided with the experimental data. The resulting channel had a thin cylindrical part of radius 0.06 mm and length of 0.2 mm near the needle's point. It was assumed that the channel shape did not change with time. Our simulations, which were carried out without any reference to the adjustable parameters, show that the region of steep gradients near the needle is, in fact, far shorter (tens rather than hundreds of microns) and that the cross-sectional area of the current channel changes significantly with time. Nevertheless, our model and the model of [10] yield similar time evolutions of the integral parameters of the corona discharge. However, the evolutionary patterns differ in details: the 1.5-dimensional model [10] predicts that an ionization wave should form along the discharge axis and should give rise to an additional current peak at the leading edge of the pulse, whereas the model developed here predicts that a cathode sheath should form near the discharge axis and, then, should expand over the cathode surface (i.e., there is only the main current peak). Since our model was constructed without any arbitrary assumptions, it seems that the evolutionary pattern in

which the cathode sheath in the discharge expands over the cathode surface in a wavelike manner is more realistic. The nature of an additional low peak (or shoulder) recorded in the leading edge of the current pulse at reduced pressures requires further investigation. In particular, it is necessary to develop a more adequate model in order to check the Morrow hypothesis [8] about the role of photoionization.

ACKNOWLEDGMENTS

REFERENCES

1. G. W. Trichel, Phys. Rev. **54**, 1078 (1938).
2. L. Loeb, *Fundamental Processes of Electric Discharges in Gases* (Wiley, New York, 1939; Gostekhteorizdat, Moscow, 1950).
3. R. Zentner, Z. Angew. Phys. **29**, 294 (1970).
4. W. L. Lama and C. F. Gallo, J. Appl. Phys. **45**, 103 (1974).
5. J. A. Cross, R. Morrow, and G. N. Haddad, J. Phys. D **19**, 1007 (1986).
6. J. A. Scott and G. N. Haddad, J. Phys. D **19**, 1507 (1986).
7. Yu. S. Akishev, M. E. Grushin, I. V. Kochetov, *et al.*, Fiz. Plazmy **25**, 998 (1999) [Plasma Phys. Rep. **25**, 922 (1999)].
8. R. Morrow, Phys. Rev. A **32**, 1799 (1985).
9. M. Cern'ak, T. Hosokawa, and I. Odrobina, J. Phys. D **26**, 607 (1993).
10. A. P. Napartovich, Yu. S. Akishev, A. A. Deryugin, *et al.*, J. Phys. D **30**, 2726 (1997).
11. G. J. Pietsch, D. Braun, and V. I. Gibalov, in *Non-Thermal Plasma Techniques for Pollution Control,* Ed. by B. M. Penetrante and S. E. Schultheis (Springer-Verlag, Berlin, 1993), NATO ASI Ser., Part A, p. 273.
12. Yu. S. Akishev, M. E. Grushin, A. A. Deryugin, *et al.*, TRINITI Report by Contract with the ABB Firm, 1997.
13. Yu. S. Akishev, I. V. Kochetov, A. I. Loboiko, and A. P. Napartovich, in *Proceedings of the International Symposium on High Pressure, Low Temperature Plasma Chemistry (Hakone VI), Cork, 1998*, p. 308.
14. Yu. S. Akishev, A. A. Deryugin, I. V. Kochetov, *et al.*, in *Proceedings of the International Symposium on High Pressure, Low Temperature Plasma Chemistry (Hakone V), Milovy, 1996*, p. 122.

Translated by G.V. Shepekina

LOW-TEMPERATURE PLASMA

Low-Pressure Glow Discharge in a Xenon/Chlorine Mixture

A. K. Shuaibov, L. L. Shimon, I. V. Shevera, and A. I. Dashchenko

Uzhhorod National University, vul. Pidgirna 46, Uzhhorod, 88000 Ukraine
Received April 5, 2002; in final form, June 26, 2002

Abstract—The spatial, electrical, and optical characteristics of a transverse glow discharge and a volume discharge with a spherical anode and plane cathode in low-pressure Xe/Cl$_2$ mixtures are studied. It is shown that the transverse glow discharge in mixtures with a low chlorine content occupies most of the interelectrode gap and exists in the form of strata. As the total pressure ($P \geq 300$ Pa) and the partial chlorine pressure ($P(\mathrm{Cl}_2) \geq 80$ Pa) increase, a solitary plasma domain with a volume of 1–2 cm^3 forms in the discharge gap. It acts as a selective source of UV radiation in the XeCl(D–X) 236-nm, Cl$_2$(D'–A') 257-nm, and XeCl(B–X) 308-nm bands. In certain Xe/Cl$_2$ mixtures, plasma self-oscillations in the frequency range 1–100 kHz are observed. The current of a low-pressure volume discharge with a spherical anode and plane cathode and the emission from it have both a dc and an ac component. The pressure and composition of the working mixture, as well as the average current of the volume discharge are optimized to attain the maximum emission intensity of the XeCl(D, B–X) bands. Low-pressure volume discharges in xenon/chlorine mixtures can be used as active media in low-pressure large-aperture planar or cylindrical excimer–halogen lamps emitting modulated or repetitive pulsed UV radiation. © 2002 MAIK "Nauka/Interperiodica".

1. INTRODUCTION

Low-pressure volume discharges with a solid cathode and a perforated anode in Xe/Cl$_2$ and Xe/HCl mixtures were used to pump the active media of planar XeCl lamps [1]. In lamps with an interelectrode distance of 3 cm, there was no dielectric wall touching the plasma and the dc voltage at the lamp anode was no higher than 1 kV. The emission efficiency in the 4π solid angle was higher than 4%. Such low-pressure excimer sources are simpler in design than planar lamps with microwave pumping [2]. In these lamps, in contrast to lamps based on a longitudinal glow discharge [3–7], the diffusion of chlorine into the glass wall of the discharge tube is absent. Note that, under elevated tube temperatures, this diffusion can lead to a significant decrease in the gas-fill lifetime of the lamp and calls for the forced cooling of both the lamp electrodes and the discharge tube. In [1], the main attention was paid to studying the spatial and energy characteristics of the volume discharge, whereas the time behavior of the discharge parameters and plasma emission was not studied. In low-pressure plasmas of noble gas–oxygen mixtures, electron attachment, electron detachment, and the diffusion of negative ions play an important role. These processes lead to the stratification of a longitudinal glow discharge and the formation of a pinch consisting of an ion–ion plasma in the center of the discharge tube [8–10]. In the case of a low-pressure volume discharge in an electronegative working mixture, the distribution of the electric field along the discharge gap can be unstable; for this reason, the creation of planar excimer lamps is problematic.

In this paper, we present the results of the experimental studies of a transverse glow discharge and a volume discharge with a spherical anode and plane cathode in low-pressure xenon/chlorine mixtures. These pumping systems can be applied to develop low-pressure planar and cylindrical excimer lamps with a large output aperture.

2. EXPERIMENTAL SETUP

The experiments were carried out with a facility that was previously used to study dc excimer–halogen lamps [11, 12]. The spatial and current–voltage characteristics of the discharge; the plasma emission spectra in the spectral range 130–350 nm; the emission intensity in the excimer molecular bands; and the waveforms of the discharge voltage, current, and total emission were investigated.

The electrode system of a transverse glow discharge (TGD) or a spherical anode–plane cathode electrode system was placed in a 10-l buffer discharge chamber (Fig. 1). The chamber was hermetically connected via an LiF window to a vacuum monochromator with a spectral resolution of 0.7 nm. An FÉU-142 photomultiplier with an LiF window was used to monitor plasma emission. The vacuum monochromator and the photomultiplier were relatively calibrated in the spectral range 165–350 nm by using the molecular hydrogen continuum. The UV–VUV emission spectra from the TGD plasma were analyzed by taking the emission from the end of the plasma column. At the opposite side of the plasma (against the quartz window of the discharge chamber), a pulsed FOTON photomultiplier was placed. The waveforms of the total emission from the plasma in the spectral range 200–700 nm were recorded using a broadband C1-99 oscilloscope. The time reso-
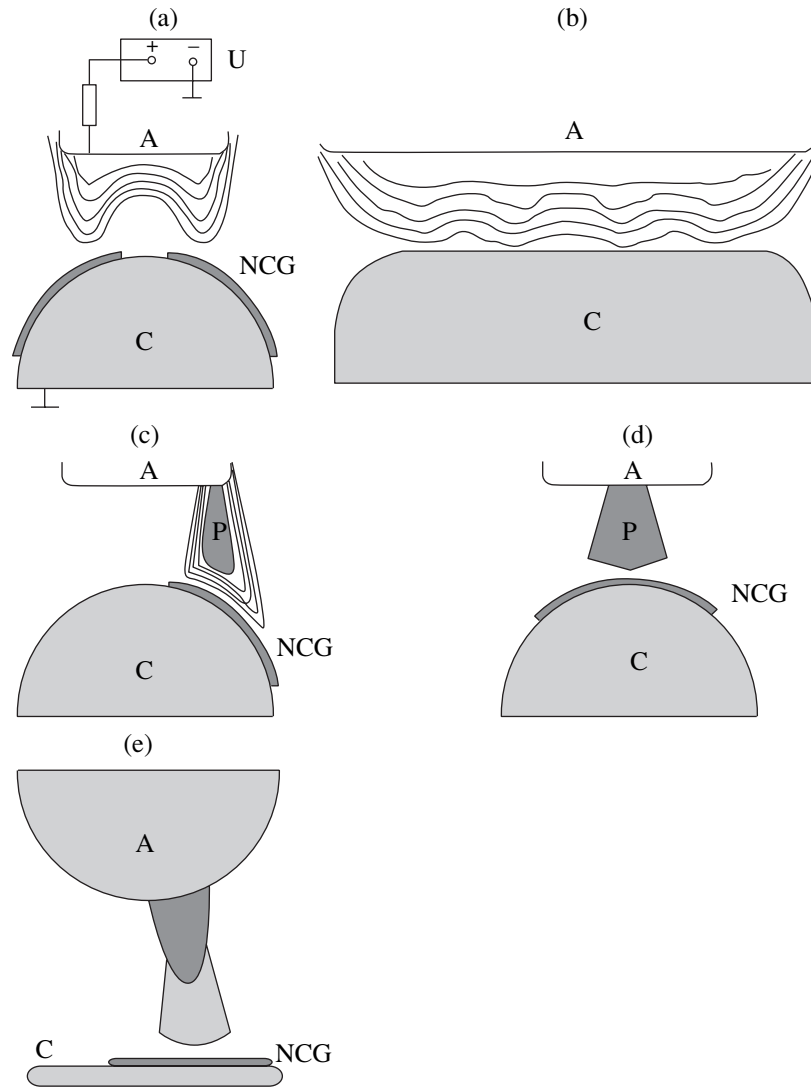
Fig. 1. (a, c, d) Transverse and (b) longitudinal cross sections of a TGD in the Xe/Cl_2 = (a, b) 120/40-Pa, (c) 240/120-Pa, and (d) 670/40-Pa mixtures and (e) a volume discharge with a spherical anode and plane cathode: (A) anode, (C) cathode, and (NCG) negative cathode glow.

lution of the recording system was no worse than 10 ns. The waveforms of the discharge current pulses were recorded with the help of a low-inductive current shunt with a resistance of R = 1–5 Ω, and a low-inductive capacitive divider (with an attenuation coefficient of 400) was used to record the discharge voltage. The input capacitance of the divider (C_0 = 200 pF) shunted the gap between the spherical anode and plane cathode of the volume discharge.

The TGD was ignited between a plane nickel anode and a massive hemicylindrical nickel-plated brass cathode. The area of the anode working surface was 4.5 × 16 cm², and the base area of the brass cathode was 7.5 × 15 cm². The interelectrode distance was 2.2 cm. The end and side edges of the TGD electrodes were

rounded. The electrode system of the volume discharge consisted of a massive hemispherical anode with a base diameter of 7 cm and a 1-cm-thick plane cathode 9 cm in diameter. The electrodes were made of duralumin and were spaced by 2.8 cm. The radius of curvature of the anode working surface was 3 cm. A dc voltage of $U_{ch} \le 1.0$ kV was applied to the anode through a 20-kΩ ballast resistor. The average discharge current was varied in the range 2–50 mA, and the total pressure of the Xe/Cl working mixture was in the range 40–2000 Pa.

3. SPATIAL CHARACTERISTICS

The spatial characteristics of the discharge were determined by taking the photographs of the discharge and processing them with a scanner and a PC. The cross

Spatial characteristics of a volume discharge with a spherical anode and a plane cathode

Xe/Cl$_2$ mixture, Pa	d_a, mm	d_c, mm
80/120	10	22
160/120	8	17
320/120	7	15
480/120	7	20 (strata)
320/200	9	20
320/320	5	12

sections of the electrode system and the low-pressure glow discharge plasma are shown in Fig. 1. At low partial pressures of xenon and chlorine (Figs. 1a, 1b), the TGD occupied most of the interelectrode gap and existed in the form of moving and stationary strata (generally, five to six stationary strata were observed). In the middle of the discharge gap, the plasma was absent. The stratified plasma was adjacent to the working surface of the anode plate and was separated from the cathode part of the discharge by a dark space. The negative cathode glow (NCG) was formed at the periphery of the cathode cylindrical surface, whereas the central part of the gap was free of plasma. In the longitudinal section of the TGD, strata directed along the TGD electrodes were observed (Fig. 1b). As the

xenon partial pressure increased, a solitary plasma domain formed near one of the ends of the TGD electrode system. The intensity of visible emission from the plasma domain was maximum in the center of the domain and decreases toward its periphery. The cathode part of the plasma domain consisted of the NCG and the cathode dark space. The formation of a domain was observed most clearly in the case of a spherical anode and plane cathode (Fig. 1e). The diameters of the anode (d_a) and cathode (d_c) parts of the plasma domain (excluding the NCG) in Xe/Cl$_2$ mixtures are presented in the table.

The diameter of the anode part of the plasma domain was always 1.5–2.0 times larger than the diameter of its cathode part. The increase in the xenon pressure $P(Xe)$ from 80 to 320 Pa at $P(Cl_2) = 120$ Pa led to a decrease in d_a and d_c. At $P(Xe) = 480$ Pa, the domain was stratified. An increase in the partial pressure of molecular chlorine resulted in a rapid decrease in the domain dimensions.

4. ELECTRICAL AND OPTICAL CHARACTERISTICS

The steady-state current–voltage characteristics of a TGD in a Xe/Cl$_2$ mixture (Fig. 2a) are similar to those of a longitudinal dc glow discharge [13]. At anode voltages of $U_{ch} \leq 650$ V, the TGD was stable. The increase in $P(Xe)$ from 120 to 670 Pa led to an increase in U_{ch} by 130–150 V; the increase was maximum at low discharge currents ($I_{ch} \leq 10$ mA). The average power deposited in the TGD was in the range 1–30 W. The steady-state current–voltage characteristics of a volume discharge with a spherical anode and plane cathode were similar to the TGD characteristic shown in Fig. 2. At $t > 1.5$ μs, there was a pronounced segment with a negative slope in the dynamic current–voltage characteristic (plotted by using the waveforms of the ac components of the discharge voltage and current) of a volume discharge in the Xe/Cl$_2$ = 160/120-Pa mixture (Fig. 2b).

The emission spectra from a TGD in different Xe/Cl$_2$ mixtures are shown in Fig. 3. The test experiment with proper light filters showed that the integral emission power in the spectral range $\lambda > 400$ nm was no higher than 10% of the total emission power. Hence, the waveforms recorded with the pulsed FOTON photomultiplier represent the emission dynamics from the XeCl(D,B–X) molecular bands. The plasma of a volume discharge in a Xe/Cl$_2$ mixture acts as a source of broadband radiation in the range 200–340 nm. The XeCl(D–X) and XeCl(B–X) bands with peaks at 236 and 308 nm, respectively, were dominant in the emission spectrum. An increase in the xenon partial pressure resulted in a decrease in the emission intensity on the short-wavelength side of spectrum and an increase in the emission intensity at $\lambda \geq 320$ nm, which is related to the process of vibrational relaxation of the B and D
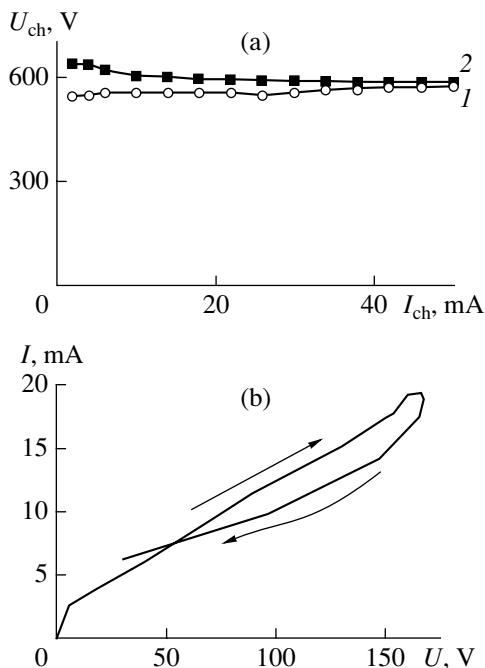

Fig. 2. (a) Steady-state current–voltage characteristics of a transverse discharge in the Xe/Cl$_2$ = (*1*) 120/40-Pa and (*2*) 670/40-Pa mixtures and (b) the dynamic current–voltage characteristic of a volume discharge with a spherical anode and a plane cathode in the Xe/Cl$_2$ = 160/120-Pa mixture.
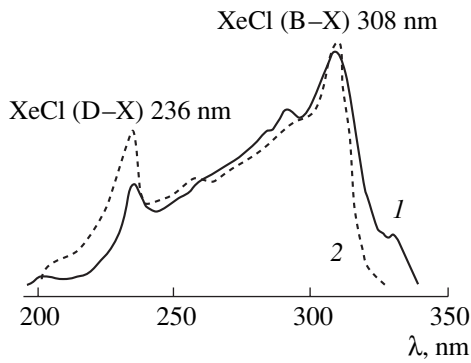
XeCl (B–X) 308 nm

XeCl (D–X) 236 nm

1

2

200   250   300   350

λ, nm

Fig. 3. Emission spectra from a transverse discharge in the Xe/Cl$_2$ = (*1*) 670/40-Pa and (*2*) 120/40-Pa mixtures for I_{ch} = 50 mA.

states of a XeCl molecule in collisions with Xe atoms [14]. After a collision event, the XeCl(B, D, v'') excimer molecule passes to a lower lying energy level. At low pressures of the Xe/Cl$_2$ mixture, the Cl$_2$(D'–A') 257-nm band was observed against the background of broadband UV emission formed due to the overlap of the XeCl(D–X) band with the XeCl(B–X) band. This fact allows us to refer to the radiation source under study as an excimer–halogen source.

The study of the time behavior of the TGD emission showed that it contained both a dc and an ac component. For example, in the case of a TGD in the Xe/Cl$_2$ = 240/120-Pa mixture at discharge currents of 8–18 mA, the dc component of the plasma emission intensity was no higher than 30%. The ac component consisted of regular pulses with a full width of 20 μs. As the average discharge current increased, the share of the dc component increased and the waveform of the total emission intensity became a damped sinusoid that reached a constant value at t = 100 μs. This value comprised about 70% of the main (first) maximum of the emission intensity. For low TGD currents ($I_{ch} \leq 4$ mA), the plasma emission intensity was nearly constant.

The dynamics of a volume discharge with a spherical anode and plane cathode was studied in more detail. The waveforms of the discharge voltage, the discharge current, and the total emission intensity from the plasma are shown in Fig. 4. In the case of a volume discharge in a low-pressure Xe/Cl$_2$ mixture, the dc component of the total UV emission from the plasma was minimum, and the emission primarily consisted of radiation pulses with a full width of 3.0 μs (Fig. 4a). The peaks in the emission intensity almost coincided in time with the discharge current maxima. The emission pulse was formed at the leading edge of the discharge voltage
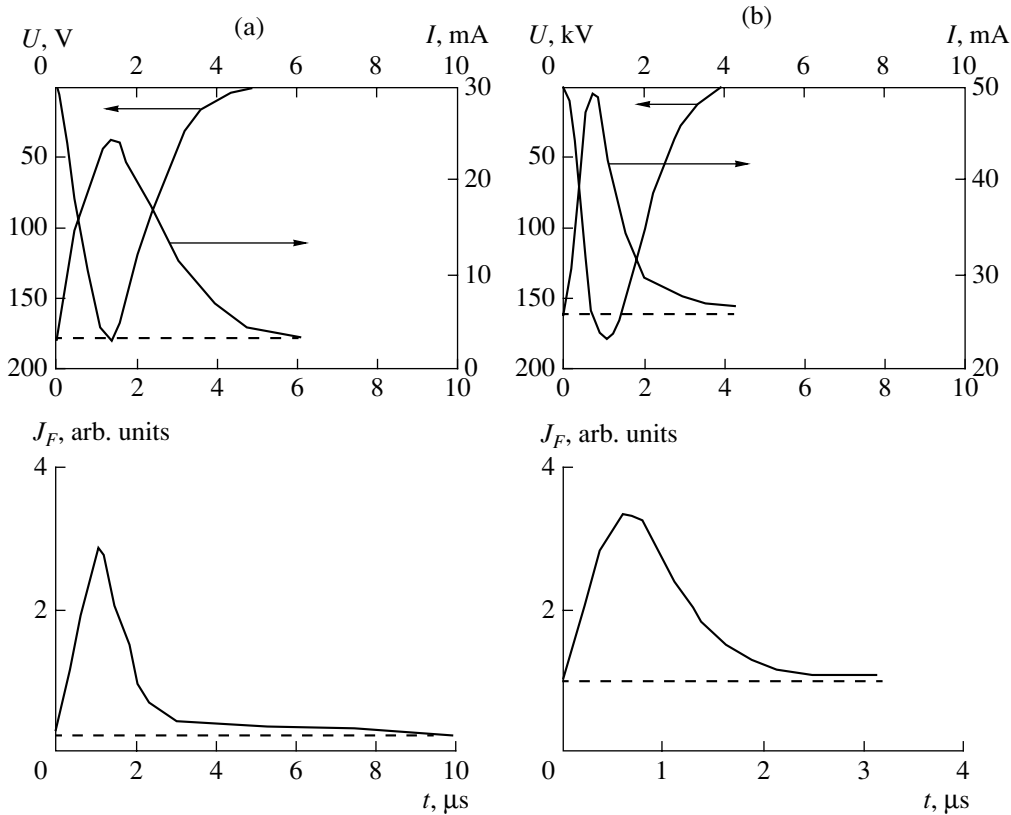
Fig. 4. Waveforms of the discharge voltage U, the discharge current I, and the total emission intensity J_F from the plasma for a volume discharge with a spherical anode and plane cathode in the Xe/Cl$_2$ = (a) 160/120-Pa and (b) 480/320-Pa mixtures (C_0 = 220 pF).
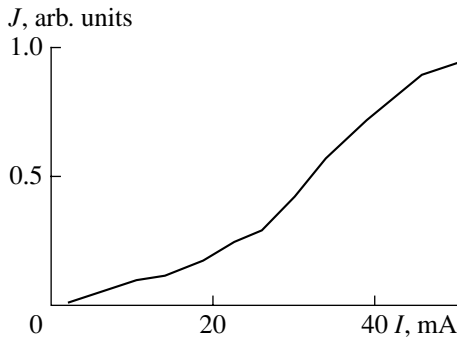
J, arb. units

Fig. 5. UV emission intensity from a discharge in the Xe/Cl$_2$ = 120/40-Pa mixture vs. average TGD current.

pulse. Figure 4 presents the waveforms of the discharge parameters for pulses with the maximum values of $U, I,$ and J_F; however, in the experiments, we recorded pulses with a rather wide scatter in the amplitudes of the discharge parameters (at a level of 30–100% of the maximum values). This points to the formation of plasma domains whose parameters vary in a fairly wide range.

An increase in the partial pressures of Xe and Cl$_2$ led to an increase in the share of the dc components in the discharge current and plasma emission (Fig. 4b), whereas the duration of the radiation pulses decreased from 3 to 2 μs. Substituting krypton or argon for xenon in a Xe/Cl$_2$ mixture resulted in the disappearance of the dc component of both the discharge current and the plasma emission between the pulses. In these media, the pulse repetition rate increased with average current and was in the range 5–100 kHz.

The emission intensity *J* from the TGD plasma in the spectral range 200–340 nm increased with the average current without any tendency to saturation (Fig. 5). At discharge currents in the range 25–50 mA, the rate at which the UV emission intensity grew with increasing current was 3 times higher than that at low currents ($I_{ch} \le 20$ mA). Similar dependences of the emission intensity from XeCl(D,B–X) molecules on the average current were also observed for a volume discharge with a spherical anode and plane cathode. To increase the UV radiation intensity from the discharge, it is promising to increase the average discharge current to 0.5–1.0 A. However, it would require the forced cooling of the discharge electrodes and manufacturing them from metals that are higher melting than duralumin.

5. CONCLUSION

It has been shown that the waveforms of the discharge voltage, discharge current, and emission intensity from a transverse glow discharge and a volume discharge with a spherical anode and plane cathode in Xe/Cl$_2$ mixtures (at $P \le 2$ kPa) have both a dc and an ac component. The discharges exist mainly in the form of plasma domains. In the absence of a dielectric wall,

there is no contact between the plasma and glass; as a result, there is no chlorine diffusion into the glass at elevated plasma temperatures. At discharge currents of $I_{ch} = 2$–50 mA, the dc voltage at the anode is no higher than 1.0 kV; in this case, no forced cooling of the discharge unit is required. Xe/Cl$_2$ = (500–700)/(120–250)-Pa mixtures are found to be optimum for attaining the maximum emission power from a volume discharge in the range 200–340 nm (the XeCl(D–X), Cl$_2$(D'–A'), and XeCl(B–X) band system with maximums at 236, 257, and 308 nm, respectively). Based on the discharges under study, it is possible to create low-pressure broadband excimer–halogen lamps in which a significant fraction of radiation will be emitted in microsecond pulses with a repetition rate of 5–100 kHz. To increase the stability of the transverse discharge, it may be promising to use an RF pumping (a γ-type discharge with stripped electrodes separated by a distance of 2–3 cm), in which case electrode sheaths are formed whose emission intensity is higher than that of the positive column of an RF discharge.

REFERENCES

1. E. A. Sosnin and V. F. Tarasenko, Zh. Tekh. Fiz. **67** (12), 43 (1997) [Tech. Phys. **42**, 1411 (1997)].
2. H. Kumagai and M. Obara, Appl. Phys. Lett. **54**, 2619 (1989).
3. A. P. Golovitskiĭ, Pis'ma Zh. Tekh. Fiz. **18** (8), 73 (1992).
4. M. I. Lomaev, A. N. Panchenko, E. A. Sosnin, *et al.*, Zh. Tekh. Fiz. **68** (2), 64 (1998) [Tech. Phys. **43**, 192 (1998)].
5. A. K. Shuaibov, A. I. Dashchenko, and I. V. Shevera, Fiz. Plazmy **27**, 573 (2001) [Plasma Phys. Rep. **27**, 542 (2001)].
6. A. K. Shuaibov, A. I. Dashchenko, and I. V. Shevera, Kvantovaya Élektron. (Moscow) **31**, 371 (2001).
7. A. K. Shuaibov, A. I. Dashchenko, and I. V. Shevera, Zh. Tekh. Fiz. **71** (8), 121 (2001) [Tech. Phys. **46**, 1049 (2001)].
8. L. D. Tsendin, Zh. Tekh. Fiz. **59** (1), 21 (1989) [Sov. Phys. Tech. Phys. **34**, 11 (1989)].
9. S. A. Gutsev, A. A. Kudryavtsev, and V. A. Romanenko, Zh. Tekh. Fiz. **65** (11), 77 (1995) [Tech. Phys. **40**, 1131 (1995)].
10. A. A. Kudryavtsev and L. D. Tsendin, Pis'ma Zh. Tekh. Fiz. **26** (13), 93 (2000) [Tech. Phys. Lett. **26**, 582 (2000)].
11. A. K. Shuaibov, L. L. Shimon, A. I. Dashchenko, and I. V. Shevera, J. Phys. Stud. **5** (2), 131 (2001).
12. A. K. Shuaibov, L. L. Shimon, A. I. Dashchenko, and I. V. Shevera, Prib. Tekh. Éksp., No. 1, 104 2002.
13. Yu. P. Raizer, *Gas Discharge Physics* (Atomizdat, Moscow, 1987; Springer-Verlag, Berlin, 1991).
14. V. V. Datsyuk, I. A. Izmailov, and V. A. Kochelap, Usp. Fiz. Nauk **168**, 439 (1998) [Phys. Usp. **41**, 379 (1998)].

Translated by N.N. Ustinovskiĭ

PARTICLE ACCELERATION
IN PLASMAS

Generation of High-Quality Charged Particle Beams during the Acceleration of Ions by High-Power Laser Radiation

S. V. Bulanov[1, 2], T. Zh. Esirkepov[3, 4], F. F. Kamenets[3], Y. Kato[2], A. V. Kuznetsov[3],
K. Nishihara[4], F. Pegoraro[5], T. Tajima[2], and V. S. Khoroshkov[6]

[1]*Institute of General Physics, Russian Academy of Sciences, ul. Vavilova 38, Moscow, 117942 Russia*
[2]*Advanced Photon Research Center, Japan Atomic Energy Research Institute (JAERI-Kansai), 619-0215 Kizu, Kyoto, Japan*
[3]*Moscow Institute of Physics and Technology, Institutskii per. 9, Dolgoprudnyĭ, Moscow oblast, 141700 Russia*
[4]*Institute of Laser Engineering, Osaka University, 2-6 Yamada-Oka, Suita, Osaka, 565-0871 Japan*
[5]*Istituto Nazionale Fisica della Materia and Dip. Fisica, Università di Pisa, 56126 Pisa, Italy*
[6]*Institute of Theoretical and Experimental Physics, ul. Bol'shaya Cheremushkinskaya 25, Moscow, 117259 Russia*
Received June 4, 2002

Abstract—Numerous applications of protons and ions accelerated by laser radiation require charged particle beams of high quality (i.e., such that the ratio of the energy width of the beam to its mean energy is small). In order to produce beams with controlled quality, it is proposed to use two-layer targets in which the first layer consists of heavy multicharged ions and the second layer (thin and narrow in the transverse direction) consists of protons. The possibility of generating a high-quality proton beam in the interaction of ultraintense laser radiation with such a two-layer target is demonstrated by two- and three-dimensional particle-in-cell computer simulations. © 2002 MAIK "Nauka/Interperiodica".

1. INTRODUCTION

At present, rapid strides are being made in developing compact laser devices capable of generating ultrashort pulses in the multi-terawatt and petawatt power range [1]. The most important possible applications of such lasers are associated with electron and ion accelerators [2–6], as well as compact sources of ions [7], pions [8], and hard X-ray and gamma radiation [9].

Laser accelerators of ions are based on the high efficiency of converting laser energy into the energy of fast ions in the interaction of petawatt laser pulses with plasma [10]. Collimated beams of fast ions were recorded in experiments on the interaction of laser pulses with solid targets [3]. The ion acceleration processes are also investigated numerically [4–6] by means of two- and three-dimensional particle-in-cell (PIC) computer simulations [11]. In the experiments reported in [3], electrons were accelerated to energies of about several hundred MeV and the energies of the accelerated ions amounted to several tens of MeV per nucleon. The number of particles in the beam can be as large as about 10^{13}, and the conversion efficiency of laser energy into the energy of fast ions can be as high as 7–12%. Computer simulations [6] showed that, by optimizing the plasma parameters of laser pulses and targets, it is possible to achieve conditions under which protons can be accelerated to energies of several hundred MeV, the number of particles accelerated by one laser pulse being about 10^{11}–10^{13}.

Note that, in the interaction of laser radiation with a sufficiently thin plasma slab (of either subcritical or overcritical density), the ions in the slab that are farthest from the laser are accelerated most efficiently. (It is clear that, when the target is thick, only the ions nearest to the laser are accelerated.) The generation of fast proton beams in the propagation direction of a laser pulse was first demonstrated in computer simulations carried out for a dense plasma [12] and a subcritical plasma [4] and, then, was observed in experiments with high-power laser pulses [3]. Such factors as a large number of accelerated protons and their high energy, as well as the high directionality of proton beams, open up a wide range of possibilities for employing laser accelerators as injectors for conventional charged particle accelerators [13], as a means for the fast ignition of thermonuclear reactions in inertial confinement fusion [14, 15] and the initiation of nuclear reactions in matter [8], and as tools for the purposes of hadron therapy in oncology [16, 17] and proton diagnostics of plasmas with high temporal and spatial resolutions [18].

In almost all of these practical applications (injectors, inertial confinement fusion, and hadron therapy), the key problem is associated with the quality of the proton beam, because the protons observed in both laboratory experiments and numerical simulations have broad quasi-thermal energy spectra. This raises the question as to how to ensure the smallness of the ratio $\Delta\mathscr{E}/\mathscr{E}$ of the energy width of the beam to its character-
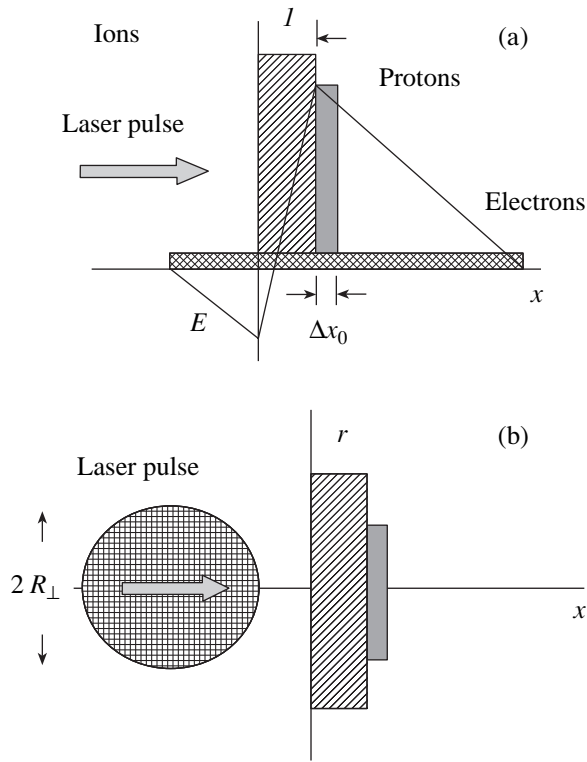
Fig. 1. Two-layer target. The rear side of the foil of heavy ions is coated with a thin hydrogen layer.

istic energy. Thus, for the purposes of hadron therapy, this ratio should be as small as $\Delta\mathscr{E}/\mathscr{E} \le 2\%$, because it is necessary to guarantee the irradiation of a malignant tumor with a sufficiently strong dose while simultaneously ensuring a minimum acceptable level of the irradiation of the surrounding healthy tissues and organs [19]. In the model of the fast ignition of precompressed targets by a beam of protons accelerated by laser radiation [14], the beam was assumed to be monoenergetic. In [20], the calculations of the laser energy required for ignition by a beam of fast protons with a quasi-Maxwellian energy distribution showed that the required laser energy is several times higher than the energy estimated in [14]. Also, in the problem of a particle injector, the energy spectrum of the beams should be sufficiently narrow to provide the beam injection into the optimum acceleration phase [21].

The results of computer simulations described in this paper show that using a two-layer target whose qualitative model was formulated in [16] makes it possible to solve the above problem of generating fast ion beams with controlled quality. Note that, in laser physics, multilayer targets have been known for a long time (see, e.g., [22], where the advantages of compressing multilayer fusion targets were discussed). In particular, in [23], it was experimentally demonstrated that the use of a two-layer target increases the efficiency of laser

acceleration of protons as compared to the case with a single-layer target. Cluster targets consisting of particles of different species were investigated experimentally in [24], where the increase in the acceleration efficiency of protons was also observed.

In contrast to the papers cited above, we propose to generate beams with controlled quality by using two-layer targets. In the scheme developed here, the target is composed of two layers in which the laser-irradiated first layer consists of heavy, partially ionized ions with the charge $Z_i e$ and the mass m_i and the second layer, which is farther from the laser, consists of ionized hydrogen atoms, i.e., protons and electrons. In the initial target configuration, the electric charge of positive ions is fully neutralized by electrons. The number of electrons in the first layer is assumed to be much larger than that in the second layer. The second layer should be of sufficiently small thickness (the layer dimension in the propagation direction of a laser pulse) and sufficiently small width (the dimension in the transverse direction). The target configuration under discussion, which was described qualitatively in [16], is illustrated in Fig. 1.

In order to explain why it is necessary to satisfy the above requirements, we describe a typical scenario of the interaction of a high-power laser pulse with a two-layer target. In the field of the incident laser pulse, the target is ionized and some electrons escape from it under the action of the ponderomotive pressure of the laser radiation. Escaping electrons give rise to the quasistatic electric field of an unneutralized electric charge. The quasistatic electric field is localized in a finite region with dimensions comparable to the transverse dimension of the laser pulse. The initial stage, during which the light ions (protons) are accelerated, is insufficiently long for the heavy ions of the first layer to start moving. If the total number of protons is small in comparison with the number of electrons that have escaped from the target, then the effect of the electric field of protons on their dynamics can be neglected, in which case the proton acceleration can be described in the approximation of test particles moving in a prescribed electric field. The fact that the thickness and width of the proton layer are both small in comparison with the scalelength of the electric field guarantees that all protons will acquire approximately the same energy. Under such conditions, the relative energy spread of the particles is proportional to the ratio of the target thickness to the inhomogeneity scale of the accelerating electric field.

Below, we will present the results of calculating the energy spectrum of protons using a simple theoretical model. We will also discuss the results of two- and three-dimensional PIC simulations of the interaction of high-power laser radiation with a two-layer target.

Our paper is organized as follows. In Section 2, based on the familiar dependence of the energy losses of protons in matter on their path length, we justify the

necessity of using monoenergetic beams. In Section 3, by using a one-dimensional static model for the electric field distribution near the target, we calculate the energy spectrum and also the longitudinal and the transverse emittance of a fast proton beam. In Section 4, we report the results obtained from PIC simulations of the interaction of high-power laser radiation with two-layer targets. In Section 5, the main results of our study are summarized.

2. ENERGY LOSSES OF A PROTON BEAM

As is known [25], a proton beam passing through matter loses energy. The energy loss rate $d\mathcal{E}/dx = -F(\mathcal{E})$ is described by the formula

$$F(\mathcal{E}) = \frac{\kappa}{\mathcal{E}}\Lambda(\alpha\mathcal{E}), \qquad (1)$$

where $\Lambda(\alpha\mathcal{E})$ is a function of energy $\mathcal{E}$. The specific form of this function depends on the state of matter (see, e.g., [25–27]). For a proton propagating in a plasma [27], we have $\kappa = 4\pi n_e e^4 m_p/m_e$ and the function $\Lambda(\alpha\mathcal{E})$ has the form $\Lambda(\alpha\mathcal{E}) = \ln(4m_e\mathcal{E}/\hbar\omega_{pe}^2 m_p)$, which gives $\alpha = 4m_e/\hbar\omega_{pe}^2 m_p$, where $\omega_{pe} = (4\pi n_e e^2/m_e)^{1/2}$ is the plasma frequency.

The distribution function $\mathcal{N}(x, \mathcal{E})$ of the fast protons satisfies the transport equation

$$\frac{\partial \mathcal{N}}{\partial x} + \frac{\partial}{\partial \mathcal{E}}[F(\mathcal{E})\mathcal{N}] = 0 \qquad (2)$$

with the boundary condition $\mathcal{N}(x = 0, \mathcal{E}) = \mathcal{N}_0(\mathcal{E})$. The solution to Eq. (2) can be represented as

$$\mathcal{N}(x, \mathcal{E}) = \mathcal{N}_0(\mathcal{E}_0)\left|\frac{d\mathcal{E}_0}{d\mathcal{E}}\right|. \qquad (3)$$

Here, $\mathcal{E}$, $\mathcal{E}_0$, and x are related by

$$\mathrm{li}[(\alpha\mathcal{E})^2] = \mathrm{li}[(\alpha\mathcal{E}_0)^2] - \kappa\alpha^2 x; \qquad (4)$$

where $\mathrm{li}(\xi) = \int_0^\xi d\xi/\ln\xi$ [28] is the logarithmic integral, which can be expressed in terms of the exponential integral $\mathrm{li}(\xi) = \mathrm{Ei}(\ln\xi)$, with $\mathrm{Ei}(\zeta) = \int_\zeta^\infty \exp(-\eta)\, d\eta/\eta$. With good accuracy, the logarithmic integral is approximated by the expression $\mathrm{li}(\xi) \approx \xi/\ln\xi$. Using formulas (1), (3), and (4), we obtain the rate of the beam energy losses, i.e., the energy deposited per unit length of the beam trajectory:

$$\langle\mathcal{E}'\rangle(x) = \int \mathcal{N}(x, \mathcal{E})F(\mathcal{E})d\mathcal{E}. \qquad (5)$$

Figure 2 shows the profiles of the energy deposited by fast proton beams that have different energy spectra at $x = 0$. Curve *1* was calculated for a beam with a quasi-thermal energy distribution such that $\mathcal{N}(x = 0, \mathcal{E}) =$
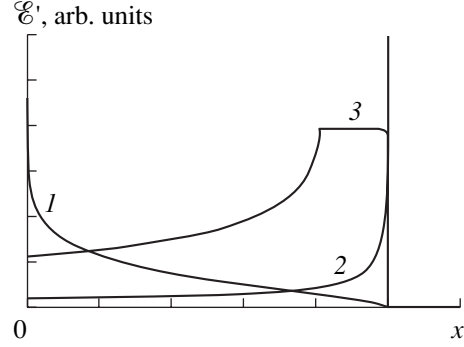

$\mathcal{E}'$, arb. units

Fig. 2. Profiles of the energy losses for fast proton beams with different energy distributions: (*1*) a quasi-thermal beam, (*2*) a monoenergetic beam, and (*3*) a beam with the energy spectrum that ensures a uniform energy deposition inside the target.

$n_0\theta(\mathcal{E} - \mathcal{E}_{max})\exp(-\mathcal{E}/T)$, where $\theta(\xi) = 1$ for $\xi > 0$ and $\theta(\xi) = 0$ for $\xi < 0$. This quasi-thermal distribution function of a fast proton beam corresponds to the dependence that is usually used to approximate the energy spectra of the fast protons recorded in experiments on the interaction of laser radiation with solid targets [3] and observed in numerical simulations of nonoptimized targets [4–6], in which case the effective beam temperature T is several times lower than the maximum energy $\mathcal{E}_{max}$ of the accelerated particles. A quasi-thermal beam is seen to lose its energy mainly at the entrance to the irradiated target. (Note that, following the generally accepted terminology, we use the term "target" for both the object irradiated by laser pulses and the object irradiated by proton beams. However, this term does not introduce any ambiguities because it is used in different contexts in different sections of the present paper.) This coordinate dependence of the energy loss rate $\langle\mathcal{E}'\rangle$ is unlikely to be acceptable for the purposes of hadron therapy. In addition, in [20], it was noted that, in order for the quasi-thermal beams to be used in the scheme of rapid ignition of a precompressed target by a proton beam [14], the required laser energy should be several times higher than that in the case of monoenergetic beams. For a monoenergetic beam with a distribution function such that $\mathcal{N}(x = 0, \mathcal{E}) = n_0\delta(\mathcal{E} - \mathcal{E}_{max})$, the loss curve (Fig. 2, curve *2*] has a sharp maximum (Bragg's peak) [26]. It is because of this property of the energy loss of ion beams that they hold promise in the hadron therapy in oncology [19, 29]. Among different methods for irradiating cancer tumors are those that make use of raster technology, which requires monoenergetic beams and beams with a finite energy width (see [19, 29]).

Neglecting the logarithmic dependence on energy in formula (1), we can obtain the sought-for distribution $\mathcal{N}_0(\mathcal{E})$ by solving integral equation (5) analytically for a prescribed distribution $\langle\mathcal{E}'\rangle(x)$ because, in this approximation, Eq. (5) reduces to the familiar Abel's

integral equation. Thus, a uniform energy input over the interval $x_1 < x < x_2$ ensures a beam with the spectrum

$$\mathcal{N}(x = 0, \mathcal{E})$$

$$= n_0 \theta(\mathcal{E} - \mathcal{E}_{max}) \theta(\mathcal{E}_{min} - \mathcal{E}) \frac{\mathcal{E}}{\sqrt{\mathcal{E}_{max}^2 - \mathcal{E}^2}}, \qquad (6)$$

where $\mathcal{E}_{max} = \sqrt{\kappa x_2}$ and $\mathcal{E}_{min} = \sqrt{\kappa x_1}$. The energy deposition profile in the case of a beam with energy spectrum (6) is shown by curve *3* in Fig. 2. A beam with this energy spectrum can be formed by appropriately shaping the proton distribution inside the target or by superposing a large number of monoenergetic beams.

In turn, monoenergetic proton beams can be formed by "cutting" a wide beam into a number of narrow beams in energy space. However, in this way, both the efficiency of converting laser energy into the energy of fast particles and, more importantly, the number of particles in the beam decrease substantially. A more promising approach is associated with the possible use of multilayer targets.

3. TWO-LAYER TARGET FOR PRODUCING HIGH-QUALITY PROTON BEAMS

In the simplest scheme of ion acceleration, a laser pulse interacts with a thin single-layer foil. For a laser operating at a wavelength of one micron, the foil thickness is usually varied from fractions of a micron to several microns and more. Under the action of multiterawatt or petawatt laser radiation, the matter of the foil is ionized almost instantaneously. The ionization proceeds through an optical mechanism analogous to that considered in [30]: the matter of the foil is ionized during a time shorter than the optical period and becomes a thin plasma layer with an overcritical density, $n_{cr} = m_e \omega^2 / 4\pi e^2$, where ω is the laser frequency. Then, the ponderomotive force of the laser radiation expels electrons from the focal spot. For ultrashort (femtosecond) laser pulses, the characteristic time of the hydrodynamic expansion of a plasma of micron thickness is longer than the pulse duration. Under such conditions, the ions remain immobile over a period of time during which the pulse interacts with the target and thus form a positively charged ion layer, i.e., a region of unneutralized positive electric charge with dimensions of about the transverse size of the focal spot of the laser beam. However, after a time of about $1/\omega_{pi} = \sqrt{m_i/4\pi n Z_i e^2}$, the ion layer begins to expand under the action of the Coulomb repulsive forces between like charges. This phenomenon is called "Coulomb explosion," the simplest example of which is the expansion of a cluster that has lost all its electrons in the field of a laser pulse. Cluster targets, which are of considerable interest for creating compact sources of neutrons and X radiation, have been studied in many papers (see [31]

and the literature cited therein). Note that the quasineutrality of a plasma irradiated by longer laser pulses of moderate intensities (the particular pulse parameters depend on many factors, including the target parameters) is violated to a smaller extent. In this case, the plasma ions are accelerated in the same manner as during the plasma expansion into a vacuum [32].

When the ratio $\mu^{1/2}/Z_i$ (where $\mu = m_i/m_p$) is sufficiently large, the characteristic time scale of the proton motion is much shorter than that of the Coulomb explosion of a layer of heavy ions. Under these conditions, the thin surface proton layer of the two-layer target is accelerated in a prescribed electric field. One of the most important requirements on such targets is that the width of the proton layer should be much smaller than the transverse dimension of the laser pulse. The transverse nonuniformity of the accelerating electric field that is associated with the finite width of the pulse gives rise to an additional energy spread of the accelerated ions. Presumably, it is this effect that was observed in the experiments of [3], in which fast protons were recorded in the interaction of laser pulses with thin metal (aluminum) foils. The protons originated from a water layer on the target surface. Obviously, the width of the proton layer was not controlled in those experiments and was on the order of the target width. In addition, the effect of the transverse nonuniformity of the accelerating electric field leads to the undesirable defocusing of an ion beam, in particular, to an increase in the beam transverse emittance. Note that, in order to reduce the effects just mentioned and to ensure a high degree of collimation of the ion beam, it was proposed to use appropriately deformed targets [6].

The characteristic energy of the accelerated ions can be estimated under the assumption that all the electrons produced by ionization in the focal spot of a laser beam escape from the spot under the action of the ponderomotive pressure of laser radiation. In this situation, which can occur in the laser field of sufficiently high intensity, the electric field strength near the positively charged layer is equal to $E_0 = 2\pi n_0 Z_i e l$, where n_0 is the ion density inside the target, $Z_i e$ is the charge of an ion, and l is the target thickness. The transverse dimension of the region of a strong electric field is about the diameter $2R_\perp$ of the focal spot. Consequently, the longitudinal dimension of this region is also about $2R_\perp$. This yields the following estimate of the energy acquired by an ion with the electric charge $Z_a e$ in the electric field E_0:

$$\mathcal{E}_{max} \approx 2\pi n_0 Z_a Z_i e^2 l R_\perp. \qquad (7)$$

Here, we have assumed that the energy of the electrons accelerated by the laser field is on the order of or higher than the energy required for them to overcome the potential of the attractive electric field in the acceleration region. The electron energy in a relativistically strong electromagnetic wave is $\mathcal{E}_e = m_e c^2 a_0^2 / 2$ (see

[33]), where the dimensionless wave amplitude $a_0 = eE/mc\omega$ is related to the radiation intensity by $I = a_0^2 1.38 \times 10^{18}(\lambda/1\mu m)^2$ W/cm^2. As a result, knowing the diameter of the focal spot, $2R_\perp$, we can determine the required power of the laser pulse and, having specified the pulse duration τ_l, we can find the pulse energy.

We assume that the layer of light ions consists of protons with $Z_a = 1$. The energy spectrum of the protons can be calculated by using a model in which the accelerating electric field is prescribed, which implies that the total electric charge of the proton layer is much smaller than that of the layer of heavy ions.

The electric field configuration can be approximated by the electrostatic field of a charged ellipsoid (an oblate ellipsoid of revolution) with its major semiaxis equal to the radius R_0 of the focal spot and its minor semiaxis (one-half of the thickness) equal to l. The expression for the field of a charged disk is presented in [25]. Using this expression, we write the coordinate dependence of the electric field outside the target:

$$E_x = \frac{4\pi e n_0 Z_i l R_0^2}{3} \frac{1}{R_\xi} \frac{\partial \xi}{\partial x}, \qquad (8)$$

$$E_\rho = \frac{4\pi e n_0 Z_i l R_0^2}{3} \frac{1}{R_\xi} \frac{\partial \xi}{\partial \rho}, \qquad (9)$$

where x and $\rho = (y^2 + z^2)^{1/2}$ are the coordinates, $R_\xi = (\xi + R_0^2)(\xi + l^2)^{1/2}$, and

$$\xi = \frac{1}{4}\left[\sqrt{\left(\rho - \sqrt{R_0^2 - l^2}\right)^2 + z^2} + \sqrt{\left(\rho - \sqrt{R_0^2 - l^2}\right)^2 + z^2} \right]^2 - R_0^2. \qquad (10)$$

From expressions (8) and (9), we can see that the electric field is strongest at the target surface and decreases sharply outside the region of radius R_0.

The proton energy spectrum can be obtained by assuming that protons are accelerated in the axial region; this assumption is consistent with the structure of the two-layer target model under discussion. At the axis, the radial component of the electric field vanishes and the longitudinal component is equal to

$$E_x(x) = \frac{8\pi e n_0 Z_i l R_0^2}{3} \frac{1}{(R_0^2 - l^2 + x^2)}. \qquad (11)$$

For a simple model dependence of the electric field on the coordinates, a detailed solution of the problem of the spectrum of average protons is given in the Appendix. It is well known that the solution to the kinetic equation for the distribution function $f(x, v, t)$ has the form

$$f(x, v, t) = f_0(x_0, v_0), \qquad (12)$$

where $f_0(x_0, v_0)$ is the distribution function at the initial time $t = 0$. We are considering the case in which, at the initial time $t = 0$, all particles are at rest and the spatial distribution of their density is defined by the function $n_0(x_0)$. These initial conditions correspond to a distribution function of the form $f_0(x_0, v_0) = n_0(x_0)\delta(v_0)$, where $\delta(v_0)$ is the Dirac delta function. The number of particles in a unit volume $dxdv$ of phase space is equal to $dn = fdxdv = fvdvdt = fd\mathcal{E}dt/m_p$. Integrating this expression over time yields the energy spectrum of the accelerated particles:

$$N(\mathcal{E})d\mathcal{E} = d\mathcal{E}\int n_0(x_0)\delta(v_0)\frac{dt}{m_p}$$
$$= \frac{n_0(x_0)}{m_p}\left|\frac{dt}{dv}\right|_{v = v_0} d\mathcal{E}; \qquad (13)$$

where the Lagrangian coordinate x_0 and the Jacobian $|dt/dv|_{v = v_0}$ are functions of the particle energy $\mathcal{E}$. The implicit dependence of the coordinate x_0 on the energy $\mathcal{E}$ is determined by the integral of motion

$$\mathcal{E}(x, x_0) = \mathcal{E}_0 + e[\varphi(x) - \varphi(x_0)], \qquad (14)$$

where $\varphi(x)$ is the electrostatic potential. For longitudinal field component (11), it has the form

$$\varphi(x) = \frac{4\pi e n_0 Z_i l R_0^2}{3\sqrt{R_0^2 - l^2}} \arctan\left(\frac{\sqrt{R_0^2 - l^2}}{x}\right), \qquad (15)$$

where x is the current particle coordinate. In the problem as formulated, we have $\mathcal{E}_0 = 0$ and $x = \infty$. The Jacobian $|dt/dv|_{v = v_0}$ is equal to the reciprocal of the particle acceleration at the initial time, i.e., to $1/|eE(x_0)|$, where the dependence $E(x)$ is given by formula (11). On the other hand, the function $1/|eE(x_0)|$ is equal to $|dx_0/d\mathcal{E}|$. Hence, we arrive at the following expression for the particle energy spectrum:

$$N(\mathcal{E})d\mathcal{E} = \frac{n_0(x_0)}{|d\mathcal{E}/dx_0|}\bigg|_{x_0 = x_0(\mathcal{E})} d\mathcal{E}. \qquad (16)$$

Note that this expression for the energy spectrum follows from the general continuity condition for the particle flux in phase space.

Expression (11) implies that, in the axial region near the target, the electric field is locally uniform: $E_x(l) = E_0 = 8\pi e n_0 Z_i l/3$; consequently, the energy spectrum is determined by the form of the dependence $n_0[\varphi^{-1}(\mathcal{E}/e)]$.

We can see that a unified approach to producing ion beams with a small energy width is based on the acceleration of an initially thin proton (ion) layer with a sufficiently small thickness Δx_0, in which case the energy spread of the proton beam is proportional to the layer
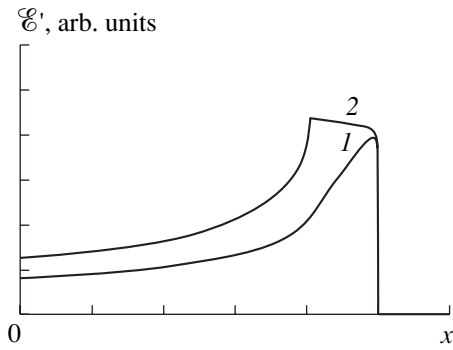
$\mathcal{E}'$, arb. units

Fig. 3. Profiles of the energy losses for proton beams with the energy spectra described by formula (20) (curve *1*) and by formula (21) (curve *2*).

thickness Δx_0 and the characteristic acceleration time is

$$t_{\text{acc}} = \sqrt{2R_0 m_p/eE_0} \approx \omega_{pp}^{-1}\sqrt{2R_0/l}.$$

The longitudinal beam emittance $\varepsilon_\parallel$ is defined as the product of the energy width $\Delta\mathcal{E}$ and the beam duration Δt. Using the above formulas, we find

$$\varepsilon_\parallel = \Delta\mathcal{E}\Delta t \approx \left(\frac{\Delta x_0}{R_0}\right)^2 \sqrt{\frac{m_p\mathcal{E}R_0^2}{2}}. \quad (17)$$

For $\Delta\mathcal{E} = 100$ MeV, $\Delta x_0 = 0.1$ μm, and $R_0 = 1$ μm, the longitudinal emittance is equal to $\varepsilon_\parallel = 2 \times 10^{-2}$ MeV ps, which is 50 times smaller than the longitudinal emittance of protons observed in experiments with non-optimized targets [34].

According to expression (9), the radial electric-field component in the axial region near the target is equal to $E_\rho \approx [8\pi e n_0 Z_i l^2/(3R_0^2)]\rho$; i.e., it is a linear function of the radius. This indicates that the trajectories of the fast particles are described by the formula

$$\rho = \rho_0 \exp(\sqrt{k}x), \quad (18)$$

where ρ_0 is the initial radial coordinate of a particle and $k = 2l/R_0^2$. As a result, the transverse emittance of the fast proton beam associated with the transverse nonuniformity of the electric field at the boundary of the acceleration region (at $x = R_0$) is equal to $\varepsilon_\perp = \pi d_0 \theta$ or

$$\varepsilon_\perp = \pi\sqrt{2}l\frac{d_0}{R_0}, \quad (19)$$

where d_0 is the transverse dimension of the proton layer and the divergence angle of the beam at $kR_0 \ll 1$ is approximately equal to $\theta \approx 2l/R_0$. Thus, for $l \approx d_0 \approx 1$ μm and $R_0 \approx 5$ μm, the transverse emittance of the beam is about $\varepsilon_\perp \approx 1$ mm mrad, which is about ten times smaller than that observed experimentally in [3]. Note

that the transverse emittance calculated in [35] for electrons accelerated in the wake of a laser pulse can be even smaller.

Energy localization requires that the denominator on the right-hand side of expression (15) be equal to zero at a certain energy $\mathcal{E} = \mathcal{E}_*$, in which case the Jacobian $|d\mathcal{E}/dx_0|$ vanishes. In turn, this indicates that, at the initial instant, the accelerated proton layer is localized near the point at which the electric field is zero (see [15]). Relationship (16) can be regarded as an equation for the function $n_0(x_0)$, provided that both the energy spectrum and the electric field are specified. Approximating the coordinate dependence of the electric field by the linear function $E(x) = hx$ and the proton density in a thin layer by the function $n(x) = n_0\theta(L - |x_0|)\theta(x_0)(1 - x_0^2/L^2)$, we obtain the following energy spectrum of fast protons:

$$N(\mathcal{E})d\mathcal{E}$$
$$= \frac{n_0\theta(\mathcal{E}_{\max} - \mathcal{E})\theta(\mathcal{E} - \mathcal{E}_{\min})(\mathcal{E} - \mathcal{E}_{\min})}{\sqrt{2eh}\Delta\mathcal{E}\sqrt{\mathcal{E}_{\max} - \mathcal{E}}}d\mathcal{E}; \quad (20)$$

where the maximum and minimum proton energies are equal to $\mathcal{E}_{\max} = ehR_0^2/2$ and $\mathcal{E}_{\min} = eh(R_0^2 - L^2)/2$; i.e., the width of the energy spectrum is $\Delta\mathcal{E} = ehL^2/2$. For a rectangular distribution of the proton density, $n(x) = n_0\theta(L - x_0)\theta(x_0)$, we obtain a spectrum of the form

$$N(\mathcal{E})d\mathcal{E} = \frac{n_0\theta(\mathcal{E}_{\max} - \mathcal{E})\theta(\mathcal{E} - \mathcal{E}_{\min})}{\sqrt{2eh(\mathcal{E}_{\max} - \mathcal{E})}}d\mathcal{E}. \quad (21)$$

Figure 3 shows the energy deposition profiles for proton beams with energy spectra given by formulas (20) (curve *1*) and (21) (curve *2*). We can see that these spectra ensure a maximum energy deposition in a region with dimensions that depend on the maximum and minimum proton energies.

4. RESULTS OF COMPUTER SIMULATIONS OF THE GENERATION OF HIGH-QUALITY PROTON BEAMS

The above discussion of the methods for producing proton beams with a small energy spread was based on a simple theoretical model. In order to take into account the numerous nonlinear and kinetic processes that occur in the interaction of high-power laser radiation with a target, as well as to generalize our analysis to two and three dimensions, we numerically modeled the acceleration of protons in a two-layer target irradiated by an ultrashort laser pulse. Below, we will present the results of the two- and three-dimensional simulations that were carried out with the REMP (Relativistic Electro-Magnetic Particle-mesh) code, which is based on the PIC method [11]. In this three-dimensional relati-

vistic electromagnetic code, the electric current density is calculated by means of a new algorithm [36], which can operate with quasi-particles of arbitrary shape and ensures that the local electric charge is exactly conserved. Here, we report the results obtained in simulations for quasi-particles with a bell-shaped form-factor (a second-order spline). This makes it possible to substantially reduce the numerical effect of the plasma heating as well as other nonphysical effects peculiar to the PIC method.

4.1. Results of Two-Dimensional Simulations of the Interaction of a Laser Pulse with a Two-Layer Target

In two-dimensional simulations, the computation region was chosen to be $30\lambda \times 20\lambda$ with cells of size $0.03\lambda \times 0.03\lambda$. The total number of particles in the simulations was approximately 10^6. The conditions at the boundaries of the computation region corresponded to the complete absorption of both the field and the particles. The calculations were carried out on personal computers.

In the numerical model, the plasma consists of particles of three species: "electrons," "protons," and "heavy ions," with different absolute values of the electric charge. The proton-to-electron mass ratio is $m_p/m_e = 1836$, and the ratio of the mass of an electron to that of a heavy ion is $m_i/m_e = 10 \times 1836$.

The target is assumed to be located near the $x = 5\lambda$ plane. The electron density inside the layer of heavy ions corresponds to the value $\omega_{pe}/\omega = 3$ of the ratio of the plasma frequency to the laser frequency. The second (thin and narrow) proton layer (or a layer of hydrogen contained in a plastic film) is on the rear side of the target. The electron density inside the proton layer is lower than the critical density ($n_{cr} = m_e\omega^2/4\pi e^2$) and corresponds to the ratio $\omega_{pe}/\omega = 0.7$. The sizes of the first layer are $0.5\lambda \times 10\lambda$, and those of the second (proton) layer are $0.1\lambda \times 5\lambda$. Therefore, the total number of electrons in the first layer is 180 times larger than that in the second layer.

A circularly polarized laser pulse is initiated at the left boundary $x = 0$ of the computation region. The dimensionless pulse amplitude is $a_0 = 20$, which corresponds to an intensity of 8×10^{20} W/cm^2 for laser radiation with a wavelength of 1 μm. The width and length of the laser pulse are 15λ and 20λ, respectively, which corresponds to the petawatt power range. The electric field amplitude inside the pulse is constant and decreases gradually toward the pulse boundaries in a transition layer of thickness 2λ.

The results of these computer simulations are illustrated in Figs. 4–7, in which the length and time units are the laser wavelength and period. Figure 4 displays the energy spectra of protons and heavy ions, and Figs. 5 and 6 depict the distributions of the transverse and longitudinal components of the electric field. Fig-
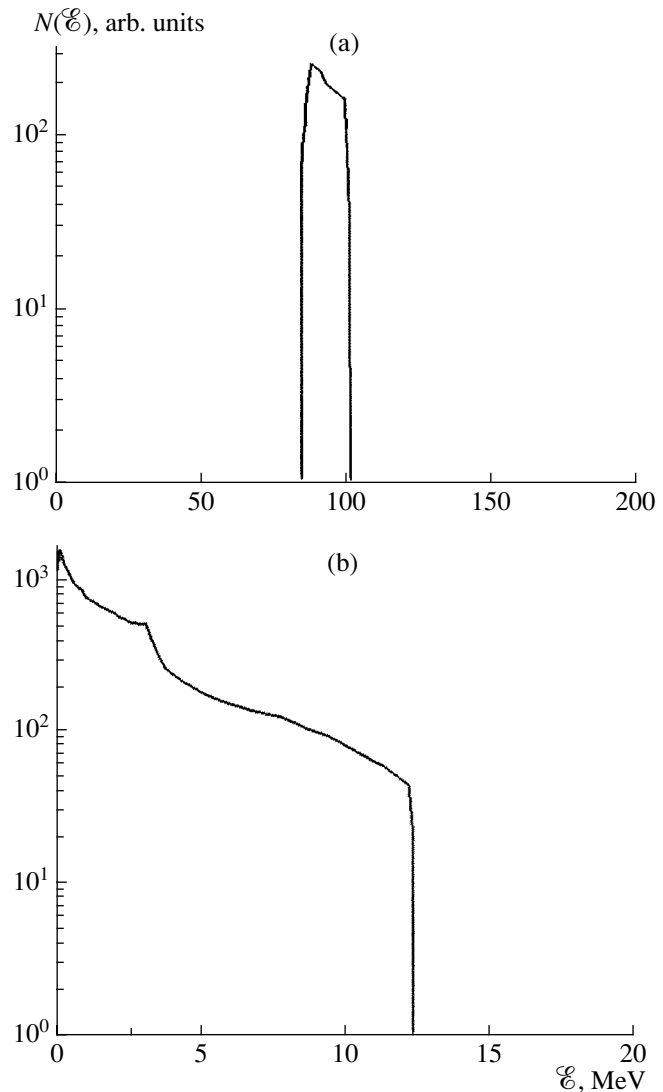

Fig. 4. Two-dimensional simulations: the energy spectra of (a) protons at $t = 45$ and (b) heavy ions at $t = 97.5$.

ure 5 shows the shape toward which the laser pulse evolves in the interaction with the target. In Fig. 6, we see the distribution of the longitudinal quasistatic electrostatic field, which accelerates the ions. The field is localized in a narrow region near the first layer of the target (the layer of heavy ions). It can be seen that the electric field distribution corresponds to that described by formula (11). Figure 7 presents the electric charge density distribution at successive times. The two vertically oriented dark regions correspond to positively charged heavy ions (the left region) and protons (the right region), and the white diffusive cloud corresponds to negatively charged electrons. We can see that the proton layer moves along the x-axis and that the distance between it and the layer of heavy ions increases with time. During Coulomb explosion, the layer of heavy ions expands and acquires a round shape. Note that, for
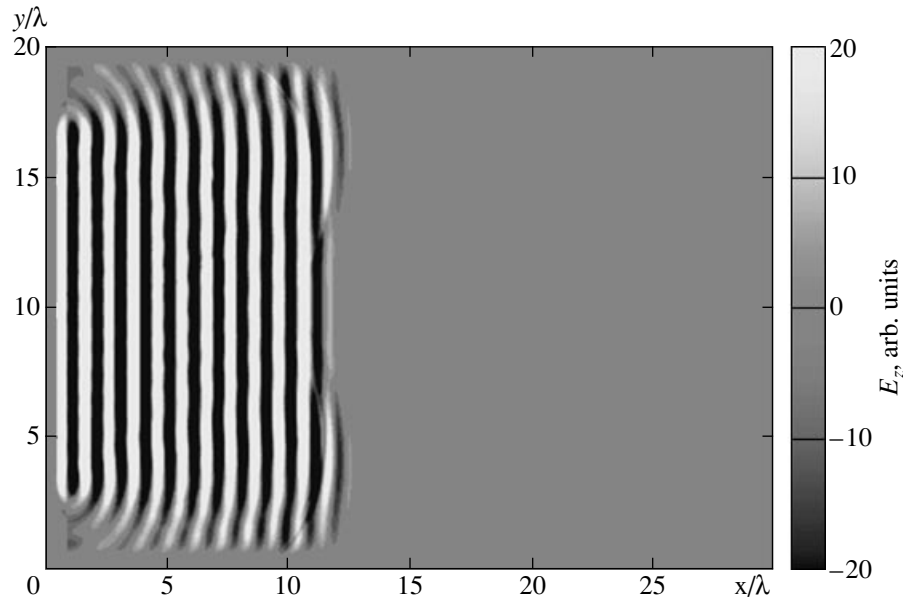
Fig. 5. Two-dimensional simulations: the distribution of the transverse electric-field component E_z in the (x, y) plane at time $t = 12$. The right vertical scale represents the electric field strength.
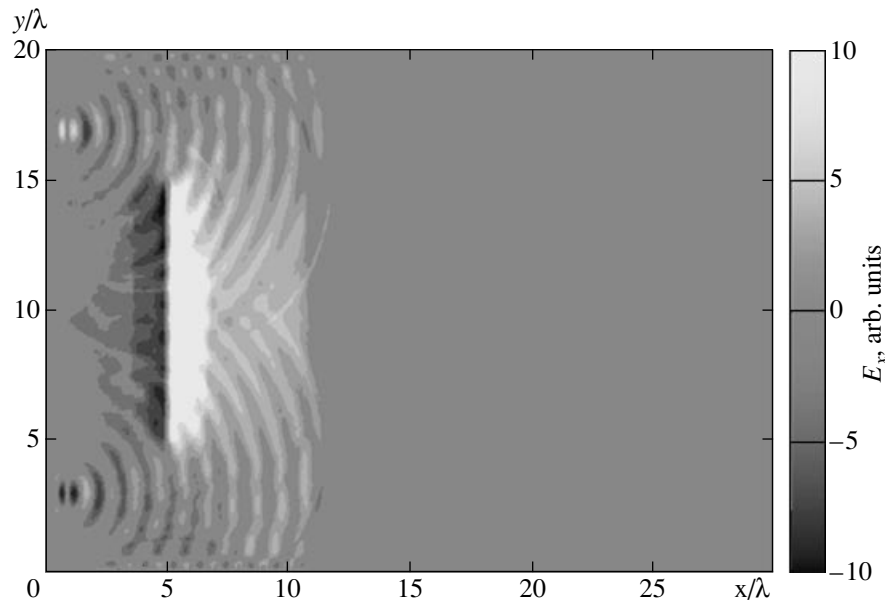

Fig. 6. Two-dimensional simulations: the distribution of the longitudinal electric-field component E_x in the (x, y) plane at time $t = 12$. The right vertical scale represents the electric field strength.

the pulse and target parameters chosen for the calculation version described here, not all the electrons are expelled from the laser-irradiated target. However, although only a fraction of the electrons are accelerated by the laser pulse and escape from the target, the resulting quasistatic electric field is sufficiently strong and the region where the field is localized is sufficiently long for the protons to be accelerated to an energy of 100 MeV. While the maximum energy of the heavy ions is of the same magnitude as the proton energy, their average energy per nucleon is ten times lower. Consequently, the heavy ion component can be removed (if
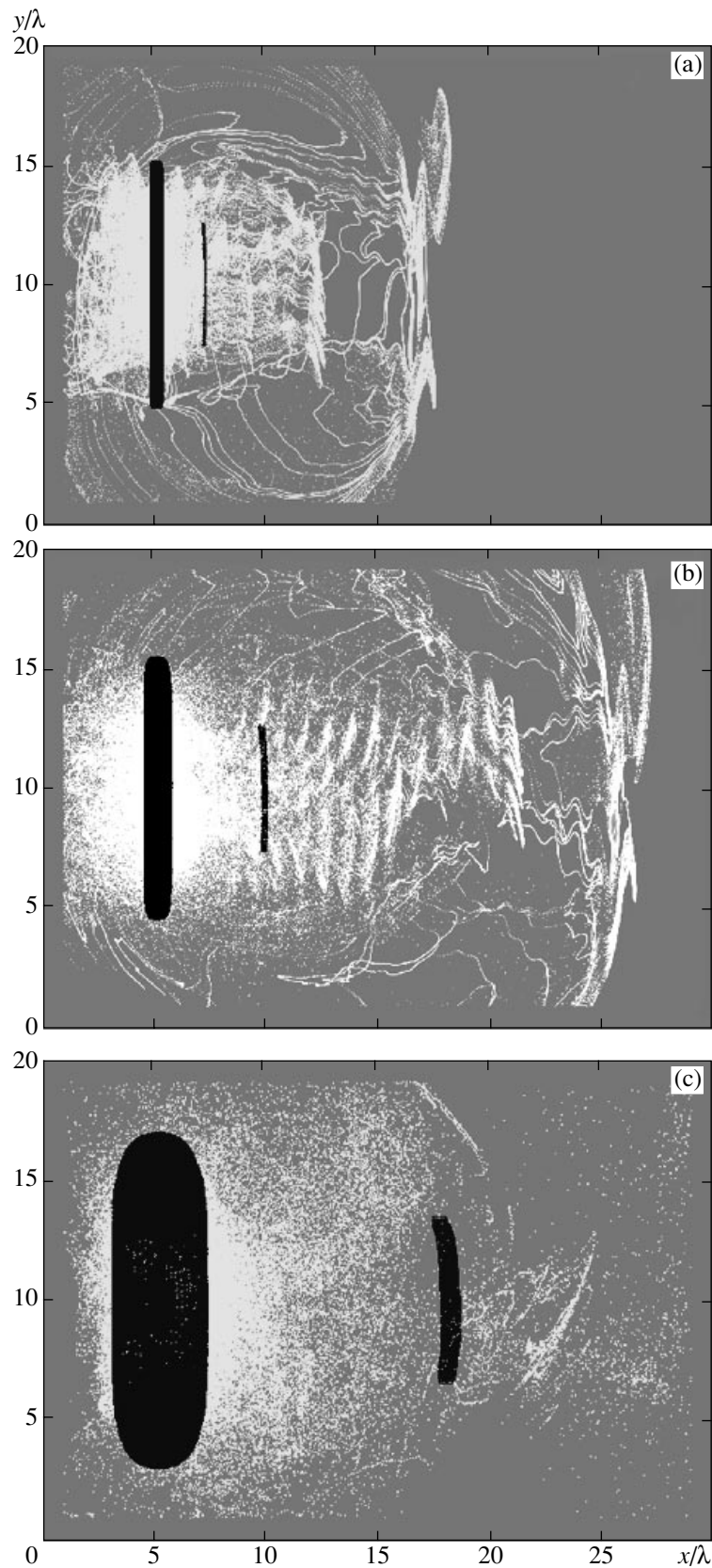
Fig. 7. Two-dimensional simulations: the distribution of the electric charge density in the (x, y) plane at the times $t =$ (a) 18, (b) 27, and (c) 51. The dark regions correspond to a positive electric charge (the layer of heavy ions is on the left, and an initially thin proton layer is on the right), and the white region corresponds to a cloud of negatively charged electrons.

necessary) by an absorber. According to Fig. 4, the energy spectrum of heavy ions is broad, while the energy spectrum of the accelerated protons is quasi-monoenergetic. We emphasize that the energy spectra in Fig. 4 are plotted on a logarithmic scale; the relative energy width $\Delta \mathcal{E}/\mathcal{E}$ of the proton energy spectrum is approximately equal to $\Delta \mathcal{E}/\mathcal{E} = 0.03$. The proton beam that forms in the course of acceleration remains well localized in both coordinate and energy spaces for a long time. The high spatial localization of the proton beam results from the above-mentioned property of the electric field that decreases linearly in space, specifically, its ability to accelerate charged particles and, at the same time, to bunch them.

4.2. Three-Dimensional Simulations Of Ion Acceleration in the Interaction of a Laser Pulse with a Two-Layer Target

In the three-dimensional simulations, the computation region was chosen to be $80\lambda \times 32\lambda \times 32\lambda$ and the spatial mesh consisted of $2560 \times 1024 \times 1024$ cells. The total number of particles in different simulation versions was varied from 62×10^6 to 820×10^6. The conditions at the longitudinal (along the *x*-axis) boundaries of the computation region corresponded to complete absorption of both the field and the particles, and the conditions at the transverse boundaries (in the *y* and *z* directions) were periodic. (Note that the waves that arose in simulations because of the periodic boundary conditions had a relatively small amplitude and thus did not significantly affect the final results.) The calculations were carried out on 64 processors of an NEC SX-5 parallel supercomputer at Osaka University (Japan).

Below, we report the results of the three-dimensional simulations of a linearly polarized (in the *z* direction) laser pulse with the maximum dimensionless amplitude $a_0 = 30$, which corresponds to a laser intensity of 10^{21} W/cm². The laser pulse was assumed to propagate along the *x*-axis and to be trapezoidal in shape: the pulse amplitude increases from zero to its maximum value in the leading edge of length 3λ, is constant over a region of length 2λ, and decreases linearly to zero in the trailing edge of length 10λ. The total diameter of the pulse is 12λ; the pulse amplitude is constant over a region of diameter 10λ and decreases to zero in a layer of thickness 1λ. Such factors as the sharp increase in the radiation intensity at the leading edge of the pulse and the absence of both the prepulse and the pedestal improve the quality of the beam of accelerated particles. The pulse shape used in our simulations models a laser pulse with a steep leading edge and with no prepulse. An analysis of the consequences of the nonlinear effects occurring in the interaction of a relativistically strong laser pulse with a subcritical plasma [10, 37] and with a thin foil [10, 38] showed that these effects can be exploited to form a laser pulse with a steep leading edge (i.e., with no prepulse).

In our model, the target is assumed to consist of two plasma layers such that the density of the heavier layer corresponds to the value $\omega_{pe}/\omega = 3$ of the ratio of the plasma frequency to the laser frequency and the density of the lighter (hydrogen) layer corresponds to the value $\omega_{pe}/\omega = 0.53$. The first (heavier) layer consists of electrons and heavy gold ions (the ratio of masses and charges is $m_i/Z_i m_e = 195.4 \times 1836/2$), and the second (lighter) layer consists of electrons and protons (the mass ratio is $m_p/m_e = 1836$). Initially, the gold foil occupies the region between the $x = 5.5\lambda$ and $x = 6\lambda$ planes. For a laser wavelength of 1 µm, the foil is half a micron thick and has a diameter of 10 µm. The hydrogen layer is farther from the laser; its thickness is 0.03 µm and its diameter is 5 µm. The total number of electrons in the denser plasma layer is approximately 2000 times larger than that in the hydrogen layer.

Note that the above collisionless model for describing a target with a prescribed degree of ionization substantially simplifies the problem. This simplification is brought about by the circumstance that, at present, taking into account collisions and ionization in three-dimensional simulations seems to be problematic for two reasons. First, for petawatt laser pulses, the present-day theory is still incapable of describing these processes adequately. The second reason is associated with the computational requirements. Note also that the way the system under discussion evolves depends on the parameter $\int Z_i e n_0 dx \approx Z_i e n_0 l$, which is the electric charge per unit area of the target surface. This indicates that, in the case of a thinner and/or lower density target, the same regime of ion acceleration can be achieved with a higher degree of ionization.

The results of our three-dimensional computer simulations are illustrated in Figs. 8–12. Figure 8 shows the energy spectra of (a) electrons, (b) protons, and (c) heavy ions at the time $t = 80$. One can see that the protons have been accelerated to an energy of about 63 MeV. The relative width of the proton energy spectrum is 5%. The energy spectrum of heavy ions is broad, the maximum energy being 37 MeV. However, the energy per nucleon is about 0.2 MeV.

Figure 9 shows how the electric field is distributed over the computation region, giving information about (a) the shape of the electromagnetic pulse that has passed through the target and (b) the structure of the accelerating electric field. In Fig. 9, we present half of the computation region and show the electric field structure in its central cross section. The longitudinal (in the *x* direction) electric-field component, which accelerates the ions, is localized near the heavier layer of the target. Recall that this field configuration can be approximated by the electrostatic field created by a charged disk. Note also that the transverse electric-field distribution (which is not presented in the figures) clearly shows the enhancement of this field component at the disk periphery.
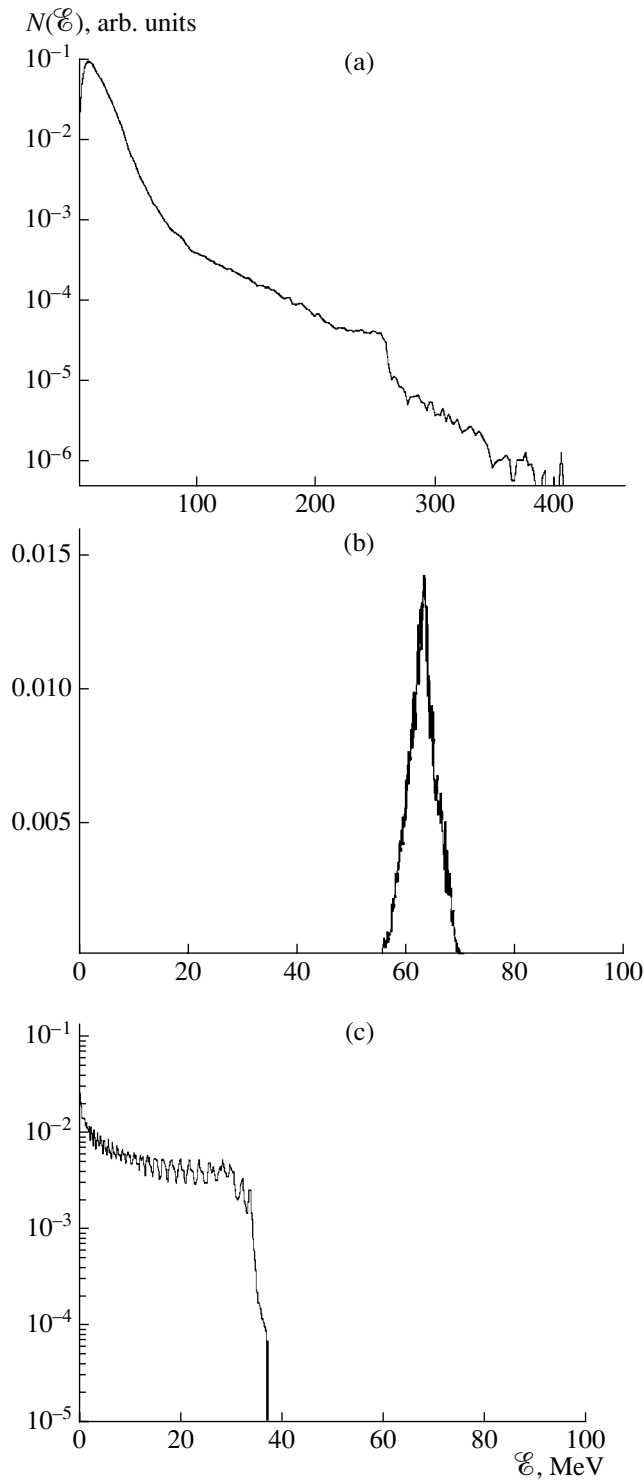
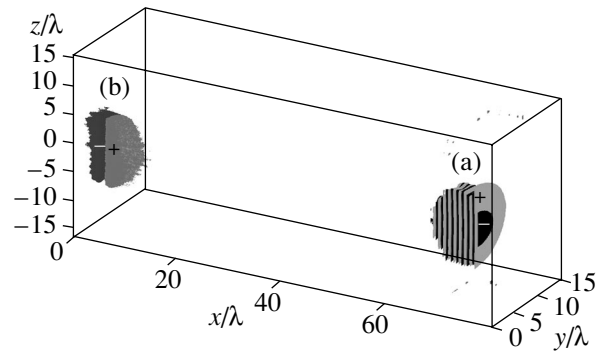$N(\mathcal{E})$, arb. units

(a)

Fig. 9. Three-dimensional simulations: the electric field distributions in a laser pulse and near the target at time $t = 80$, represented by the isosurfaces of (a) the transverse electric-field component $E_z = \pm 10$ and (b) the longitudinal electric-field component $E_x = \pm 1.5$.

three-dimensional situation, the proton beam is accelerated predominantly in the x direction, as is the case with the acceleration of protons and heavy ions in two-dimensional geometry. The layer of heavy ions expands as a result of Coulomb explosion. During the expansion, the ions can be accelerated to energies corresponding to the electrostatic potential at the initial instant. If the electric charge of the proton layer remains unneutralized, then the protons may also be subject to Coulomb explosion, in which case they acquire an additional kinetic energy due to Coulomb repulsion. However, if the total number of protons is relatively small and their density is low, this additional acceleration can be neglected.

A number of electrons move in phase with the electromagnetic wave and are accelerated by it for a long time. This group, composed of the fastest electrons, is distinctly observed in Fig. 11, which shows the phase plane of the electron plasma component. We can see that, in the wake of the laser pulse, there is a long tail of "hot" electrons with energies that are, however, lower than the electron energy within the laser pulse. In the vicinity of the target, the electrons have an isotropic distribution with a maximum energy higher than the energy of the hot electrons in the intermediate region.

Figure 12 shows the angular distribution of the energy of (a) electrons, (b) protons, and (c) heavy ions at the time $t = 80$. The angular distribution of the electrons reflects the presence of an electron beam moving behind the laser pulse in the pulse propagation direction and of an isotropic electron component. The proton layer moves in the propagation direction of the pulse, while heavy ions move not only in the direction of the pulse but also in the opposite direction, as is characteristic of the Coulomb explosion.

As was already noted, the generation of light ion beams with a small energy width requires that the layer of light ions at the target surface should be not only
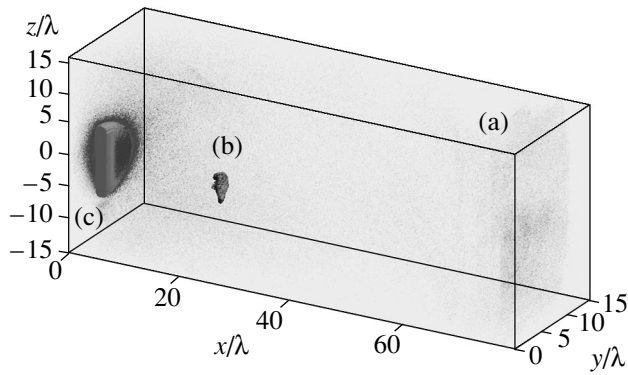
Fig. 8. Three-dimensional simulations: the energy spectra of (a) electrons, (b) protons, and (c) heavy ions at time $t = 80$.

Figure 10 displays the electric charge distribution over the computation region. Also, in this figure, we present half of the computation region and show the charge distribution in its central cross section. In this

Fig. 10. Three-dimensional simulations: the electric charge distribution over the computation region at time $t = 80$, represented by (a) the electron density distribution (obtained with the ray tracing method) and by the isosurfaces of (b) the proton density and (c) the density of heavy ions.

In order to confirm this conclusion, Figs. 13–15 illustrate the results of computer simulations of the interaction of a laser pulse with a two-layer target that is infinite in the transverse direction. In these simulations, the transverse dimensions of the layer of light atoms coincided with those of the layer of heavy atoms, the remaining parameters being the same as in the previous case.

From Fig. 13, which shows the densities of electrons, protons, and heavy ions at the time $t = 80$, we can see that the laser pulse predominantly accelerates the protons that initially occupy the axial region. The fact that the acceleration of the entire proton layer is relatively less efficient is associated with the periodicity of the boundary conditions in the transverse direction. A part of the proton layer in the axial region acquires the characteristic shape of a plug. The transverse size of the acceleration region is seen to be equal to that of the focal spot of the laser pulse.

thin, but also narrow in the transverse direction; otherwise, the light ion beam will have a broad quasi-thermal energy spectrum because of the dependence of the accelerating electric field on the transverse coordinate.

As was expected, the spatially averaged particle spectrum in this case is far from being monoenergetic (Fig. 14). The proton energy spectrum is quasi-thermal up to an energy of 25 MeV and has a nonuniform pedestal, which terminates at an energy of 47 MeV. In other
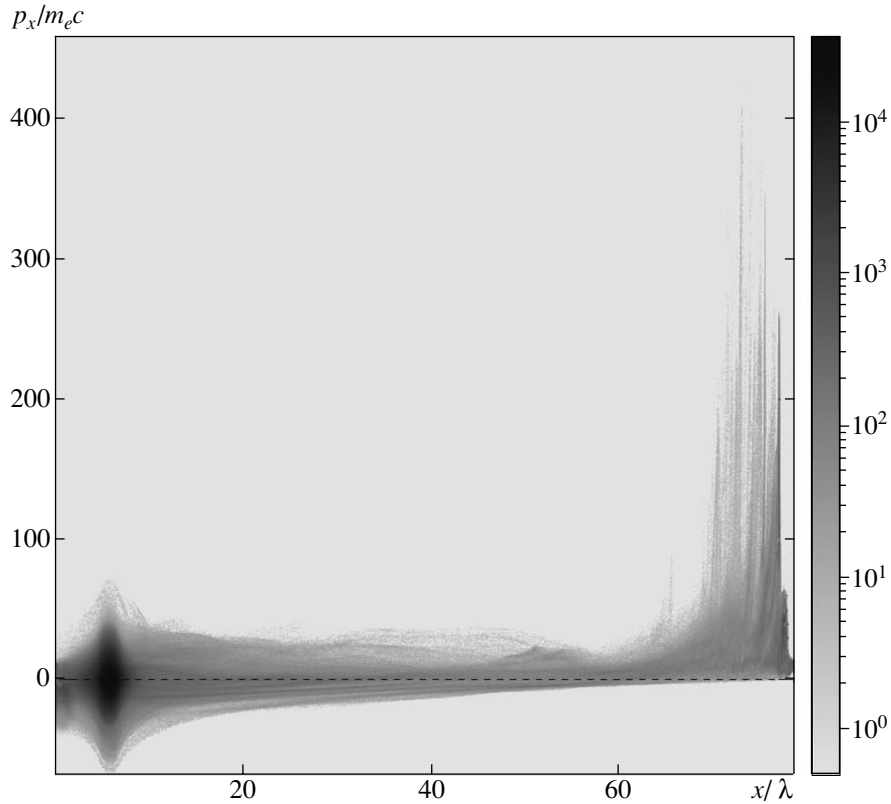

Fig. 11. Three-dimensional simulations: the projection of the electron phase space onto the (x, p_x) plane. The shades of grey reflects the number of quasi-particles in the corresponding cell of the projection.
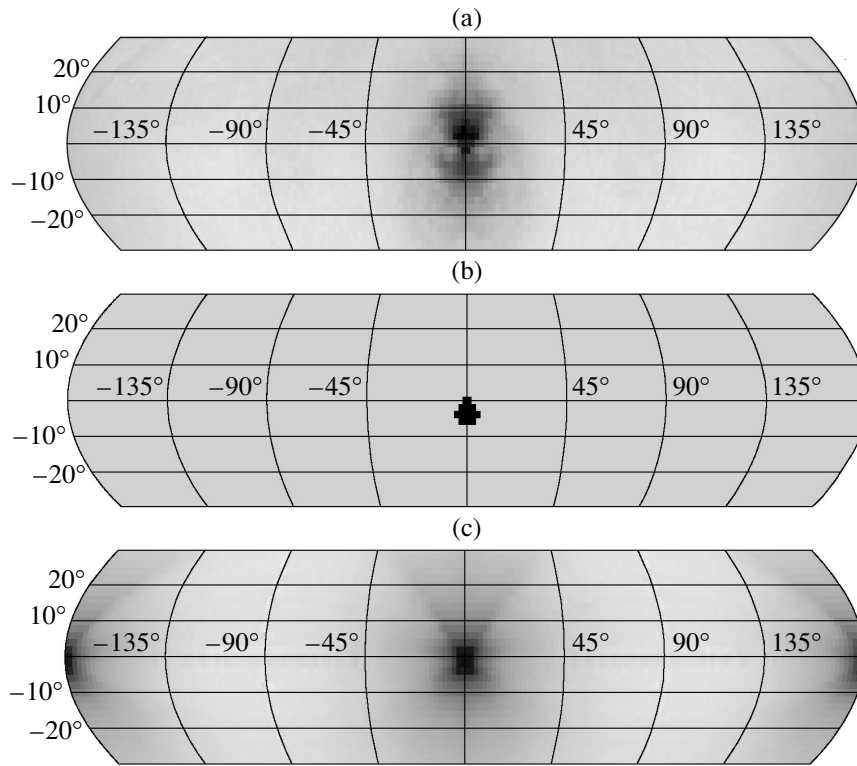
Fig. 12. Three-dimensional simulations: the angular distributions of the energy of (a) electrons, (b) protons, and (c) heavy ions at time $t = 80$. The point $(0°, 0°)$ corresponds to the propagation direction of the laser pulse, and the point $(0°, 90°)$ corresponds to the direction of the z-axis.

words, the width of the energy spectrum is comparable with the maximum proton energy.

Figure 15 shows the angular distributions of charged particles. The angular distribution of electrons (Fig. 15a) is the superposition of an isotropic distribution and a distribution corresponding to a group of electrons moving in the longitudinal direction. The angular distribution of protons is narrow, indicating that they
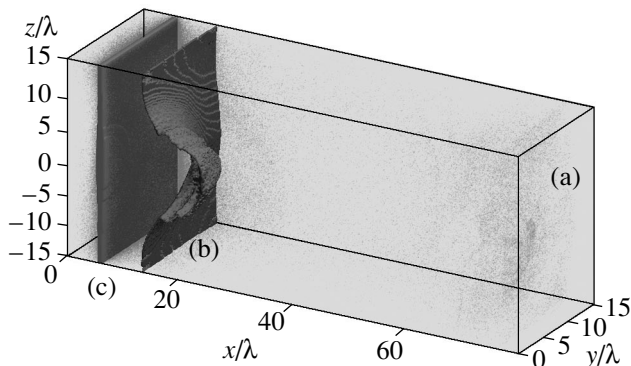

Fig. 13. Three-dimensional simulations of a target that is infinite in the transverse direction: the electric charge distribution over the computation region at time $t = 80$, represented by (a) the electron density distribution (obtained with the ray tracing method) and by the isosurfaces of (b) the proton density and (c) the density of heavy ions.
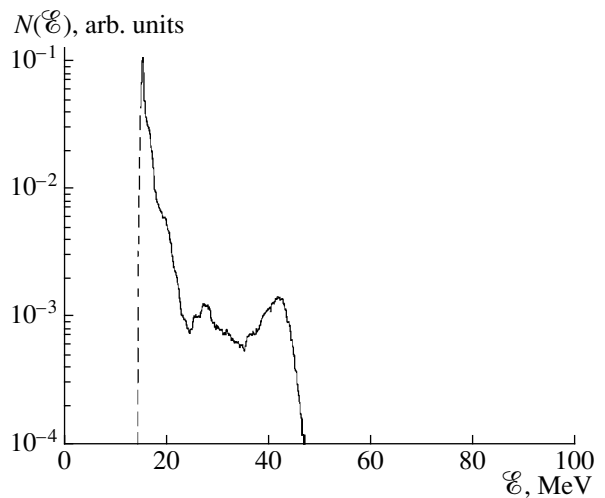

Fig. 14. Three-dimensional simulations: the energy spectrum of protons of a target that is infinite in the transverse direction.
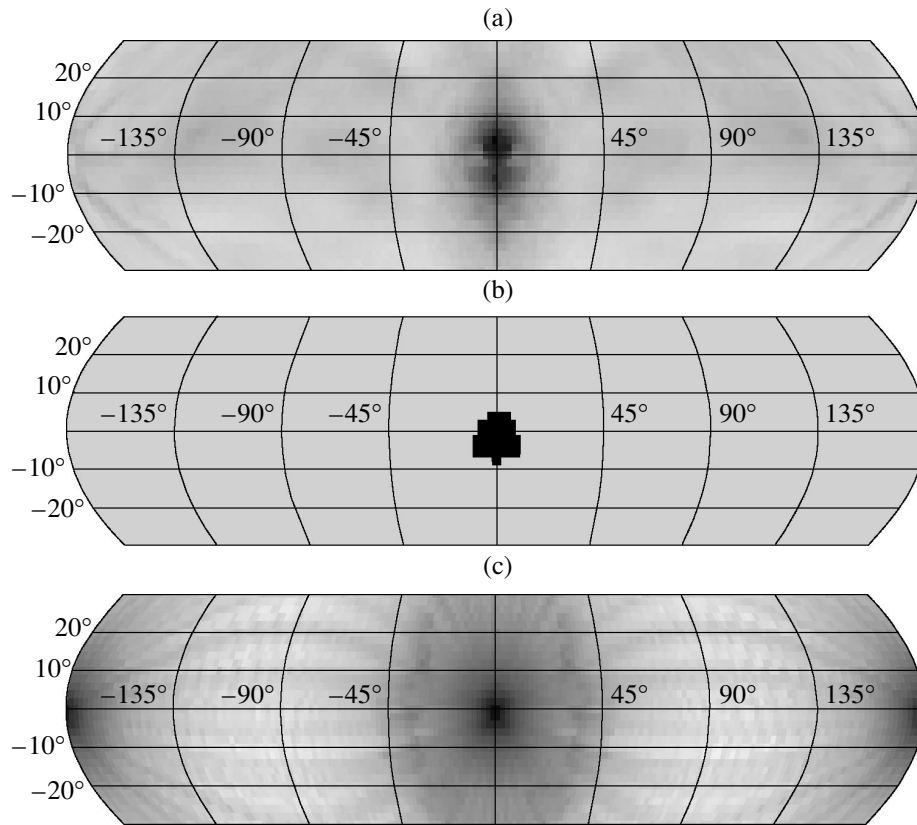
(a)

(b)

(c)

Fig. 15. Three-dimensional simulations of a target that is infinite in the transverse direction: the angular distributions of the energy of (a) electrons, (b) protons, and (c) heavy ions at time $t = 80$. The point $(0°, 0°)$ corresponds to the propagation direction of the laser pulse, and the point $(0°, 90°)$ corresponds to the direction of the z-axis.

are accelerated predominantly in the forward direction (Fig. 15b). The angular distribution of heavy ions (Fig. 15c) has a pronounced ring structure, which is associated with the divergence of an ion beam (the divergence angle being about 40°). Similar ring structures were observed experimentally in [3].

5. CONCLUSION

We have thoroughly investigated the interaction of an ultrashort, relativistically strong laser pulse with a two-layer target. Our two- and three-dimensional computer simulations have demonstrated the generation of a high-quality proton beam in this interaction process. Thus, we have fully confirmed the advantages of a two-layer target that were predicted by the qualitative model formulated in [16]. The parameters of a proton beam can be controlled by changing the target parameters, which is of considerable interest for a number of applications, e.g., in developing injectors for charged particle accelerators, in inertial confinement fusion (an approach based on the concept of the fast ignition of a thermonuclear target by laser-accelerated protons), and in hadron therapy in oncology.

In the scheme in which the proton layer of a two-layer target is accelerated by the electric field near the target, the width of the peak in the energy spectrum of a proton beam is equal to $\Delta \mathcal{E} = 2\pi n_0 Z_i e^2 l \Delta x_0$; hence, the relative energy width (which is the reciprocal of the beam "quality") is $\Delta \mathcal{E}/\mathcal{E}_{max} = \Delta x_0 / R_0$. Thus, for a proton layer with a thickness of 2×10^{-6} cm and for an acceleration region with a length of 2×10^{-4} cm, we have $\Delta \mathcal{E}/\mathcal{E}_{max} = 0.01$ with $\mathcal{E}_{max} = 200$ MeV. For a target with a thickness of 1 μm, a proton layer with a radius of 1 μm, and a laser beam with a radius of $R_\perp \approx 10$ μm, we obtain that the transverse emittance characterizing the angular spread of a proton beam is about $\varepsilon_\perp \approx 1$ mm mrad. In the acceleration scheme proposed here, the longitudinal emittance ($\Delta \mathcal{E}\Delta t$), which characterizes the longitudinal dimension of a proton beam, is about 10^{-2} MeV ps. These values of the transverse and longitudinal emittance are comparable with those for beams accelerated in standard charged particle accelerators and are much lower than the values recorded in the interaction of laser radiation with non-optimized targets. Our computer simulations have demonstrated the possibility of generating proton beams with a relative energy width on the order of several percent and with a transverse dimen-

sion of several microns, localized in a cone with an angular radius of several degrees.

That the proton layer should be narrow in the transverse direction has been demonstrated by an example a two-layer target with layers of the same width. It has been shown that the width of the energy spectrum of a proton beam generated in the interaction of a laser pulse with such a target is comparable to the maximum proton energy.

APPENDIX

To simplify matters, we assume that the electric field is nonzero in a region of radius R_0, has the strength E_0 at the target surface, and vanishes at the distance R_0 from the surface. We approximate the electric field with the expression

$$E(x) = E_0(1 - x/R_0); \qquad (A.1)$$

where the x-axis points in the propagation direction of the laser pulse and R_0 is the inhomogeneity scale of the electric field ($R_0 = 2R_\perp$).

The distribution function $f(x, v, t)$ of fast protons satisfies the kinetic equation

$$\frac{\partial f}{\partial t} + v\frac{\partial f}{\partial x} + \frac{eE(x)}{m_p}\frac{\partial f}{\partial v} = 0. \qquad (A.2)$$

It is well known that the solutions to kinetic equation (A.2) have the form $f(x, v, t) = f_0(x_0, v_0)$ where $f_0(x_0, v_0)$ is the proton distribution function at the initial time $t = 0$; i.e., the function $f(x, v, t)$ is constant along the characteristics of Eq. (A.2). These characteristics, which relate the initial coordinate and velocity (x_0, v_0) of a particle to its current coordinate and velocity (x, v) at time t, are described by the expressions

$$x = R_0 - (R_0 - x_0)\cos(\Omega_b t) + \frac{v_0}{\Omega_b}\sin(\Omega_b t), \quad (A.3)$$

$$v = v_0\cos(\Omega_b t) + (R_0 - x_0)\sin(\Omega_b t), \qquad (A.4)$$

where $\Omega_b = \sqrt{eE_0/m_p R_0}$ and it is assumed that $x \le R_0$. Expressions (A.3) and (A.4) imply that all particles with zero initial velocities ($v_0 = 0$) pass through the boundary $x = R_0$ of the acceleration region simultaneously at the time $t_b = \pi/2\Omega_b$, regardless of their initial positions. Consequently, electric field (A.1) ensures

both the acceleration of the particles and their bunching in space.

The number of particles per unit volume $dxdv$ of phase space is equal to $dn = fdxdv = fvdvdt = fd\mathscr{E}dt/m_p$. We assume that, at the initial time $t = 0$, all particles are at rest and their spatial density distribution is described by the function $n_0(x_0)$. These initial conditions are satisfied by the distribution function of the form $f_0(x_0, v_0) = n_0(x_0)\delta(v_0)$, where $\delta(v_0)$ is the Dirac delta function. In the context of the applications discussed above, we are interested exclusively in the time integral of the particle energy distribution function. Integrating the expression for $fvdvdt$ over time yields the following energy spectrum of the accelerated particles:

$$\begin{aligned} N(\mathscr{E})d\mathscr{E} &= d\mathscr{E}\int n_0(x_0)\delta(v_0)\frac{dt}{m_p} \\ &= \frac{n_0(x_0)}{m_p}\left|\frac{dt}{dv_0}\right|d\mathscr{E}. \end{aligned} \qquad (A.5)$$

Here, the dependence of the coordinate x_0 and the Jacobian $|dt/dv_0|$ on energy $\mathscr{E}$ should be determined from relationships (A.3) and (A.4) under the condition that the particle reaches the boundary R_0 of the acceleration region. The dependence the coordinate x_0 on energy $\mathscr{E}$ can be obtained by inverting the relationship $\mathscr{E} = m_p[(R_0 - x_0)\Omega_b]^2/2$:

$$x_0 = R_0 - \frac{1}{\Omega_b}\sqrt{\frac{2\mathscr{E}}{m_p}}. \qquad (A.6)$$

In turn, the Jacobian can be deduced from relationships (A.3) and (A.4) under the condition $v_0 = 0$:

$$\left|\frac{dt}{dv_0}\right| = \frac{1}{\left|\Omega_b\sqrt{2\mathscr{E}m_p}\right|}. \qquad (A.7)$$

We thus arrive at the following expression for the energy spectrum of the accelerated particles:

$$N(\mathscr{E})d\mathscr{E} = \frac{n_0(R_0 - \sqrt{2\mathscr{E}/m_p\Omega_b^2})}{\left|\Omega_b\sqrt{2\mathscr{E}m_p}\right|}d\mathscr{E}. \qquad (A.8)$$

Hence, the maximum ($\mathscr{E}_{max}$) and minimum ($\mathscr{E}_{min}$) energies of the accelerated particles are determined by the dimensions of the region in which the particles were initially localized, or, equivalently, by the form of the function $n_0(x_0)$.

REFERENCES

1. M. Perry and G. Mourou, Science **64**, 917 (1994); G. Mourou, C. Barty, and M. Perry, Phys. Today **51**, 22 (1998); G. Mourou, Z. Chang, A. Maksimchuk, *et al.*, Fiz. Plazmy **28**, 14 (2002) [Plasma Phys. Rep. **28**, 12 (2002)].

2. T. Tajima and J. M. Dawson, Phys. Rev. Lett. **43**, 267 (1979); E. Esarey, P. Sprangle, J. Krall, and A. Ting,

IEEE Trans. Plasma Sci. **24**, 252 (1996); S. V. Bulanov, T. Zh. Esirkepov, N. M. Naumova, *et al.*, IEEE Trans. Plasma Sci. **24**, 393 (1996); C. E. Clayton, K. A. Marsh, A. Dyson, *et al.*, Phys. Rev. Lett. **70**, 37 (1993); K. Nakajima, D. Fisher, T. Kawakubo, *et al.*, Phys. Rev. Lett. **74**, 4428 (1995); A. Modena, Z. Najimudin, A. E. Dangor, *et al.*, Nature (London) **337**, 606 (1995); D. Umstadter, S.-Y. Chen, A. Maksimchuk, *et al.*, Science **273**, 472 (1996); R. Wagner, S.-Y. Chen, A. Maksimchuk, and D. Umstadter, Phys. Rev. Lett. **78**, 3125 (1997); D. Gordon, K. C. Tzeng, C. E. Clayton, *et al.*, Phys. Rev. Lett. **80**, 2133 (1998); S.-Y. Chen, M. Krishnan, A. Maksimchuk, and D. Umstadter, Phys. Plasmas **6**, 4739 (1999); C. Chiu, S. Cheshkov, and T. Tajima, Phys. Rev. ST Accel. Beams **3**, 101301 (2000); H. Kotaki, M. Kando, T. Oketa, *et al.*, Phys. Plasmas **9**, 1392 (2002).

3. A. Maksimchuk, S. Gu, K. Flippo, *et al.*, Phys. Rev. Lett. **84**, 4108 (2000); E. L. Clark, K. Krushelnick, M. Zepf, *et al.*, Phys. Rev. Lett. **85**, 1654 (2000); R. A. Snavely, M. H. Key, S. P. Hatchett, *et al.*, Phys. Rev. Lett. **85**, 2945 (2000); A. J. MacKinnon, M. Borghesi, S. Hatchett, *et al.*, Phys. Rev. Lett. **86**, 1769 (2001); Y. Murakami, Y. Kitagawa, Y. Sentoku, *et al.*, Phys. Plasmas **8**, 4138 (2001); A. J. MacKinnon, Y. Sentoku, P. K. Patel, *et al.*, Phys. Rev. Lett. **88**, 215006 (2002).

4. T. Zh. Esirkepov, Y. Sentoku, K. Mima, *et al.*, Pis'ma Zh. Éksp. Teor. Fiz. **70**, 80 (1999) [JETP Lett. **70**, 82 (1999)].

5. A. G. Zhidkov, A. Sasaki, T. Tajima, *et al.*, Phys. Rev. E **60**, 3273 (1999); M. Yamagiwa, J. Koga, *et al.*, Phys. Rev. E **60**, 5987 (1999); Y. Ueshima, Y. Sentoku, and Y. Kishimoto, Nucl. Instrum. Methods Phys. Res., Sect. A **455**, 181 (2000); A. Pukhov, Phys. Rev. Lett. **86**, 3562 (2001); A. V. Kuznetsov, T. Zh. Esirkepov, F. F. Kamenets, and S. V. Bulanov, Fiz. Plazmy **27**, 225 (2001) [Plasma Phys. Rep. **27**, 211 (2001)]; Y. Sentoku, U. Yu. Bychenkov, K. Flippo, *et al.*, Appl. Phys. B **74**, 207 (2002).

6. S. V. Bulanov, N. M. Naumova, T. Zh. Esirkepov, *et al.*, Pis'ma Zh. Éksp. Teor. Fiz. **71**, 593 (2000) [JETP Lett. **71**, 407 (2000)]; Y. Sentoku, T. V. Lisseikina, T. Zh. Esirkepov, *et al.*, Phys. Rev. E **62**, 7271 (2000); S. Wilks, A. B. Langdon, T. E. Cowan, *et al.*, Phys. Plasmas **8**, 542 (2001); H. Ruhl, S. V. Bulanov, T. E. Cowan, *et al.*, Fiz. Plazmy **27**, 387 (2001) [Plasma Phys. Rep. **27**, 363 (2001)].

7. P. A. Norreys, A. P. Fews, F. N. Beg, *et al.*, Plasma Phys. Controlled Fusion **40**, 175 (1998); G. Pretzler, A. Saemann, A. Pukhov, *et al.*, Phys. Rev. E **58**, 1165 (1998); L. Disdier, J. P. Garconnet, G. Malka, and J. L. Miquel, Phys. Rev. Lett. **82**, 1454 (1999); T. Ditmire, J. Zweiback, V. P. Yanovsky, *et al.*, Nature (London) **398**, 491 (1999).

8. S. Karsch, D. Habs, T. Schatz, *et al.*, Laser Part. Beams **17**, 565 (1999); V. Yu. Bychenkov, Y. Sentoku, S. V. Bulanov, *et al.*, Pis'ma Zh. Éksp. Teor. Fiz. **74**, 664 (2001) [JETP Lett. **74**, 586 (2001)].

9. J. C. Kieffer, J. P. Matte, H. Pepin, *et al.*, Phys. Rev. Lett. **68**, 480 (1992); J. D. Kmetec, C. L. Gordon III, J. J. Macklin, *et al.*, Phys. Rev. Lett. **68**, 1527 (1992); F. Beg, A. R. Bell, A. E. Dangor, *et al.*, Phys. Plasmas **4**, 447 (1997); P. Norreys, M. Santala, E. Clark, *et al.*, Phys. Plasmas **6**, 2150 (1999).

10. S. V. Bulanov, F. Califano, G. I. Dudnikova, *et al.*, Rev. Plasma Phys. **22**, 227 (2001).

11. Yu. A. Berezin and V. A. Vshivkov, *Particle Method in the Dynamics of Rarefied Plasma* (Nauka, Novosibirsk, 1980); R. W. Hockney and J. W. Eastwood, *Computer Simulation Using Particles* (McGraw-Hill, New York, 1981).

12. J. Denavit, Phys. Rev. Lett. **69**, 3052 (1992); W. S. Lawson, P. W. Palumbo, and D. J. Larson, Phys. Plasmas **4**, 788 (1997).

13. K. Krushelnik, E. L. Clark, R. Allot, *et al.*, IEEE Trans. Plasma Sci. **28**, 1184 (2000).

14. M. Roth, T. E. Cowan, M. H. Key, *et al.*, Phys. Rev. Lett. **86**, 436 (2001).

15. V. Yu. Bychenkov, V. Rozmus, A. Maksimchuk, *et al.*, Fiz. Plazmy **27**, 1076 (2001) [Plasma Phys. Rep. **27**, 1017 (2001)].

16. S. V. Bulanov and V. S. Khoroshkov, Fiz. Plazmy **28**, 493 (2002) [Plasma Phys. Rep. **28**, 453 (2002)]; S. V. Bulanov and V. S. Khoroshkov, Med. Fiz. **1** (13), 50 (2002).

17. S. V. Bulanov, T. Zh. Esirkepov, V. S. Khoroshkov, *et al.*, Phys. Lett. A **299**, 240 (2002).

18. M. Borghesi, A. Schiavi, D. H. Campbell, *et al.*, Plasma Phys. Controlled Fusion **43**, 267 (2001); M. Borghesi, D. H. Campbell, A. Schiavi, *et al.*, Phys. Plasmas **9**, 2214 (2002); M. Borghesi, S. Bulanov, D. H. Campbell, *et al.*, Phys. Rev. Lett. **88**, 135002 (2002).

19. V. S. Khoroshkov and E. I. Minakova, Eur. J. Phys. **19**, 523 (1998).

20. S. Atzeni, M. Temporal, and J. J. Honrubia, Nucl. Fusion **42**, L1 (2002); M. Temporal, J. J. Honrubia, and S. Atzeni, Phys. Plasmas **9**, 3098 (2002).

21. A. Likhtenberg, *Particle Dynamics in Phase Space* (Atomizdat, Moscow, 1972).

22. W. S. Varnum, N. D. Delamater, S. C. Evans, *et al.*, Phys. Rev. Lett. **84**, 5153 (2000).

23. J. Badziak, E. Woryna, P. Parys, *et al.*, Phys. Rev. Lett. **87**, 215001 (2001).

24. Ph. Balcou, G. Grillon, S. Moustaizis, *et al.*, in *Proceedings of the 2nd International Conference on Superstrong Fields in Plasmas, Varenna, 2001*, Ed. by M. Lontano, G. Mourou, O. Svelto, and T. Tajima (Am. Inst. of Physics, New York, 2002), p. 244 [AIP Conf. Proc. **611**, 244 (2002)].

25. L. D. Landau and E. M. Lifshits, *Electrodynamics of Continuous Media* (Nauka, Moscow, 1982; Pergamon, New York, 1960).

26. R. B. Miller, *Introduction to the Physics of Intense Charged Particles Beams* (Plenum, New York, 1982; Mir, Moscow, 1984).

27. D. O. Gerike, M. Schlanges, and Th. Bornath, Phys. Rev. E **65**, 36406 (2002); A. I. Larkin, Zh. Éksp. Teor. Fiz. **37**, 264 (1959); J. F. Ziegler, J. Appl. Phys. **85**, 1249 (1999).

28. I. S. Gradshteyn and I. M. Ryzhik, *Tables of Integrals, Sums, Series, and Products* (Nauka, Moscow, 1971; Academic, New York, 1980).

29. G. Kraft, Physica Medica **XVII**, Suppl. 1, 13 (2001); U. Amaldi, Physica Medica **XVII**, Suppl. 1, 33 (2001); M. Goiten, A. J. Lomax, and E. S. Pedroni, Phys. Today **55**, 45 (2002).

30. D. Bauer and P. Mulser, Phys. Rev. A **59**, 569 (1999).

31. T. Ditmire, T. Donelly, A. M. Rubenchik, *et al.*, Phys. Rev. A **53**, 3379 (1996); T. Ditmire, J. W. G. Tisch, E. Springate, *et al.*, Nature (London) **386**, 54 (1997); S. Dobozh, M. Shmidt, M. Pedriks, *et al.*, Pis'ma Zh. Éksp. Teor. Fiz. **68**, 454 (1998) [JETP Lett. **68**, 485 (1998)]; J. Zweiback, R. A. Smith, T. E. Cowan, *et al.*, Phys. Rev. Lett. **84**, 2634 (2000); A. I. Magunov, T. A. Pikuz, I. Yu. Skobelev, *et al.*, Pis'ma Zh. Éksp. Teor. Fiz. **74**, 412 (2001) [JETP Lett. **74**, 375 (2001)]; T. Tajima, Y. Kishimoto, and M. C. Downer, Phys. Plasmas **6**, 3759 (1999); K. Nishihara, H. Amitani, M. Murakami, *et al.*, Nucl. Instrum. Methods Phys. Res. A **464**, 98 (2001); Y. Kishimoto, T. Masaki, and T. Tajima, Phys. Plasmas **9**, 589 (2002).

32. A. V. Gurevich, L. V. Pariĭskaya, and L. P. Pitaevskiĭ, Zh. Éksp. Teor. Fiz. **49**, 647 (1965) [Sov. Phys. JETP **22**, 449 (1966)]; A. V. Gurevich and A. P. Meshcherkin, Zh. Éksp. Teor. Fiz. **80**, 1810 (1981) [Sov. Phys. JETP **53**, 937 (1981)]; Fiz. Plazmy **8**, 502 (1982) [Sov. J. Plasma Phys. **8**, 283 (1982)]; S. G. Gitomer, R. D. Jones, F. Begay, *et al.*, Phys. Fluids **29**, 2679 (1986); V. E. Kovalev, V. Yu. Bychenkov, and V. T. Tikhonchuk, Pis'ma Zh. Éksp. Teor. Fiz. **74**, 12 (2001) [JETP Lett. **74**, 10 (2001)].

33. L. D. Landau and E. M. Lifshitz, *Course of Theoretical Physics*, Vol. 2: *The Classical Theory of Fields* (Nauka, Moscow, 1988; Pergamon, Oxford, 1975).

34. A. W. Chao, R. Pittman, T. Tajima, and D. Yeremian, Preprint No. SLAC-PUB-9189, 04 (Stanford Linear Accelerator Center, Stanford, CA, 2002).

35. M. Roth, T. E. Cowan, J. C. Gauthier, *et al.*, in *Proceedings of the 2nd International Conference on Superstrong Fields in Plasmas, Varenna, 2001*, Ed. by M. Lontano, G. Mourou, O. Svelto, and T. Tajima (Am. Inst. of Physics, New York, 2002), p. 199 [AIP Conf. Proc. **611**, 199 (2002)].

36. T. Zh. Esirkepov, Comput. Phys. Commun. **135**, 144 (2001).

37. S. V. Bulanov, I. N. Inovenkov, V. I. Kirsanov, *et al.*, Phys. Fluids B **4**, 1935 (1992); Phys. Scr. **47**, 209 (1993).

38. S. V. Bulanov, T. Zh. Esirkepov, N. M. Naumova, *et al.*, IEEE Trans. Plasma Sci. **24**, 393 (1996); S. V. Bulanov, V. A. Vshivkov, G. I. Dudnikova, *et al.*, Fiz. Plazmy **23**, 284 (1997) [Plasma Phys. Rep. **23**, 259 (1997)]; A. V. Vshivkov, N. M. Naumova, F. Pegoraro, and S. V. Bulanov, Phys. Plasmas **5**, 2727 (1998).

Translated by G.V. Shepekina

Diagnostics of a Magnetized Plasma by the Field of Surface Waves Guided by a Discharge Channel

S. B. Bodrov and G. A. Markov

Lobachevsky State University, pr. Gagarina 23, Nizhni Novgorod, 630950 Russia
Received April 8, 2002; in final form, June 4, 2002

Abstract—A diagnostic method for determining plasma density from the dispersion of surface waves guided by a discharge channel in an axial magnetic field is discussed. The diagnostic characteristics that are the easiest to record experimentally are determined by analyzing the theoretical dispersion curves, and the ways of exploiting these characteristics for plasma diagnostics are suggested. To determine the slowing-down factor of a probing wave in a plasma channel, it is proposed to use diagnostic-signal resonances that occur when the wavelength of the slowed wave becomes equal to the length of the emitting or receiving antenna. The dependence of the plasma density averaged over the cross section of the plasma column on the strength of the external magnetic field is determined for a discharge channel formed as a result of the ionization self-channeling of plasma (lower hybrid) waves and whistlers. © *2002 MAIK "Nauka/Interperiodica"*.

1. INTRODUCTION

By now, the wave diagnostics of comparatively dense plasmas with spatial scales much longer than the wavelength of the probing wave have been developed fairly well [1]. In this case, the geometrical-optics approximation can be used, which considerably simplifies the calculation of the parameters to be determined. Also, in such plasmas, the phase increments of the probing and scattered waves are sufficiently large, which simplifies experimental measurements. To diagnose low-density plasmas in thin tubes, resonance and waveguide methods have been developed, in which the parameters are calculated using perturbation theory. However, it is not always convenient to determine the parameters of moderate-power (≤ 1 kW) RF discharge plasmas by means of waveguide systems because, on the one hand, the metal components of such systems can strongly perturb the structure of the RF fields exciting the discharge and, on the other hand, the plasma parameters are such that the applicability conditions of perturbation theory are usually impossible to satisfy, which significantly complicates the calculations. For the same reasons, it is undesirable to use electric probes that are galvanically coupled with the electric circuits supplying them. Probe diagnostics are especially difficult to apply to Helicon discharge plasmas [2] because of the complexity of calculating the current–voltage characteristics of the probes in a strong magnetic field. The use of open resonators is restricted to cases of sufficiently high plasma densities in discharges ($N_e \geq 10^{13}$ cm^{-3}) [1]. For cases where the wavelength of the probing wave is on the order of the plasma dimensions and larger, the plasma density is relatively low ($N_e \leq 10^{12}$ cm^{-3}), and the magnetic field is fairly strong ($B_0 \geq$

1 kG), precise methods for determining the plasma parameters have not yet been developed.

In this paper, we analyze the potentialities of a method for diagnosing RF discharge plasmas in magnetic fields by means of surface waves guided by a discharge channel. The structure and dispersion properties of the wave fields guided by a plasma column have been investigated in many papers (see, e.g., [3, 4]). However, the knowledge of the waveguide properties of a discharge channel is as yet insufficient to determine the plasma parameters (possibly because the dispersion of the probing wave in the channel is difficult to determine experimentally). Here, we calculate the dispersion characteristics of waves and the wave field structures for a cylindrical plasma column in an axial magnetic field under conditions typical of laboratory experiments. We analyze the effect of the dielectric and metal walls of the discharge tube on the dispersion curves. We present the diagnostic characteristics and propose a method for measuring the plasma density in the channel. We describe our experiments aimed at determining the dependence of the amplitude of a diagnostic signal propagating along the discharge on the magnetic field and on the plasma density N_e. We use the experimental data and the dispersion characteristics to determine the plasma density in a discharge channel formed during the ionization self-channeling of plasma waves in a magnetic field [5, 6]. Such a discharge is similar to helicon discharges excited in the same frequency range by whistlers [2]; the main difference is the use of plasma (lower hybrid) waves, which interact most efficiently with the electrons of the discharge plasma. When the plasma density exceeds a certain level [7, 8], the whistlers begin to propagate in a wave–plasma discharge [9]. If the amplitude of the whistler electric field is sufficiently large to maintain the plasma density at the

required level, then the whistlers in the channel can undergo ionization self-channeling [10] and a helicon discharge separated from the discharge chamber wall can form.

2. THEORETICAL JUSTIFICATION OF THE MEASUREMENT METHOD

The simplest model for describing the propagation of surface waves along the plasma column of the discharge is the model of a long uniform plasma cylinder in free space, without allowance for the effect of the discharge chamber wall. The derivation of the dispersion relation in this model is described in a number of papers (see, e.g., [3]). Here, we present the dispersion relation and the set of the dispersion curves that allow us to determine the diagnostic features and to estimate the plasma parameters in the discharge from the cutoff frequency or to evaluate them with a given accuracy from a comparison between the measured and calculated slowing-down factors of the probing surface waves.

If the slowing-down factor of the wave is relatively small (i.e., the electron thermal velocities are negligible in comparison with the wave phase velocity ($V_e \ll V_{ph}$)), then the properties of the plasma in a constant magnetic field directed along the z-axis can be described in terms of the following dielectric tensor $\hat{\varepsilon}$ [7]:

$$\hat{\varepsilon} = \begin{pmatrix} \varepsilon & -ig & 0 \\ ig & \varepsilon & 0 \\ 0 & 0 & \eta \end{pmatrix},$$

where $\varepsilon = 1 - \dfrac{\omega_p^2(\omega - i\nu)}{\omega((\omega - i\nu)^2 - \omega_H^2)}$, $g = \dfrac{\omega_p^2 \omega_H}{\omega((\omega - i\nu)^2 - \omega_H^2)}$, $\eta = 1 - \dfrac{\omega_p^2}{\omega(\omega - i\nu)}$, $\omega_p = (4\pi e^2 N_e/m)^{1/2}$ is the electron plasma frequency; $\omega_H = eB_0/cm$ is the electron gyrofrequency; ν is the effective electron collision frequency; and e and m are the charge and mass of an electron, respectively. Since we are interested in the high-frequency range, we neglect the effect of the plasma ions in the expressions for the elements of the dielectric tensor $\hat{\varepsilon}$. In what follows, collisions are neglected; hence, we set $\nu = 0$ in the expressions for ε, g, and η.

We consider axisymmetric ($\partial/\partial\varphi = 0$) waves propagating along a plasma cylinder of radius a. We represent the electric and magnetic fields in the wave in the form $\mathbf{E}(r, z) = \mathbf{E}(r)\exp(i\omega t - ipk_0 z)$ and $\mathbf{H}(r, z) = \mathbf{H}(r)\exp(i\omega t - ipk_0 z)$, where $k_0 = \omega/c = 2\pi/\lambda_0$ is the wavenumber in free space, p is the slowing-down factor of the wave, and r is the distance from the z-axis, which is the symmetry axis of the cylinder. Then, from Max-

well's equations, the boundary conditions on the side surface of the plasma column ($r = a$), and the condition that the field decreases exponentially at $r > a$, we obtain the dispersion relation [3]

$$\frac{(y_+ + Z\eta)(y_- + Z)}{(y_- + Z\eta)(y_+ + Z)} = \frac{\mu_-}{\mu_+}, \tag{1}$$

where $y_\pm = \dfrac{k_\pm J_0(k_\pm a)}{J_1(k_\pm a)}$, $Z = \dfrac{k_\nu K_0(k_\nu a)}{K_1(k_\nu a)}$, $k_\pm^2 = \dfrac{\chi_1^2 + \chi_2^2}{2} \pm \sqrt{(\chi_1^2 - \chi_2^2)^2 + 4\gamma_1\gamma_2}$, $k_\nu = k_0\sqrt{p^2 - 1}$, $\mu_\pm = \dfrac{k_\pm^2 - \chi_1^2}{\gamma_1}$, $\chi_1^2 = \dfrac{k_0^2}{\varepsilon}[\varepsilon(\varepsilon - p^2) - g^2]$, $\chi_2^2 = \dfrac{k_0^2}{\varepsilon}\eta(\varepsilon - p^2)$, $\gamma_1 = \dfrac{k_0^2}{\varepsilon}g$, $\gamma_2 = \dfrac{k_0^2}{\varepsilon}p^2 g\eta$, $J_n(kr)$ is the nth-order Bessel function of the first kind, and $K_n(kr)$ is the nth-order modified Bessel function of the second kind.

Dispersion relation (1) determines the dependence of the slowing-down factor of surface waves propagating along the discharge on the following parameters of the system: the frequency ω of the probing wave, the magnetic field B_0, the plasma density N_e, and the radius a of the plasma column. In the general case, it is impossible to solve dispersion relation (1) analytically and to obtain a simple analytic dependence $p(\omega)$. In [3], this dispersion relation was analyzed qualitatively for some limiting cases. For diagnostic purposes, it is important to know the numerical values of the slowing-down factor as a function of the parameters of the problem, in particular, in the case where the frequencies ω_p, ω, and ω_H are of the same order of magnitude and change in the course of the experiment and the radius of the plasma column is small in comparison with the wavelength of the probing wave ($a < \lambda_0$). Note that this case is of great interest from the experimental standpoint.

The results of solving dispersion relation (1) numerically are presented in Figs. 1–4. Figures 1a and 1b show the slowing-down factor p of a surface wave a function of the signal frequency in the ranges $\omega_p < \omega_H$ and $\omega_p > \omega_H$, respectively. The calculations were performed for $\omega_p = 2 \times 10^{10}$ rad/s and $a\omega_p/c = 1.6$. In these figures, we have introduced the notation $\omega_{UH} = (\omega_p^2 + \omega_H^2)^{1/2}$ for the limiting frequency, which is equal to the upper hybrid frequency. The solid curve 0 refers to the fundamental axisymmetric mode. Inside the plasma cylinder, the axial component E_z of the electric field of this mode depends weakly on radius and the dependence of the radial electric-field component E_r on radius is nearly linear. The dashed curves 1, 2, and 3 refer to the higher order modes, for which the dependence $E_z(r)$ has one or more zeros in the plasma region. Figures 2a and 2b show an example of the radial distri-
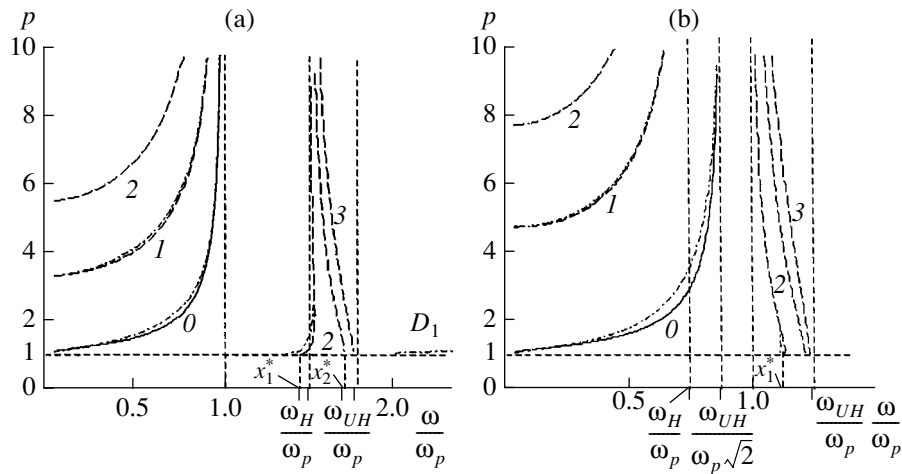
Fig. 1. Slowing-down factor p of axisymmetric waves vs. signal frequency ω for (a) $\omega_H > \omega_p$ ($\omega_H/\omega_p = 1.5$) and (b) $\omega_H < \omega_p$ ($\omega_H/\omega_p = 0.75$). The calculations were performed for $\omega_p = 2 \times 10^{10}$ rad/s and $a\omega_p/c = 1.6$. Curve 0 is for the fundamental axisymmetric mode, and curves 1–3 are for the higher order modes with the dimensionless limiting frequencies $x^*_{1,2} = \sqrt{1 + \omega_H^2/(\omega_p^2(1 + Y_{1,2}^2))}$, where $Y_{1,2} = a\omega_p/(c\vartheta_{1,2})$ and ϑ_n is the nth root of the zero-order Bessel function. In this and other figures, the dashed-and-dotted curves show the effect of the quartz wall of the discharge tube with the radius $R = 3$ cm on the dispersion of the fundamental and higher order axosymmetric modes of a plasma column. Curve D_1 is the dispersion curve of the dielectric mode guided by the tube wall.
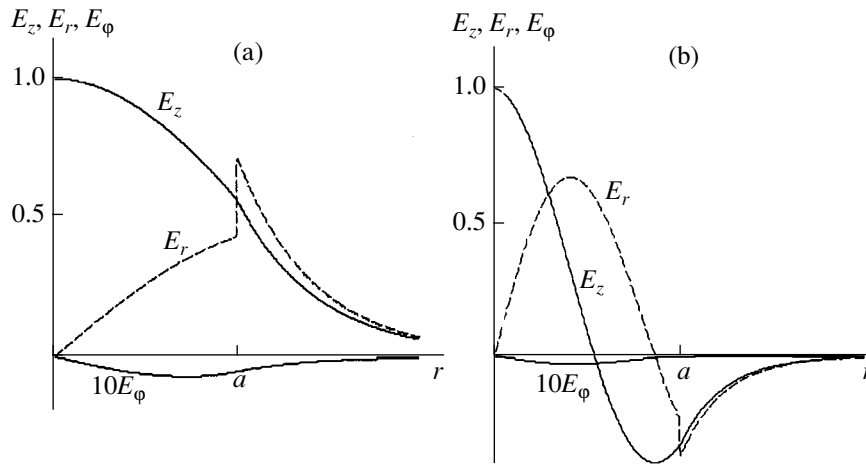

Fig. 2. Radial profiles of the electric fields of (a) the fundamental axisymmetric mode and (b) the first higher order axisymmetric mode for $\omega/\omega_H = 0.5$, $\omega_p/\omega_H = 0.7$, and $a/\lambda_0 \sim 0.1$.

bution of the axial, radial, and azimuthal components of the electric fields of the fundamental axisymmetric surface mode and the first higher order axisymmetric surface mode, respectively. In Fig. 2a, the axial component E_z of the electric field of the fundamental axisymmetric mode is seen to decrease toward the plasma boundary. However, the plasma parameters may be such that the amplitude of the axial electric-field component increases as approaching the boundary (the field is localized near the boundary), which is characteristic of true surface wave. It is worth noting that the azimuthal component of the electric field of all axisymmetric modes is small in comparison with the other field components.

The plots shown in Fig. 1 demonstrate that axisymmetric surface waves guided by a plasma cylinder can propagate only in a limited frequency band. The frequency band in which the fundamental axisymmetric
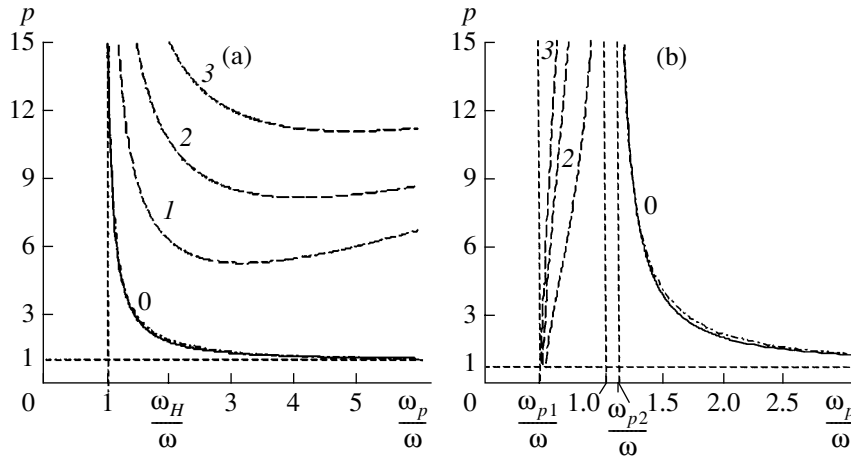
Fig. 3. Slowing-down factor p vs. plasma frequency ω_p at $a/\lambda_0 = 0.1$ and $\omega = 10^{10}$ rad/s for (a) $\omega_H > \omega$ ($\omega_H/\omega = 2$) and (b) $\omega_H < \omega$ ($\omega_H/\omega = 0.8$). Curve 0 is for the fundamental axisymmetric mode, and curves 1–3 are for the higher order axisymmetric modes. Other notation is $\omega_{p1} = \sqrt{\omega^2 - \omega_H^2}$ and $\omega_{p2} = \sqrt{2\omega^2 - \omega_H^2}$.

Fig. 4. Slowing-down factor p vs. electron gyrofrequency ω_H at $a/\lambda_0 = 0.1$ and $\omega = 10^{10}$ rad/s for (a) $\omega_p < \omega$ ($\omega_p/\omega = 0.8$), (b) $\omega < \omega_p < \sqrt{2}\omega$ ($\omega_p/\omega = 1.3$), and (c) $\omega_p > \sqrt{2}\omega$ ($\omega_p/\omega = 1.5$). Curve 0 is for the fundamental axisymmetric mode, and curves 1–3 are for the higher order axisymmetric modes. Other notation is $\omega_{H1} = \sqrt{\omega^2 - \omega_p^2}$ and $\omega_{H2} = \sqrt{2\omega^2 - \omega_p^2}$.
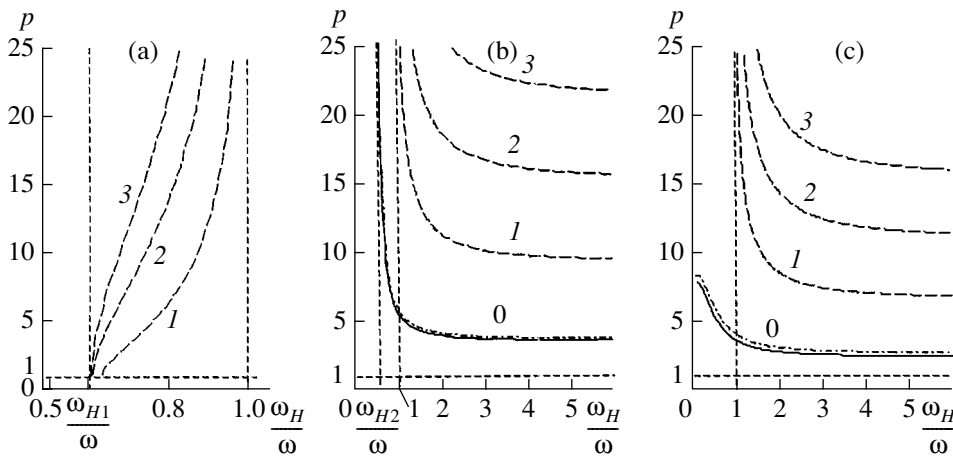
mode can exist is limited from above by $\omega = \omega_{UH}/\sqrt{2}$ for $\omega_p > \omega_H$ and by $\omega = \omega_p$ for $\omega_H > \omega_p$. The band in which the higher order modes can propagate comprises two characteristic frequency ranges. In the first range $\omega < \min(\omega_p, \omega_H)$, the slowing-down factor of these modes increases monotonically with frequency. In the second range $\min(\omega_p, \omega_H) < \omega < \omega_{UH}$, the behavior of the dispersion curves of the higher order modes is more complicated. When the slowing-down factors are large, the dispersion curves approach the frequency $\max(\omega_p, \omega_H)$. The corresponding modes are backward-

propagating waves ($\partial p/\partial \omega < 0$). For $p = 1$, the limiting frequency for the nth-order mode is equal to [3] $\omega_n^* = \sqrt{\omega_p^2 + \dfrac{\omega_H^2}{(1 + Y_n^2)^2}}$, where $Y_n = a\omega_p/(c\vartheta_n)$ and ϑ_n is the nth root of the zero-order Bessel function of the first kind. This formula implies that, for $\omega_1^* > \omega_H$, which corresponds to small values $Y \ll 1$ (a narrow plasma cylinder), the dispersion curves of the higher order modes lie in the frequency range $\max(\omega_p, \omega_H) < \omega <$

ω_{UH}. As Y increases, the dispersion of the higher order modes can change and a forward-propagating wave can appear at small p values. In this case, the frequency ω^* is shifted toward lower frequencies and, for $\omega_H > \omega_p$, it becomes lower than ω_H. Consequently, for $\omega_H > \omega_p$ and sufficiently large values of Y, the second frequency range for the higher order modes is limited from below by ω^*. For $\omega_H < \omega_p$, the limiting frequency ω^* lies within the range $\max(\omega_p, \omega_H) < \omega < \omega_{UH}$. Note that, in dispersion relation (1), the ion motion is neglected; hence, the range of validity of the relation is limited from below by the frequency $\omega \gg (\omega_H \Omega_H)^{1/2}$, where Ω_H is the ion gyrofrequency.

Figures 3a and 3b show the slowing-down factors p as a function of the plasma frequency ω_p in the ranges $\omega < \omega_H$ and $\omega > \omega_H$, respectively. Figures 4a, 4b, and 4c show the slowing-down factor p as a function of the electron gyrofrequency ω_H in the ranges $\omega_p < \omega$, $\omega < \omega_p < \sqrt{2}\,\omega$, and $\omega_p > \sqrt{2}\,\omega$, respectively. In Figs. 3 and 4, we have introduced the notation $\omega_{p1} = (\omega^2 - \omega_H^2)^{1/2}$, $\omega_{p2} = (2\omega^2 - \omega_H^2)^{1/2}$, $\omega_{H1} = (\omega^2 - \omega_p^2)^{1/2}$, and $\omega_{H2} = (2\omega^2 - \omega_p^2)^{1/2}$ and denoted the curves in the same manner as in Fig. 1. The dispersion curves in Figs. 3 and 4 are calculated for $\omega = 10^{10}$ rad/s and $a/\lambda_0 = 0.1$. As the ratio a/λ_0 increases (all other conditions being the same), the slowing-down factor decreases. For $a/\lambda_0 \sim 1$, we can use the plane boundary approximation. Another limiting case corresponds to the electrostatic wave approximation for a narrow waveguide [3]. This approximation can be used to calculate the slowing-down factor under the conditions $pa/\lambda_0 \ll 1$ and $p \gg 1$, which are satisfied only for very narrow waveguides ($a/\lambda_0 < 10^{-2}$) and for $\omega \sim \omega_p$. The set of dispersion curves presented in Figs. 1, 3, and 4 is helpful for diagnostic purposes because it makes it possible to choose the measurement method, the required frequency of the diagnostic signal, and the corresponding antenna devices.

Based on the dispersion curves obtained above, we can draw conclusions about the diagnostic characteristics related to the propagation of surface waves. As was already noted, the dispersion curves in Figs. 1, 3, and 4 show the frequency ranges where the wave is propagating and the ranges in which is evanescent. By varying the probing frequency ω, it is possible to experimentally determine the boundaries of the opaque region and, then, to determine the plasma density from the boundary frequencies. If the probing frequency is difficult to vary over a broad band in actual experiments, one can vary other parameters of the problem, e.g., the magnetic field or the plasma density.

The above method, which is similar to the cutoff method [1], is fairly rough because the boundaries of the ranges in which the surface waves exist are smoothed out due to collisions ($\nu \neq 0$) and plasma non-uniformity. More precise results can be obtained by comparing the theoretical and experimental dispersion characteristics. Here, we propose to determine these characteristics by the resonance method, whose implementation requires an antenna with pronounced resonant properties, e.g., an antenna capable of exciting waves with a maximum amplitude when the wavelength λ_s of the slowed wave is equal to the antenna length. In our experiments, we used an antenna consisting of three coaxial wire rings with their centers at the symmetry axis. The distances between the neighboring rings were the same (40 mm). The total length of the antenna was $l_a = 80$ mm. When the central and end rings are supplied in antiphase, the waves with a wavelength of $\lambda_s \approx l_a = 80$ mm are excited most efficiently. The antenna so supplied also emits short-wavelength (plasma) waves whose wavelengths λ are approximately equal to the diameter of the wire ring. These waves, however, are strongly damped because the characteristic attenuation scale Λ is proportional to the wavelength λ ($\Lambda \sim \lambda\omega/\nu$). Varying one of the parameters of the problem (the signal frequency or the magnetic field), we were able to measure the dependence of the amplitude of the excited wave on this parameter; to determine the positions of the maxima (resonances); and, knowing the slowing-down factor $p_{res} = \lambda_0/\lambda_s = \lambda_0/l_a$ of the wave, to calculate ω_p from dispersion relation (1).

Let us estimate how the discharge chamber wall affects the propagation of surface waves along the plasma column. We consider a uniform plasma column of radius a in a glass tube with the outer radius R, wall thickness d, and dielectric constant ε_g. In this case, we can divide the region in which the wave fields are examined into four domains, find the solution for each of them, and match the solutions at the domain boundaries. From the boundary conditions, we then obtain a set of linear homogeneous equations. Equating the determinant of the 12×12 matrix corresponding to these equations to zero, we arrive at the desired dispersion relation. However, since this relation is very awkward, we do not write it out here and, instead, concentrate on its numerical analysis.

The presence of a dielectric layer leads to the following two effects: the change in the dispersion of the modes considered above and the appearance of new modes, namely, those guided by a dielectric waveguide. It is known from the theory of dielectric waveguides that the frequency range in which axisymmetric surface waves can propagate is limited by a certain limiting frequency [11]. This frequency is determined by the dielectric constant of the waveguide and the characteristic dimensions of the dielectric layer. A numerical analysis of the dispersion relations in the case of quartz (glass) discharge tubes ($\varepsilon_g \sim 4$ and $R \sim 3$ cm) shows that the wave fields guided by the tube wall should be taken into account only under the condition $d\sqrt{\varepsilon_g}/\lambda_0 \geq 10^{-1}$,

i.e., when the frequency of the diagnostic signals is $f > 5$ GHz, the wall thickness being $d \sim 2$ mm. The slowing-down factor of these waves, which will be referred to as "dielectric" modes, lies in the range $1 \leq p \leq \sqrt{\varepsilon_g}$. In our problem, the dielectric waveguide contains a magnetized plasma, which can affect the dispersion of these dielectric modes only when the radius of the plasma column is comparable to the tube radius ($a \sim R$). In Figs. 1, 3, and 4, the dispersion curves of the fundamental axisymmetric mode and the first higher order axisymmetric mode are shown by the dashed-and-dotted lines, which were calculated with allowance for the effect of the tube wall. Curve $D1$ in Fig. 1 shows the initial portion of the dispersion curve of the "dielectric" mode, whose electric field structure inside the dielectric is typical of a quasi-TE-wave.

The dispersion of the fundamental axisymmetric mode is affected by the dielectric only slightly. Numerical calculations performed for a quartz wall with $d \sim 2$ mm and $R \sim 5a/4$ show that the dispersion curve of the fundamental axisymmetric mode is slightly shifted upward, the maximum amount of the shift $\Delta p/p$ being less than 10%. This shift is maximum in the region in which the dispersion curve begins to increase greatly. The thicker the dielectric, the higher the dielectric constant, and the smaller the gap between the plasma column and the tube wall, the stronger the effect of the dielectric.

An analysis of the dispersion of the fundamental axisymmetric mode shows that, for $a < 2R/3$, the effect of a thin ($d \ll a, \lambda_s$) dielectric wall can be neglected. Also, it seems reasonable to limit the slowing-down factor p from above in such a way that the distance over which the plasma boundary is fuzzy be much shorter than the scale length on which the electric field decreases.

The effect of the metal wall of the discharge tube or the wall of the magnetic solenoid on the dispersion curve of the fundamental axisymmetric mode becomes important when the difference between the wall radius and the radius of the plasma column is comparable with the scale length on which the electric field decreases, $(R - a) \sim \lambda_\perp = \lambda_0/\sqrt{p^2 - 1}$ (see also [3]). In our case, the radius of the magnetic solenoid wall is greater than the plasma radius by factor of 7. As a result, in the frequency range chosen for the diagnostic method proposed here ($f > 700$ MHz), the dispersion curves of the surface waves guided by the plasma column inside the metal cylinder essentially coincide with those of the surface waves guided by the plasma column in the absence of a metal cylinder. Consequently, the dispersion curve of the fundamental axisymmetric mode can be calculated from Eq. (1), provided that the slowing-down factor of the wave is chosen appropriately ($p = 3$–7).

3. EXPERIMENTAL CONDITIONS AND MEASUREMENT RESULTS

The feasibility of determining the plasma density by using the surface waves guided by the discharge channel was studied in experiments on the ionization self-channeling of plasma waves in a magnetic field [6]. The experimental device was a quartz discharge tube 58 mm in diameter and 1500 mm in length. The working gas was air at a pressure of $P \sim 10^{-3}$ torr. The axial magnetic field B_0 was varied over a wide range (from 100 to 1300 G). The discharge was formed as a result of the self-channeling of plasma waves excited by a quadrupole antenna consisting of three coaxial rings located in the central part of the discharge tube at a distance of 60 mm from each other. An RF voltage ($U_0 = 50$ V and $f_0 = 200$ MHz) was supplied to the exciting rings of the antenna from a GST-2 oscillator in such a way that the central ring was connected to the inner conductor of the supply cable and the end rings were connected to the outer conductor of the cable. The connecting cables were symmetric with respect to the central cable. Such an antenna turned out to be a resonant source for exciting axisymmetric wave fields with an axial wavelength of about $\lambda \sim l = 120$ mm. We also observed the excitation of smaller-scale plasma waves, which was confirmed by the direct observations of the resonance cones at comparatively high pressures in the chamber ($P > 10^{-2}$ torr). As we increased the RF power W_0 supplying the discharge above 10 W and the external magnetic field B_0 above 600 G, we observed the excitation of waves with an axial wavelength equal to the period of the ring coils of the magnetic solenoid ($\lambda_\parallel = l_{\mathrm{coil}} = 30$ cm). The structure and properties of such discharges, self-localized at the axis of the exciting antenna, were described in [5, 6]. Here, we only note that, as the external magnetic field was varied, the coupling of the exciting antenna to the discharge channel changed, leading to changes in both the plasma density inside the channel and the radius of the luminous plasma column. We measured the dependence $N_e(B_0)$ by recording the behavior of the excitation and propagation of the diagnostic wave guided by the discharge plasma column.

The diagnostic signals were excited by an antenna similar to the one exciting the discharge. The diagnostic antenna was located near the end of the discharge tube and was supplied from G4-160 and G3-2 tunable oscillators. For diagnostics at frequencies $f < 1000$ MHz, the distance between the rings was chosen to be 40 mm, while for diagnostics at higher frequencies, this distance was reduced to 25 mm. In the above two cases, the total lengths of the diagnostic antenna were $l_a = 80$ and 50 mm, respectively. The diagnostic signal was recorded at the opposite end of the discharge tube by a dipole transducer, whose role was played by the extended (by $l_r = 16$ mm for $f < 1000$ MHz or 12 mm for $f > 1000$ MHz) part of the inner conductor of the
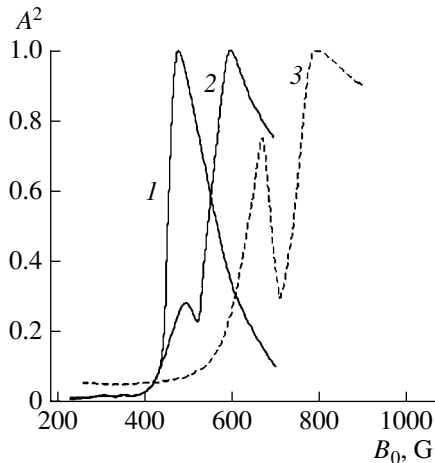
Fig. 5. An example of the experimentally obtained dependences of the squared amplitudes A^2 of the diagnostic signals (normalized to the maximum value of the squared amplitudes) on the magnetic field B_0 for the probing frequencies $f = (1)$ 700, (2) 900, and (3) 1460 MHz.
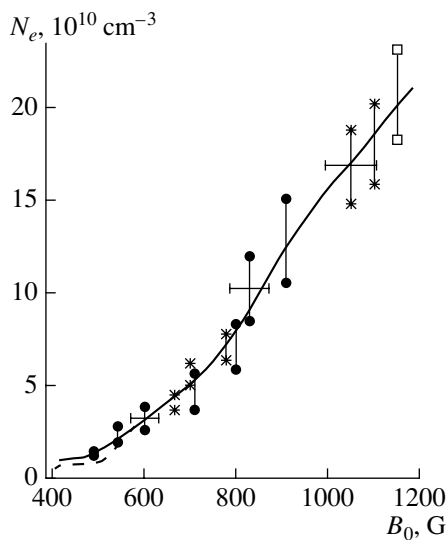

Fig. 6. Plasma density in the discharge channel as a function of the magnetic field. The circles show the N_e values calculated from the main resonance peak in the dependence $A^2(B_0)$, and the asterisks show the N_e values calculated from the secondary peak. The solid curve is obtained by averaging the experimental values of N_e, the dashed curve is the dependence $N_e(B_0)$ obtained by the dielectric waveguide method [12], and the squares show the N_e values obtained by using a 9.74-GHz microwave interferometer.

coaxial cable. The diagnostic signal was monitored by an S4-27 spectrum analyzer.

In experiments, we measured the dependence of the squared amplitude of the diagnostic wave that traveled

a distance of about 1200 mm along the plasma column of an RF discharge on the magnetic field strength. The plasma radius, required for further calculations, was determined from the visual diameter of the luminous plasma column. Figure 5 shows the representative dependences of the squared amplitude $A^2(B_0)$ of the diagnostic wave on the magnetic field. The amplitude is normalized to its maximum value. The curves were obtained from measurements at three different frequencies in the range 700–1460 MHz. A common feature of all the measured dependences is that they have pronounced peaks at magnetic fields of 480, 600, and 800 G for $f = 700$, 900, and 1460 MHz, respectively. Along with the main peaks, there are secondary peaks at weaker magnetic fields in the frequency range $f > 700$ MHz. At weak magnetic fields ($B_0 < 400$ G), we recorded low peaks, whose heights, however, are too small for them to be seen in Fig. 5. The radial profiles of the axial component of the electric field was measured by a shielded rod antenna under the conditions corresponding to the main peaks in the diagnostic signals (Fig. 5). The field amplitude is seen to decrease gradually from the axis of the plasma column toward the wall of the discharge tube and is nonzero everywhere. Consequently, we can assume that the main peaks in the curves shown in Fig. 5 are related to the resonant excitation of an axisymmetric surface mode with the wavelength $\lambda_s = l_a$. This is confirmed by direct phase measurements of the wavelength λ_s of the slowed wave. Knowing the slowing-down factor, we can use dispersion relation (1) to determine the plasma density in the discharge channel. In calculations, we took into account the dependence of the radius a of the bright (central) region of the channel on the magnetic field strength: $a(B_0 \approx 500$ G) ~ 25 mm, $a(B_0 \approx 600$ G) ~ 15 mm, $a(B_0 \approx 700$ G) ~ 13 mm, and $a(B_0 \approx 1000$ G) ~ 10 mm. In Fig. 6, the circles show the results of calculating the averaged plasma density N_e in the channel for different frequencies of the probing signal and, accordingly, for different magnetic field strengths determined from the positions of the main resonance peaks in the dependences $A^2(B_0)$. Each of the two circles at the same value of B_0 correspond to a different value of the plasma channel radius, which were used in calculations because the visual determination of the plasma boundaries was inexact. The upper circle in each pair corresponds to the smaller radius of the discharge plasma ($a - 0.2a$), and the lower circle corresponds to the larger radius ($a + 0.2a$). The dashed curve is for the dependence $N_e(B_0)$ obtained in [12] by the dielectric waveguide method for the same discharge but in a wider discharge tube. The asterisks indicate the N_e values determined from the secondary resonance peaks of the curves $A^2(B_0)$, which are related to the half-wave resonance of the receiving antenna ($\lambda_s = 2l_r$). The squares denote the N_e values obtained at a frequency of 9.74 GHz by means of a microwave interferometer [1].

4. DISCUSSION OF THE EXPERIMENTAL RESULTS

First, we note that the amplitude of the received signal depends on many factors. Here, we are considering the effect of such factors as the axial wavelength of the excited wave, the field structure of the waves, and wave damping. It is well known [4] that the electric field amplitude $A_\alpha \exp(i\omega t - ip_\alpha k_0 z)$ of the αth-order wave excited in a magnetized plasma waveguide by the electric current with the given density distribution $\mathbf{j}(r, \varphi)\exp(i\omega t)$ can be determined from Lorentz's lemma generalized to the case of gyrotropic medium [13]:

$$A_\alpha = \frac{1}{N_\alpha}\int \mathbf{j} \cdot \mathbf{E}_{-\alpha} dV; \qquad (2)$$

where N_α is the norm of the αth wave [14, 15] and $\mathbf{E}_{-\alpha}$ is the electric field of the αth wave propagating in the negative z direction in a medium described by the transposed dielectric tensor $\hat{\varepsilon}^{(T)}$ ($\hat{\varepsilon}_{ij} \longrightarrow \hat{\varepsilon}_{ji}$) [15]. In order to excite only axisymmetric wave fields, the current density distribution should be axisymmetric ($\mathbf{j} = \mathbf{j}(r)$). That is why we chose a quadrupole antenna consisting of three coaxial rings as the source of the diagnostic signal. In this case, the distribution of the exciting current density $\mathbf{j}$ in the plasma is determined by the dielectric tensor $\hat{\varepsilon}$ and by the fields of two ring capacitors fed in antiphase. The wave whose electric field is closest in structure to the antenna field is excited most efficiently. Among the modes excited by the quadrupole antenna chosen for our experiments, the amplitude of the fundamental axisymmetric mode is maximum, provided that the wavelength of the mode is close to the length of the exciting quadrupole antenna. The axial component of the electric field of the fundamental axisymmetric mode does not oscillate inside the plasma column, and the radial component increases from the column axis toward the plasma boundary and is shifted from the axial component by $\lambda/4$. The diagnostic quadrupole antenna excites waves with different wavelengths. However, fine-scale (plasma) waves are rapidly damped (see the above discussion) and waves with wavelengths of about c/f are excited inefficiently. Only when the slowing-down factor is approximately equal to the resonant value (i.e., for $\lambda_s \approx l_a$), does the amplitude of the fundamental axisymmetric mode increase sharply. Based on the above analysis, we can conclude that the main peaks in the curves shown in Fig. 5 are associated with the resonant excitation of the fundamental axisymmetric mode. Its slowing-down factor is determined by the length l_a of the diagnostic antenna: $(p_{res})_a = \lambda_0/\lambda_s \simeq \lambda_0/l_a$. This conclusion was confirmed by the experimental examination of the structure of the excited wave.

The secondary (lower) peaks in curves *2* and *3* in Fig. 5 are related to the resonances of the receiving antenna, $(p_{res})_r = \lambda_0/\lambda_s \simeq \lambda_0/2l_r$. Adjusting the length of the receiving antenna allowed us to observe its half- and quarter-wave resonances. Under the experimental conditions corresponding to Fig. 5, the secondary peaks are governed by the half-wave resonance of the receiving antenna, while the quarter-wave resonances turn out to be close to the resonance of the exciting diagnostic antenna, thereby causing an additional broadening of the main peaks in the curves in Fig. 5. The presence of several peaks in the dependences of the characteristics of the received signal on the plasma parameters or frequency makes the method more informative and more precise.

The plasma density N_e was determined from both the main and secondary peaks in the curves shown in Fig. 5. The magnetic field B_0, the radius a of the discharge tube, and the slowing-down factor $(p_{res})_a$ or $(p_{res})_r$ of the diagnostic wave were calculated from the positions of the resonance peaks in the dependence $A^2(B_0)$. Knowing these parameters, we were able to deduce the plasma density N_e in the discharge channel from dispersion relation (1).

The accuracy with which the plasma density N_e was determined was governed by the accuracy with which the channel radius was specified. From the data presented in Fig. 6, one can see that the relative error was small, $\Delta N_e/N_e < 0.3$. The error in the horizontal positions of the experimental points in the dependence $N_e(B_0)$ was governed by the nonuniformity of the external magnetic field along the discharge tube ($\Delta B/B_0 \approx 0.1$).

To increase the accuracy of the measurement, it is necessary to have more precise knowledge of the channel radius, to take into account the radial plasma density distribution in the channel, and to solve the dispersion relations for waves guided by a plasma column with fuzzy boundaries. In order to eliminate the effect of measuring devices on the RF discharge structure, it is desirable that the diagnostic signal be supplied through a directional coupler directly to the antenna that forms the discharge.

5. CONCLUSION

The results of experiments in which the plasma density in the discharge channel was determined from the observations of the resonant excitation of surface waves slowed down in a prescribed manner agree fairly well with the results obtained by means of a dielectric waveguide [12] and a microwave interferometer [1]. This agreement confirms the potential feasibility of the diagnostic method proposed here. The situation in which the main resonance peak is observed at frequencies satisfying the condition $\omega < \omega_p$, ω_H is usually easy to achieve. In this case, the plasma density is uniquely determined by the known dispersion parameters. The characteristic feature of the diagnostic method is the possibility of determining the plasma density in the parameter range in which it is difficult to use other methods. Additional diagnostic possibilities of the

method are related to the observation of the scattering of the diagnostic wave by plasma oscillations in the discharge channel [16]. The method proposed here is especially suitable for diagnosing pulsed discharges in narrow tubes such that the radius of the plasma column is determined by the tube radius. The presence of several resonance peaks in the spectra of the signals from several receiving antennas of different lengths makes it possible to determine with the desired accuracy the time dependence of the averaged plasma density in the plasma column.

ACKNOWLEDGMENTS

REFERENCES

1. V. E. Golant, in *Handbook of Plasma Physics*, Ed. by A. A. Galeev and R. Sudan (Énergoatomizdat, Moscow, 1984; North-Holland, Amsterdam, 1984), Vol. 2.

2. F. F. Chen and R. W. Boswell, IEEE Trans. Plasma Sci. **25**, 1245 (1977).

3. A. N. Kondratenko, *Plasma Waveguides* (Atomizdat, Moscow, 1976).

4. I. G. Kondrat'ev, A. V. Kudrin, and T. M. Zaboronkova, *Electrodynamics of Density Ducts in Magnetized Plasmas* (Gordon and Breach, Amsterdam, 1999).

5. G. A. Markov, V. A. Mironov, and A. M. Sergeev, Pis'ma Zh. Éksp. Teor. Fiz. **29**, 672 (1979) [JETP Lett. **29**, 617 (1979)].

6. G. A. Markov, Zh. Éksp. Teor. Fiz. **113**, 1989 (1998) [JETP **86**, 703 (1998)].

7. V. L. Ginzburg, *The Propagation of Electromagnetic Waves in Plasmas* (Nauka, Moscow, 1967; Pergamon, Oxford, 1970).

8. G. A. Markov, Fiz. Plazmy **14**, 1094 (1988) [Sov. J. Plasma Phys. **14**, 641 (1988)].

9. I. A. Vdovichenko, G. A. Markov, V. A. Mironov, and A. M. Sergeev, Pis'ma Zh. Éksp. Teor. Fiz. **44**, 216 (1986) [JETP Lett. **44**, 275 (1986)].

10. A. V. Kudrin, L. E. Kurina, and G. A. Markov, Zh. Éksp. Teor. Fiz. **112**, 1285 (1997) [JETP **85**, 697 (1997)].

11. V. F. Vzyatyshev, *Dielectric Waveguides* (Sov. Radio, Moscow, 1970).

12. I. V. Katin and G. A. Markov, Izv. Vyssh. Uchebn. Zaved., Radiofiz. **42**, 215 (1999).

13. V. V. Nikol'skiĭ, *Variational Methods for Internal Problems of Electrodynamics* (Nauka, Moscow, 1967).

14. L. A. Vainshtein, *Electromagnetic Waves* (Radio i Svyaz', Moscow, 1988), p. 300.

15. A. B. Manenkov, Izv. Vyssh. Uchebn. Zaved., Radiofiz. **24**, 84 (1981).

16. G. A. Markov and I. V. Khazanov, Fiz. Plazmy **28**, 307 (2002) [Plasma Phys. Rep. **28**, 274 (2002)].

Translated by G.V. Shepekina